Surface Brillouin scattering studies of elastic properties of materials at high temperature

A THESIS
SUBMITTED TO THE FACULTY OF SCIENCE,
UNIVERSITY OF THE WITWATERSRAND,
JOHANNESBURG,
IN FULFILMENT OF THE REQUIREMENTS
FOR THE DEGREE OF
DOCTOR OF PHILOSOPHY

Bhekumusa Abraham Mathe
Johannesburg, May 2008

I declare that this thesis is my own, unaided work. It is being submitted for the Degree of Philosophy in the University of the Witwatersrand, Johannesburg. It has not been submitted before for any degree or examination in any other University or Higher Education Institution.

(Signature of candidate)

Abstract

Brillouin scattering from surfaces, more often called surface Brillouin scattering (SBS) has been widely used to investigate elastic properties of thin films, interfaces, layered systems. In this thesis, the focus is on bulk specimens, ranging from large oriented crystals to polycrystalline layers. Well-characterised titanium alloys (TiC and TiCN) are shown to have elastic moduli that obey the quasi-harmonic approximation while retaining their refractory properties. Iron (IV) sulphide, is investigated at ambient and high temperatures where it is demonstrated that the elastic constant C_{12} has a positive value even at high temperatures, and comparison of the high temperature elastic constants data to theoretical results obtained from models developed by Sithole et. al. shows reasonably good agreement. An amorphous boron carbide film deposited on silicon is shown to undergo a phase change at about 350 - 400^{o}C to a possibly nanocrystalline state, a process that is accompanied by an increase in Young's modulus of about 14 GPa from ambient value. The combination of SBS dispersion results and Green's function analysis of organ-pipe modes observed for the boron carbide film, has the potential of being used to extract elastic constants of thin layers, where appropriate conditions for the observation of these modes are met by the layer/substrate system. An agreement to within 6% between elastic moduli determined using SAWs and with those extracted from organ-pipe modes demonstrates the applicability of this approach to the analysis of some layered systems. Boron-doped polycrystalline silicon (polysilicon in short) is a popular MEMS structural material, and high temperature measurements of this material are reported for the first time for the temperature range beyond 100^{o}C where the Young's moduli is observed to remain consistent at about 163 GPa. The increase in bulk modulus observed at about 300^{o}C is associated with growth of crystallites as a result of the very long thermal-soaking periods. High temperature Raman measurements conducted parallel to the SBS measurements show an unusual recovery of the asymmetry of the Fano-line shape on cooling down to room temperature. Grain boundary diffusion of the smaller boron atoms and lattice relaxation effects are considered to explain the phenomenon, and the results are related to the corresponding SBS elasticity measurements.

Acknowledgements

First and foremost, I would like to thank Prof. Darrell Comins and Prof Arthur Every for their total support, guidance, enthusiasm and for being there when I needed their expertise and moral support. Specifically, Prof Comins for his constant optimism, thoughtfulness and experience, especially during hard times in the laboratory and Prof. Every for the exceptional insights during consultations and his input to all the computational work that is so indispensable to experimental SBS. Special mention must be made of a dear colleague Dr Spirit Tlali (from National University of Lesotho) for introducing me to the Brillouin scatttering equipment and teaching me how to be patient, persevering and kind to it, for which Iam very thankful to him.

I should mention the indispensable services of the Physics Workshop personnel including John Augustine, Shaun Reikert and Andrew Carpede for the water cooling systems and pumps respectively, not forgetting the excellent machining skills of Bernard Kwashira, for being there when I needed them and also for the very useful technical discussions that solved many a problem in the laboratory. Many thanks are also due to Prof. Ludwig Schöning for useful discussions on x-ray experimentation and analysis, hence drawing on his huge wealth of knowledge in the subject. Special thank you to the following, Tony Voorvelt (senior electronics Technician), fellow graduate students, George Amolo, Rudolph Erasmus, Kibreab Haile, Clemence Sumanya, Thulani Kubeka; their relationship during this project was indispensable. Finally, I am very grateful for the financial assistance of the following institutions: National Research Foundation, Andrew Mellon Foundation, University of the Witwatersrand Post Graduate Merit Award and the DST/NRF Centre of Excellence Bursary; and most of all to my wife, Nobuhle and the children for putting up with me during this project.

Dedication

To all who inspired me.....

Contents

List of Figures

Chapter 1

1. Introduction

Brillouin light scattering is generally referred to as the inelastic scattering of an incident optical light beam by thermally excited acoustic waves in a sample. Brillouin (1914) [1.1] and Mandel'shtam (1926) [1.2] first investigated this subject independently for the case of scattering from transparent materials. They combined the Bragg reflection and Doppler shift to predict the appearance of frequency shifts in the spectrum of scattered light as a result of periodic perturbations generated by the passage of sound waves. These frequency shifts were experimentally observed by Gross [1.3] and later confirmed by Meyer and Ramm [1.4]. The advent of the laser opened new research areas for Brillouin scattering and widened the scope of application to such areas as characterising elastic and elasto-optic bulk properties of materials.

The concept of surface waves and the earliest writings on the subject go back to the famous paper by Lord Rayleigh (1887)[1.5], which stimulated much research and application in the field of geosciences over the following decades. In this context, surface - guided waves have been studied by Lamb (1904) [1.7] and by Love (1911) [1.8] in unsupported plates and by Sezawa (1927) [1.9] in supported plates. By extension, an interface wave is a simple generalisation of the surface wave, where the second medium is not a vacuum, and the wave propagates along the boundary between two media, a subject that was pioneered by Stoneley (1924) [1.10]. The propagation of acoustic and interface waves has attracted significant attention over the past three decades largely in part due to the work of solid-state physicists and engineers in the mid-60s who realised the significance of surface waves in real-time signal processing applications and interdigital transducers [1.6].

Taking a historical perspective, Lord Rayleigh[1.5] showed that a semi-infinite, isotropic, elastic medium, bounded by a single stress-free planar surface can support propagating modes that are wave-like in directions parallel to the surface. The excitations

are identified as surface waves because they are characterised by acoustic fields that decay exponentially with distance into the medium from the surface, and by a frequency that is proportional to a two-dimensional wave vector lying in the plane of the surface. The displacements of the medium lie in the sagittal plane defined by the normal to the surface and the direction of propagation of the wave. Notably, in seismology and ultrasonics, one is interested in externally excited waves of pre-selected wavevector and frequency. However, in a sample in thermodynamic equilibrium at a given temperature, bulk and surface phonons exist, which propagate in all directions and for all frequencies allowed by the dispersion relations. Brillouin scattering (BS) has proved to be an elegant and effective technique for measuring the spectral density of long-wavelength surface phonons in thermal equilibrium in solids, to a frequency of about 150 GHz.

The subject of BS received much greater attention with the development of the laser which led to the technique being used initially study the elastic and opto-elastic properties of transparent solids [1.11]. A significant step forward again occurred with the introduction of the high-contrast spectrometer by Sandercock in 1971 [3.3], allowing measurements on small and even opaque samples. In the same vein, the application of this technique to the study of surface excitations of opaque materials is, for a number of reasons, experimentally more demanding than the corresponding study of transparent materials. Firstly, because of the reduced interaction volume, Brillouin scattering from an opaque material is in general much weaker than that from a transparent material. Secondly, spectrometers of much higher contrast are required. This is a consequence of the fact that the intensity of the elastically scattered light from the surface of opaque materials is many orders of magnitude greater than that of the Brillouin signals themselves. Even with the use of these devices which can provide a contrast of better than 10^{12}, the surface quality still remains a critical factor. Thirdly, the relationship between the measured velocities of the surface excitations and elastic constants of the material is rather more complicated than that for bulk wave propagation. The application of BS to the determination of elastic constants as a function of temperature is thus considerably more demanding than the room temperature measurements, and the focus of this report is essentially on this subject of high temperature surface Brillouin

spectroscopy applied to a number of technologically important materials. Despite the inherent technical demands of the technique, surface Brillouin scattering (SBS), as it is known, has emerged as a technique of great utility in the field of materials science, more recently, serving to advance critical knowledge on the characteristics of materials under extreme conditions of temperature and pressure exemplified by pioneering work of Stoddart et al.(1999) and Crowhurst et al.(2001) respectively, see reference [1.12] and references therein. Besides attendant difficulties at high temperature due to increased elastic scattering and reduced Brillouin signal strength due to multiple-scattering from furnace windows etc, SBS still stands out as one of the few techniques capable of determining elastic constants as a function of temperature of thin films having thickness less than 1μm (see review by Beghi et al., in [1.13]) and also characterising accurately very small-sized samples of rare and new materials [1.14].

In the first two chapters, a comprehensive theoretical background for SBS is provided, starting from the basic classical scattering theory which, which is then analysed within the context of 'real' experimental conditions, imposing the limitations and reformulations that are consistent with recent developments in SBS. In chapter 2, a detailed discussion of the elastodynamic Green's function approach is given, highlighting its success in interpreting SBS spectra for various structural configurations, namely thin and thick films, multilayer films and bulk polycrystalline specimens. Chapter 3 gives a detailed description of the experimental apparatus, discussing the subtle but critical experimental practices that enable successful experimental SBS studies to be made. A discussion is given of the alignment procedures for the optical furnace coupled to the external optics leading into the TFPI.

Chapters 4 to 7 report on the successful new experimental results both at ambient and high temperatures for some technologically important materials such as iron sulphide, boron carbide, titanium alloys and a MEMS structural material, namely doped polycrystalline silicon (commonly referred to as polysilicon). The significance of these results impacts heavily in the materials engineering and materials science fields where materials engineers rely on simulated elastic parameters, which are themselves based on

assumed data such as Poisson ratio. In this work, this information is determined independently and more significantly as a function of temperature, thus providing reliable elastic properties from which key information can be gleaned and used to improve the current materials design models. Finally in Chapter 8, some interesting views about future research and approaches are presented in brief.

1.1 Brillouin scattering in condensed matter

Brillouin spectroscopy studies the scattering of light from the long-wavelength thermal acoustic modes present in a solid and from the random thermal density fluctuations in a liquid or gas. The dynamics of these fluctuations are reflected in the spectrum and polarisation of the scattered light. Hence, since the dynamics are determined by the viscoelastic properties of the scattering materials, the optical resolution of the Brillouin spectrum yields the elastic properties such as velocity and attenuation of sound. From these properties the elastic constants, compressibilities and bulk viscosities can be deduced. The incident light, usually a focussed laser beam and the scattered light leave the sample essentially in thermodynamic equilibrium, hence qualifying Brillouin spectroscopy as a non-contact probe for viscoelastic properties. Unlike ultrasonic techniques, no external forces are required to be applied. The thermal acoustic excitations which maintain the state of thermodynamic equilibrium are already present.

1.1.1 Classical scattering theory

Following the classical treatment by Dil [1.15] and considering a medium as a collection of atoms in thermodynamic equilibrium, the thermal motions of the atoms result in fluctuations in the number density $\boldsymbol{N}$ ($\mathbf{r}$, t), where

$$\mathrm{N}(\boldsymbol{r},t) = \mathrm{N} + \Delta\mathrm{N}(\boldsymbol{r},t) \tag{1.1}$$

where $\boldsymbol{N}$ denotes the average number density with the fluctuating part $\Delta\mathrm{N}(\boldsymbol{r},t)$ at position $\boldsymbol{r}$ and time t. When light is incident on such a fluctuating medium, the atoms act as dipoles and their motions cause a Doppler shift in the scattered light. The wave-vector $\boldsymbol{k}_s$ (spatial frequency related to periodicity of phase gratings, i.e., $2\pi/\lambda$) and angular

frequency ω_s of the scattered light depend on the corresponding values $\{\boldsymbol{k}_o, \omega_o\}$ of the incident light and the spatial and angular frequencies $\{\mathbf{q}, \Omega\}$ present in the fluctuations

$$\Delta N(\Upsilon, t) = \iint_{-\infty} \frac{d^3q}{(2\pi)^3} \frac{d\Omega}{2\pi} \Delta N(\boldsymbol{q}, \Omega) \exp[i(\boldsymbol{q}.r - \Omega t)]. \qquad (1.2)$$

Hence, from equation (1.2) the fluctuations in the number density can be considered as a superposition of phase gratings with period Λ such that

$$\Lambda \equiv 2\pi / q \qquad (1.3)$$

and the phase velocity ν, given by

$$\nu \equiv \Omega / q. \qquad (1.4)$$

The scattering of light from such phase gratings proceeds in complete analogy with the Bragg reflection of x-rays by crystals where the wave vector of the scattered light is thus determined by momentum conservation such that,

$$\vec{k}_s = \vec{k}_o + \boldsymbol{q}. \qquad (1.5)$$

The angular frequency of the scattered light has undergone a Doppler shift from the incident frequency, and is given by

$$\omega_s = \omega_o \pm \Omega \qquad (1.6)$$

that reflects the conservation of energy.

In condensed matter at room temperature and in thermodynamic equilibrium, the energy spectrum is given by $\overline{\Delta N(\boldsymbol{q}, \Omega)^2}$. Since the photon wavevector is much smaller than the dimensions of the Brillouin zone (10^5 cm^{-1} compared to about 10^8 cm^{-1} for Brillouin zone), therefore BS essentially provides information about phonons near the centre of the Brillouin zone ($\boldsymbol{q} \approx 0$) [1.16]. In this region, the dispersion relation is linear for acoustic phonons and the dispersion $\boldsymbol{q} = \boldsymbol{q}(\Omega)$ is determined by the viscoelastic transport coefficients of the scattering medium. Brillouin scattering is thus light scattering from the thermal acoustic phonons and the frequency regime probed just fills the gap between ultrasonic and neutron-scattering techniques.

In a normal scattering experiment, monochromatic incident light propagating in a direction given by the wave-vector $\boldsymbol{k}_o$ is incident on the sample. According to equation

(1.5) this light will be scattered in all directions, but in an experiment only one direction given by $\boldsymbol{k}_s$ is selected. And because $|\Omega| \ll \omega_i, \omega_s$ the frequencies of the incident and scattered light are regarded as approximately equal, as are the magnitudes of their wave-numbers $|\boldsymbol{k}_s| \approx |\boldsymbol{k}_o|$. Such a scattering geometry is illustrated in the vector diagram below,

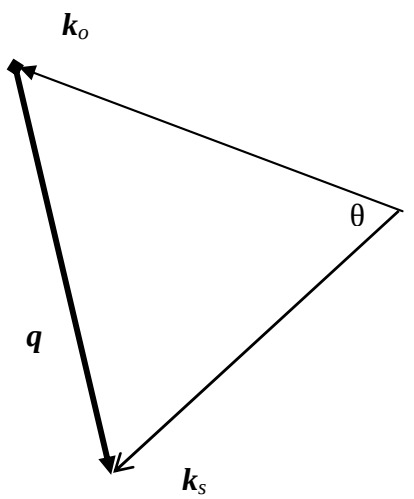

Figure 1: Wave vector conservation of the incident and scattered light.

Figure 1 shows that essentially one Fourier component of the fluctuations is involved, the wave-number of which is given by

$$q = 2k_o \sin(\theta/2), \tag{1.7}$$

where θ is the scattering angle. The spectrum of the scattered light then contains the Brillouin doublet at frequencies $\omega_s = \omega_o \pm qv$. In practice, one measures the polarization and the energy spectrum of the scattered light and hence determines the frequency shifts of the Brillouin peaks. By varying the scattering angle θ one is able to trace a small part of the dispersion curve $\Omega = \Omega(\boldsymbol{q})$, with $10^6 \leq q(\theta) \leq 10^7 \mathrm{m}^{-1}$. This is somewhat different from ultrasonic techniques where the magnitude of the wave-vector $\boldsymbol{q}$ is traditionally measured as a function of Ω. In addition, the spectral width of the Brillouin peaks is determined by the length of time that each fluctuation interacts with the monochromatic incident light and is therefore a measure of the lifetime or attenuation of the fluctuations.

Since the frequency interval of the acoustic excitations lies approximately between 1 MHz and 100 GHz (hypersonic frequency regime) and there are frequency shifts expected in the scattered light, the Fabry-Pérot interferometer is a suitable spectrometer which can resolve the spectrum.

1.2 The mechanism of Brillouin scattering

A longitudinal sound wave is associated with regions of compression and rarefaction. These regions correspond to variations in material density resulting in changes in the refractive index. The effect can be likened to a three dimensional grating moving through the medium at the speed of sound. Bragg reflected light from this grating is subject to a Doppler frequency shift.

Quantum mechanically, Brillouin scattering involves the exchange of energy corresponding to a quantised lattice vibration or phonon. Conservation of momentum and energy require

$$\boldsymbol{k}_o - \boldsymbol{k}_s = \pm\, \boldsymbol{q}\,, \quad \text{and} \quad \omega_0 - \omega_s = \pm\, \Omega\,,$$

where $\boldsymbol{k}_o$ and $\boldsymbol{k}_s$ represent the incident and scattered photon wave vectors while $\boldsymbol{q}$ and Ω represent the wave vector and angular frequency of the resultant phonon, and the ω's refer to the angular frequencies of the incident and scattered light, respectively. The plus sign (+) refers to phonon creation (Stokes process) and the minus sign (-) refers to phonon annihilation (anti-Stokes process). A simple calculation shows that the quantum of energy $\hbar\omega$ associated with an oscillator of 30 GHz frequency corresponds to an equivalent temperature $\hbar\omega/k_B$ of about 1.5 K. The significance of this equivalent temperature underlines the fact that even at rather low temperatures the classical approach is adequate to describe the Brillouin scattering process. It is only at extremely low temperatures where k_BT becomes comparable to $\hbar\omega$, and quantum mechanical effects become pronounced so that a more sophisticated analysis is required. This classical description of Brillouin scattering needs to be refined depending on what type of acoustic wave is being examined and generally these are of two forms: those confined to the sample surface and those moving through the sample bulk.

For the common SBS configuration, light of frequency ω_s and wave vector $\boldsymbol{k}_s$ is backscattered within a small cone around $-\boldsymbol{k}_i$, and is collected and analysed. Three common scattering processes are generally encountered, (a) transparent solid, (b) transparent supported layer and (c) an opaque or semi-opaque solid or supported layer. It might then be expected that scattering due to a surface wave is described by a surface rather than a bulk mechanism. This is, however, only correct to a first approximation – bulk waves do cause a surface deformation, while SAW displacements penetrate the bulk with an exponentially decaying amplitude. It is thus desirable to derive a scattering cross-section for SAWs that includes the contribution from both mechanisms as this enables a detailed quantitative evaluation of their importance. A brief mention of the two mechanisms is given below:

Historically, the fact that ripples produced by acoustic excitations on the surface of a material scatter light has been known as early as 1938 from the work of Bergmann [1.17]. In recent times, the theory has become better understood following the work of many researchers such as Maradudin and Mills (1975) [1.18] who used the integral equations; Mervin et al. (1975) [1.19] employed the boundary-matching method of Rayleigh and Fano; whilst Agarwal (1977) [1.20] used the perturbation theory. An excellent review of the development of the theory conducted by Bortolani et al. can be found in [1.21] and references therein. However, experimental validation was first presented in 1977 by Mishra and Bray [1.22] where it was shown that the ripple mechanism can be the dominant mechanism for light scattering from externally excited acoustic waves in semiconductors.

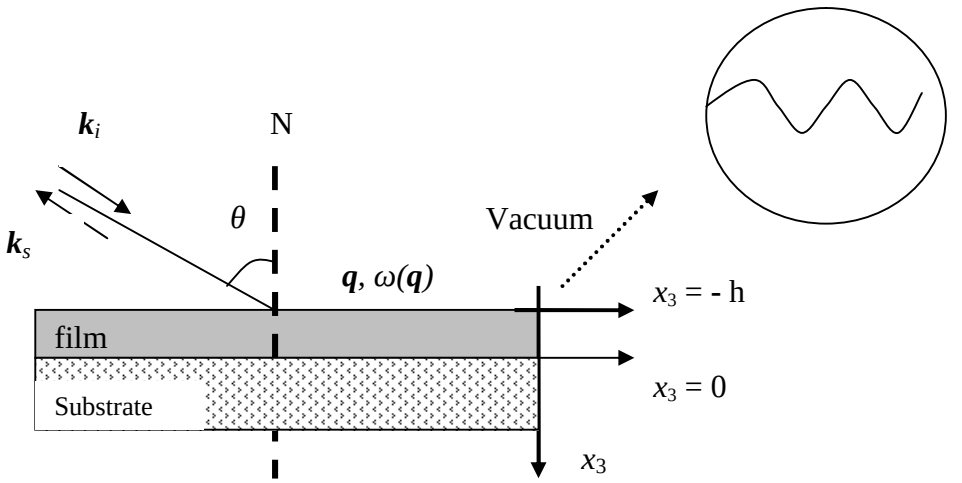

Figure 2: Surface ripple scattering mechanism and the encircled image shows the surface ripples (exaggerated)

Generally, surface acoustic waves (SAWs) are characterised by the following main attributes:

- A flow of energy parallel to the sample surface
- An exponentially decaying particle displacement amplitude beneath the surface and
- A particle motion that describes an elliptical trajectory.

The essence of ripple mechanism is as follows: the phonon vibrations cause the surface to appear as a moving grating i.e. a ripple capable by itself of producing diffraction and changing the frequency of the incoming light (Doppler Effect) without invoking any modulation of the dielectric field in the interior of the crystal (figure 2). Thus when light has a small penetration depth, one would expect the ripple mechanism to be the dominant process for the scattering cross-section.

The presence of optical absorption on the other hand allows interaction with phonons within a finite range of frequencies. This effect was confirmed by experimental results of Pine on CdS [1.23] and by Sandercock [1.24] on studies on Si and Ge. In addition, Dresselhaus and Pine [1.25] observed that the opacity broadened bulk lines were

asymmetric, and this effect was subsequently explained by Dervisch and Loudon [1.26] by considering the effect of phonon reflection at the boundary.

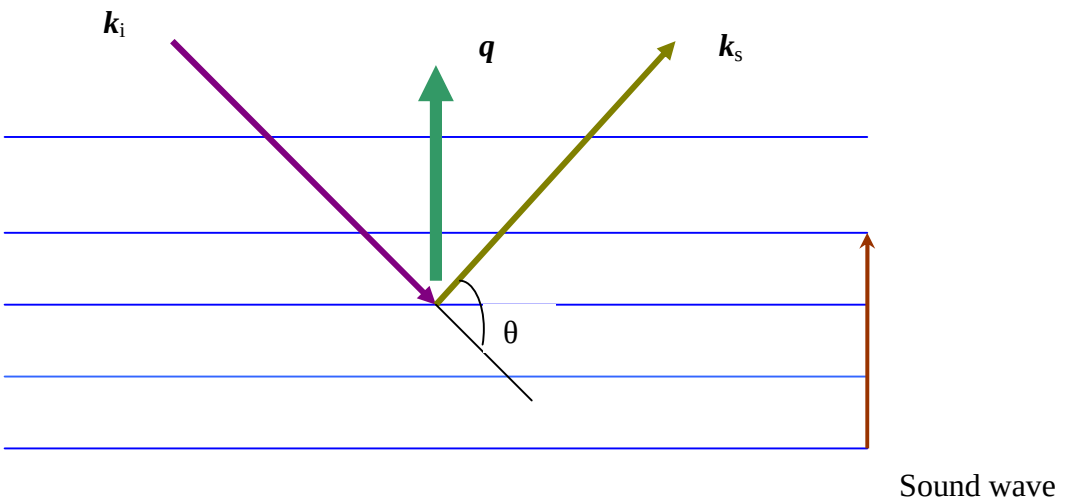

Figure 3: Brillouin scattering by means of the elasto-optic mechanism

The confinement of the elasto-optic coupling to a limited volume close to the surface was first considered by Mills et al. in 1970 [1.27] followed by Bennett et al. [1.28] in 1972. A simplified explanation considers that this scattering mechanism is associated with modulation of the sample's dielectric constant (figure 3). A sound wave travelling through a crystal modulates the interatomic spacing, hence the refractive index, the resultant scattered light experiences a Doppler - shift from which information is extracted. A more detailed quantitative treatment will be given in the following sections.

1.2.1 The SAW scattering cross section

A simplified analysis of the SAW scattering cross – section is given in Elmiger [1.29]. A backscattering geometry is considered in which the sagittal plane as defined by the surface phonon propagation direction and the surface normal, coincides with the scattering plane. Light polarised in the sagittal plane (*p*-polarised) and incident on the sample leads to the scattered electromagnetic field ***B,*** whose intensity depends on the polarisation-dependent Brillouin scattering cross-section [1.21].

With reference to figure 2, a film of thickness h is deposited over a semi-infinite substrate filling the half-space $x_3 < 0$. The free surface is located at $x_3 = -h$ while the film-substrate

interface is at $x_3 = 0$. The incoming light of frequency ω_i and wavevector $\boldsymbol{k_i}$ is assumed to form an angle θ with the surface normal (N) and to have a wavevector component parallel to the surface directed along the x_1- axis.

Acoustic waves give rise to a change in local strain field of a material with an accompanying change in dielectric constant:

$$\varepsilon_{\alpha\beta} = \varepsilon_o + \delta\varepsilon_{\alpha\beta}\,.$$

For an isotropic material this change and the Maxwell relations give,

$$\left[\nabla^2 - \frac{\varepsilon_o}{c^2}\frac{\partial^2}{\partial t^2}\right]\boldsymbol{B} = 0\,, \qquad (x_3 > 0) \tag{1.8}$$

and

$$\varepsilon_o\left[\nabla^2 - \frac{\varepsilon_o}{c^2}\frac{\partial^2}{\partial t^2}\right]\boldsymbol{B} = -\nabla\times(\delta\,\bar{\varepsilon}\,\nabla\times\boldsymbol{B})\,, \quad x_3 < 0, \tag{1.9}$$

where x_3 is the vertical coordinate relative to the scattering plane (figure 2). The isotropy of the material results in the second rank tensor, $\varepsilon_{\alpha\beta}$, having a diagonal form represented by $\vec{\varepsilon}$.

The interest herein lies in a solution for $\boldsymbol{B}$ to first order in the surface acoustic wave (SAW) displacement field $\boldsymbol{u}$**.** This is justified by the very small vibration amplitude of SAW's with respect to their wavelength. The proper solution will be the sum of a particular solution of the inhomogeneous Maxwell equation (1.9) with the general solution of the homogeneous equations (obtained with $\delta\varepsilon_{\alpha\beta} = 0$) to satisfy the following boundary conditions:

1. continuity of $\boldsymbol{B}$ at the sample surface
2. continuity at the surface of the tangential component of the electric field $\boldsymbol{E}$, i.e. $\varepsilon^{-1}(\nabla\times\boldsymbol{B})$.

These boundary conditions must be applied to the corrugated surface whose profile is given by the x_3-component of the displacement field (evaluated at $x_3 = 0$), namely

$$u(\boldsymbol{R},\times_3,t) = \frac{1}{L\rho^{1/2}}\sum_n e^{i\boldsymbol{k}.\boldsymbol{R}}U(q,\Omega_n,z)\Gamma\,(q,\Omega_n,t)$$

where L is the length of the side of the surface, ρ is the sample density, U is the polarisation vector (representing the amplitude of the vibrations), and $\Gamma\,(\boldsymbol{q},\Omega_n,t)$ is a normalisation coefficient determined by imposing the acoustic boundary conditions. The sum runs over all phonon states of wave vector $\boldsymbol{q}$ parallel to the surface and physically realisable frequencies Ω_n. The assumption of a small amplitude ripple then allows u_z to be expanded to first order. A general form of the scattered field in a vacuum is then obtained and this depends on:

1. The polarisation of incoming and scattered fields, and
2. The scattering geometry.

It is now possible to derive the differential scattering cross section; for example in the case of in-plane scattering in the limit of large ε_o yields;

$$\left[\frac{d^2\sigma}{d\Omega d\omega}\right] \cong \frac{\omega^4 k_B T}{2\pi^2 c^4 \rho(\omega_s-\omega_i)^2}\times\cos^2\theta_s\,\frac{\cos\theta_i}{\left[(\cos\theta_s+\varepsilon_o^{-1/2})(\cos\theta_i+\varepsilon_o^{-1/2})\right]}$$
$$\times\sum_n\left|\varepsilon_o^{-3/2}C(\sin\theta_i-\sin\theta_s)\frac{1}{2}U_x(q,\Omega_n,0)+(1-\sin\theta_s\sin\theta_i)\right| \qquad (1.10)$$
$$\times U_z(q,\Omega_n,0)^2\,\delta\left[\Omega_n-\left|\omega_s-\omega_i\right|\right].$$

C represents a constant determined by the elastic (c_{ij}) and elasto-optic (κ) constants of the material. Of interest is the first term in the sum proportional to the longitudinal polarisation component U_x, and the second term proportional to the vertical polarisation component U_z. These represent the elasto-optic and ripple contribution to the scattering respectively. Notably, there is a dependence of the elasto-optic term on the dielectric constant and it is therefore useful to write the cross-section for *p-p* in-plane scattering in the limit of large ε_o.

Intuitively this can be understood by the fact that the more opaque a material is, the more the scattering is limited to a volume close to the sample surface. It must also be remarked

that equation (1.10) is only suitable for describing surface Brillouin scattering, the bulk resonances being washed out by the approximation $\varepsilon_o \rightarrow \infty$. Also worth noting is that in many cases the elasto-optic contribution is not negligible and can give rise to interference effects [1.30]. This is also borne out by the graphs in figure 4 below. The two peaks on the right in figure 4(a - c) represent actual bulk waves rather than surface acoustic waves – they decrease rapidly as the dielectric constant is increased. The SAW peak itself remains relatively large due to its opacity independent component. Notably, also is the broadening or spreading in the bulk peaks – this is consistent with the uncertainty principle, i.e. an increasingly confined scattering region results in an increasing momentum spread, described in more detail below (1.2.2).

With increasing ε_2, however, their intensities diminish (note change in scale) and at $\varepsilon_2 = 1.0$, the Rayleigh surface acoustic wave (RSAW) becomes dominant (ripple scattering) and two *dips* at the frequencies Ω_L and Ω_T show up due to interference. Bulk acoustic waves incident on the surface can also cause dynamic surface corrugations, and these will be detected if the component of their wavevector in the surface is equal to q . Combined with their normal component, the wavevectors of these bulk waves take on a continuum of values, and this gives rise to a broad continuum in the Brillouin spectrum extending from the bulk transverse wave threshold to high frequencies. This is known as the Lamb shoulder, and is the broad band to the right of the RSAW peak in figure 5. The Lamb shoulder originates from a so - called '*mixture of modes*' because the modes are mixtures between sinusoidally varying (transverse) and exponentially decaying (longitudinal) modes. Below the transverse threshold Ω_T all amplitudes are decaying for $z \rightarrow -\infty$ and at ω_R we find the Rayleigh wave localised at the surface. Thus the RSAW propagates undamped along the surface and is made up of a longitudinal (or P-wave) and shear vertical wave (SV-wave) with exponentially decaying amplitudes. For $\varepsilon_2 = 10$ the bulk phonons are no more discernible.

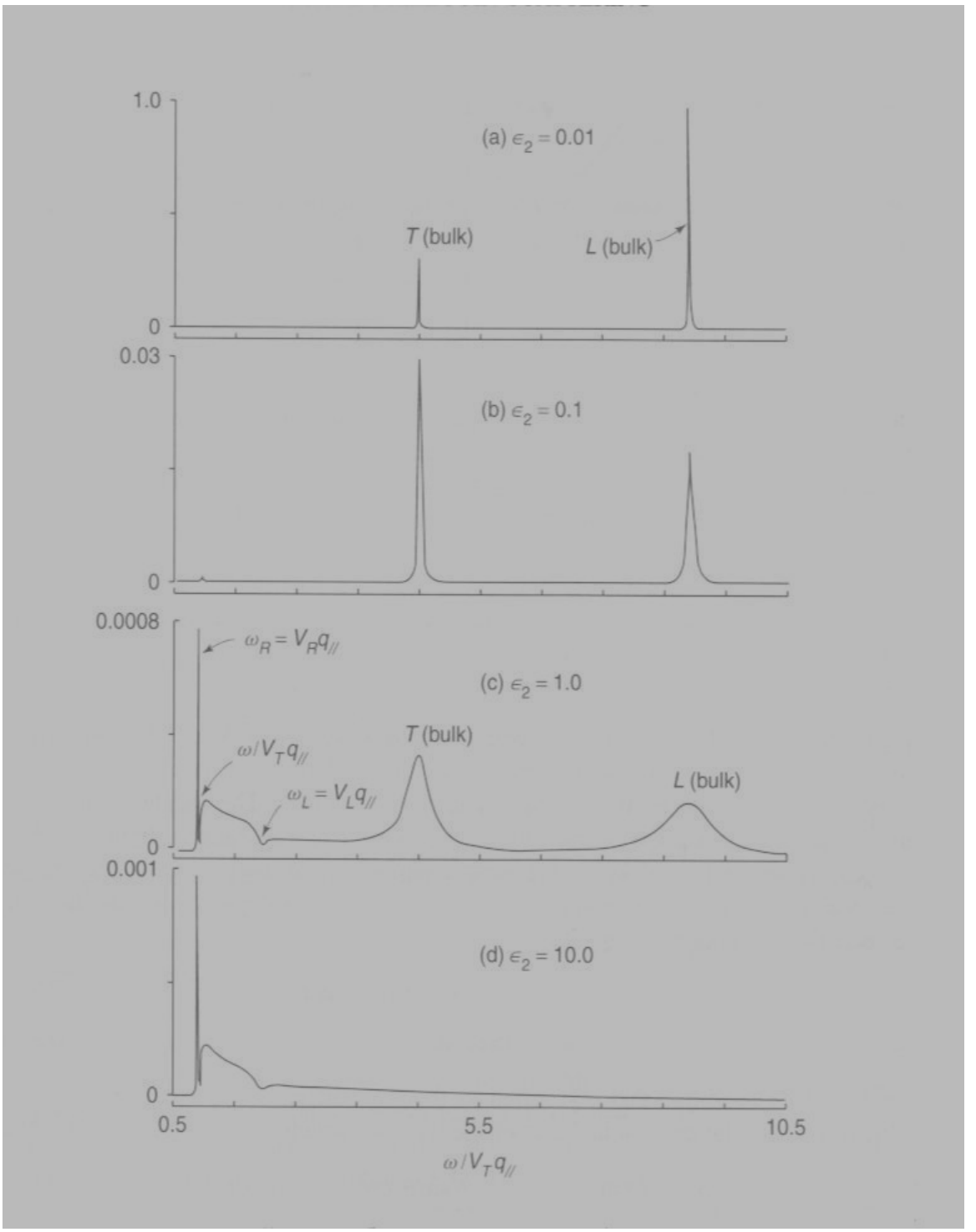

Figure 4: Plot of the scattering efficiency against the dielectric constant, plotted for various values of $\varepsilon = \varepsilon_1 + i\varepsilon_2$ using $\varepsilon_1 = 10$ fixed, (adapted from theoretical calculations of Subbaswamy and Maradudin [1.30].

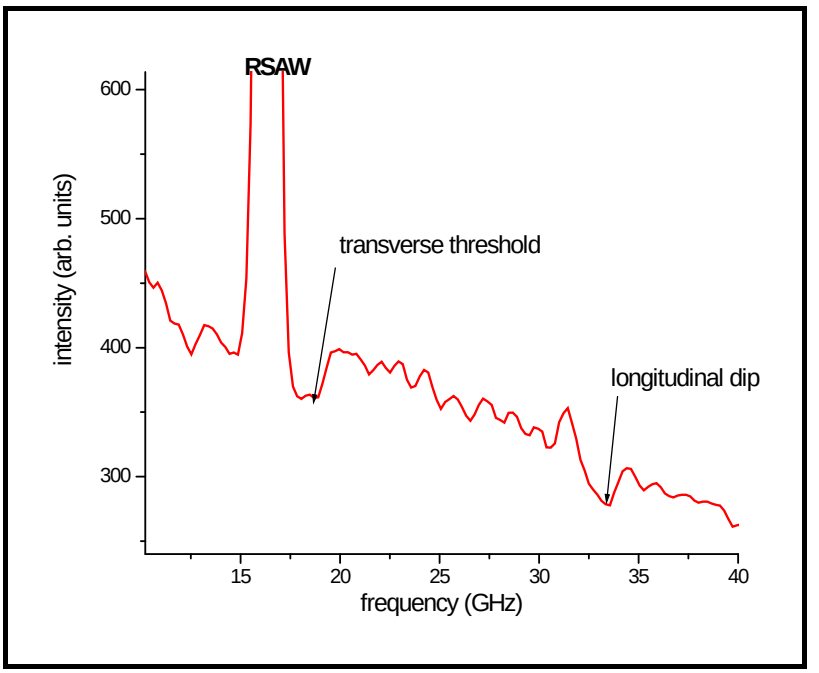

Figure 5: Experimental results obtained for boron-doped silicon showing the Lamb shoulder extending beyond RSAW and longitudinal dip at 33.8 GHz as well as the transverse threshold at 19 GHz.

On the other hand, figure 6 shows the calculated spectra of GaAs with various elasto-optic coupling constants κ (equation 1.10); notably for increasing κ up to 80 (for the broken curve) a *peak* at the longitudinal 'dip' or cut-off frequency is obtained where we had a dip previously, illustrating the significance of elasto-optic scattering. Figure 7 shows this effect obtained experimentally for a FeS_2 (pyrite) crystal, where a peak at ~ 32 GHz is observed, labelled HFPSAW. So, generally for partially opaque materials, in addition to the pseudo-SAW (PSAW)[2] [1.31], a further SBS peak within the continuum of excitations may be present that arises from elasto-optic coupling as shown also for GaAs below (figure 6).

[2] This is a sharp resonance in the bulk wave continuum, normally found close to [110] direction in anisotropic surfaces, described as a wave consisting mainly of two evanescent partial waves, but in addition there is a small bulk wave component that radiates the energy of this wave away from the surface, causing its attenuation.

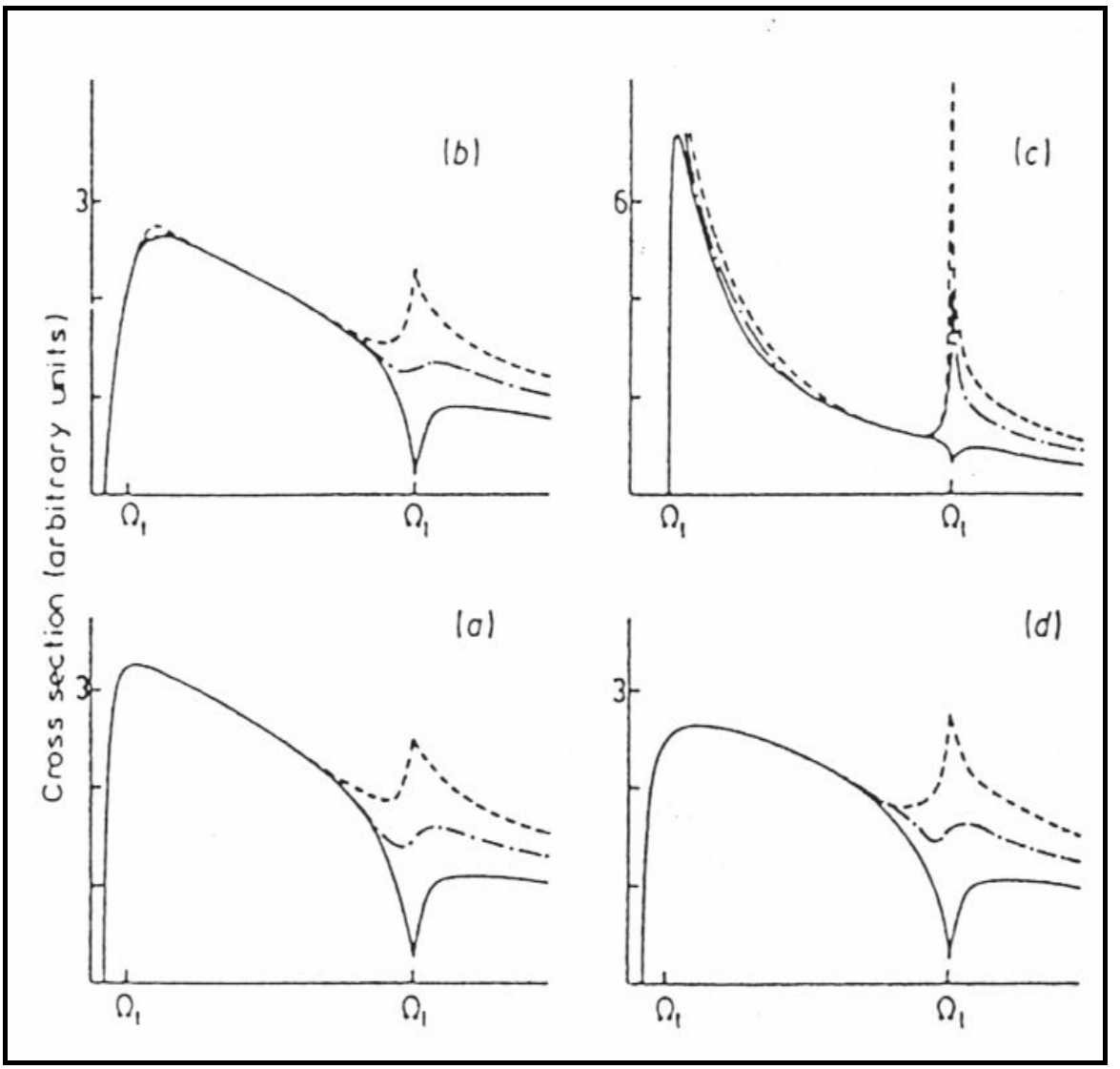

Figure 6: Calculated Brillouin cross sections for GaAs for different values of elasto-optic coupling constant, κ. where: (a) GaAs(001) $q=[100]$; (b) GaAs(001) $q=[1\bar{1}0]$ (c) GaAs(110) $q=[1\bar{1}0]$; (d) GaAs(110) $q=[001]$ while κ has values varied from 20 (*full curve*), through 60 (*chain curve*) to 80 (*broken curve*). A clear increase in intensity occurs for the peak at Ω_L when optimum conditions of surface orientation and q are met. (Adapted from reference [1.33]).

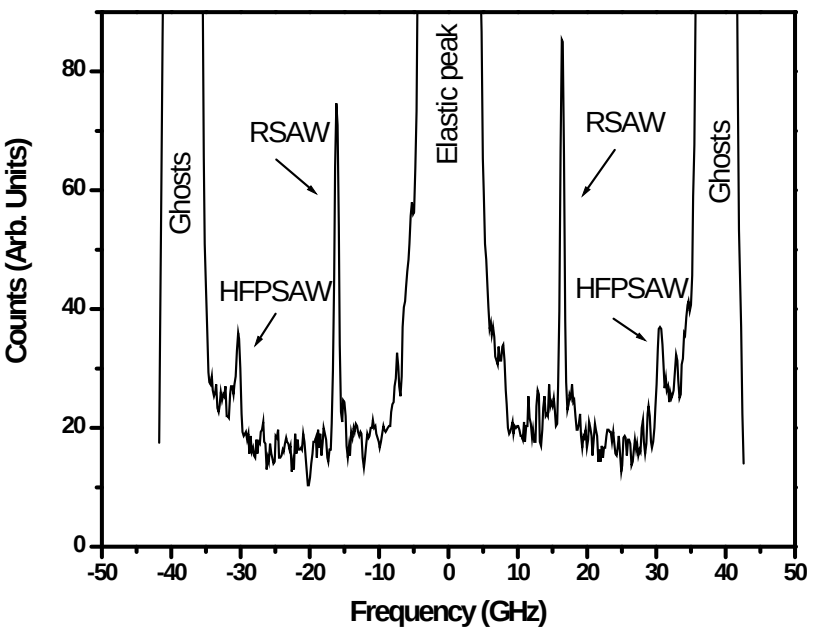

Figure 7: Typical SBS spectrum for the (110) surface of FeS_2 showing RSAW and HFPSAW modes [1.32]

This resonance has acquired various names, surface skimming mode (SLM), high-frequency pseudo-surface mode (HFPSAW) , leaky longitudinal surface wave (LLSAW), and longitudinal guided wave (LGW) or mode (LGM), depending partly on the configuration (or context) under investigation. This is a resonance that lies between the FT (fast transverse, see Section 1.3) and L thresholds where there is a corresponding peak in the surface power spectrum[3] of the longitudinal modes. This resonance is related to a maximum in the reflection coefficients for mode conversion from bulk shear to bulk longitudinal waves [1.32] and is located such that $\omega_{SLM} = \omega_L$ for materials having a Poisson ratio $\sigma < \frac{1}{3}$, whereas for materials with $\sigma > \frac{1}{3}$ there is a broad resonance in the region of ω_L .

[3] A more detailed discussion of the power spectrum is presented in Chapter 2 within the context of the Green's function formalism.

In summary, for a very transparent material (small ε_2), a large volume is illuminated and the elasto-optic mechanism produces a sharply-peaked scattering spectrum in accordance with frequency and wavevector conservation. As the transparency is reduced, the growing imaginary parts of the refracted wavevector increase the uncertainty in wavevector conservation in the direction perpendicular to the surface, and lead to broadening of the Brillouin peaks (figure 4c). In addition, as the scattering volume becomes smaller, so does the cross-section for bulk scattering. On the other hand, the cross-section for ripple scattering is proportional to the reflectivity and relatively insensitive to sample opacity. Therefore ripple scattering becomes more dominant as opacity increases. Marvin et al. [1.33] have also demonstrated using a semi-quantitative analysis that for elasto-optic scattering, the elasto-optic coupling coefficient depends on the surface orientation as well as on the wavevector $\boldsymbol{q}$, defined for in-plane scattering. Their findings helped confirm effects of boundary conditions on Brillouin spectra, such effects being important in the 'mixed mode' region where a peak may occur at $\omega = \omega_L$ if the right conditions of surface plane (110) and $q_{//}$ [110] are met as shown in figure 7(c) and proven experimentally in the case of FeS_2 (110). In addition, upon varying the incidence angle θ in a backscattering geometry, the 'HFPSAW peak' shifts proportionally to sin θ hence identifying itself as *longitudinal surface phonon.* By performing a dual dispersion analysis of the two surface modes (Rayleigh SAW and HFPSAW) it was possible to extract the full set of elastic constants for FeS_2 with significantly higher accuracy. A more detailed analysis of and results for this investigation will be discussed in Chapter 4.

1.2.2 Opacity broadening

The relative importance of the bulk and surface contributions to a particular spectrum is primarily determined by the optical transparency of the medium. In this section it will be shown how the volume illuminated by the incident light influences the wavevector conservation. The salient facts are neatly represented by the momentum-conservation illustration in figure 8, as well as in the calculated spectra for various values of dielectric constant ε_2 presented in figure 4 earlier on.

As long as the optical absorption coefficient α is less than about 10^3 cm^{-1}, i.e. if the optical penetration depth is larger than about 1000 nm, the Brillouin spectrum appears the same as that of a transparent medium. On the other hand, if light penetrates only a few wavelengths into the material, a broadening effect occurs: because of the high absorption all scattering events must occur within the optical skin depth $\delta=1/\alpha$, hence, the optical fields translation symmetry *parallel* to the surface is still conserved but destroyed in *perpendicular* direction.

Typical penetration depths are of the order of 100 nm or 200 nm for energies beyond the absorption edge of semiconductors and 10 nm or 20 nm in a metal. Consequently, the phonon wave vector component *parallel* to the surface is conserved in the scattering process but its perpendicular component is not, producing a momentum uncertainty Δq. Due to the finite slope of the dispersion of bulk acoustic phonons, the wave vector spread Δq produces a frequency spread $\Delta\omega = v\Delta q$ where the Brillouin peaks are broadened over the region $\Delta\omega$. In terms of the absorptive part of the refractive index, the full-width at half–maximum (FWHM) is given by [1.26]

$$\Delta\omega = 4v\, k_o \mathrm{Im}(n),$$

where $\boldsymbol{k}_o$ denotes the wave-vector of light in a vacuum. This effect has two detrimental consequences:

- The broadening may become so severe that no reliable peak assignment can be made.

- The scattering intensity drops by orders of magnitude and the signal-to-noise ratio may become less than one. In this case, the bulk phonons cannot be observed no matter how long the accumulation time for the spectrum.

It should be noted that the *q*-vector uncertainty is indeed also present in Raman scattering but has no such detrimental effect because the dispersion of optic phonons at the zone centre is essentially flat (zero slope) and the momentum uncertainty is not reflected in ω.

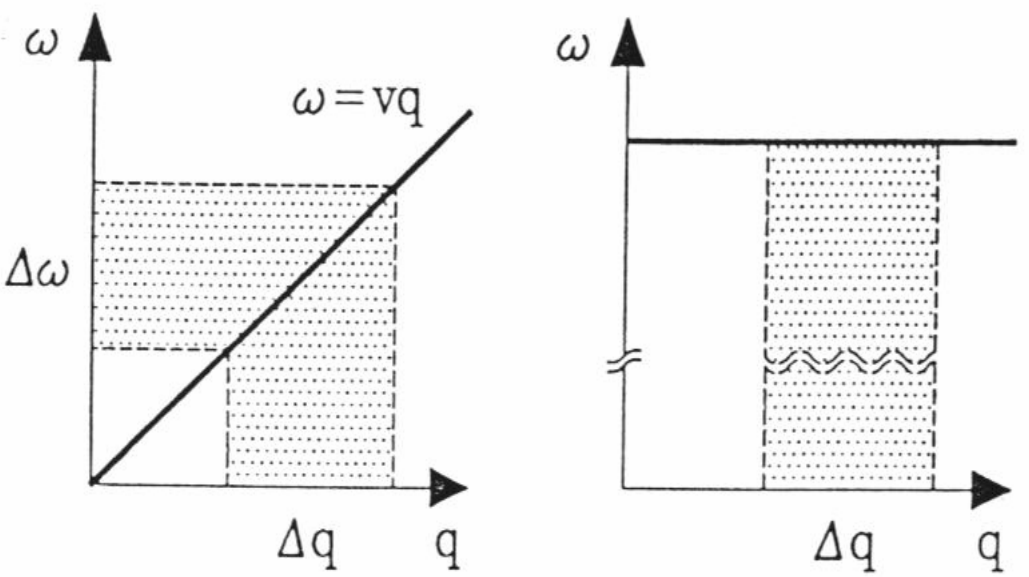

Figure 8: Opacity broadening in Brillouin spectroscopy from *acoustic* phonon (left). No broadening observed in Raman spectroscopy from *optic* phonon (right) (Adapted from reference [1.29]).

1.2.3 Acoustic phonon wave velocity calculations

Considering the geometry of Figure 2 together with momentum conservation yields

$$q = k_i \sin\theta_i + k_s \sin\theta_s . \tag{1.11}$$

To a good approximation, in a backscattering geometry $\theta_i = \theta_s$, and hence

$$(q_{//}) \text{ or } q = 2k_i \sin\theta_i . \tag{1.12}$$

The measured frequency shift is then related to the surface wave velocity, *v*, by

$$\Omega = kv$$

and thus

$$v = \frac{\Omega}{2k_i \sin\theta_i} . \tag{1.13}$$

It is to be noted that for a chosen wavelength of light, the incident angle θ_i establishes *q*, and the measurement of ω determines *v*.

Volume scattering is the scattering by bulk acoustic waves of velocity c_{acous}, where c_{acous} represents any of the three bulk waves L, FT (fast transverse) and ST (slow transverse) velocities (to be discussed in detail in section 1.3). In this case the optical wave vectors $(k_i^{'}, k_s^{'})$ are present in the bulk; their directions are determined by the incidence direction and collection directions out of the sample, and by the refractive index *n*, with $k_i^{'} = nk_i$ and $k_s^{'} = nk_s$. The angular frequencies $\omega = c_{acous}k$ and $\Omega = \left(\frac{c_{light}}{n}\right)k$ where *k* represents either the incident or the scattered wave vectors, and (c_{light}/n) is the light velocity in the medium [1.51]. From the relation $q = \pm(k_s - k_i)$ between the scattered light collected along the direction of a wave vector k_s having interacted with an acoustic wave of any kind, having wave vector ***q***, this relationship implies that $|q|$ can possibly be much smaller than $|k_s^{'}|$ and $|k_i^{'}|$ but not larger than their sum. Since $|q|$ is at best of the same order of magnitude as *k*, the ratio ω/Ω_i is at most of the same order of the ratio $\frac{nc_{acous}}{c_{light}}$ (i.e. ~ 10^{-4} to 10^{-5}) for any physical values of c_{acous} and *n*.

Thus the relative difference

$$\frac{|\Omega_s - \Omega_i|}{\Omega_i} \approx \frac{nc_{acous}}{c_{light}} \approx \frac{|k_s^{'} - k_i^{i}|}{k_i^{i}} \simeq 10^{-4} \sim 10^{-5},$$

implying therefore that the scattering event can be analysed neglecting the difference between the magnitudes of the moduli: such that $k_i^{'} \cong k_s^{'}$. Therefore in a backscattering geometry, ($k_s^{'} = -k_i^{'}$ and therefore $k_s = -k_i$) maximises the modulus of ***q***: in this geometry

$$q = 2\frac{2\pi}{\lambda_o} n. \tag{1.14}$$

In SBS, (i.e. scattering by SAWs) $q_{//} = \pm(k_s - k_i)_{//}$ for the wave vector components parallel to the surface: since Snell's law means that upon refraction both $k_{i//}$ and $k_{s//}$ remain unchanged, therefore the wave vector conservation relation can be analysed in terms of the optical wave-vectors k_i and k_s outside of the sample, hence their directions determine the acoustic wave vector $q_{//}$. Therefore in transparent or semitransparent samples, in which surface and volume scattering can be simultaneously observed, for backscattering the bulk acoustic waves are probed at wavelength $\frac{\lambda_o}{(2n)}$, while the surface waves are probed at wavelength $\frac{\lambda_o}{2\sin\theta_i}$, thus the spectral contributions from surface waves (Rayleigh) and those from bulk waves are well separated and therefore resolvable. As discussed above in figure 4 where the calculated spectrum for fixed ε_1 (=10) but varying ε_2 shows clearly the evolution of surface features as ε_2 is increased. For ε_2 =0.01 (non-absorbing), the bulk LA and TA phonons are readily seen and well-resolved.

1.3 Acoustic Modes in Anisotropic Media

Interpretation of SBS spectra can become a complex task when the spectra contain several peaks and when an estimate of the material's elastic constants is not available *a priori.* A proper peak assignment requires in-depth knowledge of the basics of SAW propagation in layered structures, especially when the layers are anisotropic. Surface waves exist as a consequence of the lack of translational invariance in the direction perpendicular to the surface of the propagation medium. The waves appear wave-like only for directions of propagation parallel to the surface and having amplitudes that decay with depth into the interior. The bulk waves of a medium of infinite spatial extent on the other hand have constant amplitude and are wave-like in all three dimensions.

Generally, as discussed in section 1.2.3 above, in isotropic solids two types of bulk acoustic modes exist: occasionally known as primary waves (or P-waves), **longitudinal**ly polarised and secondary waves (S-waves), **transverse**ly polarised. Two independent (orthogonal) transverse polarisation directions exist. In isotropic solids the secondary waves are perfectly equivalent, while in anisotropic solids they are not. These modes, called fast transverse (FT) and slow transverse (ST) from their generally different velocities, have phase velocities and polarisation vectors that depend on the propagation direction. Also, the phase velocity and polarisation vector of the longitudinal (P-mode) depend on the propagation direction. Although in the anisotropic media, the polarisation vectors are neither exactly parallel nor exactly perpendicular to the wave vector (strictly they are more quasi-longitudinal and quasi-transverse) the above names and the corresponding labels P (or L), ST, and FT are customarily used in this context, and also adopted throughout the following chapters.

The Rayleigh wave (RW) propagating along the stress-free boundary of an isotropic solid is a non-dispersive acoustic wave which has its energy and displacement field confined near the surface. Similar waves found on anisotropic surfaces [1.34] are called generalised RW (GRW). Anti-plane (transversely polarised) and in-plane modes (longitudinaly polarised) in free-standing plates are known as Lamb waves whilst

transverse modes in a thin supported layer are called Love waves. Unattenuated waves travelling along interfaces between solids known as Stoneley waves exist under certain conditions as discussed in detail in [1.35].

Furthermore, waves exist that are surface-like but slowly radiate energy away more from the surface and for which the displacement field does not vanish at infinite depth. These are not strictly surface waves but have their energy mainly confined near the surface and they are termed ‘pseudo-surface acoustic waves (PSAWs) [1.33]. PSAWs have a phase velocity higher than that of the lowest of the bulk waves in the substrate and can exist only around specific directions in some anisotropic substrates, while the HFPSAW exists along any direction for anisotropic and isotropic materials (see the discussion on page 16). The presence of a layer on a substrate can lead to the appearance of a number of waves confined to within the layer. For a single layer on a substrate, these waves are called generalised Lamb waves or Sezawa waves [1.34, 1.36], because of their similarity to Lamb waves in free-standing isotropic plates. The existence of these modes depends on the thickness of the layer in relation to the wavelength, on whether the layer is elastically stiffer than the substrate, and the relative densities of the layer and the substrate.

1.3.1 **Experimental conditions: SAW propagation along arbitrary directions**

In anisotropic media, the velocity of a SAW depends on the propagation direction. We will call the relation *velocity vs direction* and in the subsequent chapters *angular dispersion*, to make a clear distinction with the usual *ω(q)* dispersion. By rotating the sagittal plane with respect to the material’s axes, the directional dependence of the RSAW (and HFPSAW or L - guided mode) can be measured. The case of an over-layer on a substrate is not much more complicated than the case of a single crystal. In order that both cases can be treated simultaneously, the following relations are derived:

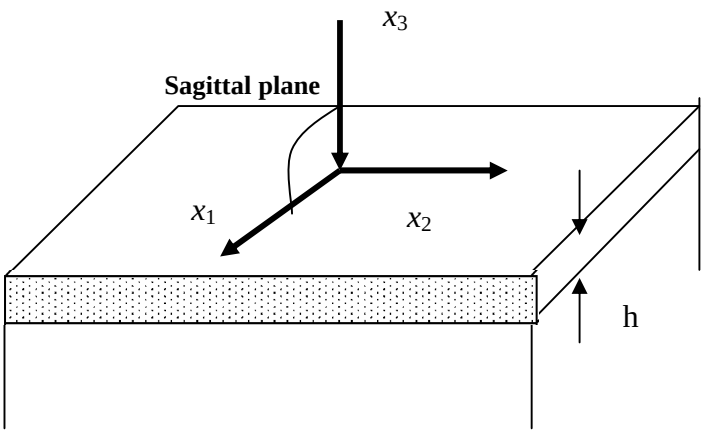

Figure 9: Reference frame used in the SBS computations showing the anisotropic thin film on a bulk substrate.

The experimentally chosen scattering geometry selects the momentum of the surface phonon and defines the reference frame (x_1, x_2, x_3,) as shown in figure 9; all calculations are done with the variables referring to this frame. We are concerned here with the acoustic properties of an anisotropic solid layer of thickness *h* perfectly bonded to a semi-infinite elastically anisotropic substrate. We make use of the coordinate system shown in figure 9, with the x_1 - and x_2 -axes lying in the *interface* between the layer and substrate and the x_3 -axis directed into the substrate. This special case of a single half-space is obtained by letting *h* tend to zero.

The mathematical treatment follows the work of Farnell and co-workers [1.36 – 1.39]. A coordinate transformation $\boldsymbol{R}$ relates the 4$^{\text{th}}$ - rank stiffness tensor c_{ijkl} to the tensor $\overline{c}_{rstv}$ given with respect to the principal axes $(\overline{x}_1, \overline{x}_2, \overline{x}_3)$.

$$c_{ijkl} = R_{ir} R_{js} R_{kt} R_{lv} \overline{c}_{rstv} \ . \tag{1.15}$$

In the absence of piezoelectricity the wave equation is given by

$$\rho \frac{\partial^2 u_j}{\partial t^2} = c_{ijkl} \frac{\partial^2 u_k}{\partial x_i \partial x_l} . \tag{1.16}$$

The displacement amplitudes are denoted by u_j and ρ is the mass density while the attenuation coefficients are represented by *b*. The ansatz

$$u_j = A_j e^{iqbx_3} e^{iq(x_1 - vt)} \tag{1.17}$$

yields

$$\left[\Gamma - \rho v^2\right] A = 0 \tag{1.18}$$

with

$$\begin{aligned}
\Gamma_{11} &= c_{55}b^2 + 2c_{15}b + c_{11} \\
\Gamma_{22} &= c_{44}b^2 + 2c_{46}b + c_{66} \\
\Gamma_{33} &= c_{33}b^2 + 2c_{35}b + c_{55} \\
\Gamma_{12} &= c_{45}b^2 + (c_{14} + c_{56})b + c_{16} \\
\Gamma_{13} &= c_{35}b^2 + (c_{13} + c_{55}) + c_{15} \\
\Gamma_{23} &= c_{34}b^2 + (c_{36} + c_{45})b + c_{56}
\end{aligned} \tag{1.19}$$

For a given trial value of velocity *v* in equation (1.18) a secular equation is produced which is a sixth order polynomial in the attenuation coefficients *b*. Energy conservation requires that in the substrate only values of *b* lying in the lower complex plane be retained, but for the layer, on the other hand, all six values are needed. The partial waves in the layer are

$$u_j = \left[\sum_n c_n A_j^n e^{iqb_n x_3}\right] e^{iq(x_1 - vt)} \tag{1.20}$$

while in the substrate,

$$u_j^+ = \left[\sum_m c_m A_j^m e^{iqb_m x_3}\right] e^{iq(x_1 - vt)}$$

where n = 1…..6 and m = 1, 2, 3; where the superscript (+) refers to quantities when they pertain specifically to the substrate e.g. displacement, u^+.

The boundary conditions now link the amplitudes in layer and substrate and the traction stress at the layer-vacuum interface must vanish (free surface):

$$\sigma_{3j} = 0 \text{ , at } x_3 = h. \tag{1.21}$$

Second, the particle displacement must be continuous across the substrate-layer boundary:

$$u_j = u_j^+ \text{ , at } x_3 = 0. \tag{1.22}$$

Finally the transverse and sagittal shear stresses and the longitudinal compressional stress must be continuous at the interface

$$\sigma_{3j} = \sigma_{3j}^{+}, \text{ at } x_3 = 0. \tag{1.23}$$

These nine conditions give an equation for the weighting coefficients C_n and C_m of equation (1.17), respectively:

$$BC = 0 \tag{1.24}$$

such that:

$$\boldsymbol{B} = \begin{bmatrix} 0 & A_j^n (b_n c_{31j3}^{+} + c_{31j1}^{+}) e^{iqb_n h} \\ 0 & A_j^n (b_n c_{32j3}^{+} + c_{32j1}^{+}) e^{iqb_n h} \\ 0 & A_j^n (b_n c_{33j3}^{+} + c_{33j1}^{+}) e^{iqb_n h} \\ A_1^m & -A_1^n \\ A_2^m & -A_2^n \\ A_3^m & -A_3^n \\ A_j^m (b_m c_{31j3} + c_{31j1}) & -A_j^n (b_n c_{31j3}^{+} + c_{31j1}^{+}) \\ A_j^m (b_m c_{32j3} + c_{32j1}) & -A_j^n (b_n c_{32j3}^{+} + c_{32j1}^{+}) \\ A_j^m (b_m c_{33j3} + c_{33j1}) & -A_j^n (b_n c_{33j3}^{+} + c_{33j1}^{+}) \end{bmatrix}$$

$$\boldsymbol{C} = \begin{bmatrix} c_m \\ c_n \end{bmatrix}.$$

These matrices are given in a compacted format: the first column of $\boldsymbol{B}$ describes the substrate and consists of three columns (m = 1, 2, 3) and the second column represents six columns (n = 1..6). Each element must be summed over *j*. Similarly, *C* is a nine- row vector. Since the solutions must be non-trivial, the determinant of $\boldsymbol{B}$ must necessarily vanish.

The computational procedure now runs as follows: for a given material and scattering geometry the stiffness tensor $\tilde{c}_{rstv}$ is transformed according to (1.15). For a given value of $\boldsymbol{q}$ one chooses a trial value for the velocity *v* and solves the secular equations derived from (1.18) (for both the layer and substrate) and selects the appropriate attenuation coefficients *b* and their corresponding amplitudes *A* (eigenvector). Inserting them into

(1.24) gives the boundary condition determinant *Det B*. The trial velocity *v* is now adjusted by repeating these steps until this determinant is *zero*; the result provides one point of the angular dispersion relation $v = v(\boldsymbol{q})$.

For the case of a single crystal without an overlayer, these steps simplify considerably as $\boldsymbol{B}$ reduces to a 3x3 matrix with only the first three columns and the last three rows retained. Inspecting (1.24) shows that *q* drops out completely; hence the surface waves on a semi-infinite medium are *dispersionless* and their velocities do not depend on the magnitude but only on the *direction* of $\vec{q}$. It is this *angular dispersion* which will be used in the method described below to obtain the elastic constants from an analysis of the surface waves.

This is done by first determining the angular dispersion of the crystal by means of surface Brillouin spectroscopy. The data points obtained in this way are fitted to the model function using a least-square analysis defined by equations (1.15) to (1.24) using the standard Levenberg-Marquardt procedure. This procedure adjusts the independent elements of the elastic stiffness tensor but often keeps the mass density fixed, (though one can allow the mass density to be used as a fitting parameter as well for some layered systems).

Since the already tedious iterative search for the roots of the model function is now embedded in another iterative process, some intensive calculation is required. Thus a program developed by Every [2.3], written in FORTRAN running on a desktop computer which uses subroutines of the IMSL math library is used to solve for the elastic constants.

1.4 Surface acoustic waves on a polycrystalline medium

The propagation of elastic waves in a polycrystalline solid has been studied for many years. Of particular interest has been the attenuation of the elastic waves as they propagate through such a medium. It has been established that this attenuation is not due to dissipation but arises from the scattering of energy out of the incident beam as it passes from one of the constituent grains to the next. This scattering is caused by the fact that the crystallographic axes of all the anisotropic, single crystal grains out of which the polycrystal is composed are rotated randomly with respect to each other. Thus as the elastic wave crosses the boundary between adjacent crystal grains it effectively moves from one anisotropic medium to a different one, due to the randomness of the orientation of the crystallographic axes, thus leading to the scattering of the wave.

Several different types of models of the grains comprising the solid have been used in numerous theoretical treatments; such as (i) individual particle, (ii) array of particles and (iii) stochastic process models by Stanke and Kino [1.40]. In the first model, each grain is treated as a single scatterer in an unperturbed medium, usually assumed to be an isotropic, homogeneous medium whose elastic moduli are the unweighted Voigt averages of the elastic moduli [1.41] of the constituent crystallites. For the array model, all of the grains are taken into account in the scattering calculations, assuming a simple and uniform shape for the particles as is done for the individual particle model. In the third model, the medium as a whole is treated in terms of the geometric statistics of the grains [1.42] which directly reflects the macroscopic elastic properties of the medium they compose. In this model it is assumed that the elastic anisotropy of the individual grains out of which the polycrystalline material is formed is small. Kaganova and Maraduduin [1.43] developed a comprehensive mathematical treatment using the dynamical Green's tensor analysis for an *elastically isotropic half-space* to derive the dispersion relation for Rayleigh waves propagating on the stress-free planar surface of a semi-infinite polycrystalline medium. A profound result they found was that the correction to the speed of the Rayleigh waves due to the polycrystallinity is exactly the result that would be obtained by the use of the static, polycrystalline, elastic moduli derived by Lifshitz and

Rosenzweig [1.44]. They also concluded that in the long wavelength limit, and for an infinitely extended polycrystalline medium, the damping of the Rayleigh and bulk waves is proportional to q^4 (q being the wave number).

1.5 Macroscopic effective constants of large volumes of polycrystalline media

Depending on a number of parameters, e.g. growth conditions, defects, substrate orientation, a polycrystalline film or body may exhibit texture along a specific direction ***A*** called the texture axis; this means that the individual ***A***'s of all crystallites are aligned normal to the substrate [1.49], while each crystallite is randomly oriented about ***A***. If the alignment of individual ***A***'s is destroyed, the growth resembles that of a polycrystalline film, wherein the crystallites are randomly oriented in three dimensions. If on the contrary, all the individual ***A***'s as well as the planes normal to them are aligned, then the growth is termed epitaxial.

In this section we will discuss the elastic behaviour of individual cubic and tetragonal crystal structures as both structures exhibit orthotropic behaviour, and in later chapters we will experimentally examine the elastic behaviour of bulk polycrystalline samples under the effect of increasing temperature.

1.5.1 Linear isotropic elasticity: Introduction

Elastic materials are characterised by a direct relation between the local stress state and the local strain state. In the case of linear elasticity this relation can be represented by the generalized Hooke's law, namely stress is proportional to strain:

$$\sigma = \boldsymbol{C}\varepsilon \tag{1.25}$$

where σ is the Cauchy stress tensor and

$$\varepsilon = \frac{1}{2}(\nabla \boldsymbol{u} + (\nabla \boldsymbol{u})^T) \tag{1.26}$$

is the infinitesimal strain tensor, where u is the displacement in the material. Equation (1.25) is usually expressed in matrix notation. Due to the symmetry of the stress tensor

and the strain tensor only six state variables need to be evaluated. Thus, the stress-strain relation is written as [1.45, 1.46]

$$\sigma = \boldsymbol{C}\varepsilon \,, \tag{1.27}$$

with

$$\sigma^T = [\sigma_{11}\,\sigma_{22}\,\sigma_{33}\,\sigma_{23}\,\sigma_{31}\,\sigma_{12}] \tag{1.28}$$

and

$$\varepsilon^T = [\varepsilon_{11}\,\varepsilon_{22}\,\varepsilon_{33}\,2\varepsilon_{23}\,2\varepsilon_{31}\,2\varepsilon_{12}]\,. \tag{1.29}$$

For general anisotropic elasticity, matrix $\boldsymbol{C}$ will be symmetric and therefore contain 21 independent components. It is well known that the behaviour of isotropic linear elastic materials can be described with a set of *two independent* parameters, for example, Young's modulus E and Poisson's ratio υ. In terms of these parameters, the elasticity matrix $\boldsymbol{C}$ for isotropic materials reads

$$\boldsymbol{C} = \frac{E}{(1+\upsilon)(1-2\upsilon)}\begin{pmatrix} 1-\upsilon & \upsilon & \upsilon & 0 & 0 & 0 \\ \upsilon & 1-\upsilon & \upsilon & 0 & 0 & 0 \\ \upsilon & \upsilon & 1-\upsilon & 0 & 0 & 0 \\ 0 & 0 & 0 & \frac{1}{2}(1-2\upsilon) & 0 & 0 \\ 0 & 0 & 0 & 0 & \frac{1}{2}(1-2\upsilon) & 0 \\ 0 & 0 & 0 & 0 & 0 & \frac{1}{2}(1-2\upsilon) \end{pmatrix}. \tag{1.30}$$

Alternatively, isotropic linear elastic behaviour can also be characterized with the shear modulus G in combination with the bulk modulus K. The sets of material parameters (E, υ) and (G, K) are related as follows:

$$G = \frac{E}{2(1+\upsilon)}; \quad K = \frac{E}{3(1-2\upsilon)}\,. \tag{1.31}$$

Generally, for isotropic solids, the engineering constants above or the Lamé constants are favoured, represented by Greek letters λ and μ such that $c_{12} = \lambda$, $c_{44} = \mu$ and $c_{11} = \lambda + 2\mu$.

1.5.2 Crystal elasticity

Single-crystal elasticity will in general not be isotropic. The number of independent material parameters depends on the level of symmetry of the crystal structure. For the cubic structure, the elasticity matrix can be written in terms of three independent material parameters

$$\boldsymbol{C} = \begin{pmatrix} c_{11} & c_{12} & c_{12} & 0 & 0 & 0 \\ c_{12} & c_{11} & c_{12} & 0 & 0 & 0 \\ c_{12} & c_{12} & c_{11} & 0 & 0 & 0 \\ 0 & 0 & 0 & c_{44} & 0 & 0 \\ 0 & 0 & 0 & 0 & c_{44} & 0 \\ 0 & 0 & 0 & 0 & 0 & c_{44} \end{pmatrix}. \tag{1.32}$$

If the relation $2c_{44} = c_{11} - c_{12}$ is satisfied, the material will be isotropic and the elasticity matrix can be written in the form of equation (1.30).

Tetragonal crystal structures have lower symmetry properties. As a result, for a complete description of the constitutive behaviour, six independent parameters are needed;

$$\boldsymbol{C} = \begin{pmatrix} c_{11} & c_{12} & c_{13} & 0 & 0 & 0 \\ c_{12} & c_{11} & c_{13} & 0 & 0 & 0 \\ c_{13} & c_{13} & c_{33} & 0 & 0 & 0 \\ 0 & 0 & 0 & c_{44} & 0 & 0 \\ 0 & 0 & 0 & 0 & c_{44} & 0 \\ 0 & 0 & 0 & 0 & 0 & c_{66} \end{pmatrix}. \tag{1.33}$$

In the following studies, there is particular interest in ceramic materials in film and bulk form, namely, a boron carbide film and refractory titanium alloys whose results are presented in detail in the chapters to follow. Again considering the cubic crystal structure for which three independent elastic constants exist, the Young's modulus is defined as the longitudinal stress produced by a unit strain when the body is unconstrained in the transverse directions yielding after elimination of ε_{22} and ε_{33} from equations (1.27),

$$E = \frac{(c_{11} - c_{12})(c_{11} + 2c_{12})}{c_{11} + c_{12}}. \tag{1.34}$$

Similarly relations for the other elastic moduli may be derived. For the velocities of elastic waves in crystals expressed in terms of the elastic constants c_{ij}, it is readily seen that

$$v_{long}[100] = \left(\frac{c_{11}}{\rho}\right)^{1/2}$$

$$v_{trans}[100] = \left(\frac{c_{44}}{\rho}\right)^{1/2} \tag{1.35}$$

$$v_{trans}[110] = \left(\frac{c_{11} - c_{12}}{2\rho}\right)^{1/2}. \tag{1.36}$$

Equations (1.35 and 1.36) provide a useful condition of isotropy, as in isotropic bodies, the transverse velocity must be the same for all directions such that from the above

$$c_{11} - c_{12} = 2c_{44}. \tag{1.37}$$

Thus the Young's modulus for an isotropic material is

$$E_{iso} = \frac{c_{44}(3c_{12} + 2c_{44})}{c_{12} + c_{44}} \tag{1.38}$$

[The corresponding expression from classical theory is $E_{iso} = \mu(3\lambda + 2\mu)/(\lambda + \mu)$ where λ and μ are Lame's constants]. The other isotropic moduli, namely bulk modulus, Poisson ratio and shear modulus are expressed respectively as follows:

$$B_{iso} = c_{12} + \frac{2}{3}c_{44}$$

$$\nu_{iso} = \frac{c_{12}}{2c_{12} + c_{44}} \tag{1.39}$$

$$G_{iso} = c_{44};$$

If the forces between atoms (or molecules) are central, no internal strains will be created by elastic stresses and the elastic constants obey the Cauchy relations for a cubic crystal $c_{12} = c_{44}$. This condition is not always valid generally, especially for anisotropic crystals and for cases where there are non-central contributions to the forces of interaction.

1.5.3 Effective elastic constants

The problem of averaging elastic coefficients to obtain engineering elastic constants such as Young's modulus, shear modulus, and the Poisson ratio is important in science and in technology. Despite much work on the problem, no final solution exists. Historically, methods proposed by Voigt and Reuss are important. Practically, methods suggested by Hill [1.47] enjoy wide use because they offer computational simplicity and acceptable agreement with measurement. A 'best' averaging method is sought mainly because (1) we can calculate more reliable values of polycrystalline elastic constants from monocrystal results, and (2) we can better understand polycrystalline-aggregate stress-strain states. All known averaging methods including those by Hearmon [1.48], Watt et al., [1.49] share common assumptions namely; (a) small grain-to-specimen sizes; (b) absence of voids, nonhomogeneities etc; (c) cohesion of crystallites occurs through very thin grain-boundary regions that are deformed relative to the crystal interiors; (d) randomly oriented grains; (e) grains large enough so that interfaces remain unimportant. In most instances, these assumptions apply fairly well to polycrystalline aggregates.

Generally a ceramic material consists of a number of grains, each with a different and unique orientation with respect to a reference frame. All individual grains will microscopically show anisotropic behaviour that is dependent on the crystal structure and orientation. However, when the number of grains is sufficiently large and the orientations are randomly distributed, the effective macroscopic behaviour is isotropic and constitutive properties can be characterized by an *effective* Young's modulus and Poisson's ratio.

The macroscopic effective elastic constants are found by averaging the anisotropic elastic properties of the individual crystals over all possible crystal orientations. To this end, a rotation tensor between a reference frame and a rotated vector basis attached to the crystal structure is defined[4]:

[4] the reference system O_c of the cubic axes $x_{c\mu}$, μ = 1 - 3, is transformed to the reference system O_A, of which the third axis coincides with $\boldsymbol{A}$ (unit vectors $[l_\lambda m_\lambda n_\lambda]$, λ = 1 - 3, by the orthogonal transformation $\mathbf{R_{cA}}$. (see text)

$$e^{'} = \mathbf{R}\underset{\sim}{e};\ \ with\ \ \mathbf{R}.\mathbf{R}^{T} = \mathbf{I}\,. \tag{1.40}$$

The components of the 4th - order elasticity tensor with respect to the rotated frame are obtained by

$$C'_{ijkl} = C_{mnop}R_{lp}R_{ko}R_{jn}R_{im}\,. \tag{1.41}$$

The macroscopic effective elastic constants are obtained by averaging this tensor over all possible rotation tensors [1.48]:

$$\overline{C}_{ijkl} = \int_{\forall R} C_{mnop}R_{lp}R_{ko}R_{jn}R_{im} \tag{1.42}$$

This average is termed the Voigt average and for orthotropic materials it results in the following relations for effective elastic constants:

$$E_V = \frac{(A-B+3C)(A+2B)}{2A+3B+C},\quad G_V = \frac{A-B+3C}{5},\quad \upsilon_V = \frac{A+4B-2C}{4A+6B+2C} \tag{1.43}$$

with

$$A = \frac{c_{11}+c_{22}+c_{33}}{3},\quad B = \frac{c_{23}+c_{13}+c_{12}}{3},\quad C = \frac{c_{44}+c_{55}+c_{66}}{3}\,. \tag{1.44}$$

Another approach is to average the inverse of the elasticity tensor i.e. the 4th –order compliance tensor **S,** over all possible orientations

$$\overline{S}_{ijkl} = \int_{\forall R} S_{mnop}R_{lp}R_{ko}R_{jn}R_{im} \tag{1.45}$$

which results in the Reuss effective elastic constants for orthotropic materials:

$$E_R = \frac{5}{3A'+2B'+C'},\quad G_R = \frac{5}{4A'-4B'+3C'},\quad \upsilon_R = -\frac{2A'+8B'-C'}{6A'+4B'+2C'} \tag{1.46}$$

with

$$A' = \frac{s_{11}+s_{22}+s_{33}}{3},\quad B' = \frac{s_{23}+s_{13}+s_{12}}{3},\quad C' = \frac{s_{44}+s_{55}+s_{66}}{3}\,. \tag{1.47}$$

The Voigt averaging method assumes the strains to be continuous across grain boundaries, whereas the stresses are allowed to be discontinuous. As a result the forces between the grains will not be in equilibrium. This method will give upper bounds for the actual effective elastic constants (*E, G*). When the Reuss averaging method is applied, the stresses are assumed to be continuous and the strains can be discontinuous across grain

boundaries, consequently the deformed grains do not fit together and lower bounds for the effective elastic constants are obtained.

The Voigt-Reuss-Hill approach combines the upper and lower bounds by assuming the average of the Voigt and the Reuss elastic constants to be a good approximation for the actual macroscopic effective elastic constants:

$$E_{VRH} = \frac{E_V + E_R}{2}, \quad G_{VRH} = \frac{G_V + G_R}{2}, \quad \upsilon_{VRH} = \frac{E_{VRH}}{2G_{VRH}} - 1. \tag{1.48}$$

Often, in order to compare the experimentally determined 'effective' elastic constants with literature values, it is necessary to compute starting from the single-crystal elastic constant values (usually available in literature), the Voigt-Reuss-Hill averaged values of the effective elastic constants that can be expected from the polycrystalline material of the same composition.

1.5.4 Elastic properties of cubic *textured* systems

Often in materials characterisation using x-rays one encounters specimen with a 'preferred orientation', a phenomenon that arises during sample preparation such as polishing, grinding, sintering etc. Normal x-ray diffraction is not sufficient to determine the preferred orientation; hence one uses 'pole-figure' analysis methods to accurately determine the preferred direction of the crystallites. In this section a theoretical model applicable to such systems will be developed and it will be demonstrated that simple approximation based on five independent elastic constants (hexagonal) adequately describes a cubic textured system thus allowing one to extract a full set of elastic constants. Starting with Hooke's law connecting stresses (σ_i) and strains (ε_i),

$$\begin{aligned} \sigma_i &= c_{ij}\varepsilon_j, \qquad (a) \\ \varepsilon_i &= s_{ij}\sigma_j \qquad (b) \end{aligned} \tag{1.49}$$

Summation over repeated indices is applied throughout. The components $c_{ij} = c_{k\lambda\mu\nu}$ and $s_{ij} = s_{\kappa\lambda\mu\nu}$ are related through

$$c_{\kappa\lambda\mu\nu} s_{\mu\nu\rho\sigma} = (\delta_{\kappa\rho}\delta_{\lambda\sigma} + \delta_{\kappa\sigma}\delta_{\lambda\rho})/2 \tag{1.50}$$

where $\delta_{\kappa\rho}$ is the Kronecker delta. All Roman indices run through 1 to 6, and all Greek indices run from 1 to 3. Equation (1.50), valid for all crystal classes, is useful in expressing c_{ij} in terms of s_{ij}, and vice versa. c_{ij} and s_{ij} are 6 x 6 matrix arrays as in section (1.5.2).

Any type of spatial averaging performed on equation (1.49a) under assumption of a constant strain gives the corresponding Voigt averages, denoted c_{ij}^{V}; similarly any spatial averaging under an assumed constant stress leads to the corresponding Reuss averages, s_{ij}^{R}. If the averaging involves all directions in the plane normal to a fixed axis ***A*,** the results correspond to a system which is textured along ***A*** (c_{ij}^{TV}, s_{ij}^{TR}).

For computational needs of the adopted system, following the treatment of Anastassakis et al. [1.49], we define a right-handed orthogonal reference system O_A, consisting of ***A*** itself and any two orthogonal axes normal to ***A***. In terms of their direction cosines relative to x_{c1}, x_{c2}, x_{c3}, the corresponding unit vectors are $[l_1m_1n_1]$, $[l_2m_2n_2]$ and $[l_3m_3n_3]$ $\equiv [lmn] \| A$. Letting $\boldsymbol{R}_{cA}$ be the orthogonal transformation taking O_c to O_A, and $\boldsymbol{R}_{A\theta}$ the transformation taking O_A to O_θ, where O_θ is reached through rotation of O_A if rotated clockwise by an arbitrary angle θ about ***A***. The corresponding matrices $\boldsymbol{R}_{cA}$ and $\boldsymbol{R}_{A\theta}$ are thus:

$$R_{cA} = \begin{pmatrix} l_1 & m_1 & n_1 \\ l_2 & m_2 & n_2 \\ l_3 & m_3 & n_3 \end{pmatrix}$$

$$R_{A\theta} = \begin{pmatrix} \cos\theta & \sin\theta & 0 \\ -\sin\theta & \cos\theta & 0 \\ 0 & 0 & 1 \end{pmatrix}$$

such that the transformation from O_c to O_θ is $\boldsymbol{R}_{c\theta}$,

$$R_{c\theta} = R_{A\theta} R_{cA} = \begin{pmatrix} L_1 & M_1 & N_1 \\ L_2 & M_2 & N_2 \\ L_3 & M_3 & N_3 \end{pmatrix}. \tag{1.51}$$

To obtain the expressions for c_{ij}^{TV} and s_{ij}^{TV} (for the textured state) using the example of component $c_{11}(\theta)$, it becomes

$$c_{11}(\theta) = c_{11} + c[T_{11}^{c}(\theta) - 1] \tag{1.52}$$

where $T_{11}^{c}(\theta) = L_1^4 + M_1^4 + N_1^4$ and c is a 6x6 matrix. Using the functions for L_1, M_1, N_1 derived from (1.51) in terms of θ and taking into account the orthonormality relations among l_λ, m_μ, n_ν, leads, after some algebra to an explicit function for $T_{11}^{c}(\theta)$ such that

$$T_{ij}^{C}(\theta) = T_{\lambda\mu\upsilon\rho} = L_\lambda L_\mu L_\upsilon L_\rho + M_\lambda M_\mu M_\upsilon M_\rho + N_\lambda N_\mu N_\upsilon N_\rho \ .$$

The component $c_{11}(\theta)$ corresponds to the crystalline state, relative to O_θ, and the only geometrical parameters required are the direction cosines of ***A*;** any other geometrical parameters are taken arbitrarily since they get eliminated at the end.

So in order to obtain c_{11}^{TV} for the textured state, we take the geometrical average of $c_{11}(\theta)$ for all values of θ, i.e.

$$\begin{aligned} c_{11}^{TV} &= \frac{1}{2\pi} \int_0^{2\pi} [c_{11} + c[T_{11}^{C}(\theta) - 1]] d\theta \\ &= c_{11} - (\frac{c}{8})(5 - 3T) \end{aligned} \tag{1.53}$$

where $T = l^4 + m^4 + n^4$. In a similar manner we find the remaining nonzero components of c_{ij}^{TV} in the textured state, i.e.

$$
\begin{aligned}
c_{22}^{TV} &= c_{11}^{TV} = c_{11} - (\frac{c}{8})(5-3T), \\
c_{33}^{TV} &= c_{11} - c(1-T), \\
c_{12}^{TV} &= c_{12} + (\frac{c}{8})(1+T), \\
c_{23}^{TV} &= c_{32}^{TV} = c_{13}^{TV} = c_{12} + (\frac{c}{2})(1-T), \\
c_{44}^{TV} &= c_{55}^{TV} = c_{44} + (\frac{c}{2})(1-T), \\
c_{66}^{TV} &= (c_{11}^{TV} - c_{12}^{TV})/2.
\end{aligned}
\tag{1.54}
$$

Recall that all C_{ij} components appearing in the right-hand side of these expressions correspond to cubic crystalline state (bulk values). Also worth noting is the following: the matrix array of non-zero components of c_{ij}^{TV} exhibits five independent components, resembling that of the hexagonal crystallographic system. Hence we can regard the textured state as an effective hexagonal class (EHC) with its six-fold symmetry axis x_{h3} pointing along $\boldsymbol{A}$ and the axes x_{h1} and x_{h2} taken arbitrarily [1.50].

$$
c_{ij}^{TV} = c_{EHC} = \begin{pmatrix}
c_{11} & c_{12} & c_{13} & 0 & 0 & 0 \\
0 & c_{11} & c_{13} & 0 & 0 & 0 \\
0 & 0 & c_{33} & 0 & 0 & 0 \\
0 & 0 & 0 & c_{44} & 0 & 0 \\
0 & 0 & 0 & 0 & c_{44} & 0 \\
0 & 0 & 0 & 0 & 0 & c_{66}
\end{pmatrix}
$$

where $c_{66} = (c_{11} - c_{12})/2$, $s_{66} = 2(s_{11} - s_{12})$, thus making a total of five independent elastic constants.

Chapter 2

2 Theoretical aspects of SBS

2.1 Power Spectrum in SBS

The spectrum obtained in a traditional frequency-domain SBS measurement contains peaks corresponding to the inelastically scattered light from thermally generated acoustic excitations localised in the vicinity of the sample surface. The frequencies at which these peaks are located, their shapes and relative intensities constitute valuable experimental information. To elucidate the elastic properties from this information, a prescription is necessary that relates the observed scattered intensity to the elements of the elastic tensor specific to the relevant crystalline symmetry. This scattering function in practice depends not only on mechanical but also the optical properties of the sample which have been shown to play a significant role, in addition to a myriad of experimental parameters to be considered. Thus, the term "power spectrum of fluctuations" in this context represents the pre-eminent contribution to the scattering function, and contains all the information on the elastic properties of the system that can be extracted from a Brillouin scattering measurement.

The general treatment of the thermally- generated surface acoustic waves of SBS depends partly on the connection between the power spectrum, and the response of the medium to a generalised fictitious force. This connection is established by the fluctuation-dissipation theorem and the associated response functions take the form of the Green's functions [2.1]. This chapter will give details of the calculations performed for the case of an anisotropic half space, relevant to the work of this thesis. In the following chapters the Green's function technique will be applied to enable a deeper insight to be obtained into the characteristics of the acoustic phonons encountered in various media as well as in the extraction of their elastic constants; high temperature situations form an important aspect of the present work.

2.1.1 Green's function method applied to surface lattice dynamics

The mathematical technique for studying the dynamics of perturbed systems, known as the Green's function method, was first applied to solid state problems by Lifshitz [2.1] in 1846, whilst Fredholm [2.2] in 1900 gave the first implicit expression for a general anisotropic solid. They stimulated the development of the Green's function method (GF) as a powerful tool in the quantum theory of scattering. The GF method in surface dynamics as a subject is now progressing further because of recent advances in surface phonon spectroscopy and phonon focusing with its important technological applications, especially in solid state electronics.

Alongside the advances in the subject have been the developments in the computational approach or tools developed by Every et al. [2.3] for solving the free-surface GF problem, which are conceptually simpler than other techniques, for example, the Cagniard de Hoop method [2.4]. As explained above (section 2.1), the SBS cross-section depends in some way on the surface displacements produced by the passage of the surface excitations. However, since the SBS technique probes thermally generated acoustic waves, for which their displacement is a statistical quantity, which is better represented by its corresponding power spectrum, i.e. the Fourier components of its mean square amplitude. In the case of opaque materials, the inelastic scattering of the incident light is governed entirely by the 'ripple scattering' mechanism of section 1.2 as shown by Loudon [2.5], the cross section itself is proportional to the power spectrum of the normal displacements of the surface associated with surface waves of wave vector component $q_{//}$ parallel to the surface, which according to the fluctuation dissipation theorem is proportional to the imaginary part of a Fourier domain Green's function.

2.1.1.1 The Green's function of an elastically anisotropic half-space

Following the computational approach developed by Every [2.6], consider an elastically anisotropic half-space of density ρ and elastic stiffness tensor c_{ijkl} occupying the region (z) or $x_3 < 0$ (refer to figure 2 on page 9). A point force $\boldsymbol{F}$ with a delta function time

dependence acts at the origin on the otherwise free surface of the half-space[5]. Components of the displacement field in response to this force are given by

$$u_i(x,t) = G_{ij}F_j \tag{2.1}$$

where G_{ij} are the elements of the elastodynamic Green's tensor. Once again, the displacement field must satisfy the wave equation subject to the relevant boundary conditions. In this case, the latter take the form

$$\sigma_{l3}(\boldsymbol{x}_{//}, x_3 = 0\_, t) = -F_j\delta_{jl}\delta(\boldsymbol{x}_{//})\delta(t)\,. \tag{2.2}$$

i.e. continuity of traction forces (stress components $\sigma_{l3}(\boldsymbol{x}_{//},\omega);\ l = 1,2,3$) and displacement field *u* at the interface, where $\boldsymbol{x}_{//} = (x_1, x_2)$.

Expressing equation (2.2) in terms of its Fourier transform with respect to both $x_{//}$ and *t* gives

$$\sigma_{l3}(\boldsymbol{x}_{//}, x_3 = 0\_, t) = -\int_{-\infty}^{\infty}\frac{d^2q_{//}}{(2\pi)^2}\int_{-\infty}^{\infty}\frac{d\omega}{2\pi}F_j\delta_{jl}e^{i(\boldsymbol{q}_{//}.\boldsymbol{x}_{//}-\omega t)}\,. \tag{2.3}$$

A general solution is assumed to be a superposition of plane waves whose amplitudes are proportional to the force *F*. In other words, u_i can be written as,

$$u_i(x,t) = \int_{-\infty}^{\infty}\frac{d^2q_{//}}{(2\pi)^2}\int_{-\infty}^{\infty}\frac{d\omega}{2\pi}\sum_{n=1}^{3}A_j^{(n)}F_jU_i^{(n)}e^{i(\boldsymbol{q}_{//}.\boldsymbol{x}_{//}+Q_3^{(n)}x_3-\omega t)}\,. \tag{2.4}$$

For a given value of $\boldsymbol{q}_{//}$ and ω, the third component q_3, is once again determined by the characteristic Christoffel equation, $\det\left|c_{ijkl}l_jl_k - \rho\upsilon^2\delta_{il}\right| = 0$.

The three roots are again chosen on the basis that they correspond to either evanescent waves that decay into the interior, or bulk waves with energy flow directed into the interior.

Inserting equation (2.4) into the constitutive relation $\sigma_{lm} = c_{lmpq}\,\partial u_p/\partial x_q$ gives

$$\sigma_{l3}(\boldsymbol{x}_{//}, x_3 = 0_+, t) = \int_{-\infty}^{\infty}\frac{d^2q_{//}}{(2\pi)^2}\int_{-\infty}^{\infty}\frac{d\omega}{2\pi}i\omega\sum_{n=1}^{3}A_j^{(n)}F_jB_l^{(n)}e^{i(\boldsymbol{q}_{//}.\boldsymbol{x}_{//}-\omega t)} \tag{2.5}$$

where

$$B_l^{(n)} = \sum_{pq}c_{3lpq}U_p^{(n)}q_q^{(n)}/\omega\,. \tag{2.6}$$

[5] This force is not due to the incident light but a fictitious tool for the evaluation of G_{33}

Comparison of equations (2.3) and (2.5) results in a set of three linear equations which determine the partial wave amplitudes $A_j^{(n)}$, described by

$$\sum_{n=1}^{3} B_l^{(n)} A_j^{(n)} = i\delta_{lj}/\omega \tag{2.7}$$

with solution

$$A_j^{(n)} = \frac{i}{\omega}(\boldsymbol{B}^{-1})_j^{(n)} \tag{2.8}$$

which for computational purposes may be written as

$$\frac{i}{\omega}(\boldsymbol{B}^{-1})_j^{(n)} = \frac{i}{\omega}\frac{adj(\boldsymbol{B})_j^{(n)}}{|\boldsymbol{B}|}. \tag{2.9}$$

From equations (2.3), (2.6) and (2.8), the elastodynamic Green's tensor is then

$$G_{ij}(\boldsymbol{x},t) = \int_{-\infty}^{\infty}\frac{d^2q_{//}}{(2\pi)^2}\int_{-\infty}^{\infty}\frac{d\omega}{2\pi}\frac{i}{\omega}\sum_{n=1}^{3}\Lambda_{ij}^{(n)}e^{i(\boldsymbol{q}_{//}.\boldsymbol{x}_{//}+q_3^{(n)}x_3-\omega t)} \tag{2.10}$$

where

$$\Lambda_{ij}^{(n)} = (\boldsymbol{B}^{-1})_j^{(n)}U_i^{(n)} = \frac{i}{\omega}\frac{adj(\boldsymbol{B})_3^{(n)}U_3^{(n)}}{|\boldsymbol{B}|}. \tag{2.11}$$

In order to obtain the Green's function of the differential scattering cross section of an anisotropic solid, G_{ij} is obtained by taking the limit $x_3 \to 0\_$ and setting $ij = 33$ in equation (2.4):

$$G_{33}(\boldsymbol{x}_{//}, x_3 = 0\_, t) = \int_{-\infty}^{\infty}\frac{d^2q_{//}}{(2\pi)^2}\int_{-\infty}^{\infty}\frac{d\omega}{2\pi}\left[\frac{i}{\omega}\sum_{n=1}^{3}\Lambda_{33}^{(n)}\right]e^{i(\boldsymbol{q}_{//}.\boldsymbol{x}_{//}-\omega t)} = \frac{i}{\omega}\sum_{n=1}^{3}\frac{adj(\boldsymbol{B})_3^{(n)}U_3^{(n)}}{|\boldsymbol{B}|} \tag{2.12}$$

The Fourier transform of this expression, namely,

$$G_{ij}(\boldsymbol{q}_{//},\omega) = \frac{i}{\omega}\Psi_{33}(\boldsymbol{q}_{//}/\omega) \tag{2.13}$$

where

$$\Psi_{33}(\boldsymbol{q}_{//},\omega) = \sum_{n=1}^{3}\Lambda_{33}^{(n)}(\boldsymbol{q}_{//}/\omega) \tag{2.14}$$

is the Fourier domain surface Green's function that determines the Brillouin spectrum. The expression for the differential cross section can thus be written as

$$\frac{d^2I}{d\Omega d\omega} = \frac{k_B TA}{\rho\omega^2}\,\mathrm{Re}\{\psi_{33}[\boldsymbol{q}_{//}/(\omega + i0)]\} \tag{2.15}$$

where A is a constant for a particular scattering polarisation and geometry, relative permittivity, and frequency of incident light, and in the classical limit $k_B T \gg \hbar\omega$.

The determinant of the matrix ***B*** appearing in equations (2.15) above must be zero for a true surface wave (compare with section 1.3.1). At this point there is a simple pole in ψ_{33}, which is invisible in a numerical calculation. In order to render it visible, it is artificially broadened by inserting some form of damping.

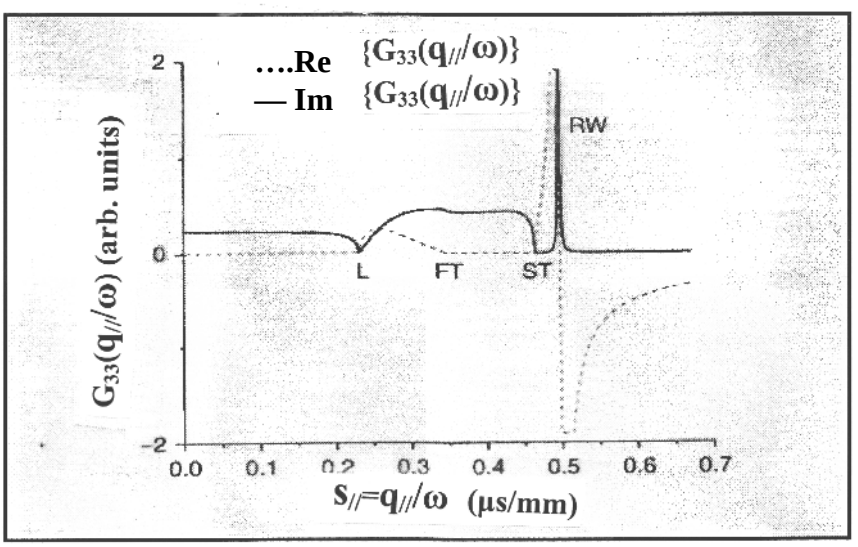

Figure 10: Green's function for [100] direction in the Cu (001) surface. The delta function has been broadened through introduction of some damping for graphic purposes [2.4].

Figure 10 shows G_{33} as a function of slowness[6] $s_{\parallel} = \boldsymbol{q}_{\parallel}/\omega$ at fixed frequency for the [100] direction in the (100) surface of an anisotropic cubic copper crystal. The imaginary part *ImG* has kinks at the limiting L, FT, and ST slownesses and is zero after the ST threshold (transonic state), except at the Rayleigh wave slowness (RW) where there is a sharp spike associated with the pole of *G*, determined by the vanishing of the boundary condition determinant $|B|$.

[6] The slowness surface depicts the directional dependence of the slowness or inverse phase velocity *s=1/v* .See section 2.1.1.3 and following sections below for more details:

2.1.1.2 Slowness (or inverse velocity) surface

The propagation characteristics of plane waves in an anisotropic solid may be found by rewriting the Christoffel equation as

$$[q^2\Gamma_{ij} - \rho\omega^2\delta_{ij}][v_j] = 0 \tag{2.16}$$

where $\Gamma_{ij} = c_{ijkl}l_l l_k$ is a tensor with normally three distinct eigenvalues (phase velocities) and eigenvectors (displacement directions) in any given direction of the wave normal *l*. A dispersion relation is then obtained by setting the characteristic determinant of (2.16) equal to zero,

$$\Omega(\omega, q_x, q_y, q_z) = \left|q^2\Gamma_{ij}(l_x, l_y, l_z) - \rho\omega^2\delta_{ij}\right| = 0\,. \tag{2.17}$$

At fixed ω, (2.17) defines a surface in q-space that gives q as a function of its direction $\hat{q}$. This is called the *wave vector surface*. Since the first term in the dispersion relation is proportional to q^2 and the second term proportional to ω^2, the relation can always be expressed entirely in terms of the variable q/ω. The wave vector q is therefore always proportional to ω and it is more convenient to consider the *slowness (or inverse velocity) surface* – which gives the inverse of the reciprocal phase velocity $s = q/\omega = 1/v$ as a function of propagation direction and is independent of ω – rather than the wave vector surface, which scales with ω. Some of the important properties of the slowness surface have been examined in figure 10 above for an anisotropic surface of cubic copper. The slowness surfaces have three sheets with the slowness surface corresponding to the quasi-longitudinal (L) wave with the highest phase velocity contained within the other two surfaces. This means that a line drawn parallel to the wave normal from the origin will in general intersect the surfaces three times. For crystals of most materials in certain directions, the slowness surfaces do intersect or become tangential to one another. In the crystal of GaAs for example, the three slowness surfaces do not cross one another along the face of the cube but become tangential along the acoustic axis as shown in figure 11 in which its calculation was performed using Mathematica [2.6].

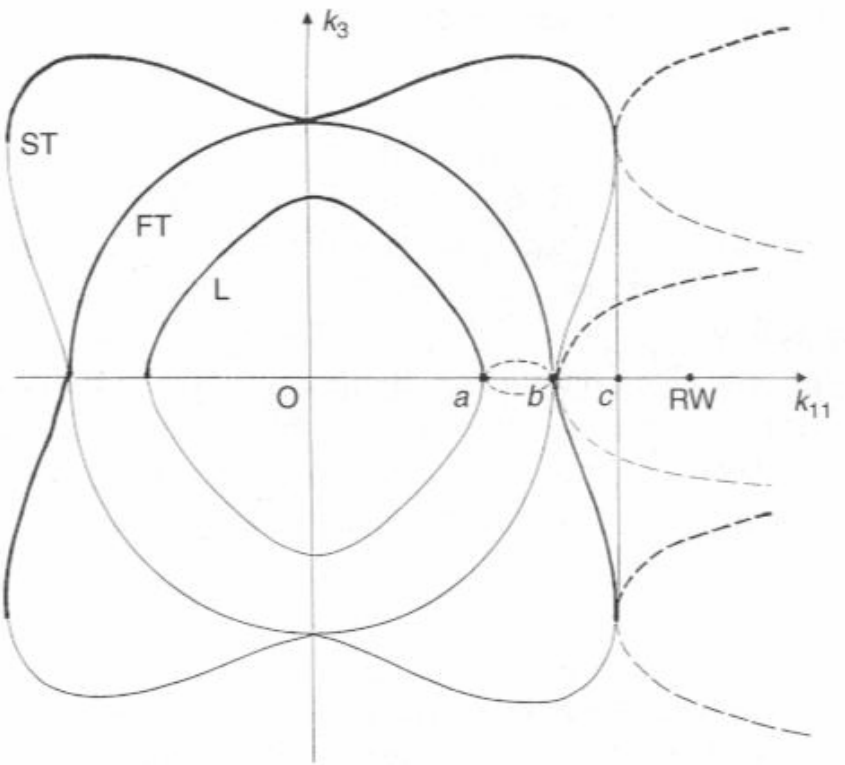

Figure 11: Schematic section of an acoustic slowness surface of an anisotropic solid, namely GaAs

For q values that lie beyond point a in figure 11, one or more pairs of complex conjugate solutions occur for q parallel to the surface (q_3) and there are correspondingly fewer bulk wave solutions. The existence of an imaginary part of q_3 has the consequence that the wave is not simply oscillatory but grows or falls exponentially with distance from the surface. For each pair of complex solutions, the one having a positive imaginary part (Im ($q_3 > 0$) (denoted by a *bold dashed* line in figure 11), corresponds to an evanescent wave whose displacement falls off exponentially away from the surface, and this is regarded as an outgoing wave. The other exponentially growing wave with Im ($q_3 < 0$), denoted by lighter dashed line is discarded as it has no physical meaning. Thus, real or evanescent, there are always three outgoing waves. Thus points a and c are threshold values for q where solutions change from real to complex, and b is a coincidence of two opposite thresholds where a pair of real fast transverse (FT) solutions appears. The limiting bulk waves at these q values have ray vectors that are parallel to the sample. They are known as surface skimming waves or lateral waves, and they feature in the determination of

elastic constants using SBS as has been discussed in Chapter 1 as applied to isotropic conditions. Beyond *c*, known as the transonic state, the solutions are all complex, and in this region, not too far from the threshold point *c*, is to be found the Rayleigh wave solution, RW. The RW is a superposition of three phase-matched evanescent waves that satisfies the free surface boundary conditions, thus the amplitude falls off to a negligible value within a few wavelengths of the surface.

2.2 Temperature dependence of the elastic constants in a lattice

Introduction

The classical harmonic approximation implies that the elastic constants are independent of temperature and pressure, and therefore the adiabatic and isothermal elastic constants are equal. However, in real crystals these assertions are not realized, and in addition, the approximation cannot explain phonon-phonon interactions or thermal expansion, and it predicts that that the heat capacity becomes constant at high temperatures [2.7]. Thus in order to account for the above phenomena, it is necessary to include higher order terms (anharmonic) in the atomic displacements. This corresponds to the fact that Hooke's law no longer holds for finite strains, so that the stress-strain relationship is no longer linear.
The deformation energy of the solid is rewritten thus,

$$U = \frac{1}{2} c_{ijkl} \eta_{ij} \eta_{kl} + \frac{1}{6} c_{ijklmn} \eta_{ij} \eta_{kl} \eta_{mn} + \ldots + \frac{1}{n!} c_{ij\ldots op} \eta_{ij\ldots} \eta_{op} + \ldots \qquad (2.18)$$

if the initial energy and deformation of the body are zero.

The constants c_{ijklmn} are termed the third-order elastic constants, in the sense that three strains are involved in the definition. This follows for n^{th} order elastic constants, while the familiar c_{ijkl}*'s* are sometimes called the second order elastic constants. Thus the higher order elastic constants describe the asymmetry of the lattice potential energy with respect to particle separation, and are accordingly a measure of the anharmonicity. The higher order elastic constants can be defined in terms of thermodynamic quantities according to references [2.8] and [2.9].

Experimental results indicate that the second-order elastic constants of many materials have the temperature dependence of the form shown by the solid curve in figure 12. This demonstrates distinctive behaviour at high- and low- temperatures; where the deviation at low temperatures is associated with the zero-point motion of the atoms. Several theoretical studies of the temperature dependence of the elastic constants have been reported. Hiki et al. [2.10] and Swartz [2.11] considered the contributions of elastic

waves travelling in many different directions in anisotropic crystals to determine the variation of elastic constants in the high-temperature region. Garber and Granato [2.12] derived the temperature dependence of the elastic constants in both the low- and high-temperature regions on the basis of a quasi-harmonic anisotropic continuum model.

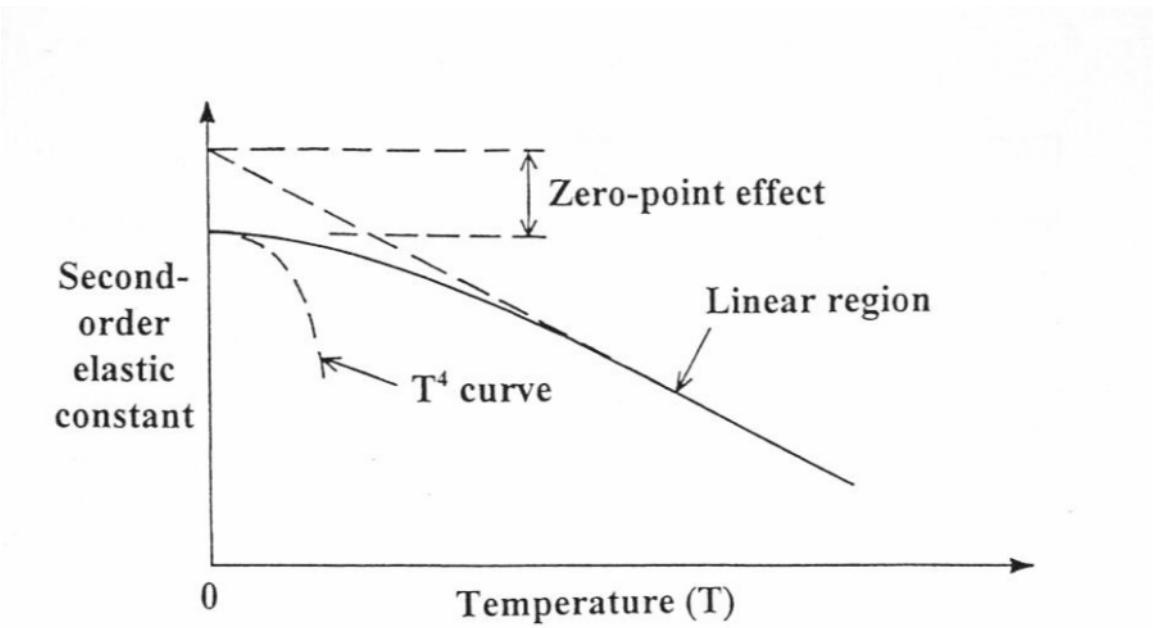

Figure 12: The elastic constants of many materials exhibit the characteristic behaviour at low- and high-temperatures shown above. [2.12]

The quasiharmonic approximation traditionally plays a central role in thermodynamic modelling and theory of equations of state of solids. In this approximation, thermodynamic properties are calculated from the vibrational spectrum, which is assumed to depend only on volume and not on temperature. However, the intrinsic anharmonic effects, ignored in this approximation and leading to the temperature dependence of phonon frequencies, become important at high temperatures (and especially at low pressures). The temperature dependence is expressed in terms of the second-, third- and fourth-order elastic constants. Tests of the quasi-harmonic theory by Garber and Granato [2.13] against experiment met with some general success, however the results to be presented in this thesis demonstrate clearly the importance of incrorporating the higher order terms at high temperatures. In the following section only the qualitative results using a simplified quasiharmonic model will be reproduced, and

later in chapter 4, 5, and 6 this model will be compared with quantitative or experimental results of iron pyrite crystal and other materials obtained using SBS for the first time.

2.2.1 Theory of the quasi-harmonic approximation.

The elastic constant $c_p(\boldsymbol{q})$ relevant to an elastic wave branch p propagating with wave-vector $\boldsymbol{q}$ is related to the velocity $\boldsymbol{\upsilon}_p$ of the mode through

$$c_p(\boldsymbol{q}) = \rho \upsilon_p^2 . \tag{2.19}$$

This relation has been shown to be related in a simple way to the constants c_{ij} for some high symmetry directions in the crystal [2.11]. For the long- wavelength zone-centre photons of interest in Brillouin scattering ($\boldsymbol{q} \leq 10^5$ cm^{-1}), the velocity depends on the mode frequency ω_p according to,

$$\upsilon_p = \frac{\omega_p}{q} . \tag{2.20}$$

In the harmonic approximation, the frequency of a mode is independent of either temperature or strain. However, in a real crystal the phonon frequencies do depend on the equilibrium volume. This forms the basis of the quasi-harmonic approximation where the phonon frequency depends indirectly on temperature through the temperature dependence of the lattice dimensions. Taking the derivative of $c_p(\boldsymbol{q})$ with respect to temperature gives:

$$\frac{\partial c_p(\boldsymbol{q})}{\partial T} = \upsilon_p^2 \frac{\partial \rho}{\partial T} + 2\rho\upsilon_p \frac{\partial \upsilon_p}{\partial T} . \tag{2.21}$$

From the relationship between density and the coefficient of thermal expansion α, we find

$$\frac{\partial \rho}{\partial T} = -3\alpha\rho . \tag{2.22}$$

We use the chain rule and equation (2.20) to obtain

$$\frac{\partial c_p(\boldsymbol{q})}{\partial T} = -3\alpha\rho\upsilon_p^2 + \frac{2\rho\upsilon_p}{q} \frac{\partial \omega_p}{\partial V} \frac{\partial V}{\partial T} . \tag{2.23}$$

The last derivative is again related to the thermal expansion coefficient. We now define the Grünieisen parameter in the usual way

$$\gamma_p = -\frac{V}{\omega_p}\frac{\partial \omega_p}{\partial V} \tag{2.24}$$

which leaves equation (2.23) in the form

$$\frac{\partial c_p(\boldsymbol{q})}{\partial T} = -3(1+2\gamma_p)\alpha c_p(\boldsymbol{q})\,. \tag{2.25}$$

In simple models, such as the Debye model, the volume dependence of the normal mode frequencies is contained in a universal multiplicative factor. Thus the γ_p are constant and the same for all modes, while the elastic constants themselves change relatively little with temperature. Thus the temperature dependence should largely be determined by α. Using similar arguments to those above; it is possible to show that the coefficient of thermal expansion has the same temperature dependence as the specific heat in the high- and low-temperature limits [2.14]. Consequently we find that

$$\begin{aligned} &\frac{\partial c_p(\boldsymbol{q})}{\partial T} \sim -T^3, \quad T \to 0 \\ &\frac{\partial c_p(\boldsymbol{q})}{\partial T} \sim \text{constant} < 0, \quad T \gg \theta_D, \end{aligned} \tag{2.26}$$

where θ_D is the Debye temperature.

These results qualitatively reproduce the temperature dependence of the second order elastic constants seen in many materials. In this way we can think of the changes in the elastic constants observed immediately after the Debye temperature as *being the result of thermal expansion* [2.15]. For temperature regions further away from θ_D the equation (2.26) is shown to be indequate to describe fully the high temperature profiles of the elastic moduli as shall be shown in the results of iron pyrite, titanium alloys and boron-doped silicon. The temperature dependence is best expressed in terms of the second-, third- and fourth-order elastic constants in order to explain observed curvature in the variation of the elastic constants as the temperature is increased.

Chapter 3

3 SBS Experimental Apparatus and Measurement Precision.

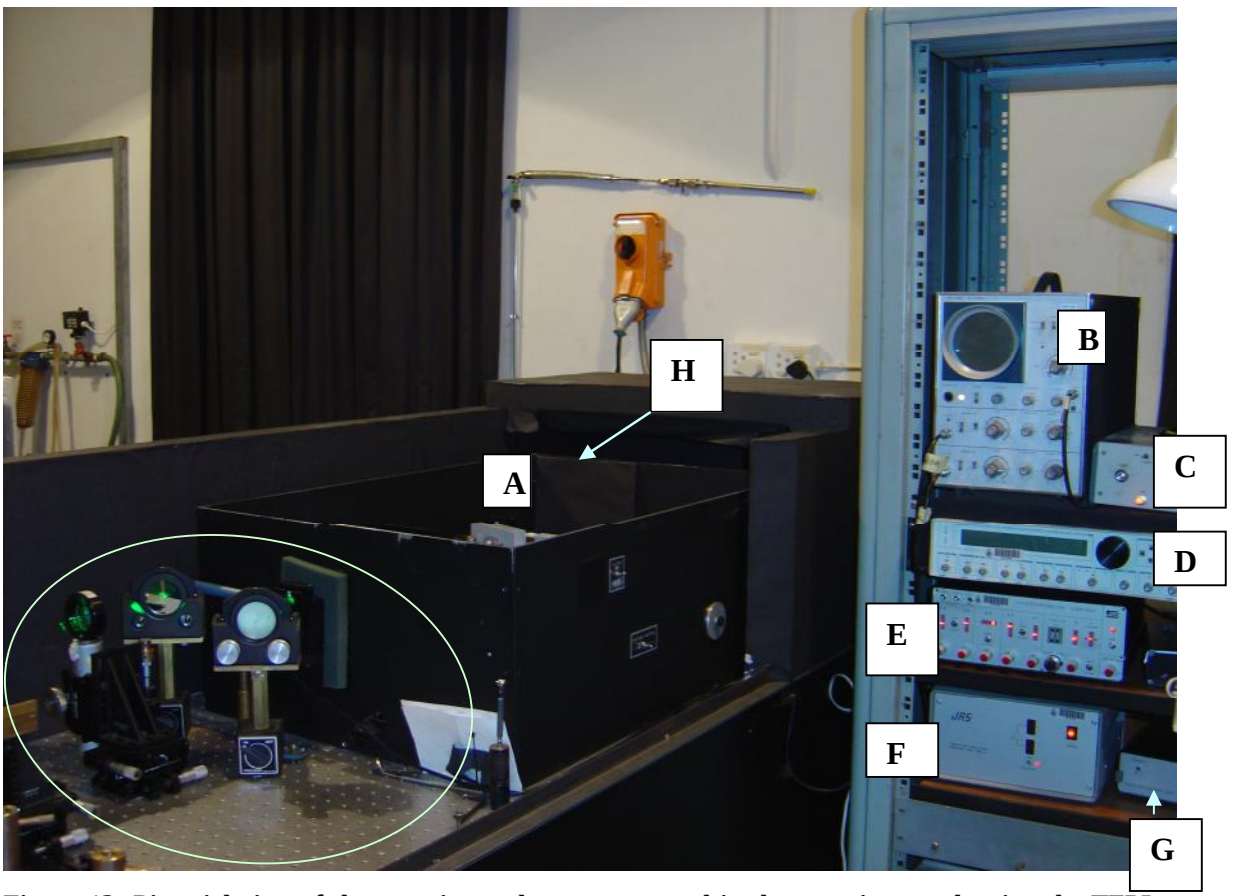

Figure 13 Pictorial view of the experimental apparatus used in the experiments showing the TFPI and auxiliary electronics detailed in figure 14 below.

A - TFPI; B – high-persistence CRO; C – AOM control unit; D – pulse shaper for PMT(not used); E – TFPI control unit; F – JRS anti-vibration stabilizer power unit; G – shutter control unit; encircled part contains part of the auxiliary optics arrangement. H-silicon avalanche diode detector and photon counting unit

Glossary of acronyms in figure 13

TFPI	Sandercock-type tandem Fabry-Pérot interferometer
CRO	Cathode ray oscilloscope, fitted with a high persistence screen
AOM	Acousto-optic modulator, device for regulating laser intensity
PMT	Photomultiplier tube, photon detector (not used in this body of work)
JRS	JR Sandercock trading name

Since the earliest work by Gross in 1930, Brillouin scattering (BS) using a Fabry-Pérot interferometer (FPI) has been a well established method for the investigation of thermally excited sound waves in liquids and solids [3.1]. The high resolution required to perform Brillouin scattering experiments, coupled with the usually intense unshifted radiation due to sample surface imperfections and scattering thereof) made the technique applicable to only the purest of materials, such as highly purified liquids and very clear solids. An excellent review of experiments carried in the early days has been given by Fleury [3.2] where in almost all experiments the Fabry-Pérot has been the instrument of choice. There are only a few cases where the Brillouin frequency shifts can be resolved using grating spectrometers. It was widely recognized that a standard Fabry-Pérot interferometer has too low a contrast to allow for the weak Brillouin signals to be resolved against the background of the normally extremely intense elastically scattered light. Although index matching techniques and resonant absorption of the elastically scattered light somewhat alleviated this problem, it was the high contrast [3.3] of the multipass interferometer developed by Sandercock which reduced BS to a relatively simple and widely applicable technique.

A multipass interferometer suffers, however, like the simple interferometer, from the overlapping of neighbouring interference orders which introduces ambiguity into analysis and interpretation of the measured spectra. Although it had been known for decades that a tandem interferometer, by suppressing the neighbouring spectral orders, would allow spectra with many, not-so-sharp spectral features to be resolved, it was the advent of a more practicable tandem combination of multipassed interferometers based on a common

translation stage that provided the solution [3.4]. This instrument offers very high resolution, contrast and free spectral range.

The first part of this chapter will focus on the instrumental details of the apparatus used to perform SBS measurements, namely the laser and tandem FPI, and related optics and sample holders/mountings and lastly the high temperature furnace that enables high temperature SBS measurements to be conducted. The last part of the chapter will identify and describe sources of error that are important to be considered for high precision measurements.

3.1 Experimental apparatus

Successful measurements in SBS require very specialized equipment, since the scattering cross-section associated with surface acoustic waves is very small, while the frequency shifts of the scattered light lie in the range 0.1 – 5 cm^{-1} (3 – 150 GHz). Although it is sometimes possible to resolve these shifts with a grating instrument, the Fabry-Pérot interferometer is the instrument of choice since its resolution is ideally suited for this frequency range. An intense source of highly monochromatic light, a sensitive detector, a spectrometer of high resolution and high contrast, operator's skill, and scattering geometry are all key elements of successful SBS experimentation. Long accumulation times are the norm hence it is also important for the system to remain stable over the duration of the measurement. A schematic diagram of the apparatus is given in figure 14 below. An Ar^{+} -ion laser with an intra-cavity etalon serves as a light source with a wavelength of 514.5nm. With the aid of an acousto-optic modulator (AOM), the intensity of the laser beam can be changed leaving the intensity of the reference beam at a constant value. Using a JRS double-shutter system during the period within the TFPI scan in which the elastically scattered light is most intense, the scattered light shutter closes, while simultaneously opening the reference beam shutter to inject the reference signal (which has a lower intensity ~ 1mW, compared to the elastically scattered light). In this way, a constant reference signal is provided for stabilising of the interferometer while also protecting the detector from overload.

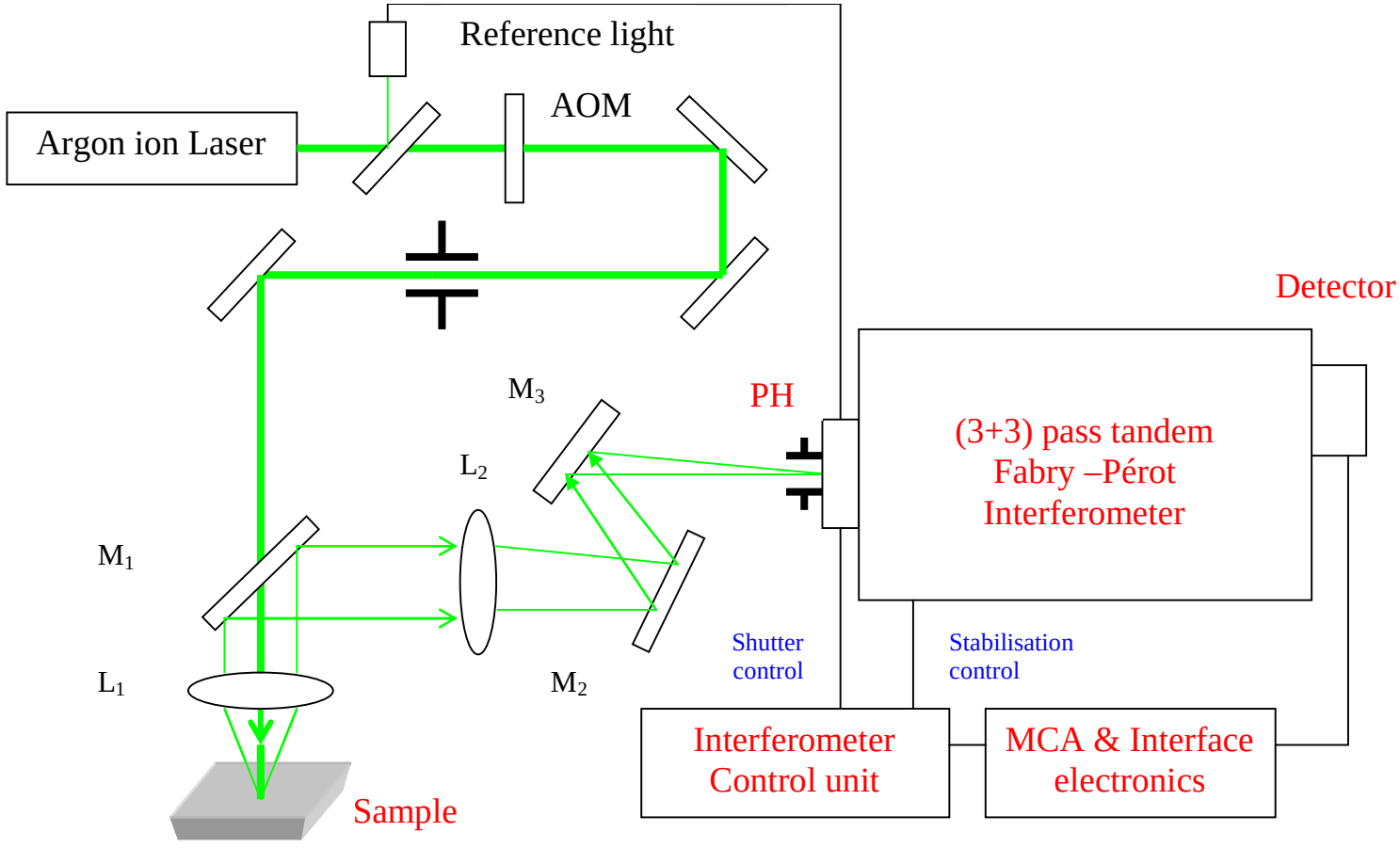

Figure 14: Surface Brillouin scattering configuration used for conducting experiments in this work

3.1.1 The laser

The two lasers used for this research work were both water-cooled cw Ar^+- ion devices manufactured by the Spectra-Physics company. The older, more powerful (18 Watt) 171 model was used as a stand-by for the smaller (5W) 2020 model during major breakdowns.

In Ar^+- ion laser systems, population inversion is achieved the following way: the gaseous argon is first converted into excited plasma by an electric discharge. The ions then decay into the metastable 4p state which may also be reached by direct excitation. The eventual decay to the 4s level, via stimulated emission, accounts for the visible laser radiation. The latter has a wavelength of between 450 and 530nm, depending on the decay scheme involved.

A number of mechanisms conspire to broaden the theoretically narrow line width of the laser frequency to a gain profile of around 6 GHz [3.4]. This profile comprises the resonant longitudinal modes whose wavelengths depend on the distance between front and rear laser mirrors via the condition

$$D = \frac{1}{2} n\lambda \tag{3.1}$$

for integral *n*.

The output power depends on the frequency, while the power distribution across the beam is further modified by the presence of transverse electromagnetic modes (TEM). The true, TEM_{00} mode is the most useful as it provides a Gaussian distribution, with minimum beam divergence and smallest beam diameter [3.5]. Throughout all the measurements the mode wavelength used is 514.5nm. However, the gain profile is far too wide to be useful in SBS measurements

The solution to this problem is to select from it a single longitudinal mode. This is achieved through the use of a temperature-controlled intra-cavity etalon; the point at which the transmission loss for the etalon is a minimum is made to coincide with the longitudinal cavity mode of the highest intensity. Practically, this is achieved by first aligning the etalon perpendicular to the beam, corresponding to a position of virtually no loss in power. To avoid lasing between the front of the etalon and the output laser mirror, the etalon must be slightly misaligned until a drop of about 50 % in output power is registered. Finally by adjusting the etalon temperature, and thereby changing the optical path length, the desired longitudinal cavity mode corresponding to the (TEM_{00}) mode is selected. Temperature drifts in the cavity can cause variation in the cavity spacing, with a consequent broadening of the laser line or even mode hopping in the laser output. The laser output power is also kept fixed by means of a control loop inserted in the input laser current. Since the windows of the laser plasma tube are inclined at the Brewster angle, the output is polarised in the scattering plane, which gives zero at the Brewster angle; $\theta_B = \arctan\sqrt{\varepsilon}$. In the laboratory set-up, the orientation of the tube was such that the polarisation was perpendicular to the optics table; and to take advantage of the most efficient SBS scattering process *p-p*, the incident angle θ_i was always measured in the vertical plane.

Photo - detectors

Given the low intensity of the Brillouin signals, single-photon counting is desirable for the detection system. Low-noise photomultiplier tubes (PMT) having dark counts not higher than 1-2 counts per second (actually 0.3 per second) are generally used for this purpose. A drawback of this type of detector is the low quantum efficiency of the photocathode. A newer generation of low-background noise, single-photon avalanche photodiodes with higher quantum efficiency (45%) than typical PMT (at 15%), were once available (though they are now out of production). In our laboratory we used exclusively the EG&G Optoelectronics Canada SPCM-200-PQ silicon avalanche photodiode for all the experiments. This device has the important advantage over a PMT, that of higher

quantum efficiency; however, it has a disadvantage of a higher dark count of 1 per second compared to 0.3 per second for the PMT. In practice though, the higher quantum efficiency translates to reduced time to accumulate a spectrum of between four and five times for the EG& G device compared to a PMT.

3.1.2 Multipass tandem Fabry-Pérot interferometer

In Brillouin scattering spectroscopy from surfaces, acoustic phonons with frequencies normally in the range 15 - 150 GHz are measured. In some cases frequencies lower than 15 GHz have been observed. The frequency shift of the scattered light is therefore 10^4-10^5 times smaller than the central frequency of the laser light and therefore a high-resolution spectrometer, such as the plane Fabry-Pérot interferometer (PFP) is used.

A single PFP interferometer consists of two partially reflecting plane mirrors mounted parallel to each other at a distance *L*. For normal incidence, the instrument transmits light of wavelength λ only if the distance *L* is equal to a multiple of half the value of the incident wavelength, namely $L = m\lambda/2$ where *m* is an integer. This can be understood by considering the interference between the ray directly transmitted by the two mirrors and the ray that experiences double reflection inside the interferometer cavity. Neighbouring orders of interference are therefore separated in frequency by an amount $\Delta\nu = L/2$ wavenumbers, i.e. $(\Delta\nu = c/2L) = 150/L$ GHz mm^{-1}). The inter-order spacing is called the *free spectral range* (FSR).

If we take into account multiple reflections inside the interferometer cavity, then the transmitted intensity is given by the Airy function *T*(L/λ)

$$T(L/\lambda) = \frac{T_o}{1 + (\frac{4F^2}{\pi^2})\sin^2(2\pi L/\lambda)} \qquad (3.2)$$

where T_o is the maximum transmission and parameter *F*, the *finesse* of the interferometer, determines the width of the fringes and depends on the flatness and reflectivity of the mirrors. The transmission as a function of wavelength is plotted in figure 15 below. The resolving power of the interferometer is defined as $\delta\lambda$, being the full width at half

maximum (FWHM) of the peaks of figure 15 and this can be shown to be equal to the ratio between the FSR and the finesse,

$$\delta\lambda = \Delta\lambda / F \ . \tag{3.3}$$

From the equation (2.28), it is easy to show that that if instead of the wavelength, the mirror spacing *L* is varied or scanned, a similar transmission profile to that of figure 15 is produced. In this way the transmission can be tuned to analyse spectral components, and the FPI takes the role of a spectrometer. In plane Fabry-Pérot (PFP) interferometry, a tilt - free scanning stage must be used in order to preserve the alignment of the mirrors. The scanning stage used in the experiments consists of a deformable parallelogram platform mounted on top of a roller translation stage for fine and coarse scanning [3.5]. A screw made of low-thermal expansion material positions the mirror spacing while the scan is performed with a piezoelectric transducer. Mirror spacing is measured by a plane capacitor, and an active loop is used for regulating the scan voltage to the transducer.

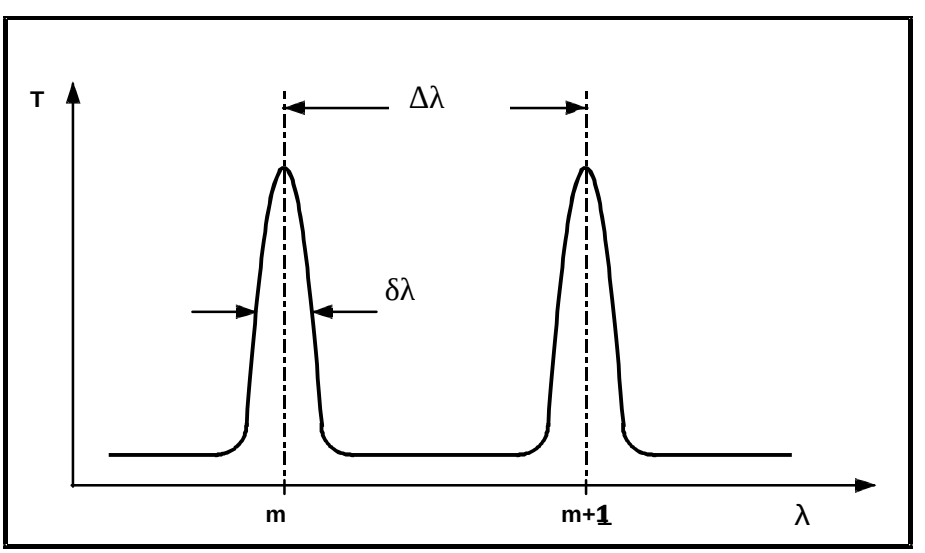

Figure 15: Transmission profile of a single FPI

The PFP is extremely sensitive to mirror misalignment and an active feedback loop is used to regulate parallelism between the mirrors using a system of piezo-electric transducers to preserve this parallelism (see JRS TFPI manual for more details). The scanning stage is then mounted on top of a dynamic vibration isolation system made by JRS. This is necessary, since mirror displacements as small as 2 nm are necessary to scan

the PFP interferometer through a transmission peak. Spectral distortions can easily occur for any mechanical disturbance that changes the mirror spacing by as little as a few tenths of a nanometer.

In a Brillouin spectrum, elastically scattered light from surface roughness and irregularities is usually many orders of magnitude more intense than Brillouin signals. This makes a surface - Brillouin scattering experiment feasible only if very high contrast interferometers are used to resolve the Brillouin peaks from the more intense elastically scattered light. High contrast is even more important when the small scattering volume associated with surface phonons, usually limited to a few acoustic wavelengths, is considered. Signals of surface acoustic phonons are therefore very weak compared with Brillouin scattering from bulk phonons in transparent materials.

Significance of contrast in interferometers

The contrast C of the interferometer can be defined as the ratio between maximum and minimum transmission of the Airy function: hence C is given by

$$C = 1 + (2F/\pi)^2. \tag{3.4}$$

Since the finesse of an interferometer cannot be much higher than 100, a single pass interferometer cannot have a contrast higher than 10^4. The contrast is greatly enhanced if multiple passes of light through the interferometer are performed. In this case the form of the transmission coefficient is ideally obtained by raising the single pass Airy function to the *n*th power where *n* is the number of passes. The contrast for a multipass interferometer becomes

$$C_n = [1 + (2F/\pi)^2]^n, \tag{3.5}$$

which can be raised to 10^9 – 10^{11}. This happens only if separate passes are truly decoupled from one another. In practice coupling between passes does occur leading to some loss in the contrast of a multipass interferometer with respect to its theoretical value. In the present work the experimental set-up used is a (3+3) multipass configuration originally proposed by Mock et al. [3.6].

Problems of overlapping interference orders

A major problem encountered in PFP interferometers is the overlapping of interference orders of different spectral features of the scattered signal. When scattered light is composed of frequencies extending to a maximum frequency υ_{max}, an unambiguous interpretation of the spectrum can be given only if the FSR is chosen such that *FSR* $>2\upsilon_{max}$. This sets a limit on the spectral resolution, since by using a large value of FSR, low-energy peaks in the spectrum cannot be resolved from the central elastic peak. To increase the FSR without degrading the spectral resolution involves using a cascade of two or more PFP interferometers having different spacing (*tandem interferometers).*

Tandem interferometers

If two interferometers with mirror distances L_1 and L_2 are placed in cascade to transmit two different interference orders $m_1 = 2L_1/\lambda$ and $m_2 = 2L_2/\lambda$ of the incident wavelength λ, the transmitted intensity is composed of the product of the Airy function of both interferometers. The total transmission curve is composed of a central elastic peak corresponding to exact coincidence of one of the orders of each FPI, and small ghosts representing weakly transmitted interference orders of the two interferometers. In figure 16 below is a schematic of the transmission curves of the etalon (a) FP2, (b) FP1 and (c) of both etalons in series (tandem operation) as a function of the mirror separation of the first etalon, L_1.

Assuming that for a given value of L_1 both etalons are in transmission, a change of $\lambda/2$ in L_1 puts FP1 into the next transmission order. Due to the common mounting of the movable mirrors the change in the spacing of the second etalon is smaller by a factor of $\cos\Theta$ with Θ the angle between the optical axes of the two interferometers as displayed in the figure. Thus FP2 is now not in transmission, and the transmission maxima of both etalons lie at different values of L_1. The same argument applies for inelastic excitations, which are transmitted only if they belong to the common transmission order. The inelastic signal represents closely the scattering cross section of the sample.

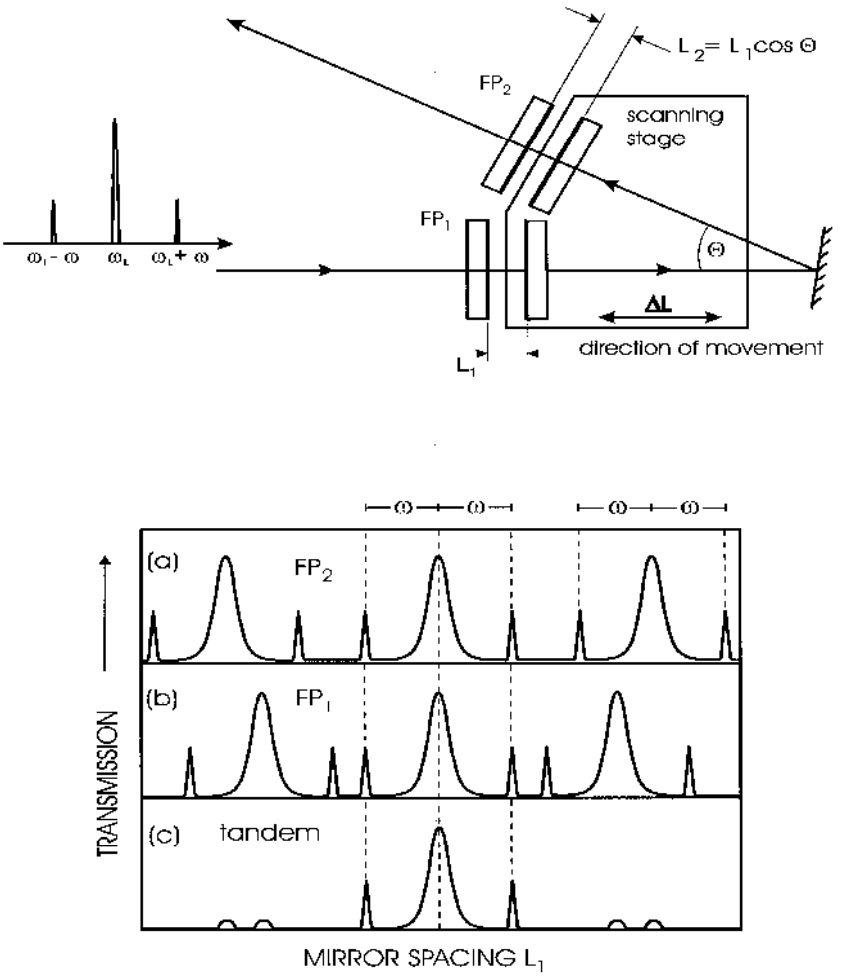

Figure 16 Schematic view of the operation of a Sandercock-type tandem Fabry-Pérot interferometer. Top: View of the light pass. Bottom: Transmitted intensity of first (FP1), second (FP2) and both etalons in series. The inelastic contributions due to an inelastic light scattering process are indicated by ω. [courtesy of JRS Instrumentation [3.5]].

For an experimental realization of the transmission, a flatness of the mirror surfaces of better than $\lambda/200$ and a parallelism of $\lambda/100$ of the two mirrors of each etalon are necessary. To maintain the latter, a sophisticated active stabilization of the mirror alignment is needed, as discussed above. In order to obtain the high contrast necessary to detect the weak inelastic signals the light is sent several times through both interferometers using a system of retro-reflectors and mirrors.

The overall free spectral range can be increased 10 - 20 times over the FSR of a single interferometer. Usually distances L_1 and L_2 are chosen such that $L_2 / L_1 = k / n$, where k

and *n* are incommensurate prime numbers. The effective FSR becomes *k* times the free spectral range of the first interferometer. The major difficulty of tandem interferometry is represented by the synchronisation of the two interferometer scans. The relation $\delta L_1 / L_1 = \delta L_2 / L_2$ between the increments in the mirror distances L_1 and L_2 must be satisfied during the scan with sub-nanometer accuracy. In order to realize physically the synchronously scanned tandem interferometers, the two scanning mirrors are mounted on the same scanning stage at an angle Θ. (See figures 16 and 17).

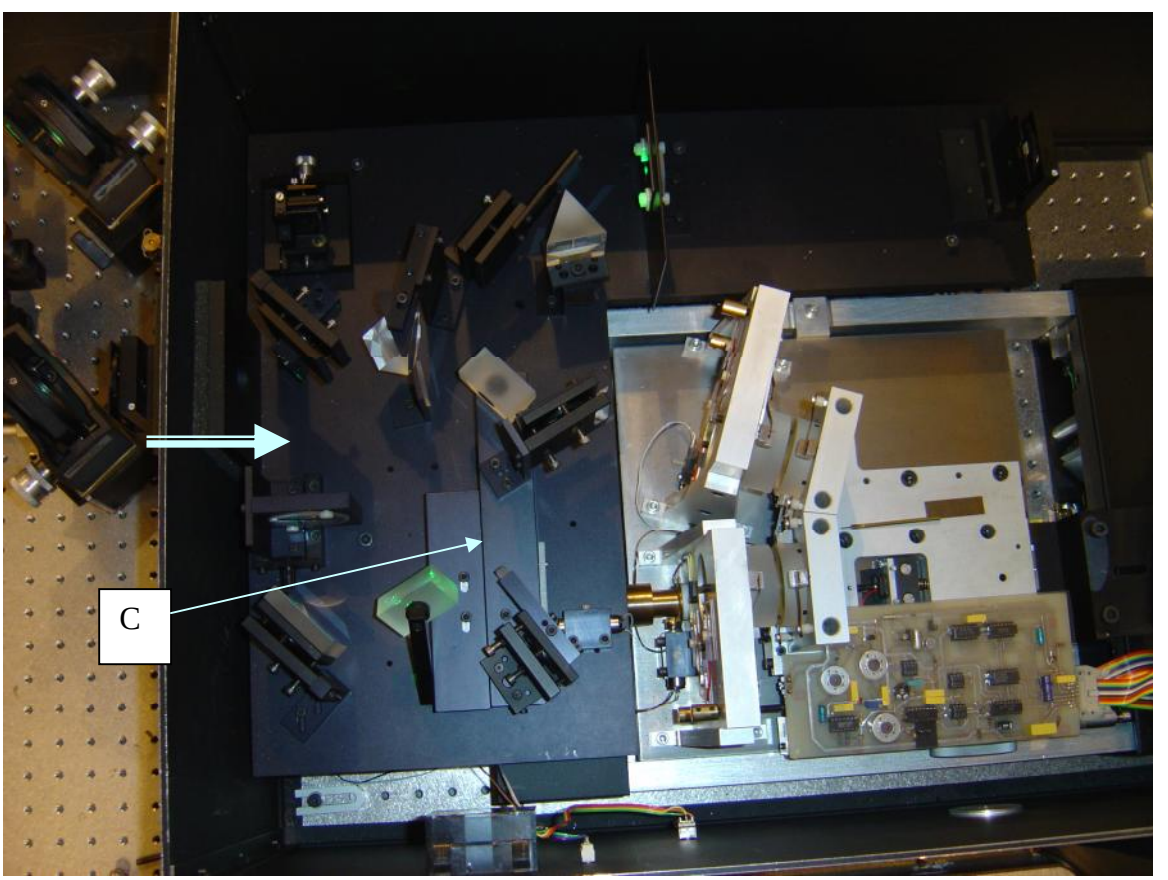

Figure 17: Aerial view of the JRS Instruments (3+3) multipass tandem FPI used in the experiments showing the tandem/scanning stage (white metal). The large arrow shows the position of the entrance pinhole for entry of the laser light. C marks the position of a translation stage for switching between *alignment* mode and *tandem* mode during the set-up procedure.

In this way, $L_2 = L_1 \cos\Theta$ and thus the ratio $\delta L_1 / L_1 = \delta L_2 / L_2$ is satisfied. In the tandem interferometer used for the measurements, $L_2 / L_1 = 19/20$, corresponding to $\Theta \approx 18^o$.

The Shutter Assembly

A JRS Scientific Instruments LM2 shutter assembly is used to introduce the reference signal that is needed by the automatic alignment system. The device is programmed to close shutter 1 as the scan approaches the unshifted laser frequency, and open shutter 2 to admit the reference signal obtained from the laser beam before the AOM, using a simple glass slide beam splitter and a system of mirrors to deflect the light onto the LM2 aperture to shutter 2. Once the unshifted laser frequency has been traversed, shutter 2 is closed and shutter 1 reopens. The TFPI control unit which is linked to the shutter control unit to provide the synchronisation of the timing is used to set the position and width of the reference window. With the instrument in operation, the incident laser intensity can be safely increased to enhance the Brillouin signal. The reference light intensity can be adjusted easily using the optical polarizer inserted just before the light enters the shutter, which is mounted outside the TFPI housing. This system for the reference light proved to be the most stable and generally very reliable for our work compared to the earlier technique of using fibre optic cable to relay the light; however, some patience and due care is required not to bump any of the optics and electrical cabling (for the AOM) to avoid unnecessary downtime while re-aligning the beam – which is not a simple task!

Data collection

SBS spectra were recorded by a multichannel analyzer, namely, a Nucleus Personal Computer Analyser PCA-II, operating in the multichannnel scaling mode. The action of this mode is to divide the interferometer scan into a preset number (always set at 512) of sequentially opened channels. During the open period all incoming photon counts are added to the total accumulated in the corresponding channel. This is repeated until a spectrum of sufficient quality is obtained. The components and signals required for synchronisation of the data acquisition are the following: a positive TTL pulse is generated by the detector and its photon counting module and is directed to the TFPI control unit (see figure 13) and also to the multichannel scaler (MCS) input of the MCA; synchronisation between the interferometer scan and the MCS is maintained by TTL pulses generated by the control unit [3.5].

The acquisition software is Microsoft DOS based, very basic and robust. The software is run on a simple PC synchronously; hence usually no other programs must be running when the accumulation is taking place. The software has simple fitting and smoothing capabilities seldom used as most often the spectra were converted from binary to ASCII format then transferred via diskettes to be analysed using commercially written software such as OriginLab and SigmaPlot.

Calibration of the FSR

In order to calculate the frequency shift of the Brillouin signal with respect to that of the unshifted, elastically scattered light, and hence the frequency of the acoustic waves themselves, it is necessary to determine the relevant frequency - per - channel calibration factor. The procedure used amounts to extracting from the spectra the difference, in channels, between the positions of the two ghosts and comparing this to the FSR, in units of GHz. A program written in FORTRAN by Stoddart et al. [1.12], to automatically extract the calibration factor by fitting the ghosts with the applicable product of transmission functions was used to produce the velocity of the acoustic wave. However, during the later stages after a change of the electronic board inside the TFPI, the peak-fitting procedure had to be adjusted for one to continue using the program.

3.1.3 Auxiliary optics

The optical arrangement used for directing light onto the sample and the scattered light into the TFPI is shown schematically in figure 14 and shown encircled in figure 13 (see page 52). The beam-steering mirrors, M2 and M3, also known as ‘gymbal mirrors’, because of their special type of mounting that allows the mirrors to move about z- and *x*-axis without changing the optical path-length and hence do not change the focus on the entrance pinhole. These two mirrors are critical for steering-in the inelastically scattered light through the entrance pinhole for which we use a white plain card placed in the position marked C so the light images on it. By assessing the image which is manipulated using focal length adjustments, beam-steering mirrors and the surface condition of the sample, one determines whether the signal is well focused or not. The clearer and more distinctly-featured the image is, having small bright spots against a dark background

which are well -resolved, i.e. a granular rather than a hazy or smeared out image, the greater the likelihood of obtaining a good spectrum. This process is done in 'Tandem' mode; thereafter one switches over to 'Align' mode in order to optimise the transmission(s) through the FPs.

3.1.4 Alignment of the TFPI

The pre-alignment method is based on the fact that when a Fabry-Pérot interferometer is transmitting, the reflected intensity tends to zero, a minimum value being obtained when the interferometer is optimally aligned and one observes on the CRO the so - called 'dips'. On scanning the interferometer the detector signal will, therefore, show a background intensity punctuated by minima whenever either FP1 or FP2 transmits. This is illustrated for a poorly aligned interferometer in Figure 18b. Two clearly distinct series of dips are seen. On independently optimising the alignment (i.e. angular position) of FP1 and FP2 using the alignment transducers, the minima approach zero, as seen in figure 18c. An adjustment of the relative spacing L_1-L_2 using the appropriate control knob of the TFPI control unit labelled E in figure 13 will now bring a pair of peaks into coincidence and the pre-alignment of the tandem interferometer is complete. On switching the optical system back to the multi-pass measurement configuration, transmission will be observed with only minor adjustments necessary to optimise the transmission. Finally the system is locked in-position by engaging 'stabilisers', which is an automatic alignment system that continually monitors the intensity of the strong elastic light now supplied by reference signal through the shutter system and making suitable corrections to the mirror alignments via the alignment transducers. The resulting transmission *maximum* is then moved to the centre of the scan by adjusting the Z – control of the control unit E and the system is then switched to 'tandem' mode and ready to acquire spectra.

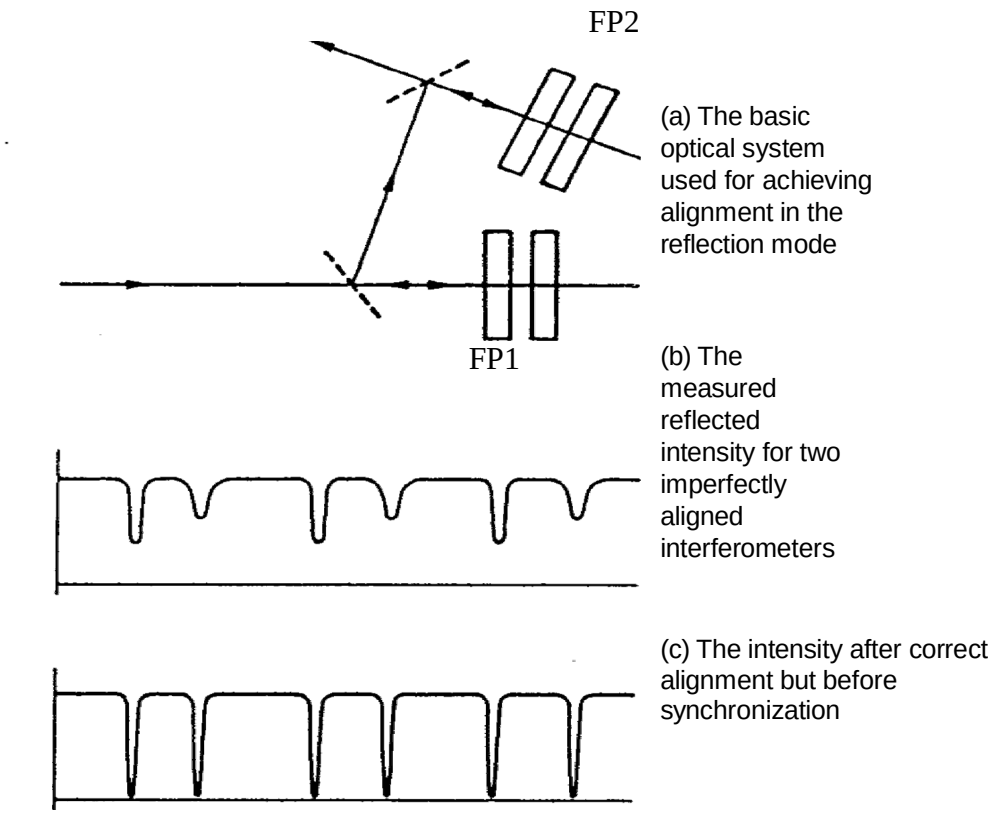

Figure 18: Diagrammatic representation of the pre-alignment process for the TFPI system. (diagram courtesy of JRS Instruments [3.5])

As shown in figure 18a light is passed through a beam-splitter onto the first interferometer FP1. The reflected light passes via a second beam-splitter onto FP2 whence the doubly reflected beam is directed to the photo-detector. In figure 14, mirror M1 is an elliptical dielectric mirror with a 2mm central hole through which the incident light is made to pass enroute to the sample surface. The scattered light is collimated by the lens (**L**1) and reflected by the mirror M1 towards lens **L**2, which focuses it via the steering mirrors onto the pinhole PH. The elliptical mirror is an improvement on the small steering mirror which was originally used in earlier work [3.6] to direct light onto the sample, since it removes asymmetries in the peaks.

For high temperature work, the positioning of the focusing lens **L**1 (120mm focal length) is critical to the successful collection of inelastically scattered light from inside the furnace since the sample is now mounted inside a cavity (the furnace chamber) and there are spurious reflections inside the chamber that add to the difficulty in both aligning the system as well as reducing signal-to-noise.

3.2 Calibration and error analysis in SBS

Determining acoustic wave velocity from surface Brillouin spectroscopy depends on measuring frequency shifts in the phonon peaks in the spectrum. To accomplish this, it is necessary to calibrate the scale of the MCA on a sample of known acoustic characteristics e.g. undoped crystalline silicon wafers or high-purity fused silica. The calibration can be performed by using the *first* ghost of the interferometer and knowing the separation distance of one of the two mirrors. From the position of the corresponding ghost peak, it is possible to determine the FSR and calibrate the MCA scale. Some difficulties occur when the intensity of the ghost is either too low or too high. In the first case, the shape of the ghost 'peak' is rather distorted, so that fluctuations in the counts can misdirect positioning the peak. If the intensity of the ghost is higher than the dynamic range of the detection system, this can produce a flat and featureless ghost peak. In this case, it is impossible to determine ghost peak position. An alternative procedure uses the Stokes and anti-Stokes longitudinal bulk modes of a sample of known optical and acoustic properties as markers in the spectrum. For example, high-purity fused silica has a longitudinal velocity v_l = 5970 m/s and optical refractive index n = 1.458, where the n is measured independently with a precision of one part in a thousand. Thus by taking several spectra in backscattering, changing the separation distance of the mirrors and scan amplitude, and measuring each time the position of the Stokes and anti-Stokes longitudinal bulk phonon peaks, it is possible to calibrate the interferometer. Using the relationship below for calculating the frequency shift of a phonon peak from positions in the MCA of the anti-Stokes and Stokes lines defined by N_{as} and N_s is

$$\Delta\nu = \frac{(N_{as} - N_s)\gamma\, xN_{cal}}{2DN_{ch}}[\text{GHz}] \tag{3.6}$$

where γ is the calibration constants expressed in (GHz mm), x is the reading of the scan amplitude, N_{cal} is the number of MCA channels used in calibration and N_{ch} is the number of channels used in the acquisition, while D is mirror-separation distance of the interferometer.

Using the ghosts to calibrate the instrument one obtains an error in determining the undoped *c*-Si longitudinal velocity of the same order as the indeterminacy in the

refractive index and generally the two approaches have yielded the same precision. While it can be argued that readings for x and D are themselves subject to errors of measurement, the position of the scan amplitude potentiometer can be kept fixed for all of the measurements, while mirror spacing necessarily has to be changed. In our instrument, the reading of D is made by watching a precision clock gauge (0.01mm) or $\pm 10\mu m$ error estimate can occur due to positioning the mirror seperation. Since a typical mirror separation for observing surface acoustic phonons is on the order of 5-10mm, an error on the order of 0.1% can take place in setting the FSR. If the peak position is measured directly without applying fitting, a source of error in determining frequency shifts is given by the discreteness of the frequency axis in the MCA. For example, with N_{ch} = 512, D = 10mm, an error of one MCA channel in the position of the peak corresponds to approximately 60 MHz. For a SAW, velocity v_{saw} = 3000m/s and an angle of incidence θ_i = 60^o, the relative error in the velocity is $\Delta\nu_{saw}/\nu_{saw} \approx 0.4\%$. When measuring frequency shifts, it is critical to position correctly the centre ($\Delta\nu$ = 0) in the MCA scale. To eliminate this error caused by jitter in the elastic peak position, it is always necessary to consider the arithmetical average of the Stokes and anti-Stokes frequency shifts.

The second aspect that must be considered when determining the SAW velocity is the angle of incidence measurement, since this parameter enters directly into the estimation of the transferred parallel wave-vector. Although a rotation stage with very good precision can be used (a goniometer is used for these measurements) an error can still be introduced when fixing the parallelism between the incident laser beam and the normal to the surface (θ_i = 0). This is usually done by visually checking that the laser beam reflected from the sample is returned parallel to the incident beam. It is difficult to assess the precision in setting θ_i = 0, but we calculate that it may be of the order of $\pm 0.1^o$. For a typical measurement at θ_i = 60, this uncertainty in the angle of incidence yields a relative error in the velocity on the order of

$$\frac{[\sin(60.1^o) - \sin(60^o)]}{\sin(60^o)} \approx 1\times10^{-3} \qquad (3.7)$$

A worst case consideration for the relative error in estimating SAW velocity may therefore be of the order of 0.5 %.

A final note to consider concerns precision in measuring surface phonon velocity for anisotropic materials such as single crystals [3.7]. In single crystals, the acoustic wave velocity is usually anisotropic, and it is necessary to align the crystallographic axes of the sample with respect to the propagation direction. Given the long accumulation time that is necessary in Brillouin scattering spectroscopy, it is not easy (but feasible) to check crystal alignment using the acoustic wave velocity itself in conjunction with the use of Green's function dispersion calculations for the specified surface orientation; however, sometimes sample alignment is made visually using the cleavage plane of the specimen as an indicator resulting in an error estimate for the latter technique of $\pm 1^o$.

3.2.1 Geometrical aperture effects on measurement accuracy

Accuracy in determining SAW velocity and attenuation using SBS is influenced by the finite aperture of the collection lens. Given the low intensity of signals, it is often necessary to use a large aperture collection lens to allow enough scattered radiation to be analysed. This broadens the phonon line shape and introduces a systematic shift in the position of the peak. The cause of the broadening is best understood in this way: it arises because scattered light is not collected at a single scattering angle θ but over a range of angles $\theta \pm \Delta\theta$. Thus a range of surface phonons are probed with a consequent distribution of frequencies. In backscattering if $\Delta\theta \ll \theta_i$, the spread in parallel transferred momentum q induced by the finite collection aperture is $\Delta q = 2k_o \cos\theta_i \sin\Delta\theta$. Broadening is minimized by reducing the collection lens aperture and increasing the angle of incidence. For a collection lens diameter D = 24mm and focal length F = 50 mm, the subtended semi-angle is $\Delta\theta \sim 13.5^o$. Taking a typical Rayleigh velocity v_R = 3000m/s and an incidence angle $\theta_i = 60^o$, the width of the spectral line shape induced by the geometrical aperture is $\Delta\omega = \Delta q_{v_R} \approx 1.2$ GHz. The geometrical aperture broadening can be orders of magnitude higher than the FWHM associated with the surface phonon lifetime.

According to Mutti et al. [3.7], there are two primary reasons for the systematic shift in the position of the surface phonon peak introduced by the finite collection aperture. Firstly, when a finite collection aperture is used in backscattering, instead of the

transferred parallel momentum $\boldsymbol{q} = 2k_o \sin\theta_i$, its mean value on the distribution of θ, $\langle q \rangle = 2k_o \langle \sin\theta_i \rangle$ should be considered as being more realistic. The factor $\langle \sin\theta_i \rangle$ is given by the relation

$$\langle \sin\theta_i \rangle = \frac{\int_{\theta_i-\Delta\theta}^{\theta_i+\Delta\theta} \sin\theta \, d\theta}{\int_{\theta_i-\Delta\theta}^{\theta_i+\Delta\theta} d\theta} = \sin\theta_i \frac{\sin\Delta\theta}{\Delta\theta} \qquad (3.8)$$

The mean value of the transferred parallel momentum is therefore smaller than the ideal backscattered value, and for a semi-angle $\Delta\theta \sim 13.5^o$ and $\theta_i = 60^o$ we have that $\langle q \rangle / q \approx 99\%$.

The second aspect to be considered as well is the *angular dependence* of the Brillouin scattering cross section. This can be done more easily if only the *p-p* ripple contribution is considered. For surface sagittal modes in opaque materials, this is the dominant term in the cross section. As shown in figure 19 variation with the incidence angle of the *p-p* reflection coefficient is quite uneven and drops sharply to zero beyond 70^o. For backscattering at $\theta_i = 70^o$, the reflection coefficient (scattering cross-section) weighs more heavily to contributions centred at smaller angles, with a consequent shift in the position of the peak in the spectrum. This reasoning was used by Loudon and Sandercock [3.8] to explain the discrepancy between the velocities determined using SBS and those obtained from ultrasonic measurements. Since the resultant shift is more towards smaller angles using q would result in underestimation of velocities. However, it was again pointed out by Elmiger [3.9] that the same reasoning could be used to show that velocities should be overestimated near incidence angle 45^o, though such an overestimation has not been confirmed in practise. An excellent analysis that was given by Stoddart et al. [3.10] details how the *range of the scattered angle about the fixed angle of incidence* explains the overestimation, and the implication of this is that the cross section is not symmetric in θ_i and θ_s. The red lines in figure 19 show the range of θ_s and θ_i admitted by the collection lens of aperture *f*/2.3 and notice that the slope is negative for all values of θ_i as before.

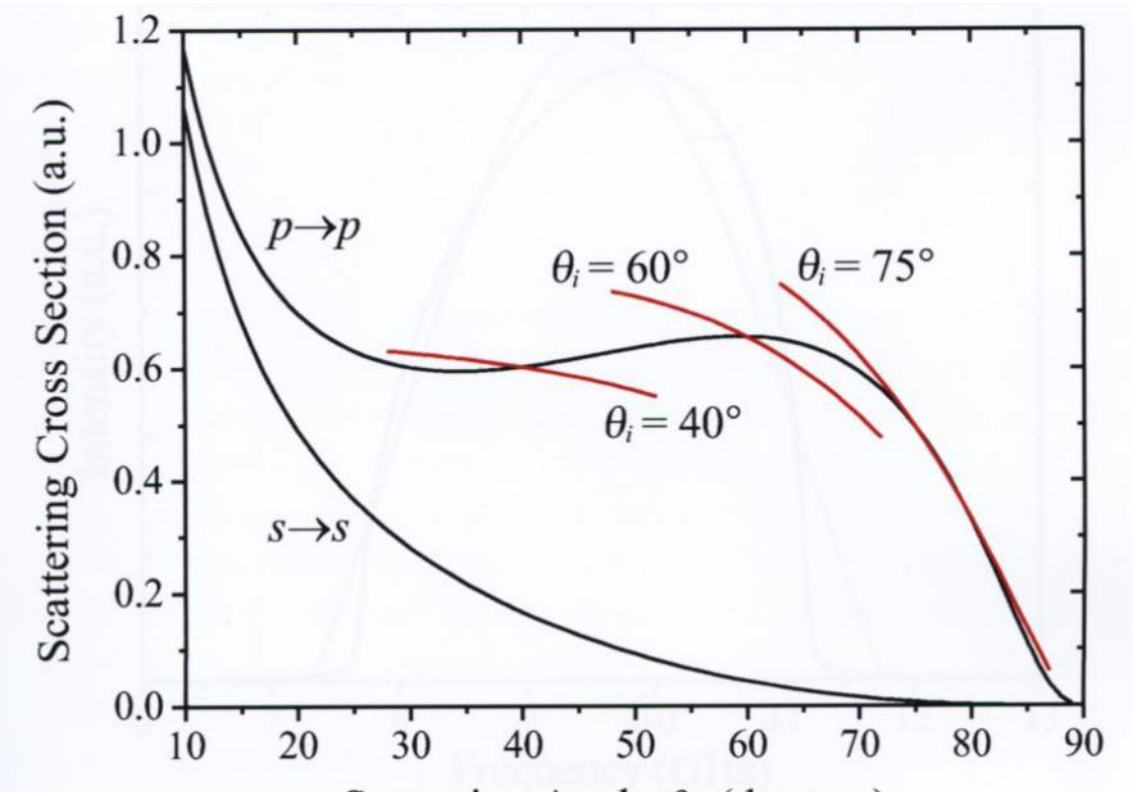

Figure 19: Cross section for backscattering from silicon (001) along [100] direction (black lines). The *p-p* scattering process dominates that of *s-s* in this configuration. The red lines correspond to a range of θ_s about the fixed incidence angle θ_i. [3.10]

Thus in a real experiment, the finite collection aperture allows both in-plane scattering events as well as out -of- plane scattering events to contribute to the total cross-section as shown in the geometry in figure 20. Hence in backscattering, transferred parallel wave vectors become $q = k_o(\sin\theta_i + \sin\theta\cos\phi)$, where ϕ is illustrated in the geometry of the total collection aperture in figure 20 below.

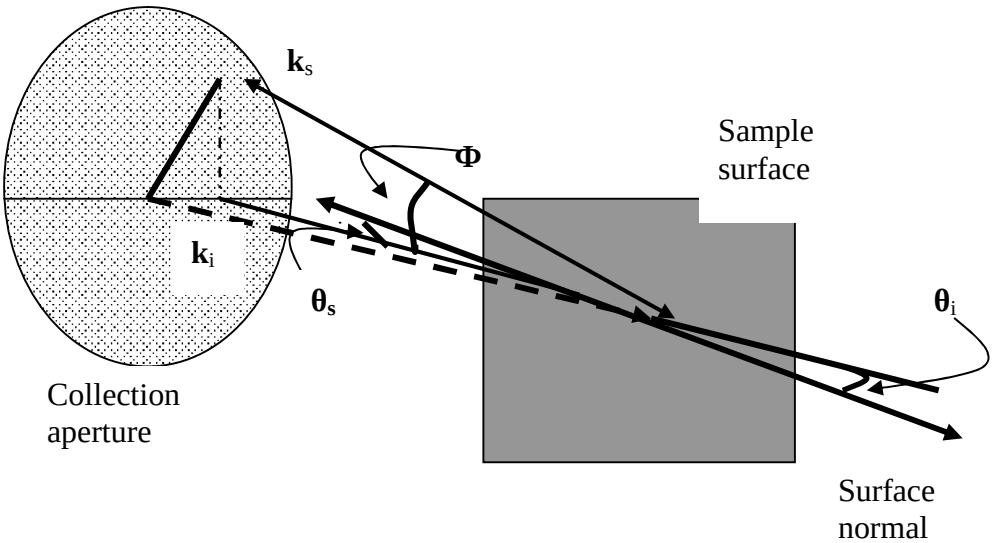

Figure 20: Diagram showing the geometry of the collection aperture in a SBS backscattering experiment [3.11]

The effect of the finite collection aperture on the Brillouin spectrum can be calculated as an integral over the collection solid angle assuming Lorentzian lineshape for the SAW. A detailed computation is provided elsewhere [3.11]. Hence for an accurate measurement of SAW velocity we must take into account the effect of using a finite aperture in the collection. This can be done if the experimental surface phonon line shape is fitted using equation (3.8) as trial function, assuming that the line shape of the SAW is a Lorentzian curve. It has been observed by Mutti et al.[1.27], verified by Stoddart et al. [3.10] in a comprehensive study that the difference between the curves for the calculated fit and the line shape of the intrinsic surface phonon becomes negligible when the line-width has the same order as the geometrical aperture broadening.

Restricting the aperture

Once the origins of the aperture effect has been appreciated, in practice one attempts to solve the problem in the case where high intensity scattering occurs by use of rectangular masks, for example in the work on titanium compounds. It has been shown by Stoddart et al. [3.10] that the contribution of the variation in Φ is less important than that due to the variation in θ_i, thus the simple process of placing a rectangular mask of about 4 mm width over the collection lens with the long axis perpendicular to the x_1-x_3 plane usually serves to reduce the effect to negligible levels, especially for highly scattering materials such as Ti compounds and other rare-earth metals e.g. Rh_3Nb alloys.

3.2.2 Instrumental response linewidth

Analysis of the Brillouin spectra allows the measurement of optical constants assuming that the phonon velocity is known, i.e. one can determine for example, the refractive index from the spectral phonon width information. However, a number of factors contribute to the phonon width broadening and for one to extract information arising from true opacity there is a need separate the various constituents to the overall spectral width. The laser instrumental function can be approximated as a delta function, while the spectrograph response is given by the appropriate transmission function of the interferometer. Following Mutti et.al [1.16], we have approximated the transmission function as a Lorentzian curve having a FWHM equal to the *FSR* divided by the overall finesse. The effect of the instrumental resposne on the measured spectral phonon line-shape introduces further broadening, which may be, according to the selected *FSR*, the dominant term in the lineshape FWHM. For most measurements, we used *FSR* = 30 GHz, which corresponds to a spectral width of the interferometer transmission curve of approximately 300 MHz. An acceptable ‘rule of thumb’ requires that the instrumental response line-width must be less than 10% of the spectral phonon width for it to be acceptable without applying deconvolution methods. Therefore any measured spectral widths or FWHM data less than 300 MHz, for example, are not realistic since they are smaller than the broadening induced by the interferometer response line shape.

3.3 High temperature optical furnace

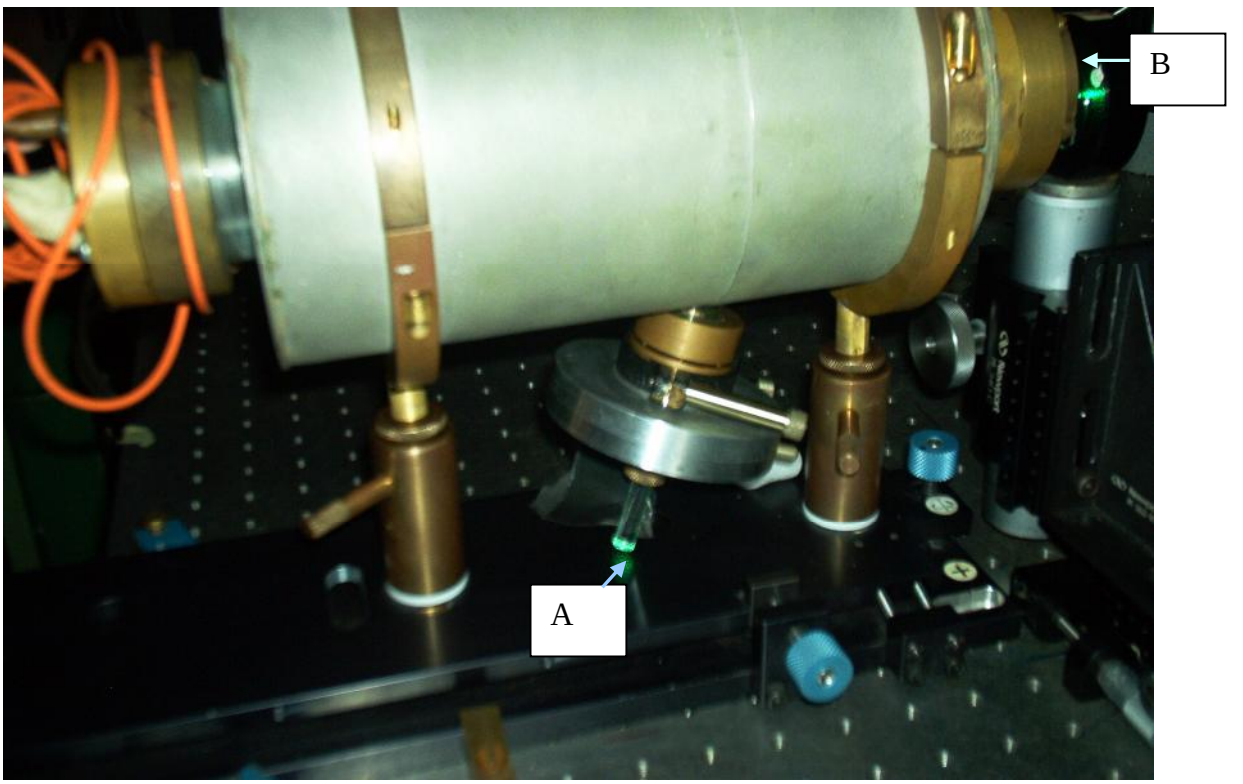

Figure 21: Side view of the high- temperature optical furnace showing the entry point of the laser beam (B) and the quartz rod and the graduated rotation stage assembly (A).

For high temperature measurements the samples were mounted on a quartz rod inside a specially designed furnace (figure 21) at a fixed angle of incidence of 70.9^{o} measured using an angle gauge relative to the furnace body. The quartz rod is held in position within a precision rotation stage fitted with an angular scale in degrees. The insert point of the quartz rod is made vacuum tight using a system of O-rings. The sample holder is selected to be made of quartz in order to minimise heat loss from the sample and variation of the sample position caused by thermal expansion. A recess approximately 4× 4×3 mm^3, matched to the sample dimensions, is drilled using an ultrasonic drill into which the sample is positioned and held steady. The furnace has a hot zone which is provided by a molybdenum wire heating coil and surrounded by two cylindrical tantalum shields to prevent heat loss. The sample temperature is monitored by a Pt-Pt (13% Rh) type K thermocouple placed approximately 3 – 4 mm from the sample.

A Eurotherm 818P/TC temperature controller was used to regulate the heating of the sample maintaining a stable temperature of better than $\pm 1^{o}\mathrm{C}$ during the lengthy spectral accumulations. A cross-section schematic diagram of the furnace is shown in Figure 22 below. The sample recessed into the quartz rod makes a 70.9^{o} angle between the sample surface normal and the incident laser light. The fused quartz front window allows the Brillouin scattering to be performed in a backscattering geometry with laser beam incident through point marked [B] in figure 21.

3.3.1 Alignment of the optical furnace

A 120 mm focal length lens of aperture f/5.3 was used throughout all measurements using the furnace to illuminate the sample and collect the scattered light. In a similar manner to an externally mounted sample, one has to ensure that the incoming beam path is exactly parallel to the elastically scattered beam by visually checking the reflected spots on the elliptical mirror shown in Figure 13. However, this exercise is made considerably more difficult by the spurious or multiple scattering within the furnace as well as from the quartz windows. This therefore means that one has to look for and identify the right spot or reflected beam coming off the sample surface (neglect the other stray beams) and direct it to the collection lens L1 onto the elliptical mirror. The elliptical mirror has a 2mm hole drilled at its centre and so if one makes a perfect alignment, the beam coming off the sample passes neatly through the hole and results in a ‘black’ shadow spot, 4-5 mm diameter, seen at pinhole PH.

Normally the input pinhole diameter is set at 450 microns and the output pinhole to the detector set at 300 microns for optimum signal collection without undue loss of spectral information. Examination of the reflections or bright spots on the elliptical mirror M1 shows a bright diffuse spot some 15 mm above the drilled hole. This spot is important as a guide to the alignment, and originates from reflections off the front surface of the front quartz window. It should not be allowed to be parallel to the incoming beam, i.e. pass through the drilled hole; hence the normal to the front window is deliberately offset from the incident beam path such that reflections off the front window can be observed about 15mm above drilled hole whilst allowing inelasticallly scattered light from the sample to

pass through the hole. If this is not done then the inelastically scattered light is off-alignment, missing the drilled hole irrespective of what one observes on the card positioned inside the TFPI and if this is not observed carefully one will spend countless hours aligning the optical furnace and observing 'ghost' images on the card, and even accumulating a spectrum which yields no Rayleigh peaks at all. If the alignment is good, the clear, sharply defined Rayleigh peaks should appear within about 20 – 30 minutes of accumulation time corresponding to about 1800 counts and this should be repeatable when one rotates the rotation stage through an arbitrary angle. To achieve this correct alignment one uses a system of X- and Z- adjustments mounted on the flat base of the furnace together with fine-tuning of the focusing lens L2. The final stage of alignment is done using the steering mirrors to check that the image formed by the inelastically scattered light from the sample surface is almost perfectly round in shape, 'zooms in and out' remaining perfectly shaped on 'moving in and out' of focus using L2. A special alignment manual was prepared to assist users; however the old adage practice still makes one perfect!

A rotary pump backed by a diffusion pump is used to generate a vacuum of better than 5 x 10^{-5} Torr within the furnace sustained over very long accumulation times by the vacuum tight seals. Normal measurements are carried out after repeated vacuum and argon flushing and then finally bleeding–in ultra pure argon (99.99%) to a pressure of 18 mmHg to facilitate good thermal contact by improving conduction and ensuring that temperature read by thermocouple is essentially the same as the temperature of the sample. Beyond 600^{o}C, the argon is pumped out and vacuum regenerated since the predominant heating conduction mechanism is now radiative. Although the furnace is designed to operate up to 1200^{o}C, sample surface deterioration has usually limited the experiments to maximum of 700^{o}C and this has been identified as being due to the surface quality deterioration due to material evaporating from the molybdenum heating coil as well as oxidation effects.

A new ultra high vacuum furnace with better capabilities such as variable incidence angle, angular dispersion capabilities and numerous fail-safe features, whose vacuum is

to be generated by a turbo-molecular pump has been designed and is currently under construction and testing. This new furnace is designed to reach temperatures as high as 1800 ^{o}C and ultra high vacuum so that SBS experiments can be conducted at very high temperatures and still retain good surface quality of the samples. The artist's impression of this furnace is shown below in Figure 23.

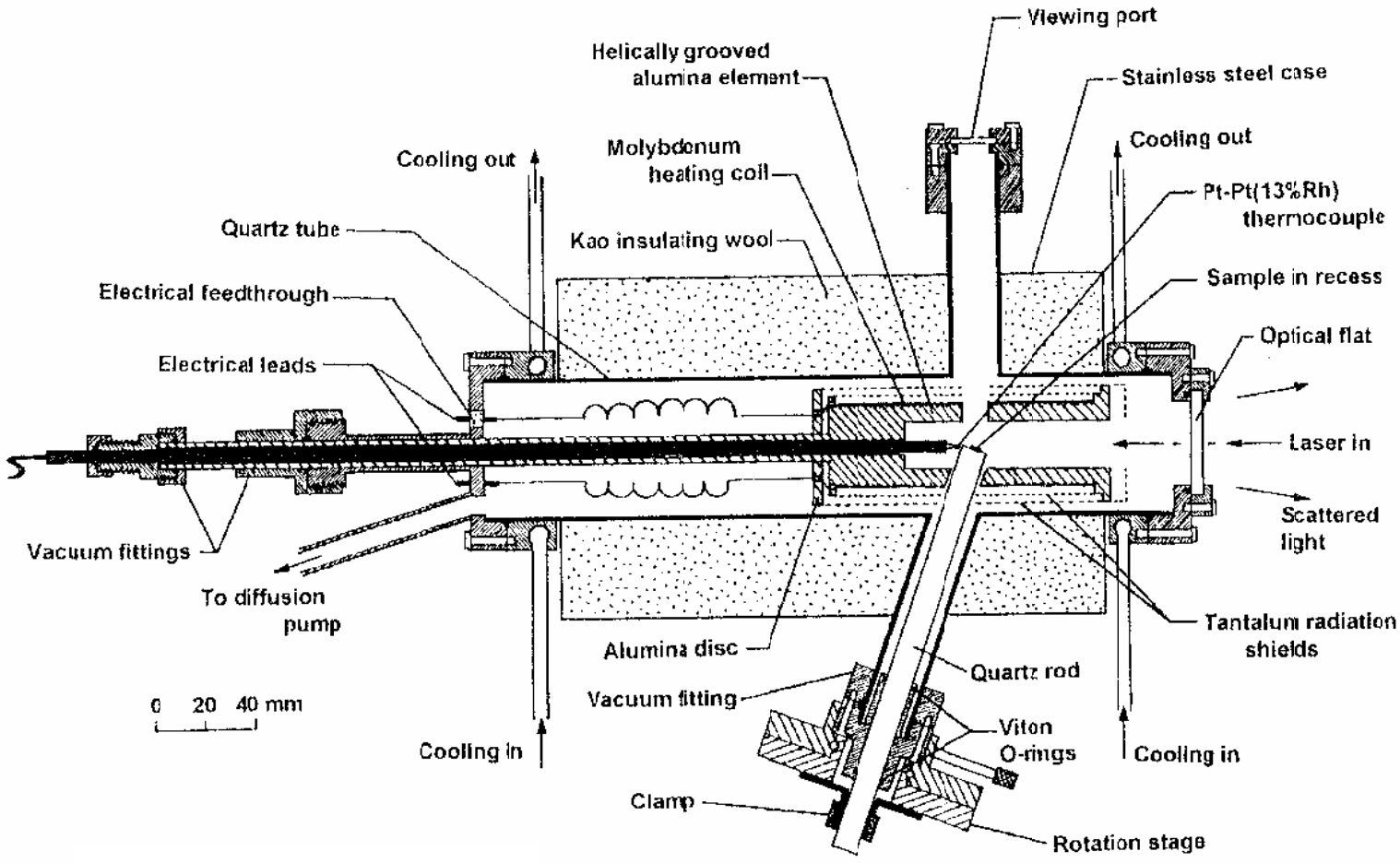

Figure 22: Schematic of the high temperature optical furnace currently used in high temperature SBS measurements showing the fixed incidence angle signalled by the quarts rod.

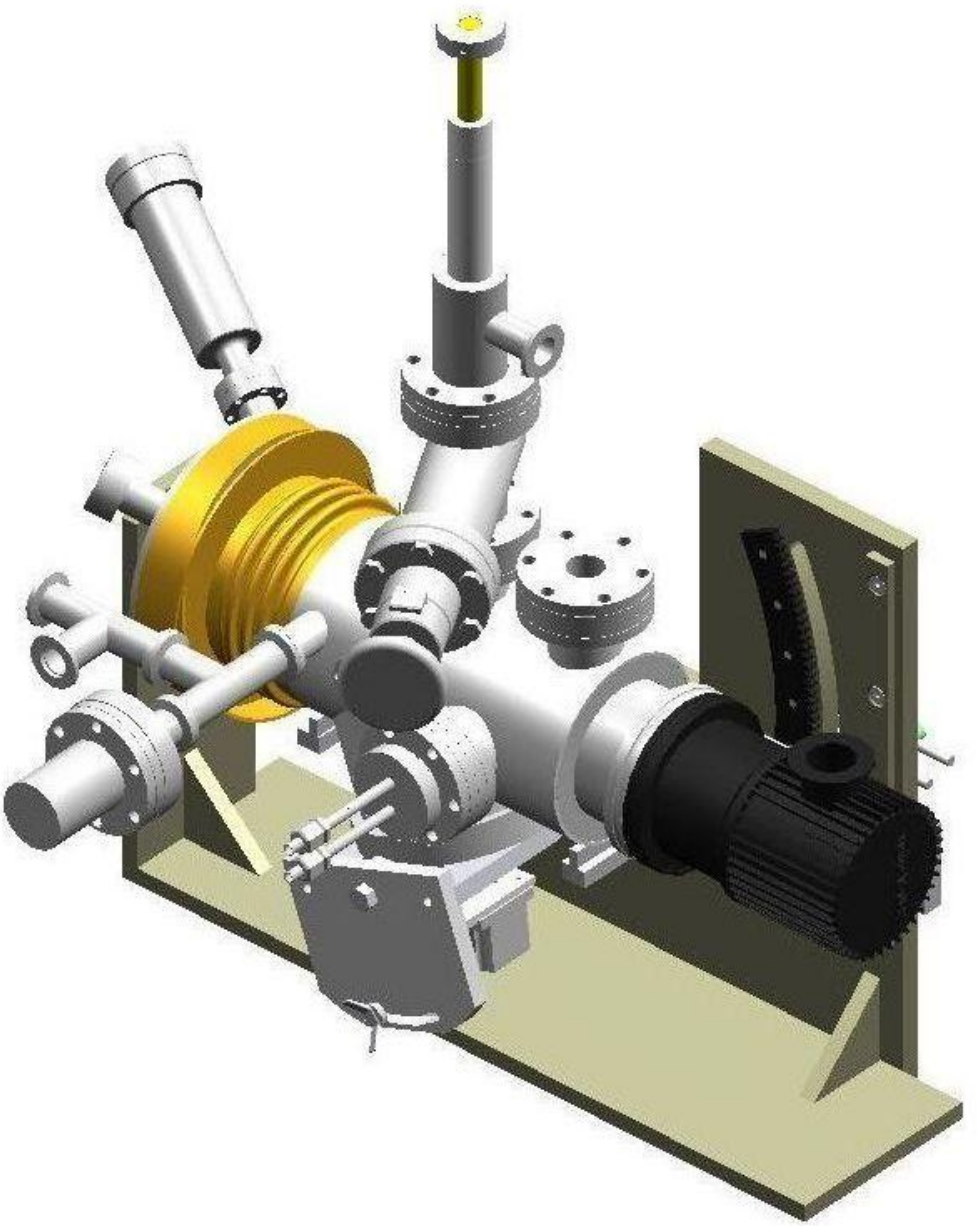

Figure 23: Artist's impression of the design of the new optical furnace designed to attain temperatures up to 1800^{o}C and equipped with functions for variable incidence angle measurements as well as SBS dispersion measurements at high temperature[6].

[6] Product is copyright of Witwatersrand University, School of Physics

3.4 Raman Spectroscopy

Principles

When monochromatic light impinges on a sample, some of the light is transmitted, some absorbed and some of it is scattered by the material. Most of the scattered light has the same frequency as the incident light and is termed Rayleigh scattered light. However, some of the photons will be scattered with different energies from the incident photons, and this inelastic scattering is called Raman scattering. Raman scattering occurs with a change in vibrational, rotational or electronic energy of the sample. The Raman spectrum of a sample shows discrete frequencies both higher and lower than the exciting radiation frequency. These frequencies are called Raman bands and those bands lower in frequency than the exciting radiation are called Stokes lines while those with higher frequencies are called anti-Stokes lines. The frequency shift of the scattered photons is characteristic of the sample, an aspect that makes Raman spectroscopy a powerful, non-destructive technique for characterising materials. In the following sections, basic introductory details of Raman effect will be given, followed by a description of the Raman spectrometer.

Scattering Process: Classical Approach and Quantum Mechanical

Below is given a brief description of the two approaches, a more detailed discussion is given in reference [3.12]. Raman scattering can be described in two ways; classical approach or the quantum mechanical approach. In the classical approach, an assumption is made that the Raman effect arises from the interaction of the incident light photon and the electric dipole of the molecule. The electric field of the incident light causes a perturbation of the molecule's dipole moment. The scattered light is therefore generated by the oscillating electric dipoles induced by the electric field of the incident radiation.

On the other hand, the quantum mechanical approach considers Raman scattering as a two-photon process. This process involves two almost simultaneous transitions via a virtual state. A photon of incident radiation is absorbed, raising the system to an excited state, e.g. a molecule is illuminated by incident radiation and the interaction of the

radiation or photons with the molecule raises the potential energy of the molecule to a virtual state above the ground state. This state has a very short lifetime (~ 10^{-14}s), following which the system makes a downward transition with the creation of a phonon of a given energy and scattering a photon in the process. According to this approach, Rayleigh scattering occurs when the energy of the scattered and incident photons is the same. If the energy of the scattered photon is less than the energy of the incident photon, this process is then known as Stokes Raman scattering. If the system was initially in an excited state, the scattered photon can make a transition from the virtual state to a lower energy state than the initial one, and its energy will therefore be higher than that of the incident photon. This process is called anti-Stokes Raman scattering. Energy and momentum are conserved in the Raman scattering process.

3.4.1 The Raman Spectrometer

Figure 24 shows a schematic diagram of the Jobin-Yvon T64000 Raman spectrometer used in the investigations detailed in the thesis. This is a triple-spectrograph system and contains integrated software and hardware package, which provides the control of the whole system. The spectrometer is equipped with three monochromators, a detector and two sample chambers. Laser radiation can be reflected either to the micro-chamber (microscope) or to the macro-chamber. Laser light is directed into the spectrometer by optical mirrors; the light can be focussed on the sample using an Olympus BX40 microscope attached to the spectrograph. A narrow band-pass filter removes the laser plasma lines and allows only the selected wavelength into the spectrometer.

Scattered light from the sample returns through the microscope into the spectrometer where it is processed in any one of three possible configurations of the spectrograph. In the single spectrograph mode, the light is directed to a holographic notch filter which strongly suppresses the elastically scattered light but allows the Raman scattered light to pass through. The transmitted light then passes through an entrance slit and falls on a grating where it is dispersed. Two types of grating are available with the spectrometer and can be used interchangeably using the software. The choice of the grating is determined by the resolution and spectral range required. The 600grooves/mm grating

offers a wide spectral range in the region 300 to 1800 cm^{-1} but limited to a resolution not better than 1.3 cm^{-1}, whereas the 1800grooves/mm grating has a narrow spectral range (1100 to 1760 cm^{-1}) but improved resolution of about 0.5 cm^{-1}.

Light dispersed by the grating falls on the charge coupled device (CCD) detector which detects the scattered light and produces a spectrum. The CCD detector is a rectangular chip comprising of 1024 X 256 pixels, each pixel being a silicon photosensor. When the scattered radiation falls on a pixel, photoelectrons are produced in numbers proportional to the intensity of the radiation. For optimum performance, the CCD is cooled to 140 K by liquid nitrogen. The advantage of the single spectrograph mode is that it has a higher throughput and offers rapid analysis time. Its disadvantage, however, is that it cannot be used for Raman bands close to the frequency of the laser line.

In triple *subtractive* mode, the two pre-monochromators work as filters by dispersing the scattered light and recombining part of it, before it is re-dispersed by the spectrograph. The advantage of this mode is that it is more efficient in removing the stray light resulting from the laser exciting line and thereby allowing for analysis at low wavenumbers. However, throughput is considerably weaker than that obtained in the single spectrograph mode.

In the triple *additive* mode, all three monochromators act as dispersers, and this results in a narrow range of wavelengths being spread across the detector, and therefore offering very high resolution of a small spectral range. This mode has its major disadvantage in that it is not possible to perform analysis close to the laser line. The output from the detector is analysed on a computer using Labspec Scientific software supplied by Jobin-Yvon. The spectra can be saved in the form of data or text files which can be exported to a spreadsheet for analysis.

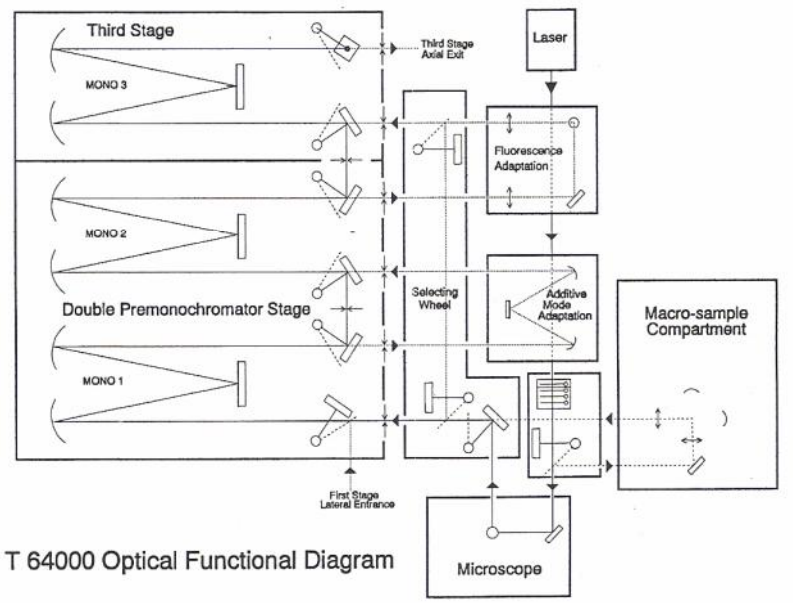

Figure 24: Schematic diagram of the T64000 Raman spectrograph showing the beam path (from the Instruction manual for the Jobin-Yvon T64000 Raman spectrograph).

3.4.2 X-Ray Powder Diffraction

An x-ray diffractometer is primarily used for the identification of phases in a powder. An x-ray beam of known wavelength is focused on a powdered sample and x-ray diffraction peaks are measured using a germanium detector or scintillation counter; the *d*-spacing of the observed diffraction peaks is calculated using Bragg's Law ($n\lambda = 2d\sin\theta$) and indexing i.e. *hkl* assignment done using applicable selection rules. The Philips 1820 powder diffractometer uses a Cu x-ray tube with two beam slits, a set of beam and detector slits that balance the needs of resolution and intensity for typical runs. The goniometer is automated, and is scanned in normal mode i.e. θ and 2θ are scanned in synchronism. The pulse height analyser which processes the detected x-ray pulses from the detector was set for narrow discrimination of Cu K_α pulses. All other energy ranges are rejected, and in this way any x-ray fluorescence emanating from the sample is rejected via pulse-height analysis. In chapters 4 and 5 specific details of the x-ray studies are given.

Preamble: Materials investigations

In this work, a number of different materials have been investigated for their elastic properties at ambient and at high temperature in certain instances; these include the semiconductor iron pyrite, titanium alloys, a boron carbide film, and a MEMS structural material, boron-doped polysilicon film. Various approaches are used to extract the elastic constants of the different materials and some interesting discoveries (acoustically) will be reported and discussed in terms of their value in enabling successful characterisation of these technologically important materials. Surface elastodynamic Green's functions are shown to be a vital component in elucidating information about phonons from various configurations and systems encountered in the following chapters, as well as in the extraction of the elastic constants. Each project reported is the result of collaborations with various groups involved in materials research.

Chapter 4

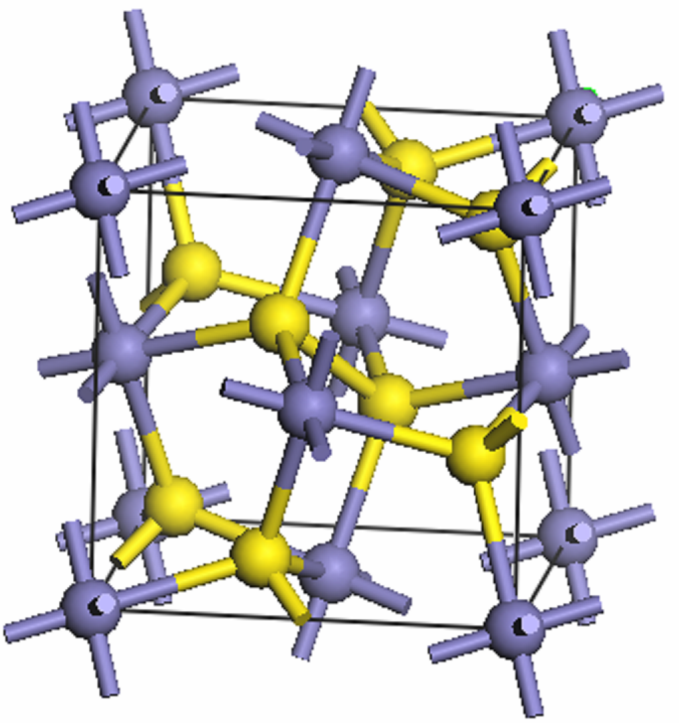

4 Iron (IV) Sulphide

4.1 SBS investigation of high temperature elasticity of iron (IV) sulphide

Introduction

The 3d transition metal chalcogenides MX_2 containing the dianion groups X_2^{2-} include compounds of major mineralogical importance and are interesting physically because of their wide range of electrical and magnetic properties. Amongst the four major MX_2 structural types is the iron pyrite (FeS_2), whose chemical bonding, surface reactivity and relation to band spectra as well as nature and strength of interatomic binding forces have been and still remain subjects of wide interest [4.1].

The elastic properties of this semiconductor material can provide valuable insights into the nature and strength of interatomic binding forces in the crystal. From static bending and twisting of oriented plates of iron pyrite, Voigt [4.2] determined a set of elastic stiffness constants which showed a curious feature that C_{12} was negative and therefore compliance S_{12} was positive, which would imply a *negative Poisson ratio*. This observation interest from several researchers using various techniques [4.3] to validate this observation. In general, ultrasonic methods which have a relatively higher accuracy and are less sensitive to microcracks than static methods, gave a positive value for C_{12} consistently, which implied a normal positive Poisson ratio. Benbattouche et al., [4.3] recently conducted ultrasonic pulse echo measurements on hydrostatic pressure derivatives of elastic stiffness and their result was also a *positive* value for $C_{12,}$ further fuelling interest in view of Voigt's earlier results, where it was suggested by Love [4.4] that the negative Poisson value might possibly be the effect of a twinned crystal. A summary of the reported values can be found in table III of reference [4.5]; the signs and magnitudes obtained for C_{12} show wide discrepancies, stemming in part from its small value and from the fact that it can only be measured in combination with other stiffnesses and so is particularly subject to experimental error. Thus, despite the trend of seemingly positive values of C_{12} from ultrasonic measurements, this has not negated the interest in establishing conclusively the elastic constants of the material using a different technique.

The experimental results obtained in this work are compared to computational modelling data projected to the same temperature range and very good agreement is obtained.

Iron pyrite has a cubic structure and belongs to the T_h^6 (Pa3) space group. In an ideal pyrite structure the arrangements of the sulphur atoms are treated as S_2 dimers (or dianions) in which the centre of mass of each dimer coincides with an equivalent position of Cl atoms in the NaCl structure. In the pyrite structure the distorted octahedral crystal symmetry splits the cation d band into two sections: the bonding t_{2g}, containing six electrons, and the higher energy, antibonding e_g which can hold four electrons. The Fermi energy is close to the d band and its relationship across the series of transition metal chalcogenides MX_2 to antibonding and bonding states as the number of 3d electrons changes leads to the wide range of properties observed for these compounds. Comparison between the elastic stiffness tensor components of MnS_2 and FeS_2 at room temperature shows that elastically FeS_2 is much the stiffer crystal. C_{11} is more than three times larger for FeS_2 than for MnS_2. The bulk moduli of these two isostructural compounds are in the ratio 2.4:1. [4.1]. These structural properties of iron pyrites were interpreted by Pauling [4.6] in terms of covalent bonding and the large values of C_{11} and bulk modulus are consistent with strong, essentially covalent bonding.

Motivation

A major motivation for the present study of the FeS_2 at high temperatures is the work of Sithole et al. [4.7] who have computationally simulated the values of the elastic constants using newly developed interatomic potentials as well as their temperature dependence. To our knowledge this is also the first time that the high temperature dependence of the FeS_2 elastic constants is reported using SBS technique and thus provide an opportunity to compare the experimental results with the theoretical predictions. Thus, in this work efforts have been made to find out if these simulations at high temperature are correct, covering a sufficiently wider temperature range to make a good comparison than previously done by Benbattouche et al. [4.3]; and also confirm the reliability of the models. Additionally, Benbattouche et al. [4.3] measured the dependencies of the elastic stiffness moduli and Poisson ratio of natural pyrite and although they confirmed the

positive value of the Poisson ratio, the question was left unanswered as to whether the same assertion can be made for temperatures above room temperature. In our study we seek to affirm that the value of C_{12} and the sign of the Poisson ratio for temperatures significantly above room temperature remains positive.

4.2 Sample preparation and characterisation

A block of natural single crystal FeS_2 was purchased from African Gems and Minerals in Johannesburg, South Africa. Samples of different crystallographic orientations were then cut to about 4x4x3 mm^3 in dimension using a slow-speed diamond wire-saw. Laue x-ray diffraction was utilized for orienting (001) and (110) planes on two separate prepared samples. The samples were then mechanically polished down to 0.1µm with diamond paste and cleaned ultrasonically with high purity acetone. The composition of the main constituents of the sample was found using a Mark V Cambridge electron microprobe to be 46.39 at% Fe and 53.57 at% S. These values are in good agreement with values of stoicheometric pyrite [4.3]. In addition, the following trace elements Al, Ti, Ca and silicate were found to be present as inclusions on the sample surface, sparsely distributed. Raman spectra obtained at room temperature confirmed the iron pyrite structure and the characteristic peaks at 377 cm^{-1} and 341 cm^{-1} had narrow linewidths indicating monocrystallinity [4.11] of the natural sample (figure 25) in further agreement with Laue x-ray results. A high temperature Raman investigation under constant argon flow confirmed the initialisation of the thermal decomposition of pyrite to pyrrhotite (Fe_xS) with the subsequent release of elemental sulphur at temperatures around 550 – 600 ^oC [4.9]. The Raman peaks recorded after heating to temperatures of 700^oC, and cooling down in air show strong peaks of typical haematite [4.8] at 292 cm^{-1} and 409 cm^{-1} which are significantly broadened (figure 26), and the final product is soft and black in colour, indicative of the formation of one of the decomposition products in the presence of air, an iron oxide known as haematite [4.12] (see figure 26).

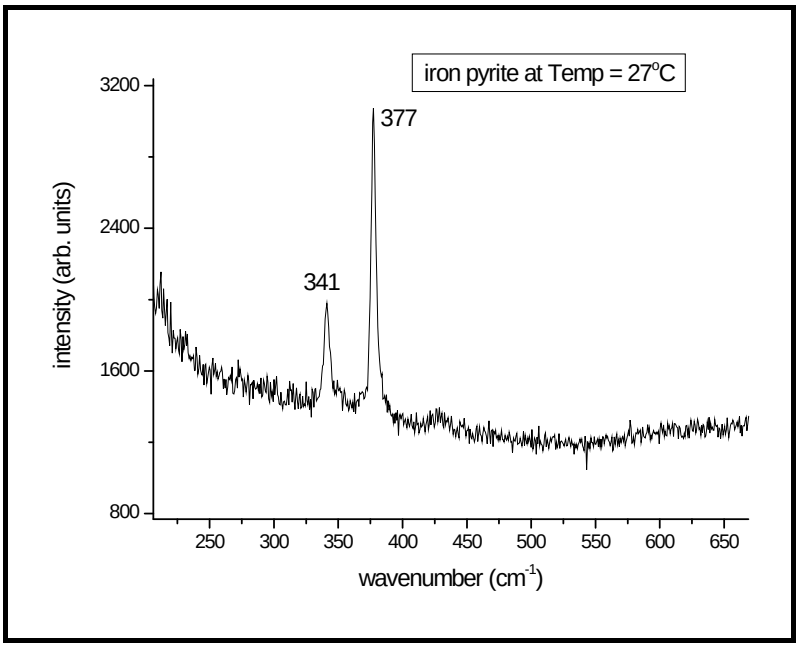

Figure 25: Raman spectrum of natural single-crystal iron pyrite recorded at room temperature

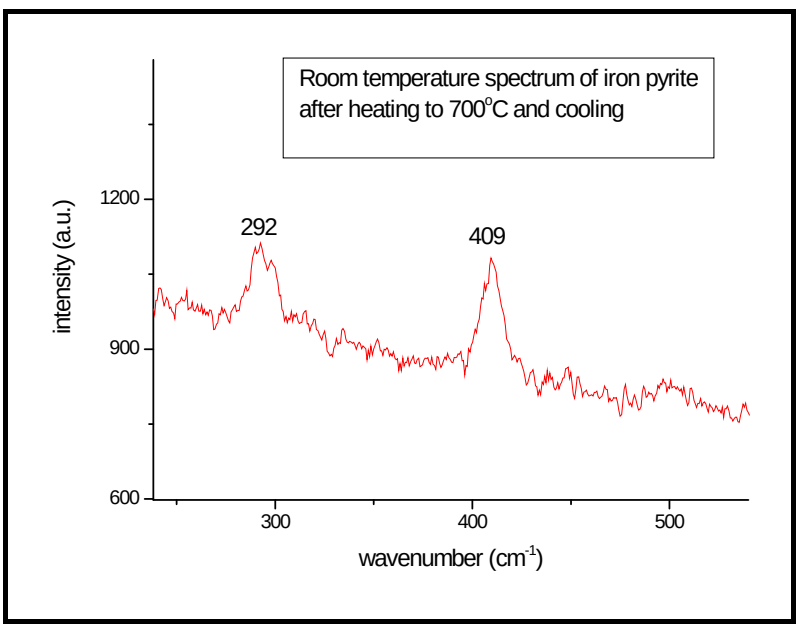

Figure 26: Room temperature Raman spectrum recorded after cooling down from 700°C showing strong presence of haematite (Fe_2O_3) signifying oxidation effects.

4.3 High temperature density measurements

4.3.1 XRD Measurements to determine the room temperature lattice constant

The x-ray spectrum in figure 27 was performed using a Philips PW1830 diffractometer (Cu Kα radiation at 40kV and 20 mA) using a slow scan (gear ratio 0.125).

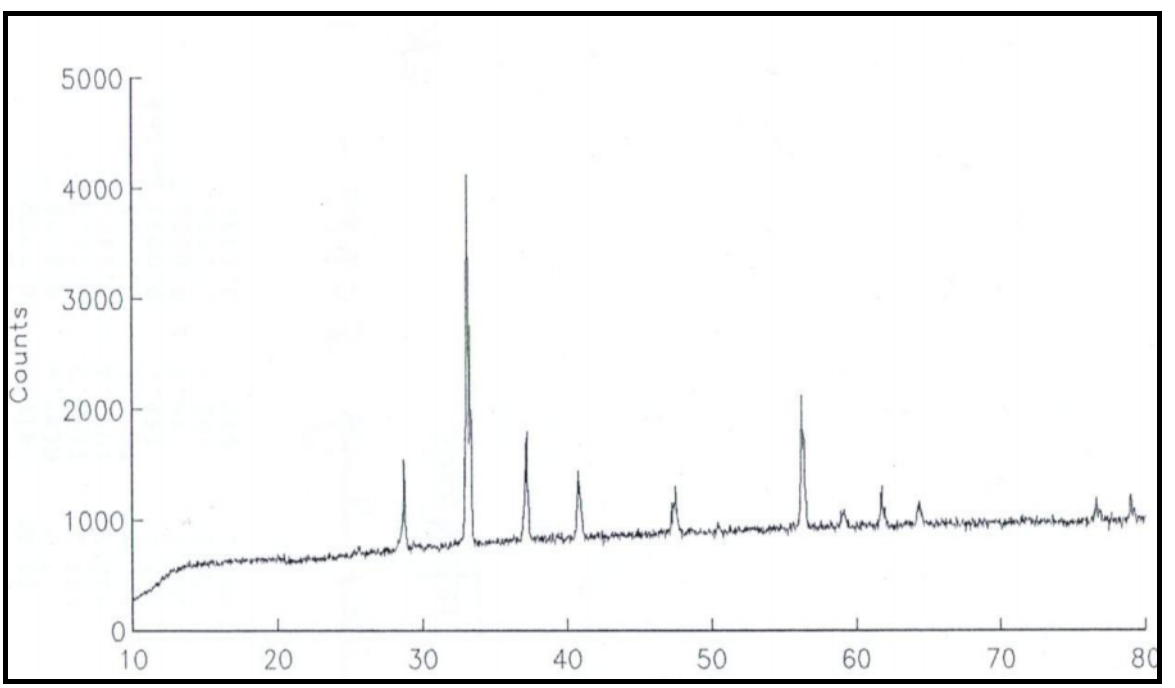

Figure 27: X-ray diffractogram for natural FeS_2 powder obtained using Cu radiation at room temperature.

The solid specimen was ground into a fine powder and mounted on a glass slide for the XRD run. Analysis of the spectrum gives a lattice parameter value of 5.414 Å in agreement with literature values for both synthetic pyrite (ranging from 5.416 – 5.419 Å) and eleven pyrite specimens measured by Lindroth [4.13] that gave an average value of 5.417 Å. The XRD patterns were identical to that of a pyrite standard (JCPDS pattern 42-1340), for which the x-ray density was obtained as 5.106 g/cm^3.

4.3.2 Measurement of thermal linear expansion coefficient

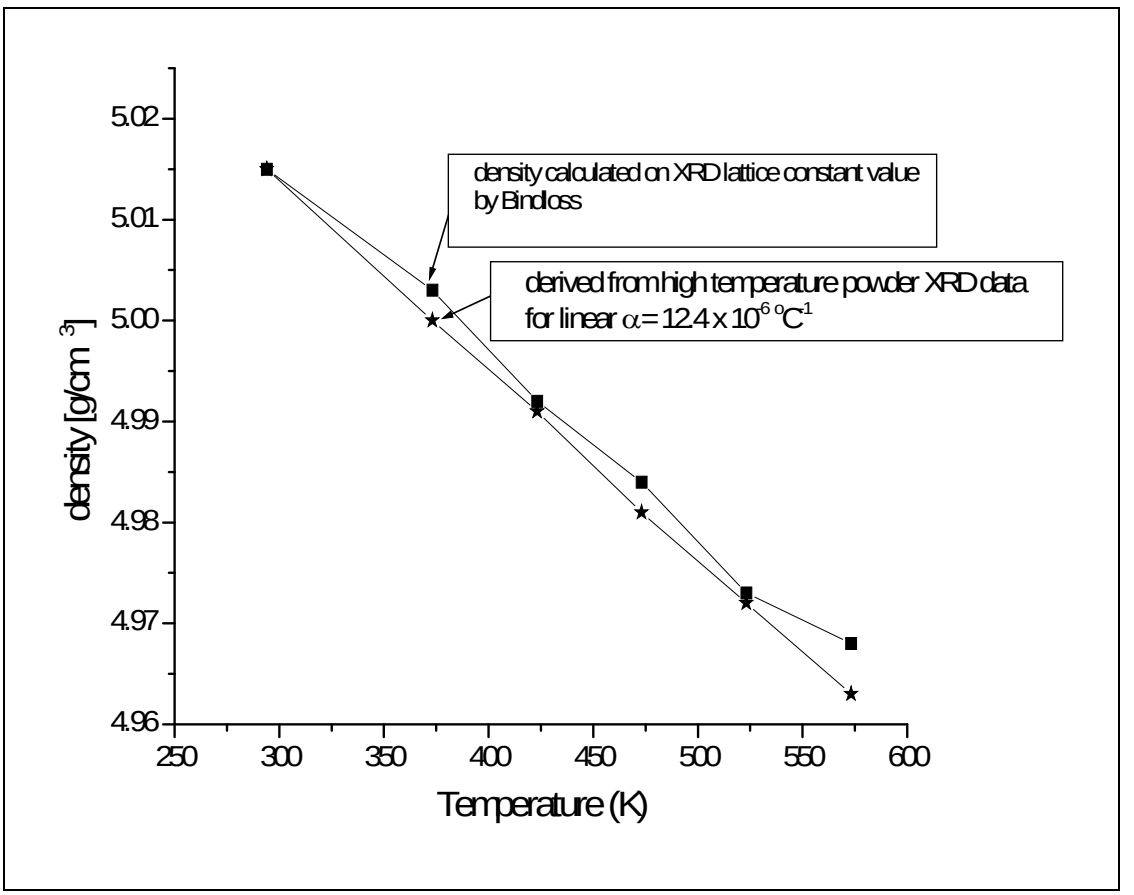

Figure 28: High –temperature x-ray density data plotted against results by Bindloss [4.7] based on lattice parameter change with temperature, represented by closed squares.

The experiment was conducted using a Rigaku x-ray spectrometer fitted with a special high-temperature camera, and the specimen was immersed in He gas during the high temperature runs in order to prevent decomposition. The thermal linear expansion coefficient for iron pyrite was measured using a procedure where the pyrite expansion is measured relative to that of an internal standard, in this case, rocksalt. Rocksalt (NaCl) was selected because it has a well known expansion coefficient and hardly any diffraction lines overlapped with those of pyrite. A decision was made to use a Cu anode tube as the best radiation source despite that it is characteristic radiation is known to suffer high absorption in Fe containing specimens. The alternative, Co, which is a hardly absorbed by Fe, is however, heavily absorbed by the heat shields and windows of the high -

temperature camera and molybdenum, which suffers little absorption has the disadvantage of compressing the diffraction lines into the low-angle region where the accuracy is very poor.

It is well known that the shift $\Delta\theta$, in the angular position of characteristic spectral peaks, is related to the fractional change of the lattice spacing *d*, by $\Delta\theta = -\tan\theta \times \Delta d / d$. On the other hand, $\frac{\Delta d}{d} = \alpha\,(T_2 - T_1)$ where α is the linear thermal expansion coefficient. Hence, $\frac{\Delta\theta}{\tan\theta} = \alpha\,(T_1 - T_2)$, thus for the ratio of the linear expansion coefficient of pyrite to rocksalt,

$$\frac{\alpha_{pyrite}}{\alpha_{rocksalt}} = \left(\frac{\Delta\theta}{\tan\theta}\right)_{pyrite} / \left(\frac{\Delta\theta}{\tan\theta}\right)_{rocksalt} . \qquad (4.1)$$

The ratio was measured to be 0.31 ($\pm$ 15%), so that α_{pyrite} = 12.4 x 10^{-6} $^{o}C^{-1}$ ($\pm$15%) for the temperature range 20^{o} to 338 ^{o}C. The results obtained by this technique are plotted in figure 28 with the results extrapolated from the x-ray lattice parameter values (hence density) measured at the corresponding temperature points. Good agreement is obtained between the present results and those obtained using thermal expansion coefficient data determined by Bindloss [4.7] extrapolated to the same temperatures.

4.4 Experimental procedure

High temperature measurements were performed using the high-temperature furnace described in detail in Chapter 3. SBS spectra were acquired in a backscattering configuration detailed in section 3.1 using an average incident laser power of 55 mW on the sample. The incident beam, which was linearly polarized in the sagittal plane (*p-p*), was kept at 70.9^{o} relative to the sample surface normal. In order to control the direction of propagation in the sample plane of the selected surface waves, the quartz rod was attached to a rotation stage (described in detail in section 3.3.) which allowed for azimuthal angular variation at the fixed incident angle, thus permitting one to measure the in-plane anisotropy of surface modes. The Fabry-Pérot interferometer was set up with a finesse of about 100 and a free spectral range (FSR) of 37.5 GHz. The spectral

acquisition time was about 150 minutes on average. Spectra were taken at various intervals (100^{o}C and 50^{o} C) for temperatures ranging from 20^{o}C to 350 ^{o}C.

4.4.1 Results and analysis

A typical room temperature spectrum for single-crystal pyrite for the (110)-oriented plane is shown in figure 29 using an azimuthal angle of 10^{o}. The peak centred at zero frequency-shift corresponds to the intense elastically scattered light. The Rayleigh wave is shown as a set of two prominent peaks at ±16.2 GHz. The other peaks at ±30.5 GHz are identified as HFPSAW (section 1.2.2), indicating that although there is significant optical absorption and thus the scattering volume is near surface, but with the large elasto-optic scattering one can still obtain a peak.

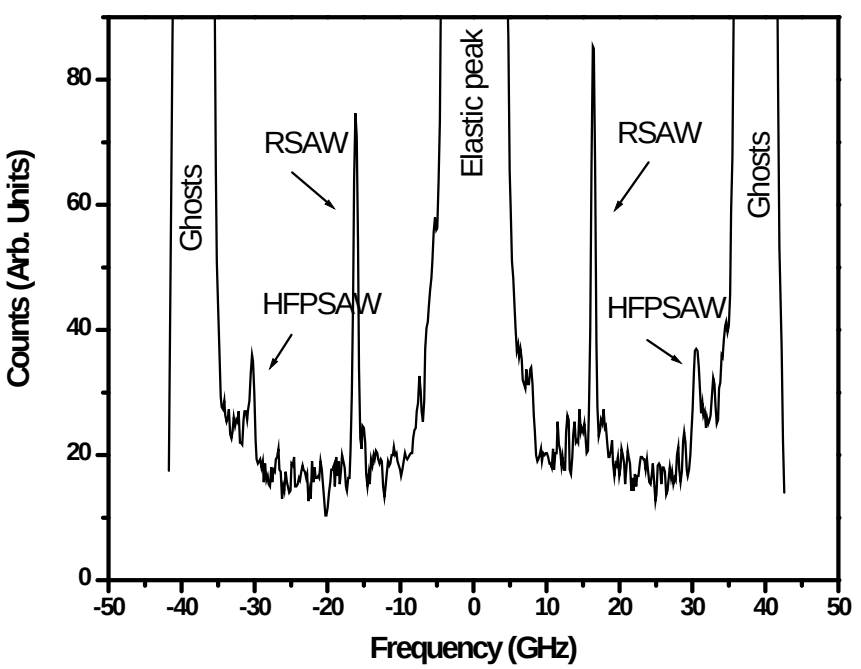

Figure 29: SBS spectrum for FeS_2 (110) showing RW and HFPSAW modes measured at room temperature for azimuthal angle of 10^{o}.

Figures 29 and 31 provide examples of the angular variation of the RSAW and HFPSAW on the (110) plane measured at room temperature and at an elevated temperature, namely 350^{o}C. A weighted least-squares dual fit of the velocity dispersion curves using as free parameters the effective elastic constants c_{11} c_{12} and c_{44} was performed involving the

minimisation of χ^2. The continuous lines represent computed best fit to the experimental data for the two modes using the Green's function analysis as shown in figures 30 and 32. It is important to mention that one cannot determine c_{11} and c_{12} individually with only the Rayleigh dispersion data. The Rayleigh fit is highly sensitive to c_{44} and mildly sensitive to the difference ($c_{11}-c_{12}$). Therefore the presence of HFPSAW provided additional information for extracting all the three independent elastic constants from the angular dependence of both RSAW and HFPSAW. The respective peak positions of HFPSAW are given by $V_l = (c_{11}/\rho)^{1/2}$ for the [001] direction and $V_l = [(C_{11}+C_{12}+2C_{44})/2\rho]^{1/2}$ for the [110] direction on this (110) plane. For the intermediate directions the peak position varies sinusoidally with azimuthal angle φ.

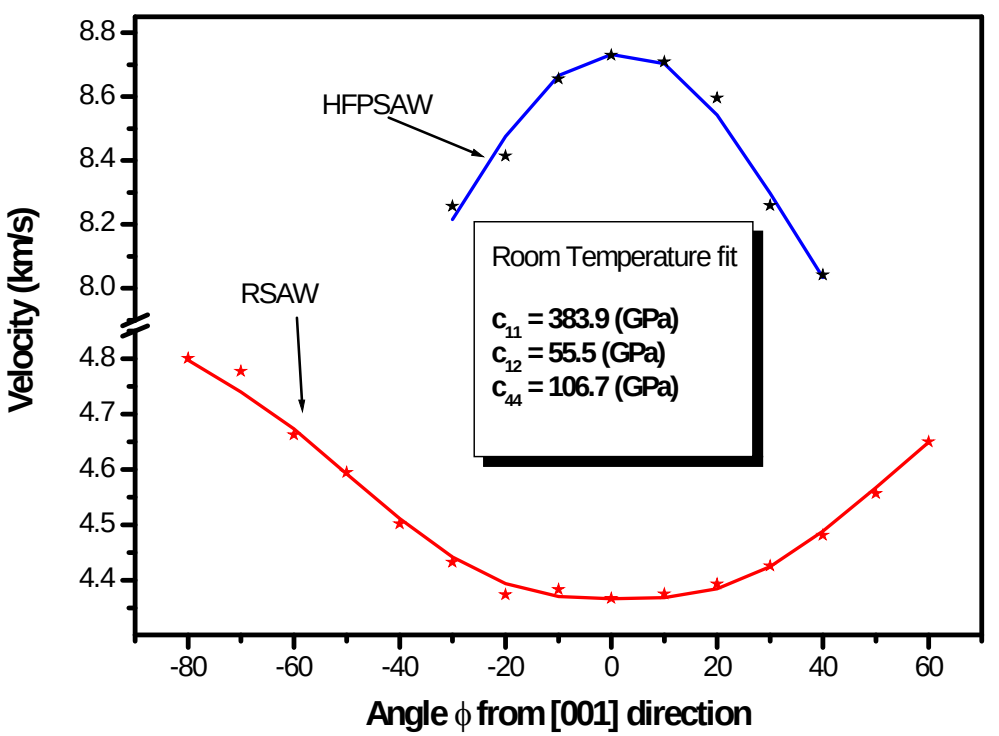

Figure 30: Least-squares fit of the angular dependence of the velocity of the RSAW and HFPSAW and the resultant elastic constants obtained using the Green's function method.

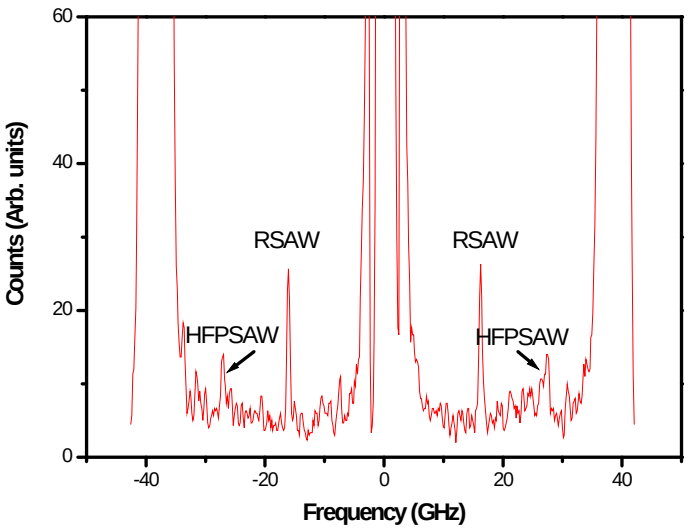

Figure 31: SBS spectrum of iron pyrite recorded at temperature of 350°C for azimuthal angle Φ=160°. Figure 32 below shows the dispersion results incorporating SAWs in figure 31.

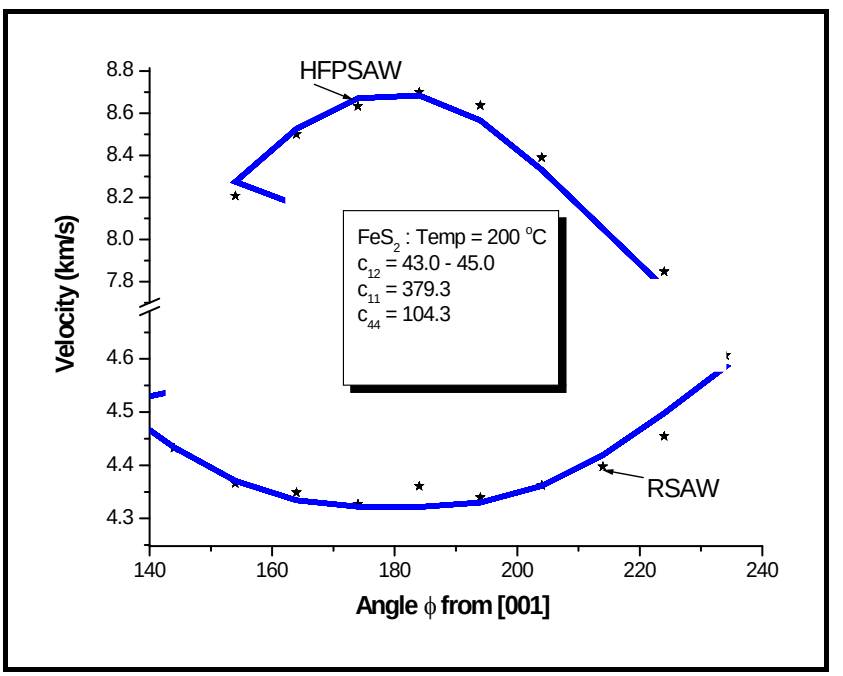

Figure 32 : Typical least –squares fit to the two modes (RSAW and HFPSAW) using the Green's function method applied to a dispersion plot obtained at 200 °C. A similar procedure was conducted at every set-point up to 350 °C, in order to extract the elastic constants plotted in figure 34 below.

Figure 32 demonstrates the least-squares minimization procedure used to extract the elastic constants, c_{11}, c_{12} and c_{44}. The process of fitting the dispersion of the two surface

acoustic modes is one of inversion. Sets of velocities $V_i^{calc}(c_j)$ can be computed as a function of one or more free parameters c_j (typically, but not necessarily, elastic moduli), the index *i* standing for a set of values of the propagation direction for anisotropic semi-infinite medium; or in the case of a film thickness *h*, the propagation velocity depends on the dimensionless product $k_{//}h$. A weighted least-squares minimisation of the elastic constants

$$\chi^2 = \sum_{i=1}^{n} (V_i^{meas} - V_i^{calc})_{RSAW}{}^2 w_i + \sum_{j=1}^{m} (V_j^{meas} - V_j^{cal})^2_{HFPSAW} w_j \qquad (4.2)$$

permits a best fit to the angular dispersion relations for observed RSAW and HFPSAW in the SBS experiment. In the summation is the complete set of data for the RSAW (first term) and that of the HFPSAW (second term). The weighting factors w_i and w_j were determined from the individual measurement errors on the RSAW and HFPSAW respectively. According to standard estimation theory, the minimum of χ^2 identifies the most probable values of the free parameters (in this case, the elastic constants C_{ij}) in the (V_i) space. The poor or good identification of the minimum $\chi^2(C_{ij})$ depends on the amount of available information. In this case, the availability of additional information in the form of HFPSAW mode enabled us get a good determination on one parameter, namely C_{11} which we could then fix and obtain the other two. The elastic constant , c_{11} is obtained from the frequency of the HFPSAW whose frequency corresponds to the longitudinal threshold frequency. Figure 33(a) shows the extraction of elastic constants, where C_{11} is fixed, allowing C_{12} and C_{44} to vary until a stable chi-square minimum value is obtained. A well-defined minimum for χ^2 allows good identification of the elastic moduli C_{44}. The density and shape of the contour lines of constant chi-squared is also an indication of the high sensitivity of the two elastic constants to the fitting procedure. In figure 33(b), C_{12} is fixed while allowing C_{11} and C_{44} to vary to a chi-sqaure minimum whose value should also lie close to the one in figure 33(a). Finally in figure 33(c) using the optimised elastic constants, C_{11} and C_{44}, obtained from the first and second optimisations respectively, the same procedure is used to look for a stable chi-square minimum value for C_{12}. It is clear from the shape of the contour lines in figure 33(c) that the extent of the uncertainty for C_{12} is relatively larger than that observed for C_{44}.

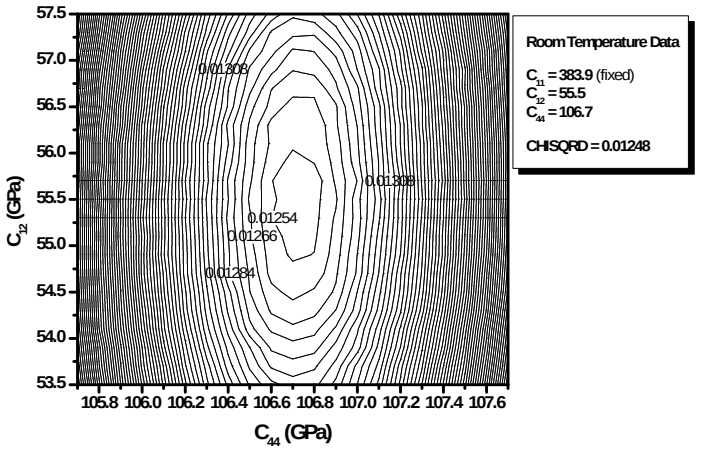

(a)

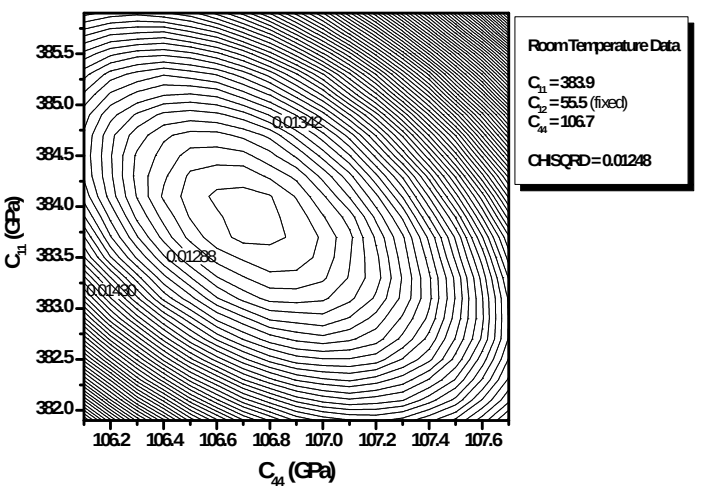

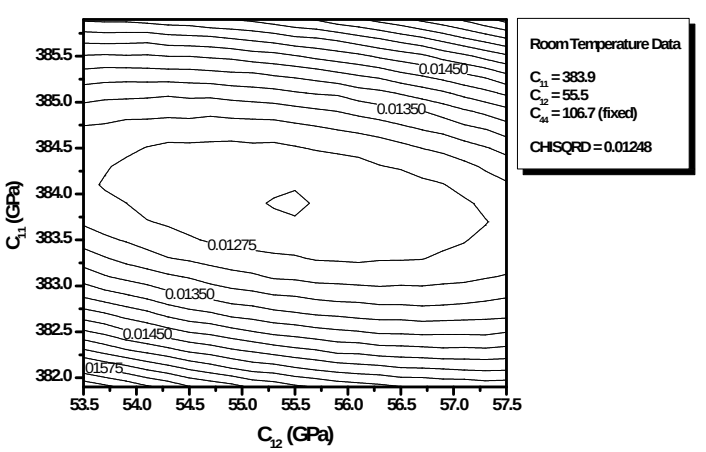

(c)

Figure 33: Least-squares minimization process in the extraction of the elastic constants showing the stability of the values, with top figure labelled as (a), followed by (b) and (c).

In Figure 34 the behaviour of the set of elastic constants is shown as a function of temperature. It is observed that the three elastic constants, C_{11}, C_{12} and C_{44}, gradually decrease with increase in temperature as expected. In particular, C_{12} is consistently observed to have a *positive value* and it is decreasing with temperature. In the work conducted by Benbattouche et al., [4.3] C_{12} was shown to have a small linear increase from 100 K to room temperature. They alluded this increase to the fact that this stiffness tensor component does not correspond to any vibration mode of the crystal [4.14]. The change in magnitude of C_{12} with temperature is so small that the Poisson ratio can be expected to remain positive. In all the measurements, the changes in the density as a function of temperature, obtained from the high temperature XRD measurements, were incorporated into the calculations of the elastic constants at temperature.

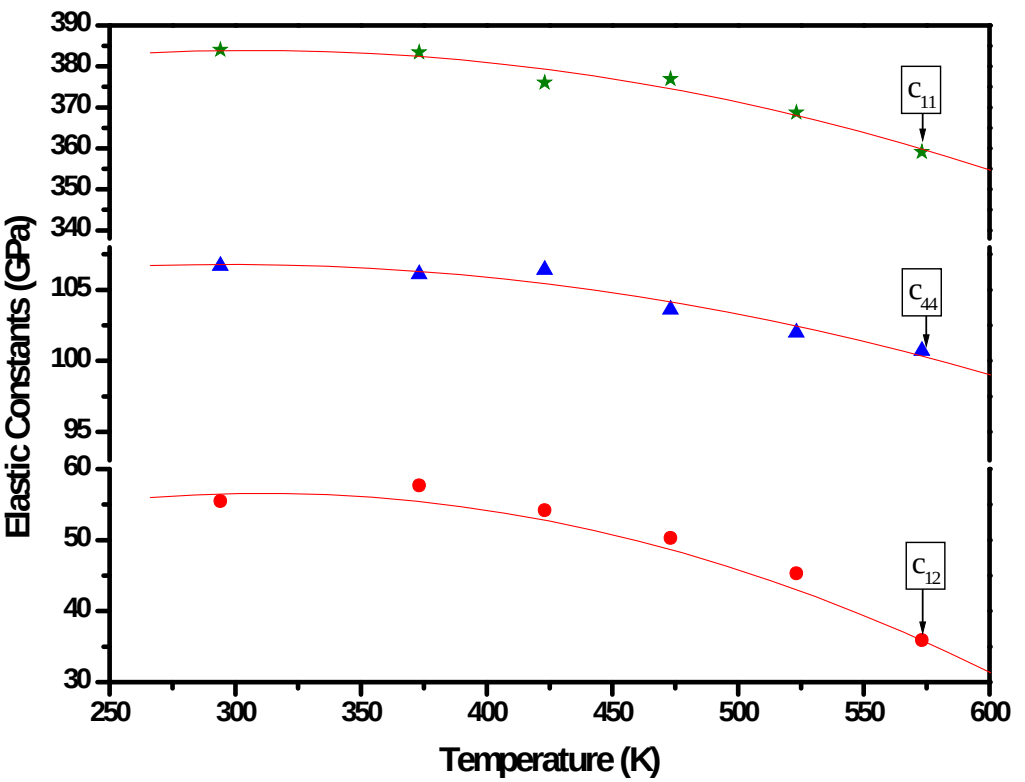

Figure 34: Elastic constants of FeS_2 crystal as a function of temperature showing the quasi-linear decrease as a function of temperature shown enhanced by the use of different scales.

A detailed examination of the cumulative error in the surface velocity as introduced by errors in: (a) angle of incidence [4.11] (~0.12%); (b) uncertainty in free spectral range calibration(~0.2-0.3%); (c) peak analysis procedures (~0.3%); (d) an estimated 0.4% uncertainty due to geometrical effects (peak broadening, etc) lead to an estimated 0.41% uncertainty in the measured surface wave velocity. A possible additional source of uncertainty in SBS is the surface damage induced by the mechanical polishing process of the crystal, which is rather difficult to quantify.

4.5 Computational approach for determining elastic properties of pyrite and comparison with this work

This section discusses results of computational studies by Sithole et al. [4.10] being complementary to the present work on iron pyrite and permits comparisons of two different computational models with experimental data. Good agreement was obtained for the results from the two approaches and the experimental data provided invaluable feedback information to further refine the original models used for research on sulphides, which includes those of the platinum group. Theoretical studies of materials require a model of forces acting between the atoms in a solid. The atomistic simulation method uses interatomic potential functions to describe the total energy of a system in terms of atomic coordinates. Thus the equilibrium positions of atoms or ions in a system are evaluated by minimising the lattice energy until all strains acting on the crystal are removed.

The lattice energy can be defined as the sum of the electrostatic or Coulombic forces acting between atoms, and the short-range repulsive forces produced by the overlap of nearest neighbour electron clouds. These short-range forces act between bonded and non-bonded atoms in the crystal where non-bonded interactions can be effectively modelled by the Buckingham potential:

$$U = A_{ij} \exp\left(-r_{ij} / \rho_{ij}\right) - B_{ij} r_{ij}^{-6}. \qquad (4.3)$$

The parameters A_{ij} and ρ_{ij} describe the repulsion between two ions i and j at separation distance r_{ij}, and B_{ij} is a term included to model dispersion. Bonded interactions can be

described by a combination of two-body bond stretching potentials such as a harmonic potential of the form:

$$U = 0.5k_s(r_{ij} - r_0)^2 . \quad (4.4)$$

Three-body bond bending terms that are exponentially decaying, can be used to include the effects of directionality in S-S-Fe bonds;

$$U_b = 0.5k_b(\theta_{213} - \theta_0)^2 \exp\left(r_{12}/\rho_1\right)\exp\left(-r_{13}/\rho_2\right) . \quad (4.5)$$

In equations (4.4) and (4.5), k_s and k_b are the bond-stretching and bond-bending force constants respectively and θ_0 the equilibrium bond angle. The short-range potential parameters used to describe interactions in pyrite were derived by a least squares fitting procedure using the GULP code [4.24]. Potential P1 incorporates a Buckingham term for Fe–Fe interactions, which is absent in P2. This is offset in P2 by the large ***A*** value in the S-S and S-Fe Buckingham terms. Both potentials perform well at 0K and 300K and reproduce the cell parameter, bond lengths and bond angles to within a percent of the measured values. Further details of the fitting are discussed by Sithole et al. [4.10,4.15]. The calculated elastic properties of pyrite are within 5% of the experimental data for potential P1, and 7% for P2. Given the approximate nature of the model, the agreement is extremely good in both cases. Several attempts were made to integrate the effects of polarisability on the S ion by the use of a shell model [4.25]. However, acording to Sithole et al., adding this term did not lead to any improvement in the model and thus was ultimately not included. Also for every temperature value, only optimisation of the structure was performed without refitting the potential parameters, thus the model was left intact.

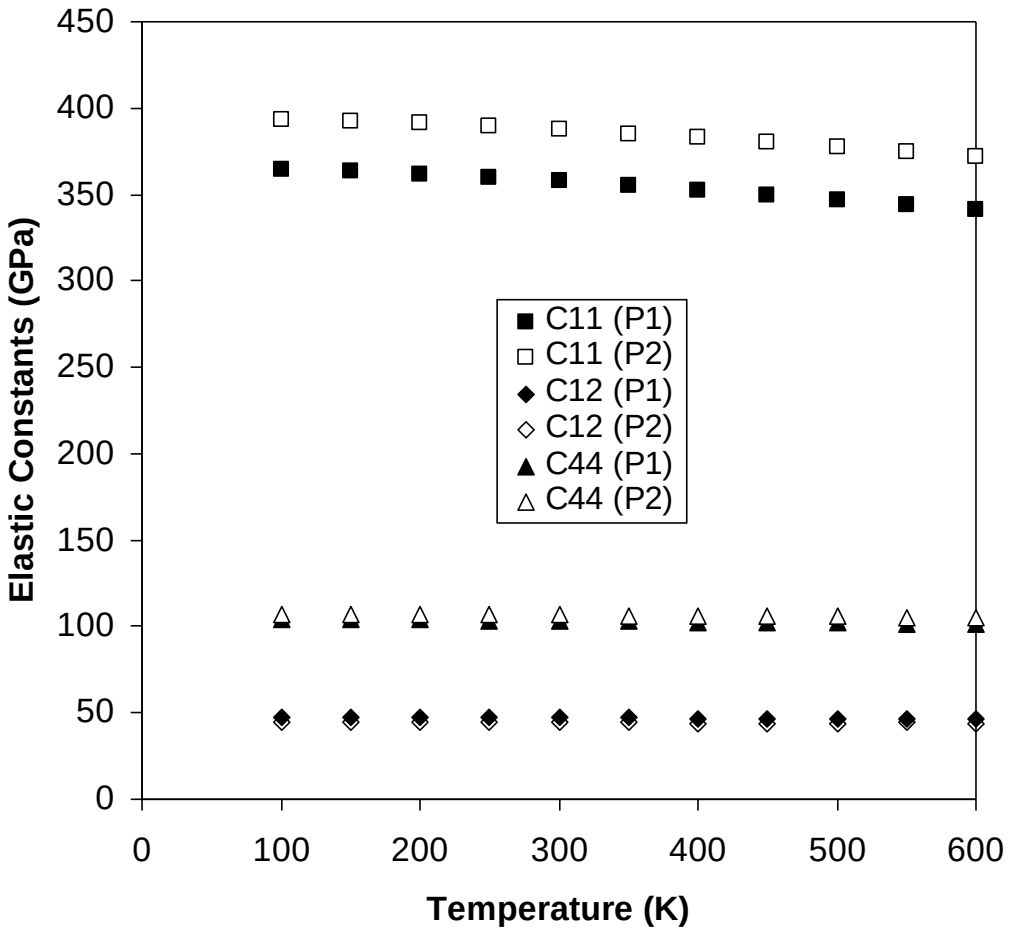

Figure 35: Calculated temperature variation of elastic constants of pyrite FeS_2 by Sithole et al. extracted from reference [4.15]. The results for the two potentials P1 and P2 (as described in the previous page) show gradual linear decrease with temperature corroborated by experimental results in figure 34.

4.5.1 Discussion

This comprehensive high temperature surface Brillouin scattering study of acoustic waves in bulk iron pyrite has identified the HFPSAW which exhibits significant angular velocity dispersion as a very useful source of acoustic wave information. The presence of this mode has led us to use combined least-squares fitting of the associated angular dispersion curves of both RSAW and HFPSAW to successfully determine the elastic constants C_{11}, C_{12} and C_{44}, of the bulk material. It is the first time that the variation of the iron pyrite elastic constants with temperature is performed from room temperature to 350^{o}C, and also in which the use of a dual fitting technique based on Green's function

calculations of the angular variation of the velocities of the RW and HFPSAW modes is applied to extract elastic constants. The room temperature values of C_{11}, C_{12} and C_{44} agree reasonably well with those obtained by Benbattouche et al. [4.3] and those of Merkel et al. [4.16] using ultrasonic technique.

The results of this work further together with the computed data confirm that C_{12} remains positive *beyond* room temperature as well, and moreover, as temperature is increased it is observed that the three elastic constants decrease with increasing temperature. It is worth mentioning that the appearance of HFPSAW in FeS_2 spectrum indicates that elasto-optic scattering plays a role in the scattering, and therefore the material is not completely opaque, but typical of semiconductors.

From the computational results; elastic constants at 300K, using both models, compare quite well with Brillouin scattering and ultrasonic measurements for the elastic constants and moduli of FeS_2; generally, two regions of interest are observed in figure 35. Firstly, all elastic constants (C_{11}, C_{12} and C_{44}) change very slowly, and appear almost near constant, from 100 K to 200 K for which there is some comparative experimental data from Brillouin scattering measurements [4.18]. Focussing on the region of interest, which extends from 300K to 600K, all elastic constants, determined by the calculations vary 'more linearly' with temperature whilst the experimental results show a higher curvature with increasing temperature. These effects evident from the high temperature elastic constant measurements are not reproduced very well by the simulations, especially at higher temperatures, though the computed elastic constants at room temperature agree well.

In previous Brillouin scattering measurements and calculations on metal oxides, e.g. yttria stabilized cubic zirconia [4.19, 4.20], halides, e.g. LaF_3 [4.20] and CdF_2 [4.21], and sulphides, e.g. Li_2S [4.23], such a 'linear' behaviour of the elastic constants with temperature was noted and shown to be consistent with the quasi-harmonic approximation. However, the SBS experimental results presented in the present work suggests that the potential model used by Sithole et al. [4.10], needs to incorporate higher

order anharmonic terms in order to reproduce the experimentally observed curvature of these iron sulphides.

4.5.2 Conclusion

Despite the apparently covalent nature of iron pyrite, it has been possible to derive classical interatomic potential models with which to describe pyrite. The first high temperature measurements of elastic constants of pyrite FeS_2 have been successfully conducted. The good agreement with the computed results is an indication that the quality of the potentials is good, as is also shown by the agreement between calculated and experimental structure [4.15] of pyrite at ambient temperature. In addition, the study has shown good agreement between simulated and experimental elastic constants at high temperatures and both results validate the assertion that C_{12} has a positive value, hence a positive Poisson's ratio. The ability to reasonably predict high temperature behaviour, demonstrated in the potentials developed to complement this study, and high pressure elastic constants, shown in the previous computational study [4.23], clearly demonstrates the robustness of the potential model of iron pyrite FeS_2 when applied to extend or further our knowledge of the behaviour of these compounds under various conditions. It is also evident that higher order terms (due to intrinsic phonon-phonon interaction) need to be incorporated to the present potentials so as to fully account for the experimentally observed curvature at higher temperatures. This curvature is atributed to anharmonicity due to phonon coupling which occurs at high temperatures, whilst for the intermediate temperatures i.e beyond Debye temperature, the 'classical quasiharmonic' approach is adequate to describe the temperature dependence of the moduli. However, for the low temperature range, below Debye temperature, or 'quantum regime', quantum effects that determine the low-temperature behaviour of thermodynamic functions need to be taken into account such that heat capacity $C \sim T^4$ rather than $C \sim T$, where T is temperature.

In the following chapter, an investigation of titanium alloys is reported in which their elastic properties as a function of temperature are determined. The complications arising from a lack of adequate standardized characterisation of the sub-stoicheometric compounds will be highlighted, while the temperature dependence of the elastic constants do follow the quasi-harmonic approximation. The high temperature results will provide an important source of data for checking the accuracy of models presently used to simulate mechanical behaviour of these compounds, in thin coatings and in use as cermets in industry.

Chapter 5

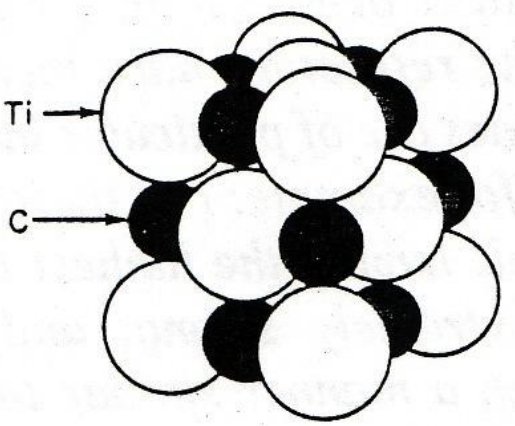

5 Titanium Alloys

5.1 High temperature elastic properties of titanium compounds

The carbides of the transition metals in Groups IV - VI have extremely high melting points and are therefore referred to collectively as the “refractory carbides.” These transition metal compounds are of the type MX, where M denotes a transition metal element (Ta,V, W, Zr, Nb, Hf and Ti) and X denotes one of the non-metallic elements C, N or O. In addition to their stability at high temperatures, these compounds are extremely hard and so find industrial use in cutting tools and wear-resistant parts. Their hardness is retained to very high temperatures, and they have low chemical reactivity – they are attacked only by concentrated acid or base in the presence of oxidizing agents at room temperature, and retain good corrosion resistance to high temperatures [5.1-5.4]. The refractory carbides are strong, with Young’s modulus values – a measure of elastic deformation resistance – rivalling those of SiC at room temperature. In addition, they have good thermal shock resistance and good thermal conductivity, permitting heat to be drawn away from the working surface of the tool. This gives them a benefit over other refractory materials, which do not conduct heat so well.

In the comprehensive review by Lengauer [5.5], an observation is made that many binary transition metal carbides and nitrides especially the face - centred cubic δ phases of the group IV, exist over broad ranges of composition with an upper limit of the non-metal/metal ratio near unity. Practically all solid state properties show a gradual change with this ratio. Other carbides with a different structure such as tungsten carbide and chromium carbides have a very narrow homogeneity range. Transition metal carbides and nitrides often form solid solutions resulting in carbonitrides of which also the solid state properties vary with the [C]/([C]+[N]) ratio [5.6, 5.7]. This behaviour offers a large field for tailoring carbonitrides, but presents a huge complexity in terms of characterisation and profiling as there is very limited reliable data [5.8]. The thermal stability of the metal carbides, nitrides and carbonitrides is connected with their free energy of formation, the stability decreasing with increasing group number [5.9]. While the group IV transition metal nitrides TiN, ZrN and HfN and respective carbonitrides Metal(C,N) can be melted without decomposition, the nitrides and carbonitrides of the other groups decompose

before melting points are reached, releasing nitrogen in the process and this makes the reliable determination of properties at temperature extremely complicated. However, the aim of the present work on these materials was to characterise their mechanical strength in a more structured manner in order to provide reliable and traceable data on the elastic constants of these materials while taking into account the numerous complications highlighted above. In the cases of carbonitrides there is practically no high temperature data of the dependence of the elastic constants [5.5], hence SBS technique would provide invaluable information on the high-temperature characteristics of these important alloys. SBS, being a near-surface SAW measuring technique provided the added advantage of working with small well-prepared and characterised samples which are crucial for traceability and repeatability of measurements. In the following sections details of the various procedures undertaken to ensure reliability of data will be discussed as well as other considerations that help to consolidate the final results.

5.1.1 Structure and bonding

Transition metal carbides, nitrides and carbonitrides belong to the family of interstitial alloys or compounds. The common features of this class of materials are: very simple metallic structures with small carbon and/or nitrogen atoms in the interstitial voids of the often densely-packed host lattice [5.5]. They generally have face-centred cubic (fcc) or close-packed hexagonal (cph) metal lattices with non-metal atoms more or less randomly distributed on the interstitial sites. The phenomenon of vacancy ordering is often observed especially in the transition metal carbides [5.10].

A mixture of metallic, covalent and ionic components prevail in the bonding of transition metal carbides, nitrides and carbonitrides. The metallic character is evidenced by the high electrical conductivities of these compounds. The bonding mechanism has been described extensively by a variety of approaches [5.7, 5.11] for calculating the density of states (DOS) and hence the electron density in fcc transition metal carbides, nitrides and oxides. In the DOS of these compounds there is a minimum at a valence electron concentration of 8, corresponding to the stoichiometric composition of the group IVB carbides TiC, ZrC and HfC. Transition metal carbides have a lower DOS at the Fermi level than the

corresponding transition metal nitrides; hence electrical properties such as electrical and thermal conductivity and the superconducting transition temperature T_c are lower than those of nitrides [5.7].

5.2 Elastic properties and determining factors

Transition metal carbides, nitrides and carbonitrides exhibit high Young's moduli, appreciably higher than those of the transition metals themselves. Many of the carbide and nitride phases have been investigated for their elastic properties, mainly the Young's modulus *E*, and the Poisson ratio *v*. Both bulk samples as well as thin film samples were measured and generally polycrystalline material was studied [5.12]. Among these studies, many of the data suffer from a lack of or inappropriate characterisation of composition and microstructure. The porosity of bulk samples as well as the substrate of thin films can influence the results substantially and correction procedures for accounting for such influences are sometimes inappropriate [5.13]. For example, depending on the correction function 5% porosity can cause a drop in *E* of about 50 GPa. For TiC most values for the Young's modulus group around 450 – 460 GPa for a composition around 50 at% carbon, while the Poisson ratio is reported in the range 0.17 – 0.19 [5.5]. The Young's modulus of the important hexagonal phase of WC is very high at room temperature, about 707 GPa [5.7] and drops by about 20% upon reaching 2000K.

Although the measured Young's modulus on TiN_{1-x} show quite a scatter because of the above-mentioned problems (see figure 36), it can be stated that *E* increases with increasing nitrogen content. Many of the thin film samples show a higher *E* than bulk samples. Poisson ratios of 0.18 – 0.32 have been reported, though the most probable value would be about 0.22. Young's modulus data on group VB transition metal nitrides are scarce though they have been measured for single crystals of δ-VN and δ-NbN [5.14], yielding the maximum values in (100) direction of 487 GPa and 490 GPa, respectively. For CrN, values up to 520 GPa have been reported.

For Ti(C,N) an increase of *E* with carbon content has been reported for several samples, the porosity of which is rather large and different in different samples (see citations in

Kral [5.13]), whereas theoretical studies by Jhi et al. [5.15] show an increase in bulk moduli as N replaces C, an increase associated with the influence of the extra electrons from N in a smaller unit-cell volume. In the available literature, there is one well-characterised sample $Ti(C_{0.2}\ N_{0.8})$ with a porosity of only 3.5% [5.7] which yielded the highest value of E = 451 GPa (with ν = 0.212), which probably comes very near to the value for an ideal zero-porosity sample.

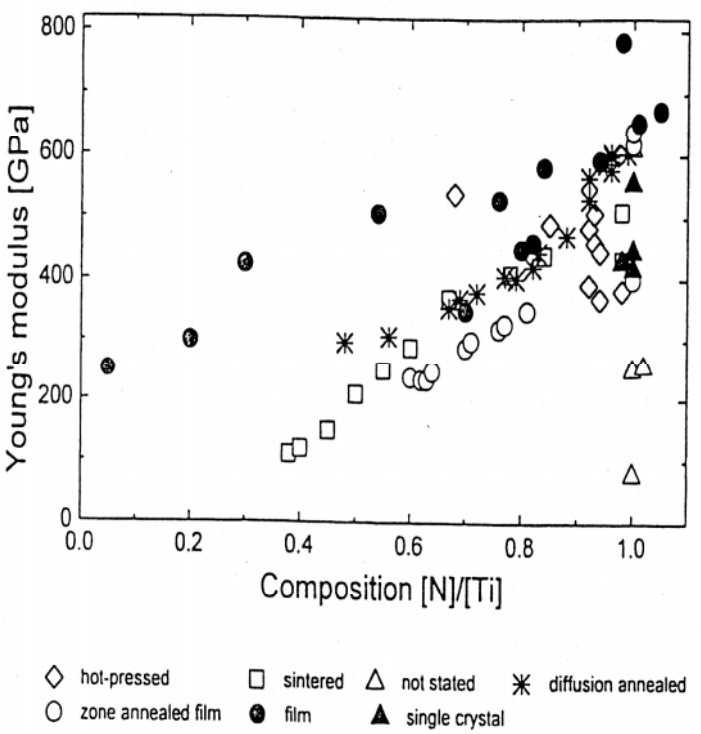

Figure 36: Room temperature Young's modulus of TiN_{1-x} as a function of composition and for different sample types [5.13]

An investigation of the E and G behaviour for TiCN (for a composition of 50 at% N) as a function of temperature up to 1000 K was conducted on a polycrystalline sample [5.5], where a linear relationship was reported for both quantities.

Slow diffusion of carbon in all of the refractory carbides results in stoichiometry gradients which are difficult to detect in bulk materials but which may compromise the

material strength, hardness, and high-temperature behaviour [5.3,5.7]. The lattice parameter and the sharpness of the XRD pattern can give some rough indication of the homogeneity, however. It must be noted that there is some variation in the literature with respect to the reports of assorted mechanical and thermodynamic properties of the refractory carbides as has been highlighted above. The transition metal carbides and nitrides show a range of non-stoichiometries and possibilities for vacancy ordering, so the precise phases being tested for a given property are often unclear. Furthermore, the small concentrations of oxygen present as metal oxide are famously difficult to remove – or even detect – and can be expected to affect the properties of the material.

5.2.1 Motivation for current study.

Despite the wide use of transition metal alloys in industry as coatings and cermets involving application to hostile environments, especially high temperatures generated due to friction in drill bits, metal cutting tools etc, there is hardly any information available on high temperature elastic properties. These high-temperature properties are poorly investigated [5.8] and there is a great need of data in the hardmetal community. The objective in this research is to provide experimental data for these high temperature properties (*E* and *G*) for well-characterised samples so that a traceable, repeatable data set can be established from which modelling studies can base their results on [5.15]. The focus of the present work is on on titanium carbide (TiC_x) and titanium carbonitrides (TiC_xN_y). The samples were provided courtesy of Prof Dr. W. Lengauer of Vienna University of Technology, from the Institute for Chemical Technology of Inorganic Materials, Vienna, Austria. The samples are hot-pressed, polycrystalline and the surfaces lapped plane-parallel. It is also important to note that mechanical characteristics of hard constituents critically influence the performance of composites and cermets, since they are subjected to loads not only at ambient temperatures and their response to load and cyclic heating is therefore critical for final performance. To calculate the elastic properties from the measured sound velocities it is important that the longitudinal as well as the shear velocity is taken into account to obtain precise data for Young's modulus and Poisson's ratio. This is due to the fact that without the data for the shear velocity, only estimated data can be taken for the Poisson's ratio to calculate Young's modulus. But

with the SBS technique one is able to independently measure the shear velocity, hence obtain the complete set of elastic constants, most importantly as a function of temperature.

5.2.2 Overview of available characterisation techniques

Complete characterization of the refractory carbides is difficult. Since many of the important mechanical and catalytic properties are sensitive to a number of factors which tend to vary widely among samples, there is a variation in literature reports regarding measurement of these properties. These factors include (1) the crystal structure and lattice parameters, including the presence of vacancy ordering; (2) the chemical composition, including not only the overall carbon-to-metal ratio present in the bulk sample, but the amount of free carbon versus combined (lattice) carbon; (3) the impurity concentration, particularly that of oxygen; (4) the overall defect structure, including grain size, dislocations, and porosity; and (5) the sample homogeneity.

A summary of some characterisation techniques extracted from reports [5.31] and publications by Young [5.37], Klug and Cheetam [5.38] as applied to titanium alloys is given below. Traditionally, the crystal structure can be found and the lattice parameters measured by X-ray and neutron diffraction experiments. Sample homogeneity may be deduced from X-ray diffraction (XRD) data by noting the sharpness of the splitting between the K alpha-1 and K alpha-2 lines of the characteristic radiation, and crystalline impurity phases present in concentrations over approximately 5% may often be detected using XRD [5.16]. Even large oxygen impurity concentrations, however, may escape notice due to the formation of a solid solution with the carbide. The effects of medium-to-large oxygen impurity concentrations on lattice parameters are not well-described. Very careful XRD analysis may also detect ordering of carbon atoms or vacancies in the structures of the carbides of the lighter metals, when such ordering is accompanied by a distortion of the lattice [5.17, 5.37]. The specific details of the ordering would not be easy to determine even using modelling techniques such as Rietveld analysis; ordering without an accompanying symmetry or lattice parameter change would only be detectable using a complex Fourier analysis of the XRD peak intensities [5.18,5.38]. Neutron or electron

diffraction experiments, on the other hand, would give unambiguous information regarding the ordering of carbon atoms on the interstitial sites, however, electron diffraction sample preparation is made difficult by the need to make a thin section of the brittle and possibly porous carbide material, and neutron diffraction is not immediately available to most researchers.

Oxygen analysis is extremely difficult because once the solid solution M(C,O) has formed the oxygen is nearly impossible to remove. This is particularly true in the case of non-stoichiometric carbides MC_{1-x}, where empty octahedral interstitial sites are very inviting to the stray oxygen atom. Vacuum-fusion techniques, e.g. heating the refractory carbide to 2400-2800 ^{o}C in a graphite mould or platinum bath under vacuum, followed by determination of the oxygen removed as CO_x, are the major methods available, but are often only partially successful. This is particularly true of the carbides of the Group IV metals. Neutron activation analysis, in which oxygen is activated by the reaction $^{16}O(n,p)^{16}N$, then monitored using the 6.1 and 7.1 MeV gamma-radiation from ^{16}N, has proven useful. Sample homogeneity and local compositions may be measured by microprobe analysis, in which the X-ray emission of elements on irradiation with an electron beam, as in an electron microscope, is measured and correlated with the concentration of the element [5.19]. The microprobe must be equipped with a thin detector window to give good quantitative information regarding light elements (Z<10), however. Electron energy loss spectroscopy (EELS), on the other hand, can sensitively detect elements in the Z<10 region [5.20]. Both of these methods are extremely localized, however, and multiple areas of several samples must be examined for conclusions regarding the bulk material to be validly made.

Vacancy concentration is likewise difficult to measure due to the ambiguities in chemical composition measurements. Where the composition is well-known, comparison of X-ray density with a physically-measured density will give a good estimate of the vacancy concentration. Likewise, density measurements can give information regarding larger-scale defects such as porosity [5.25]. Electron microscopy can give reasonable estimates of the grain size [5.31].

In this Chapter it is intended to demonstrate that SBS is a useful characterization technique enabling one to directly obtain the dynamic elastic constants from which the mechanical/engineering moduli are obtained and *bulk* polycrystalline TiC_x and TiC_xN_{1-x} samples were investigated as detailed in the following sections.

5.3 High temperature SBS investigation of bulk polycrystalline TiC_x (x~ 0.97)

Introduction:

"….approximate preparation of transition metal carbides is straightforward, but ensuring a given stoichiometry and purity against oxygen contamination is famously difficult. Variations in the quantity of vacancies on the carbon (or less frequently, the metal lattice), as well as variations in the amount of dissolved oxygen, lead to a wide range of claims regarding even basic thermodynamic, mechanical and electromagnetic data for the early transition metal carbides……."- The Refractory Carbides by E.K. Storms; Academic Press, New York, 1967 [5.4]

5.3.1 Sample characterisation

XRD analysis

The XRD spectrum indicated that the sample was of good homogeneity as shown by the narrow peaks (see figure 37), with an estimated average grain size of 90 nm. The presence of second pair of [111] and [200] peaks is not well understood, but is thought to be indicative of the presence of small amounts of TiC_x with a different stoichiometry and/ or existence of polytypes. It has been reported that group IV metals tend to form a single cubic phase with a limiting stoichiometry near $MC_{1.0}$, but which normally varies from $MC_{0.5}$ to $MC_{0.97}$, depending on the synthesis conditions [5.4]. The XRD results performed using a Philips 1050/30 diffractometer (Cu Kα radiation) in figure 36 gave a lattice constant value of 4.330 Å, which compares very well with Lengauer's result [5.8] of 4.328 Å for $TiC_{0.95}$ sample and the value of 4.332 Å determined by Jhi et al. [5.15] for a modelled sample of stoichiometric TiC. The crystal structure was confirmed as f.c.c. in agreement with the literature [5.21]. The XRD spectrum was identical to the TiC

spectrum on the JCPDS card number 32-1383, stock number 5220HT, thus confirming the identity of the sample and the crystal structure.

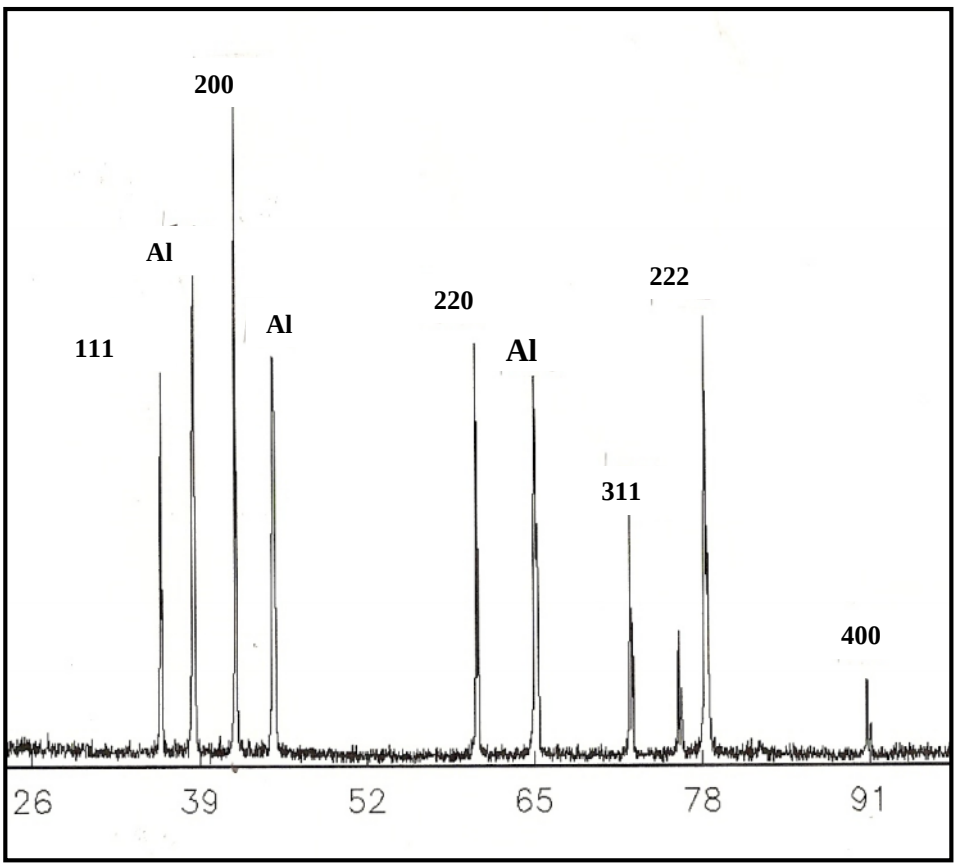

Figure 37: X-ray diffractogram for the hot-pressed TiC sample taken using Cu radiation. Only the most intense (200) peak was considered for the *d*-spacing calculations. Al reflections originate from the aluminium sample holder.

Estimation of Carbon concentration

By considering the *d*-spacing for the intense (200) peak in figure 37 which obeys a linear Vegard relation to the carbon concentration, from which the bonded carbon content was estimated. From the XRD spectrograph in figure 37, *d*-spacing for the (200) peak is 2.164 Å. Using the relation the relation in reference [5.22], namely,

$$\text{fractional carbon content } C_x = \frac{d_{(200)}peak - 2.12}{0.045} \quad \ldots\ldots\ldots\ldots\ldots\ldots (5\text{-}1)$$

a value for x ~ 0.97 is determined for TiC_x. This signifies that the sample is well prepared and almost stoichiometric, as well as indicating a small concentration of carbon

vacancies. It is important to note that Pintschovius et al. [5.23], using inelastic neutron scattering and by analysis of the phonon dispersion curves, observed that acoustic modes were less sensitive to carbon content than optic modes that suffered a 3.5 % drop when x-value changed from 0.95 to 0.89. This implies that the elastic constants within this narrow stoichiometric range are not expected to differ significantly for samples of identical porosity and density.

This TiC stoichiometry correlates very well with the Raman investigations conducted on the same sample using 514.5 nm Ar^+ line on a Dilor-Jobin-Yvon spectrometer, where the TiC sample was scanned at various locations on the sample and found to be Raman-inactive [5.24], hence it is inferred that the composition must be very nearly stoichiometric.

Density measurements

The analysis of the XRD results confirmed the f.c.c. NaCl-structure (*B1*) of the TiC specimen, having a lattice parameter of 4.330Å from which a theoretical x-ray density of 4.899g/cm^3 is obtained. This value of the density is quite close to the macroscopically determined value of 4.836g/cm^3, implying a better than 98.7 % density for the specimen. The density values also compare very well with the mean value stated in the CRC Materials Handbook [5.49]. The theoretical density of 4.901 g/cm^3 determined by Erhlich [5.25] based on a measured lattice parameter of 4.32 Å agrees closely with the computed value of x-ray density.

5.3.2 High temperature SBS measurements and analysis

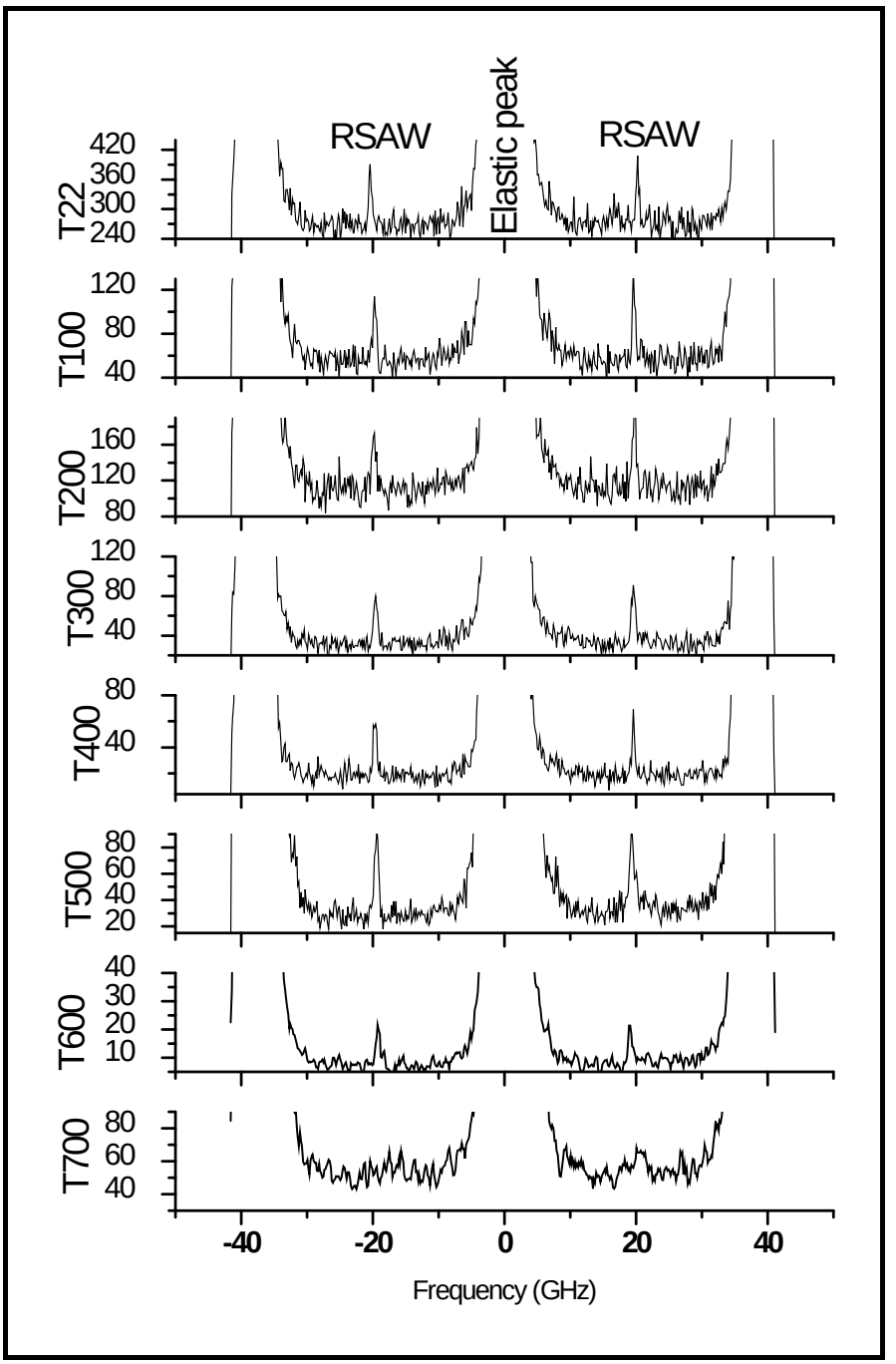

Figure 38: Plot of high temperature results for TiC showing the anti-Stokes Rayleigh SAW as the only experimentally observable mode, note the scale on the vertical axis which shows the decrease in peak intensity as temperature approaches 700 ^{o}C due to surface deterioration. Temperatures are indicated as follows: T100 = 100^{o}C etc.

Following the approach of Kueny and Grimsditch [5.34] where careful consideration is paid to the Rayleigh mode as the only available SAW (figure 38), and the relationship between elastic constants C_{11} and C_{12} expressed through the Poisson's ratio; it was necessary to assume a value for the Poisson's ratio for the $TiC_{0.97}$ bulk sample based on considerations of samples of similar composition and of close or similar configuration reported in literature and then deduce the elastic constants. Of note here, is that Poisson's ratio, defined as the lateral contraction per unit breadth divided by the longitudinal extension per unit length in simple tension, provides more information about the character of the bonding forces than any of the other elastic coefficients.

Török et al. [5.12] reported a Young's modulus value of 456 GPa for a film of almost stoichiometric composition, while Chang et al. [5.35] reported for a sintered bulk sample of zero porosity, Poisson's ratio of 0.17, and [C]/[Ti] composition of 0.91, for which they found the Young's modulus to be 438 GPa. The CRC Materials Science and Engineering Handbook (page 537) gives a narrow range for Poisson ratio of 0.187-0.189 for bulk TiC ceramics used for MEMS with a density range 4920 – 4938 kg/m^3, without specifying the porosities. Speck et al. [5.36] investigated the temperature and porosity dependence of the Young's modulus and the Poisson's ratio for $NbC_{0.97}$, and observed that with increasing temperature up to 800^{o}C, *E* starts to decrease in contrast to Poisson ratio for which they did not observe any significant temperature dependence. Porosity gives rise to increased brittleness since the pores act as crack nuclei at low temperatures and restrict grain boundary sliding at high temperatures. For the TiC_x sample we used the approximate Poisson ratio of 0.19 in view of the almost perfect stoichiometry and low concentration of vacancies and the high content of bonded carbon which is an indication of strength and hardness in refractory carbides [5.4, 5.7].

According to Kueny and Grimsditch [5.34] using a variation to the Viktorov relation, which is an approximate relation between transverse velocity and Rayleigh velocity (V_R) valid for an isotropic medium such that;

$$V_R = \left[1 - \frac{0.13}{(1 + 2c_{12}/c_{11})}\right] V_T \quad \text{.....(5-2)}$$

It is then simple to calculate the longitudinal acoustic elastic constant (C_{11}) with input values of the Poisson ratio and the independently measured Rayleigh velocity (see Table 5.1 below), which then allows for the computation of the two elastic moduli (*E*, *B*) and thereafter plotting them as a function of temperature as shown in figure 38. The linear thermal expansion coefficient, (9.9-1.4× [**C**]/[**C**+**N**]) × 10^{-6} K^{-1} (valid for the temperature range 273 to 1600 K, where [**C**]/[**C**+**N**] is the carbon/mettaloid ratio) used to adjust the density as a function of temperature was obtained from reference [5.48].

For an isotropic body, $\frac{c_{11}}{c_{12}} = \frac{(1-v)}{v}$, where *v* is Poisson's ratio which is assumed to be reasonably unchanged over this temperature range [5.36]. The shear modulus and density are related by $G = \rho V_T^2$, and *E* is related to *v* by the expression

$$G = \frac{E}{2(1+\nu)} \quad \text{.....(5-3)}$$

which is valid for isotropic materials. It has been shown by Gillman [5.7] that there is a dependence of microhardness on the elastic constant C_{44} in a group of materials of similar structure. This appears to be obeyed in carbides with the microhardness generally decreasing with C_{44}.

From figure 39, an approximately 20 GPa drop in the elastic moduli is observed when the sample is heated from ambient to 100^{o}C which is thought to be associated with remnant sintering, comprised of remnants of undissolved TiC [5.29]. Thereafter the *E* -moduli and *B*-moduli exhibit quasi-linear decrease with temperature associated with thermally-induced volume expansion described in Chapter 2. Beyond about 500^{o} C, the viscous flow of grain boundaries is thought to also contribute to the anomalous decrease in *E* and *B*. Similar behaviour has been observed for $NbC_{0.97}$ (with less than 5 % porosity) [7] and in tantalum carbide [5.39].

[7] Porosity here refers to cavities or pores in a prepared specimen which can act as crack nuclei at low temperatures and restrict grain boundary sliding at high temperatures; to be contrasted with vacancy concentration.

Table 5.1: Temperature dependence of the transverse and longitudinal acoustic elastic constants used to calculate the elastic moduli in figure 39.

Temp (^{o}C)	**C_{44} (GPa)**	**C_{11} (GPa)**
23	187	489
100	173	452
200	175	457
300	172	450
400	172	450
500	169	442
600	162	423
700	147	384

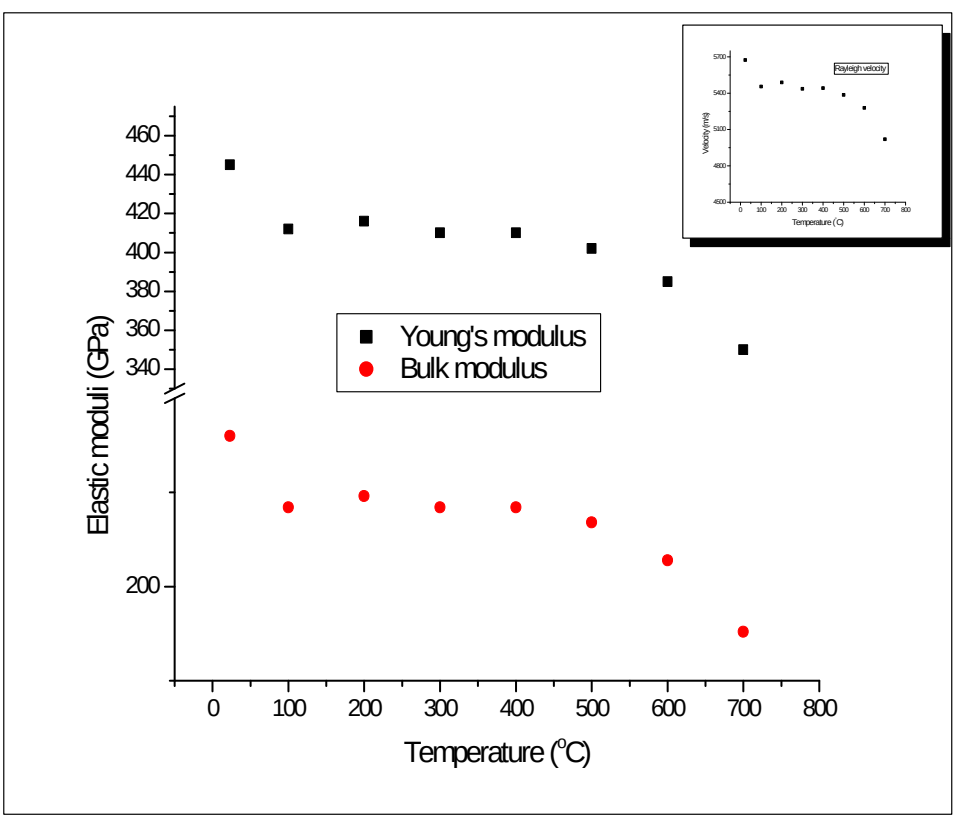

Figure 39: Plot of the variation of the Young's modulus *E*, and bulk modulus *B* of $TiC_{0.97}$ with temperature showing the characteristic linear expansion up to 450^{o} followed by an anomalous steep decrease. Higher order terms need to be added to the simple quasi- harmonic theory in section 2.3 in order to reproduce this non-linearity. The inset shows a similar temperature profile for the RSAW.

5.4 SBS investigation of elasticity of bulk polycrystalline TiC_xN_{1-x} alloy as a function of temperature.

Introduction:

Refractory carbides, nitrides and carbonitrides of the Group IV transition metals are used as the hard phase in sintered cermet alloys and for protective layers on hard metals. The mechanical characteristics of hard constituents critically influence the performance of composites because they are subjected to loads not just at ambient conditions but also elevated temperatures and pressure. The response of their elastic properties to load and temperature cycling is important in applications and engineering design. However, it is also important to recognise that there is very little experimental information on the carbonitrides for one to do comparisons adequately. The difficulty in preparing nominally stoichiometric specimens and controlling the density as well as inadequate characterization of specimens does not enable enable a systematic comparison of data. In this investigation it is intended that elastic moduli will be determined on a well-characterised specimen at ambient as well as higher temperatures.

5.4.1 XRD investigation and stoichiometry determination

A TiCN specimen approximately 4×4×2 mm^3 was analysed for the variation of elastic properties as a function of temperature up to 700^o C. Laue x-ray analysis did not reveal any obvious preferred orientation implying good homogeneity of particulates. Analysis of XRD data (figure 40) obtained at room temperature using a Philips PW1050 diffractometer system (Cu Kα) radiation (40kV, 20mA) confirmed the NaCl/tetragonal structure and the lattice spacing was measured to be 4.270 Å. This value compares very well with results reported by Ivanov et al. [5.41] of 4.276 Å for a sample with composition $TiC_{0.41}N_{0.50}$. Also, the lattice parameters of TiC and TiN are 4.332 and 4.261 Å respectively [5.40] and so the measured value lies within the two limits though being closer to the value for TiN, which signifies that the sample has high nitrogen content. The x-ray density is calculated to be 4.73g/cm^3 which compares very well with the macroscopically determined value of 4.73g/cm^3 (±0.15 or 3%) indicating a practically zero porosity. From the shift of the *d*-value of {200} peak (2.138 Å), the carbon concentration [5.22] is estimated to be x ~ 0.4 so that the sample's composition is stated

as $TiC_{0.4}N_{0.60}$. The peak positions for TiCN shown in fig 40 lie between those for pure TiC and TiN JCPDS powder diffractograms, and it is important to note the these three alloys (TiN, TiC and TiCN) have very similar diffractograms and their peak positions lie very close to each other. TiC peaks appear on the low angle side e.g at $2\theta = 36.5^{o}$ for [111] reflection. The peak due to [220] reflections occur at $2\theta = 61.5^{o}$ for TiCN in this sample. Al reflections originate from the aluminium sample holder used.

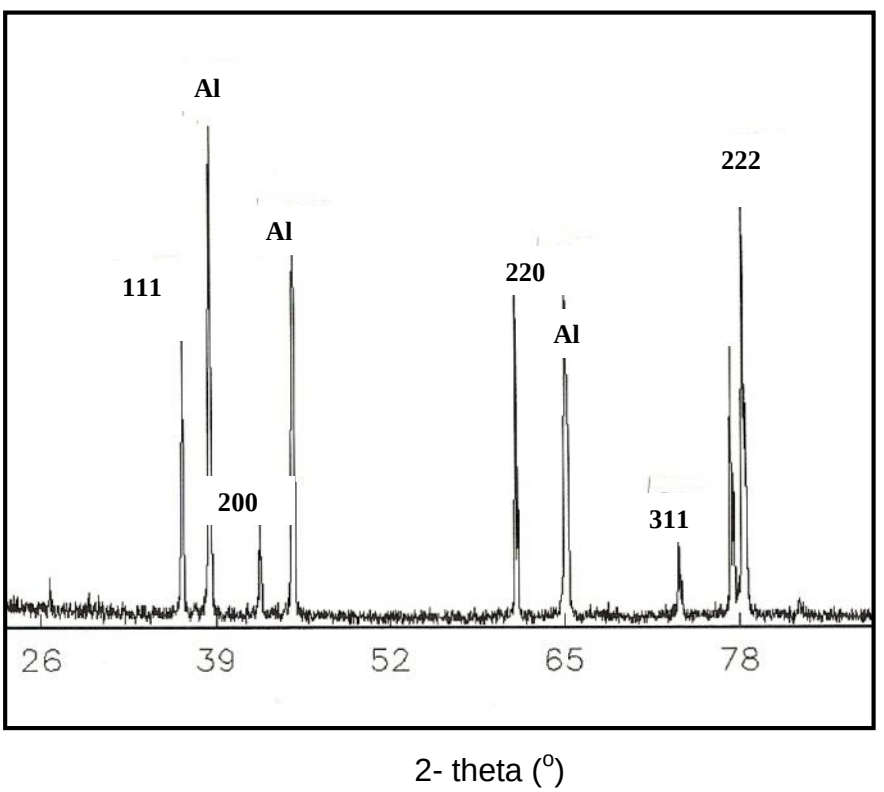

Figure 40: X-ray diffractogram for TiCN sample measured using Cu radiation (1.542 Å).

5.4.1.1 Structure refinement of TiCN

Levi et al. [5.42], using Rietveld refinement analysis on theoretical TiCN samples of different stoichiometry, observed no ordering/disordering tendencies for the non-metallic lattice of TiCN from which they then concluded that TiCN structure can be best described as based on the TiN structure with occupation of N-sites by C resulting in an f.c.c or tetragonal structure depending on how the substitution takes place. They also noted that a very low concentration of vacancies (< 2%) can be present in this sub-lattice. Thus following this analysis, a good agreement is obtained between the simulated XRD

pattern by Levi (Model II) and the experimental spectrograph when considering the lattice parameters as well as peak positions and the low vacancy concentration deduced from density measurements.

5.4.2 SBS high temperature investigation

To conduct the high temperature measurements in the optical furnace, a decision was made to follow the same approach as in the case of TiC, and observe the Raleigh mode as a function of temperature as shown in figures 41 and 42. The sample was mounted in the special high temperature furnace where the temperature was increased uniformly at 14.6 ^{o}C per minute using steps of 100^{o} C. A typical SBS spectrum recorded at 500^{o}C is shown in figure 41, showing the intense Rayleigh SAW at about 20 GHz.

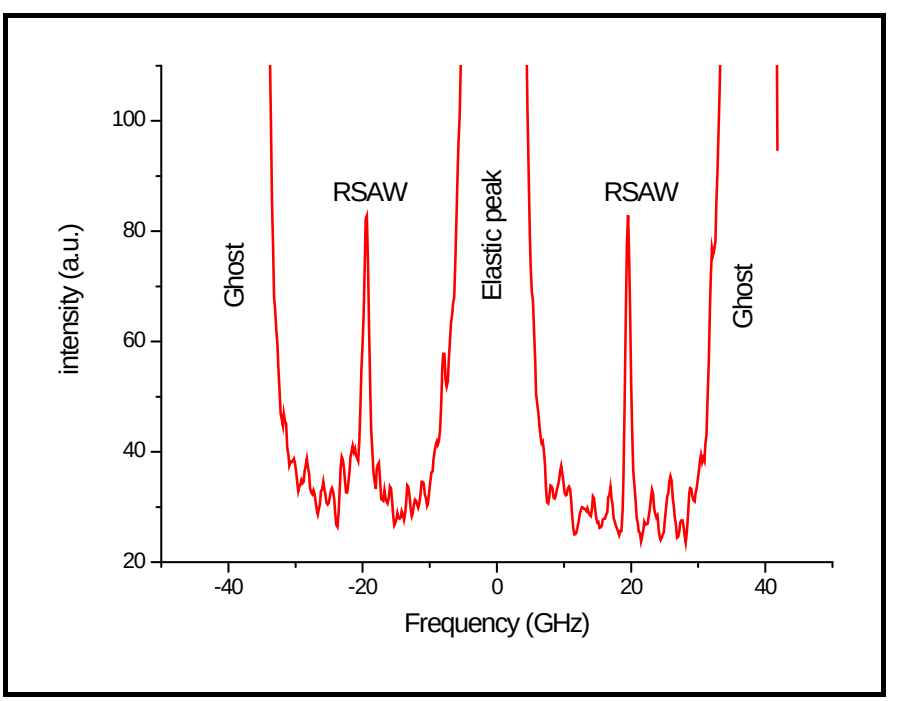

Figure 41: A SBS spectrum recorded at 500^{o}C for $TiC_{0.4}N_{0.6}$ collected at incidence angle 70.9^{o} showing the sharp and intense Brillouin peak.

It is to be appreciated that these refractory materials are highly scattering (more intense than aluminium) and therefore one has of necessity compromise on the laser power viz spectrum accumulation times (and lifetime of detector). It was not possible to observe unambiguously the Lamb shoulder under the circumstances due to the intense

background noise, let alone observe any additional modes conclusively as a function of temperature. Secondly, the optical furnace has a major limitation in that the angle of incidence cannot be varied, therefore such dispersion analysis could not be conducted at temperature. A new furnace has thus been designed to overcome this limitation and provide more flexibility and superior overall performance (see section 3.3.1). In figure 42 below, the RSAW is observed to gradually shift to lower frequencies as the sample is heated and beyond 600^{o} C the intensity of the peaks is observed to decrease. This is caused by the sample surface deterioration as a result of the molybdeum heating coil outgassing and depositing on the sample. Thus the spectra observed at 700^{o} C and beyond is treated with caution.

5.4.2.1 Analysis of high temperature SBS data

Ivanov et al. [5.41] prepared TiCN samples of different stoichiometry from powders which were hot-pressed and sintered at high temperatures under an inert gas, with an objective of investigating the influence of the [C]/[N] ratio on the elastic properties of the Ti-C-N system. For their carbonitride sample with a stoichiometry $TiC_{0.41}N_{0.5}$ they measured the porosity to be 12.2 %, the Poisson ratio 0.212, and they determined the Young's modulus to be 410 GPa at room temperature using ultrasound techniques. While for another specimen $TiC_{0.4}N_{0.60}$ with a 3.3% porosity, the *E* value was measured to be 459 GPa and a Poisson's ratio of 0.178. The specimen under investigation in this report was prepared in Vienna, Austria by hot pressing isostatically the constituent powders at high temperatures. Using the Rayleigh velocity obtained from the SBS measurements in figure 42 together with the estimated Poisson's ratio of 0.17 (based on considerations of similar specimen as highlighted in the paragraph), the Kueny and Grimsditch [5.34] relation (equation 5.2) was used as was done in the study of TiC, from which the C_{11} elastic constant was determined; this process was repeated at each temperature set-point to give the plot in figure 43.

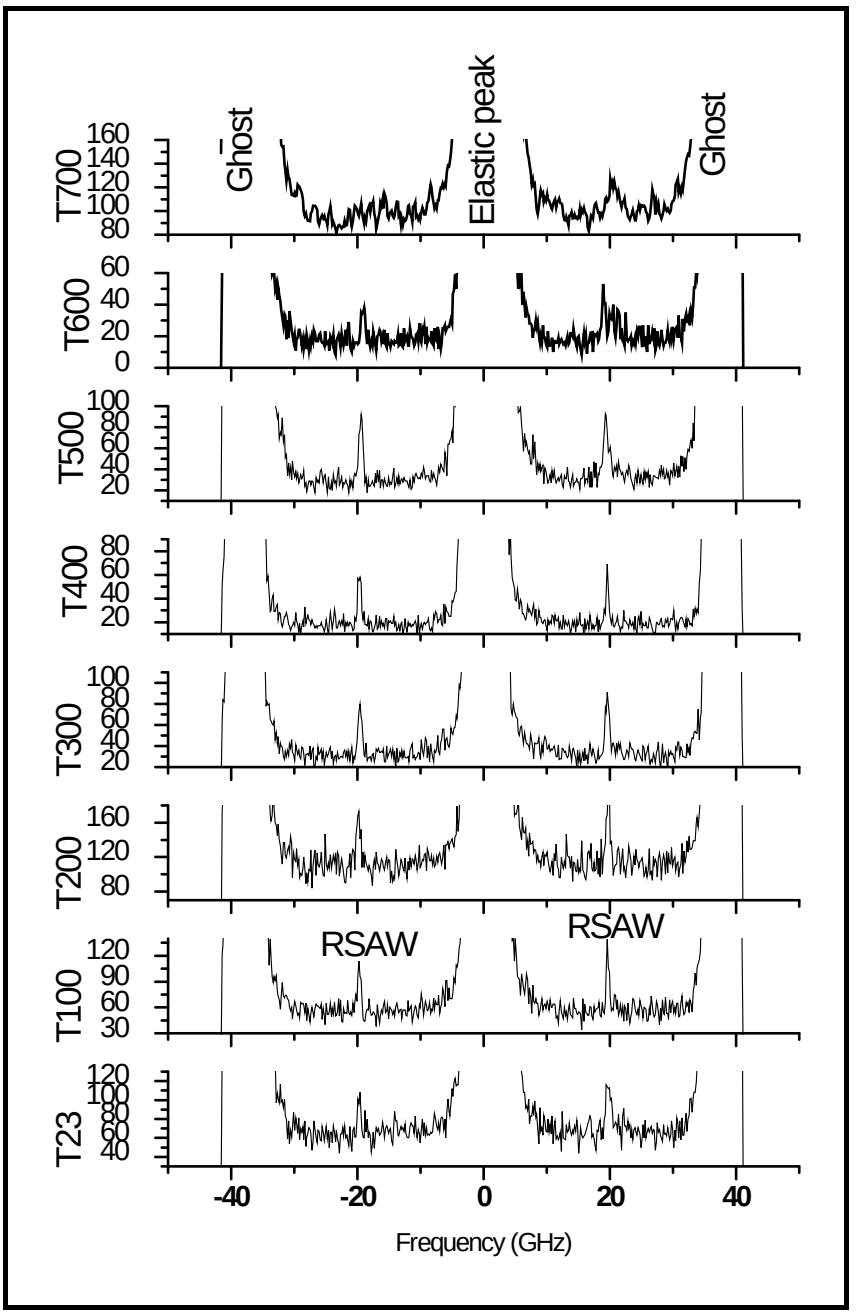

Figure 42 : Red shift of the RSAW peak for TiCN as the temperature is increased to 600^{o} C where the peak intensity is reduced due to surface deterioration. Temperatures are indicated as follows: T100 = 100^{o}C etc.

As shown in figure 42, the RSAW peaks undergo a gradual decrease in frequency from 20.7 GHz to 18.4 GHz as temperature is increased to 600^{o} C. At 700^{o} C, the spectrum is too noisy for the accurate determination of the RSAW frequency.

Table 5.2: Temperature dependence of elastic constants C_{11} and C_{44} for TiCN

Temp (^{o}C)	**C_{44} (GPa)**	**C_{11} (GPa)**
22	198	517
100	198	517
200	199	520
300	194	507
400	196	512
500	190	496
600	185	483

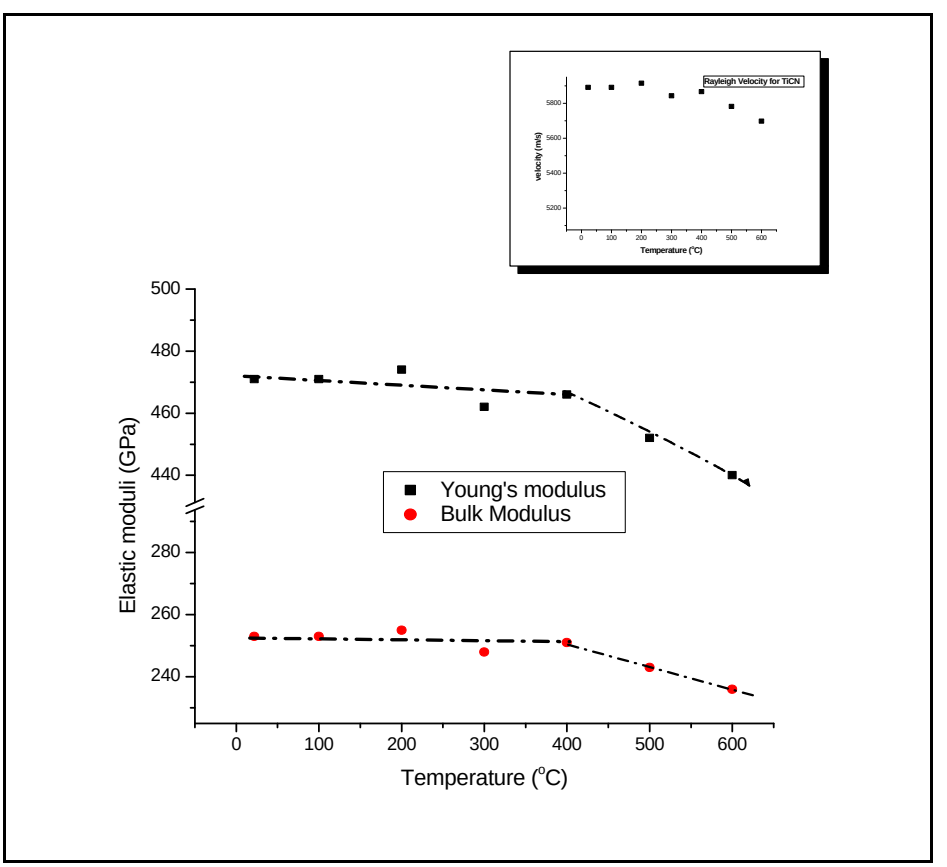

Figure 43: Plot of the variation of the Young's and Bulk moduli with temperature showing the gradual decrease of the moduli. In the inset is shown the evolution of the RSAW for TiCN as a function of temperature, which follows the same profile as *E* and *B*.

The room temperature elastic moduli values agree reasonably well with, albeit, taking cognisance of the differing porosity values, the work by Ivanov et al. [5.41], for the composition $TiC_{0.40}N_{0.60}$ which had a porosity of 3.3% and a Young's modulus of 459

GPa [5.41, 5.43], ultrasonically measured. These results (470 GPa) compare very well with other reported results in literature (459 GPa) while the additional strength in this sample can be attributed to the smaller porosity. The fact that by observing RSAW measured using SBS, enabled the extraction of elastic constants and the computation of appropriate engineering moduli as a function of temperature (figure 43), provides further proof that SBS has a great potential in high temperature materials investigations. Table 5.2 above gives the values of the elastic constants as a function of temperature.

5.4.2.2 Complex atomic interactions in TiCN

In nonstoichiometric refractory compounds it is often necessary to recognise the complex nature of metal-metal interactions in order to distinguish between screened and unscreened M-M bonds. Unscreened M-M bonds appear due to the presence of vacancies in the metalloid sublattice of the titanium carbonitrides [5.41]. As the nitrogen concentration increases, implying increased number of electrons in M-M bonds, the unscreened M-M interactions possibly cause a redistribution of vacancies in the metalloid sublattice giving rise to short-range order in their arrangement. This could then be associated with increase in atomic interactions, hence an increase in moduli of elasticity. Jhi and Ihm [5.40] while working on the structural stability of the TiC_xN_y alloys using *ab initio* pseudopotential total method, predicted an increase of the bulk modulus as the nitrogen content increases, a statement that is confirmed by the SBS measurements for the present sample relative to work by Ivanov [5.41], in as much as comparison with the earlier results of $TiC_{0.97}$ confirms the influence of nitrogen. It is important to recall that in the case of metals, conduction electrons also contribute to the quadratic term (in T) to the free energy, and hence the observed deviation at high temperatures for TiCN. For 'regular metals' at normal temperatures, the normalised temperature $\tau > 0.03$ (defined as $\tau = T/\theta_D$, θ_D is the characteristic Debye temperature) will result in an almost linear relation to the free energy, ΔF_e, hence specific heat, defined for the first order anharmonic correction of the Mie-Gruneisen approach [5.44].

5.4.2.3 Summary and conclusions

The complexities of studying elastic behaviour of bulk, isotropic specimens are evident, the room temperature elastic constants for TiCN, namely C_{11} = 580 GPa and C_{44} = 220 GPa compare favourably with computed results by Jhi et al. [5.43] for $TiC_{0.75}N_{0.25}$ where they reported the following elastic constants: C_{11} = 553 GPa, C_{44} = 189 GPa and C_{12} = 128 GPa. It is to be noted that the present results for the elastic constants lie mid-way the range $TiC_{0.5}N_{0.5}$ < (*E*,*B*) < $TiC_{0.25}N_{0.75}$, where each of the two alloy compositions represent upper and lower extremes for the reported elastic constants respectively. This conclusion is appreciated more in light of the very low measured porosity of the specimen, which is an indication of increased strength. The sample used in this study had a stoichiometry of $TiC_{0.4}N_{0.6}$ as reported in section 5.4.1 which would mean that theoretically the elastic constants of the specimen should lie closer to those of $TiC_{0.5}N_{0.5}$ and so factoring-in the very small porosity (< 1%), it can be confidently stated that the room temperature elastic constants for isotropic/homogeneous compound $TiC_{0.4}N_{0.6}$ are C_{11} = 580 GPa, C_{44} = 220 GPa for an independently measured density of 4.73 g/cm^3.

As pointed out in section 5.4.2.1 the elastic moduli (*E*,*B*) obtained for these refractory alloys agree quite closely with the few reported values obtained using the ultrasonic technique as well as computationally determined results, as indeed do the Poisson's ratios. This observation is important in asserting SBS as a useful technique even for bulk untextured/polycrystalline specimens which are the more frequently encountered systems in real engineering applications and coatings. A more profound result is the observation that the elastic moduli of $TiC_{0.97}$ and $TiC_{0.4}N_{0.6}$ do not exhibit quasi-linear behaviour predicted by classical quasi-harmonic theory as the temperature increases, but have significant curvature, especially for TiC. These experimental results point to the fact that the intrinsic phonon-phonon interaction and electronic effects contribute to the total anharmonicity which is normally neglected by the classical quasi-harmonic approximation. These effects become prominent at even moderate temperatures of 400^o C for TiCN. The slight increase observed at about 200^{o}C for TiCN is attributed to experimental scatter as it is not significant to be associated with any physical processes. Additionally, the sharp decline in the Young's and Bulk moduli at the highest

temperatures in both specimen may not be due to anharmonic effects alone, but could be the result of some form of structural change, although this awaits further study. These high temperature results obtained for the first time using SBS technique are of immense technological value as they enable more accurate numerical modelling of the composite and cermet systems used in the hardmetal industry by providing the experimental data for fitting interatomic potential parameters.

As an aside, clearly, with only one SAW available for use to determine two unknowns, the technique suffers a handicap; to remove the ambiguity introduced by assigning a value for Poisson's ratio as was done in this report, it is proposed that the native oxide film present in such systems be explored with a view to use it in a film-on-a substrate system exploiting the known elastic constants of the film (see comments in Chapter 8).

Finally, Surface Brillouin spectroscopy (SBS) is once again confirmed as an elegant material characterization technique for studying elastic behaviour of materials in various structural configurations and phases.

In the next chapter, an SBS investigation on the hard ceramic boron carbide reveals the presence of organ-pipe modes in addition to the normal SAWs, which have been observed only for the second time. In this report a reasonably successful attempt to use organ-pipe modes to obtain elastic constants of a film as a function of temperature will be discussed and contrasted with a parallel measurement using SAWs, from which an interesting phase transformation is observed using SBS for the first time.

Chapter 6

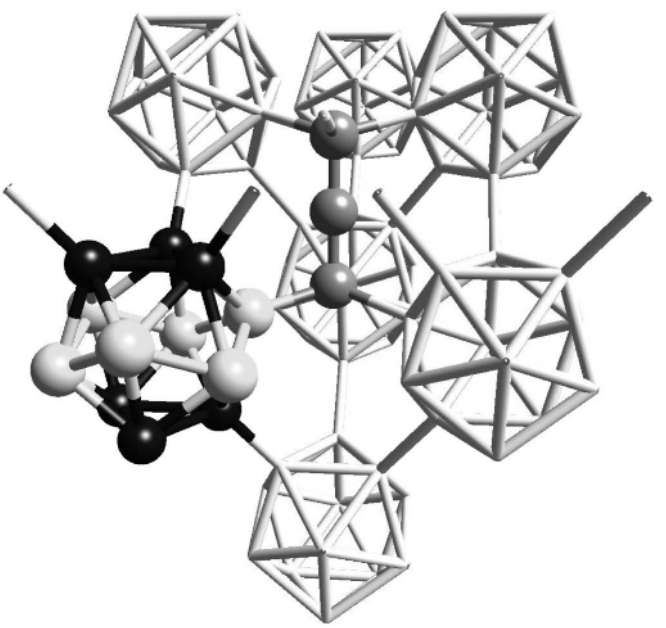

6 Boron Carbide

[8]The Atomic Structure of B_4C.

[8] The black atoms are on the so-called polar sites, bonded to neighbouring icosahedra. The white atoms form a puckered hexagon and are in equatorial sites. The grey atoms form the chain, to which the equatorial atoms are bonded.

6.1 High temperature surface Brillouin scattering study of an amorphous boron carbide film

Introduction

Boron carbide belongs to a technologically important group of hard covalent ceramics, e.g. SiC, Si_3N_4, and diamond. Interestingly, the study of brittle materials and their dynamic response results mainly originate from interest in their possible use as armour materials or as engine turbine blades. The foundations of the field were set by a range of workers [6.1 – 6.3] who showed that these ceramics exhibited high dynamic compressive strengths [6.2]. The drive to investigate boron carbides stems from their low density and high compressive strength and more recently there has been considerable interest because of their potential applications as high-temperature semiconductors [6.3]. In addition, boron carbide exhibits many other attractive properties, such as low specific weight and high hardness, even surpassing diamond and cubic boron nitride at temperatures over 1100 ^{o}C [6.4]. Moreover, it presents high melting point (2450 ^{o}C) and modulus of elasticity as well as a great resistance to chemical attack.

Rhombohedral boron carbide, usually denoted as B_4C (the correct composition is $B_{4.3}C$) since its composition was established by Ridgeway in 1934 [6.5], is the most stable in the boron-carbon system and exists as a single-phase material over a wide range of solubility, generally accepted to be from 9 to about 20 at% C. The variable carbon content is accommodated by the C and B atoms partially substituting for each other in both the icosahedra and the chains. The most widely accepted model for the B_4C structure considers $B_{11}C$ 12 –atom icosahedra clusters directly linked by covalent bonds [6.3] and indirectly linked by a C-B-C and C-B-B 3-atom chains (see figure 44). Even the ideal B_4C structure with $B_{11}C$ icosahedra and C-B-C chains, is disordered due to the location of carbon atoms among different icosahedral sites. Manifestations of this disorder and its progression have become more evident in many physical properties [6.1] including those addressed in this report as the quality of the samples improves.

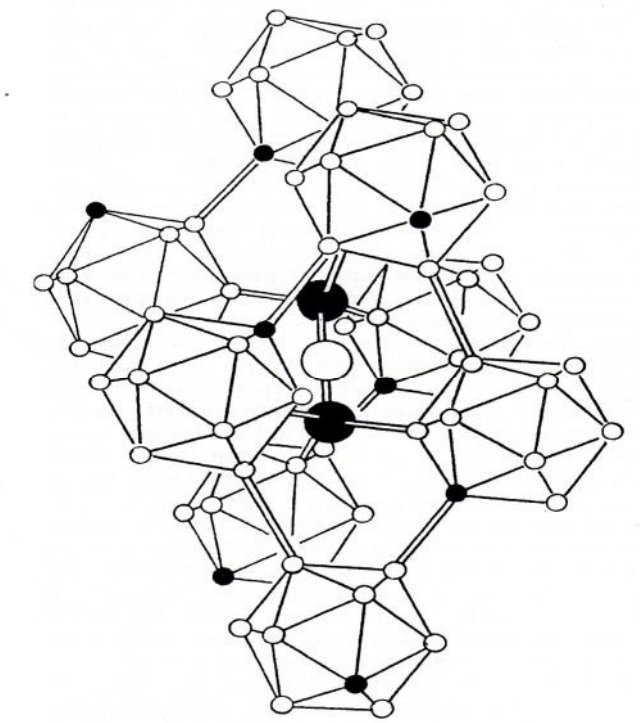

Figure 44: The structure of boron carbides showing the icosahedra and connecting 3- atom chains. Solid circles represent C-sites for B_4C. Size of the chain atoms has been exaggerated [6.3]

Of late, much effort has been paid to the realisation of superhardness in (nano) composite coatings. However, it is important to point out that a coating with superhardness alone is not enough for industrial applications. Good mechanical properties of a coating also require high toughness, low friction, high adhesion with the substrate, good load support capability, etc. Also if the hardness of the coating is near or even greater than diamond, it certainly will bring quite a lot of confusion and difficulties in hardness determination and interpretation since most indenter tips are made from diamond. Therefore, at present nanoindentation testing is still regarded as a good method by most researchers in hardness determination of thin films and coatings, even though the microhardness tester is also frequently applied as well [6.6, 6.7]. In nanoindentation testing, a diamond indenter is forced into the surface with the load displacement curve and depth of indentation recorded, from which the hardness and elastic properties are calculated. However, many issues remain unresolved e.g. several models or methods exist for hardness calculation from loading and unloading curves in nanoindentation such as Oliver and Pharr method

[6.7,6.8], the deformation method [6.9], etc.; hence the technique will always be subject to the indeterminacy derived from the criterion used to select one method over the others.

In this report, experimental results of the mechanical properties of a hard film at ambient and high temperature are presented using the technique of SBS without assuming any fundamental parameters such as Poisson's ratio, or using an indenter or any contact with the film. Using SBS it is also demonstrated that it is feasible to follow phase transformations within thin hard films to a reasonable accuracy. Through this report it will be demonstrated that SBS does have a great potential for characterising superhard coatings and films and can even resolve the problem of use of indenters for the superhard and ultrahard materials, by measuring independently the actual elastic constants, and Poisson's ratio, from which hardness can be inferred through use of existing models.

Motivation for the study

Nanostructured coatings have recently attracted increasing interest because of the possibilities of synthesizing materials with unique physico-chemical properties. Highly sophisticated surface related properties, such as optical, magnetic, electronic, catalytic, mechanical, chemical and tribological properties can be obtained by use of advanced nanostructured coatings [6.10]. Nanocomposite coatings have been investigated that comprise at least two phases, one being nanocrystalline and the other being an amorphous phase, or sometimes both phases of the constituent materials are nanocrystalline [6.11, 6.12], with successful examples of the latter being TiN-TiB_2 and other carbide/boride systems. Another popular design method is to embed nanocrystalline phases in an amorphous phase matrix where diamond-like carbon (DLC), amorphous carbon nitride and other hard amorphous materials (with high hardness and elastic modulus) have given promising results [6.13] when used as amorphous matrix while nano-sized refractory nitrides (AlN, BN, TiN) are employed as strengthening phases [6.14,6.15]. These materials exhibit hardness significantly exceeding that given by the rule of mixtures. By convention, hard materials usually refer to materials with hardness greater than 20 GPa. Materials with hardness above 40 GPa are classified as superhard, and those with

hardness above 80 GPa are often called ultrahard materials. Nanocomposite coatings can be hard, superhard or even ultrahard, depending on coating design and application.

Magnetron sputtering [6.17, 6.18] is the preferred deposition process as it can be tailored to achieve films with controlled texture and crystallite size. A minimum temperature is generally required to promote growth of crystalline phase with crystallites having dimensions of a few nm as designed, and/or to allow a sufficient diffusion within the segregating system. A relatively low deposition temperature is also necessary to prevent substrate distortion and loss of mechanical properties. In general, the choice of specific deposition conditions is determined by consideration of such factors as coating applications, desired coating properties, cost, and temperature limitation of the substrate used. With this background, it is also known that nano-crystalline B_4C films can be deposited under the same conditions as the amorphous films but at higher substrate temperatures of about 400^oC [6.19, 6.20]. This implies therefore that 400^oC can be regarded as the lower limit for a possible phase transition occurring in the amorphous films. In a controlled process, ideally one can produce a unique composite of nano-B_4C supported in a amorphous boron carbide matrix with interesting elastic properties. However, in this report, the first aim was to investigate and present experimental results on the variation of the elasticity with temperature, of an amorphous boron carbide film deposited on crystalline silicon substrate using surface Brillouin scattering spectroscopy, and secondly, within the same experiment, seek to observe the phase transition in the film which would give an indication of the potential qualities that a nano-B_4C/amorphous B_4C composite holds. Within the same experiment it would in principle be possible to determine the mechanical properties of the film as function of temperature and possibly infer on changes to the hardness as the temperature is increased.

Sample Preparation and experimental conditions:

The samples were supplied by Dr. T. Wittkowski of the University of Kaiserslautern in Germany. The amorphous films were deposited at room temperature on crystalline silicon and the density reported as 2.0 g/cm^3 [6.20] for the 2.0 micron thick boron carbide film.

The samples were thoroughly cleaned with alcohol and acetone before mounting on sample holders for dispersion measurements and in-furnace measurements. The SBS measurements were performed in backscattering initially at ambient temperature for the dispersion analysis using approximately 55 - 80 mW (measured on the sample) *p*-polarised 514.5 nm radiation. Later high-temperature measurements were conducted using the same backscattering configuration with the sample mounted in the special high-temperature furnace. The sample was gradually heated at a rate of 14.7^{o} C per minute to about 85% of the set-point; thereafter the heating rate was reduced to 2.3^{o} C per minute until set-point was reached. Intervals of 50^{o} C were used from ambient temperature to 500^{o} C, thereafter 100 ^{o} C intervals were used until 700^{o} C. The FSR of the inteferometer was set at 60GHz (L = 2.5mm), and scanned with an amplitude of 5.0 orders (3000 nm) for all the temperature points. In both instances the signals sampled were collected from within the finite solid angle of a *f*/2.3 collection lens.

6.1.1 SBS Dispersion analysis and organ - pipe modes

In surface Brillouin spectroscopy, dispersion analysis of films is useful as a source of additional information for one to fully characterise the films. Currently, due to the difficulties in determining Poisson's ratio for a film specimen, it is often assumed to be the same as that of bulk material, which is often not true for thin films. Hence, using the SBS technique, it is posssible to obtain the full-set of elastic constants and thus accurately determining such moduli (E, B) readily, hence the Poisson's ratio as well. The 2 micron thick, amorphous boron carbide film on a silicon substrate was mounted on a special sample holder fitted with a goniometer to enable variation of angle of incidence. The resulting dispersion profile (plot of $k_{//}d$ vs frequency of the modes) was intended to reveal useful surface, and pseudosurface modes that would enable a more accurate extraction of elastic constants of the film.

Scanning with an amplitude of between 5 and 6 on the JRS control electronics and using FSR of 60 GHz (L = 2.5 mm), the angle of incidence was varied from 30 to 71^{o} in steps of 10^{o} and spectra acquired using collection times up to 7 hours due to the weak

reflectivity of the film. Figures 45 and 46, show the experimental spectra where the Rayleigh SAW is clearly seen together with peaks of almost equal spacing occurring within the continuum as the frequency extends towards 110 GHz. These modes were later identified as organ-pipe modes and their behaviour explored using the Green's function analysis as detailed below in section 6.1.2. Four angles of incidence were used with spectra measured at 40, 50 , 60 and 71^{o} , the last angle chosen to coincide with the in-furnace conditions. Also for $\theta_i = 71^{o}$, an additional measurement was conducted scanning at much higher frequencies up to 160 GHz (figure 46).

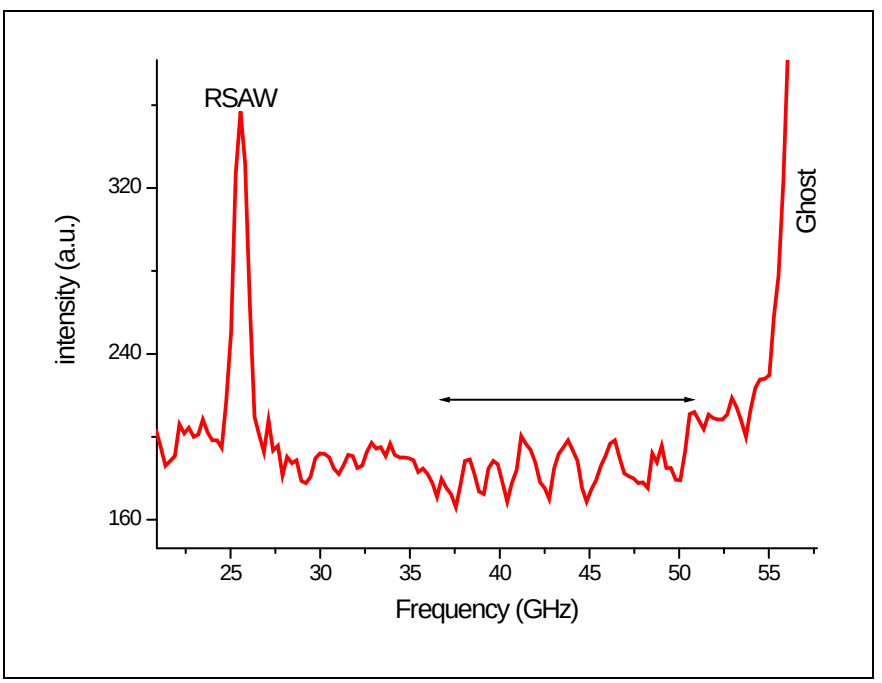

Figure 45: SBS spectrum for boron carbide film recorded with $\theta_i = 71^{o}$ showing the RSAW and organ pipe modes of spacing of about 2.4 GHz within the range 38 to 50 GHz.

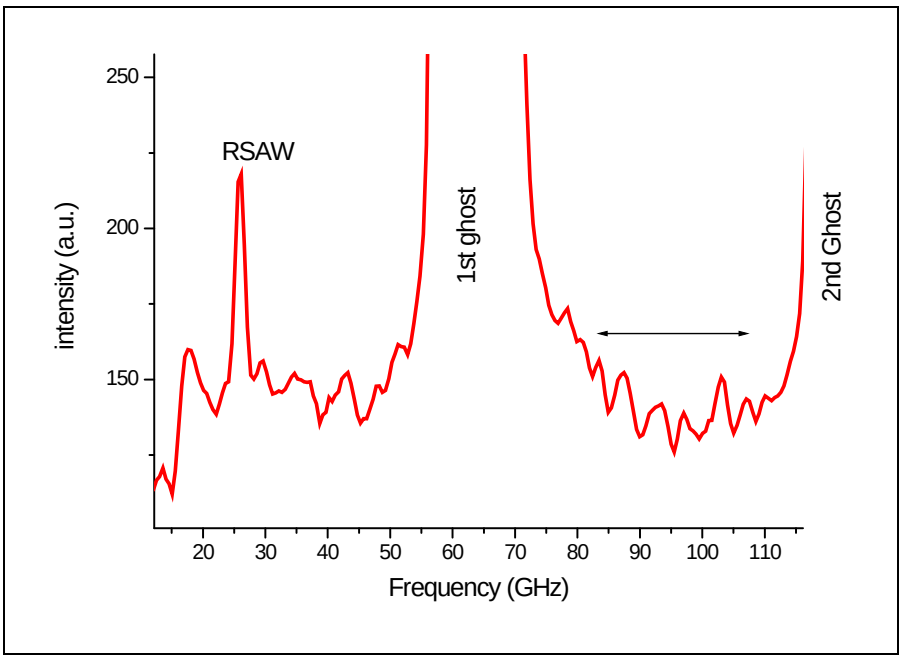

Figure 46: SBS spectrum for boron carbide showing the extended frequency range to 110 GHz where again organ pipe modes are observed with a spacing of about 3 - 4 GHz with $\Theta_i = 71^o$.

6.1.2 Green's function analysis as applied to organ - pipe modes

Organ-pipe modes were discovered many years ago at Max Planck Institute (MPISF) using helium atom scattering (HAT) measurements [6.21] on monolayer films and were subsequently given this name because their origin is the same as that of vibrations in an organ pipe. Gibson and Sibener [6.22] reported the first successful inelastic HAT measurements on epitaxial films in 1985 and since then there have been very few reported studies [6.23, 6.24, 6.28] of standing acoustic - wave excitations occurring in thin films. Standing wave excitations are generally characterized only by wave-vector components perpendicular to film surface ($q_\perp$). Due to the constrained or limited film thickness (d) and applicable boundary conditions, the allowed values for $q_\perp$ are quantized to a series of discrete values [6.23]. Such constraints on the wave-vector are in contrast to modes with finite wave-vector ($q_\parallel$) components that take on a continuum of values and describe acoustic wave excitations normally observed for SBS. It is thus notably difficult to experimentally observe the standing - wave modes for scattering angles away from nominal zero ($\theta = 0$), as finite $q_\parallel$ effects are operative and the modes become more dispersive.

Thus these observed periodic peaks are a special type of Lamb waves where the $q_{\|}$ components are essentially zero. As the scattering angle is increased, the peak widths of the low-lying modes generally remain nearly constant, a behaviour different from that observed for surface acoustic waves whose peaks generally broaden at small incidence angles. Also the finite frequencies of these modes increase with increasing θ (figure 47), a behaviour that differentiates them from Rayleigh surface waves whose frequency are proportional to $\sin\theta$ and therefore normally vanish with $\theta \to 0$.

Thus, in order to evaluate the properties of these excitations, the projected local density of states D_i was evaluated within the Green's function formalism

$$D_i(\omega^2, q, x_3) = -(\pi)^{-1} \operatorname{Im} G_{ii}(q, x_3, \omega^2) \text{ , } \ldots\ldots\ldots\

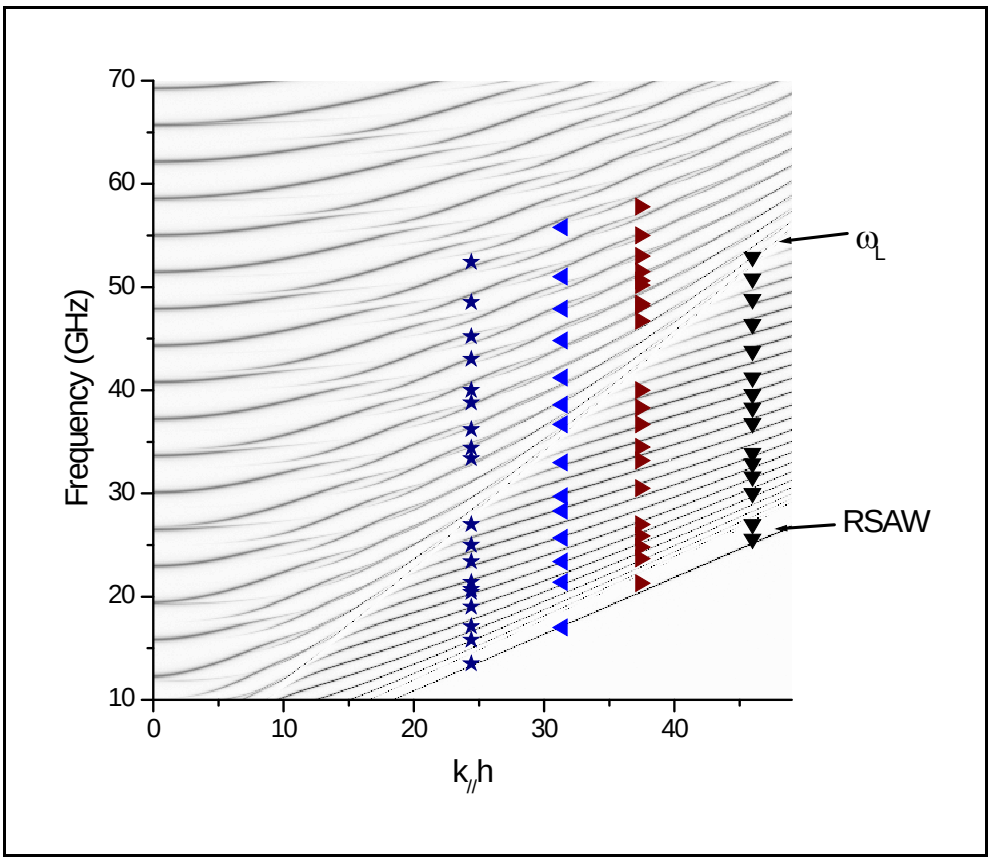

Figure 47: Grey scale image of the Green's function plot for B_4C shown together with experimental results superimposed, showing the modest agreement of the frequency spacing of the modes, albeit, with some gaps owing to the difficulty in resolving closely spaced modes for some θ_i. The best fit elastic constants were obtained as c_{11} = 396 GPa and c_{44} = 108 GPa. ω_L represents the longitudinal threshold.

The experimentally observed mode spacing in the frequency region up to about 60 GHz correlates very well with the Green's function calculated using the best-fit elastic constants c_{11} = 396 GPa, c_{44} = 108 GPa. A closer observation of figure 48 at the region $k_{//}h$~ 0 shows the presence of regularly spaced modes (~ 3.5 GHz apart), identified as standing acoustic waves, whose frequency approximates very well to that of an ideal organ-pipe. Thus, by extension, it can be inferred that for the region under experimental investigation, namely large θ_i, there also exist organ-pipe modes whose interesting characteristics are be the subject of this section.

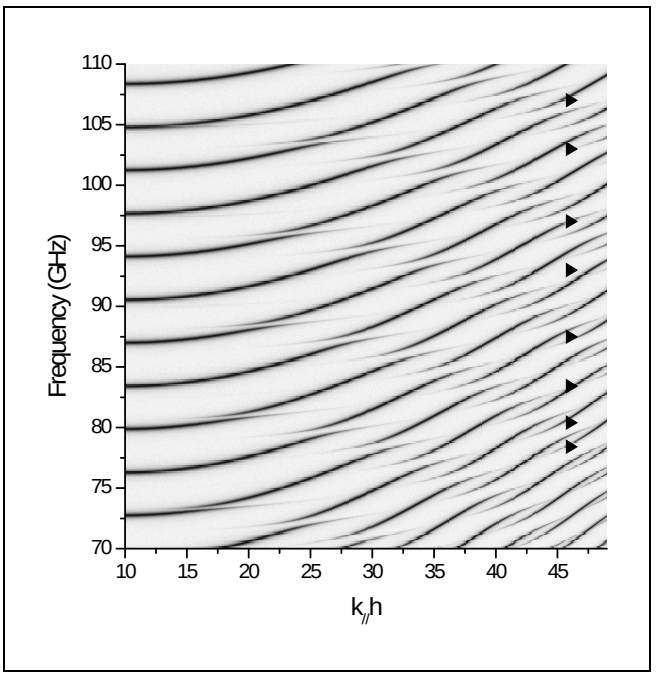

Figure 48: Green's function plot together with experimental data for the high - frequency region 70 – 110 GHz showing some degree of regularity for the organ pipe modes (experimental Δf ~ 3 - 4 GHz) for the incidence angle 71^{o}.

The Green's function dispersion in figure 48 sheds some more light on the complex nature of excitations contributing to the formation of 'organ - pipe' modes; as the frequency increases towards the normal bulk mode (TA and LA) regions for sufficiently large $k_{//}h$, it is noted that a complicated mix of both longitudinal and transverse excitations and or hybridisation [6.28] contributes to the observed dispersive spectral features. This phenomenon occuring in such thin films has not been observed before experimentally as previous workers [6.23] limited themselves to the normal incidence ($k_{//}h = 0$) region where purely longitudinal resonances are responsible for standing waves, while Link *et al*. investigated ultrathin films [6.28] where modes associated with the substrate were coupling to those of the film. It is thus significant to be able to experimentally observe standing - wave excitations at large incidence angles. Another important observation is that the frequency - spacing of the organ - pipe modes gradually increases from about 1.4 GHz to 2.6 GHz (see also figure 52), rising to about 3 - 4 GHz as the mode frequency increases towards about 150 GHz. This observation is true for the $k_{//}h$ region considered here, which lies farther from the normal incidence region.

To elucidate some more useful information from these modes it is necessary to also understand their origin. Here the vibrational spectrum of the film is dominated by resonances which originate from the presence of the interface between film and substrate. In the present case, the relative densities of the film and the silicon substrate are such that reflections of the elastic waves within the film from the interface and from the film surface, respectively, result in the formation of standing waves. These have longitudinal polarization in the direction of the surface normal, with nodes at the interface and anti-nodes at the surface in the simplest case. As boron carbide is semi-opaque, one can consider that the light scattered from the top and bottom interfaces (assumed reasonably smooth) will have similar intensities and therefore interfere. The resulting scattering profile depends on the signs of the displacement components U_3 at the two film interfaces and the associated phase difference. Hence, the only time there would be constructive interference or non-suppression of alternate peaks is when the phase difference of photons scattered from the two film interfaces were in quadrature (i.e. $4\times\pi/2$), whereas a small deviation, from quadrature will result in one set of peaks having lower intensity than the others [6.24]. The phase difference (δ) is thus estimated using the relationship of the optical path lengths, $n2d/\lambda$ (in multiples of 2π), where n is the refractive index of the film and λ is photon wavelength and d is effective film thickness.

For this amorphous B_4C film with d = 2.0 μm this phase difference having a value of 23.32 would suggest that there will be minimal suppression of alternate peaks (i.e $\delta \sim 4\times 2\pi$), notwithstanding the influence of elasto-optic scattering on the overall scattering profile which tends to modify the scattering intensities. As demonstrated in the present chapter, when the mode spacing is frequency-matched between the experimental results and the computed results for the dispersion plot, where the two elastic constants are treated as free paramaters in the computation, the reasonable agreement demonstrates that organ-pipe modes can be successfully used to extract elastic constants of a film provided some necessary conditions are met.

6.1.2.1 Analysis of the bulk LA mode and comparison with Green's function calculations.

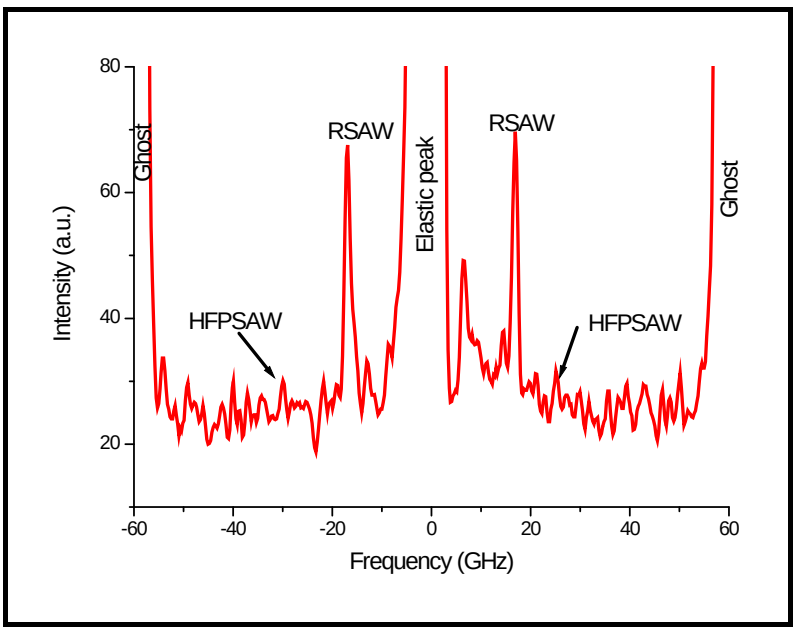

Figure 49: SBS spectrum of B_4C recorded at $\theta_i = 40^o$, L = 4mm and scan amplitude of 2.10 sufficiently large to observe the two surface modes, RSAW and HFPSAW located at 16.4 GHz and 32 GHz respectively.

In figure 49, using $\theta_i = 40^o$ and L = 4 mm, a second SAW is observed and identified as the HFPSAW by means of its sinθ behaviour with varying θ_i. This mode occuring at $\omega = \omega_L$ generally has a higher intensity than organ - pipe modes since it results from elasto-optic scattering. This mode provides an independent verification or validation of the organ-pipe modes as it provides an independent value for C_{11} as detailed below.

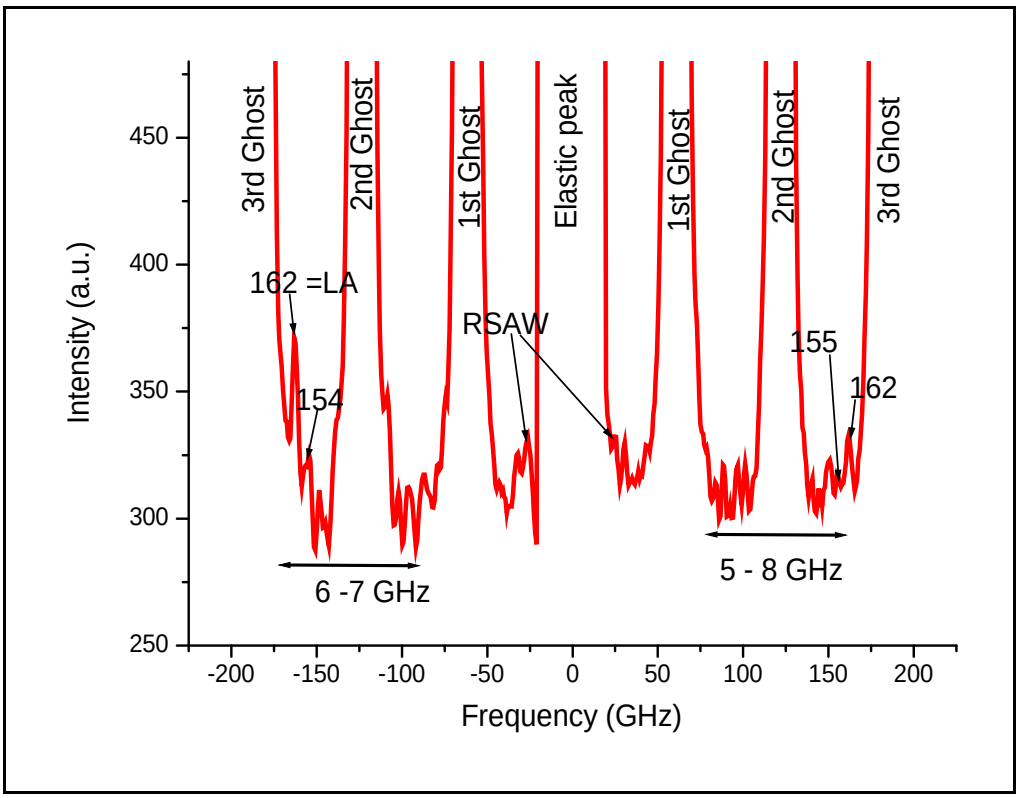

Figure 50: SBS spectrum collected by scanning across almost six orders shows the organ pipe mode at the highest frequency of 154 GHz near the LA mode (at 162 GHz). In this region the organ-pipe modes are a result of acousto-elastic mediated scattering and have higher intensity as observed in the figure. Measurement was conducted inside the furnace at $\theta_i = 71^o$ and mirror spacing L = 3 mm.

In figure 50, using using $\theta_i = 71^o$ and L = 3.0 mm, in which the scan amplitude was increased to show almost six spectral orders, it is noted that the bulk LA mode is observed at 162 GHz [6.23]. The strong peaks observed within the *vicinity* of the bulk LA mode in figures 50 and 51, are standing-wave modes mediated by elasto-optic scattering. In certain instances these modes contain double (sometimes triple) structures, similar to the ones first observed in 1972 by Sandercock [6.27] and later observed by Zhang and co-workers in 2001 [6.23]. Additional SAWs are not observable from this figure.

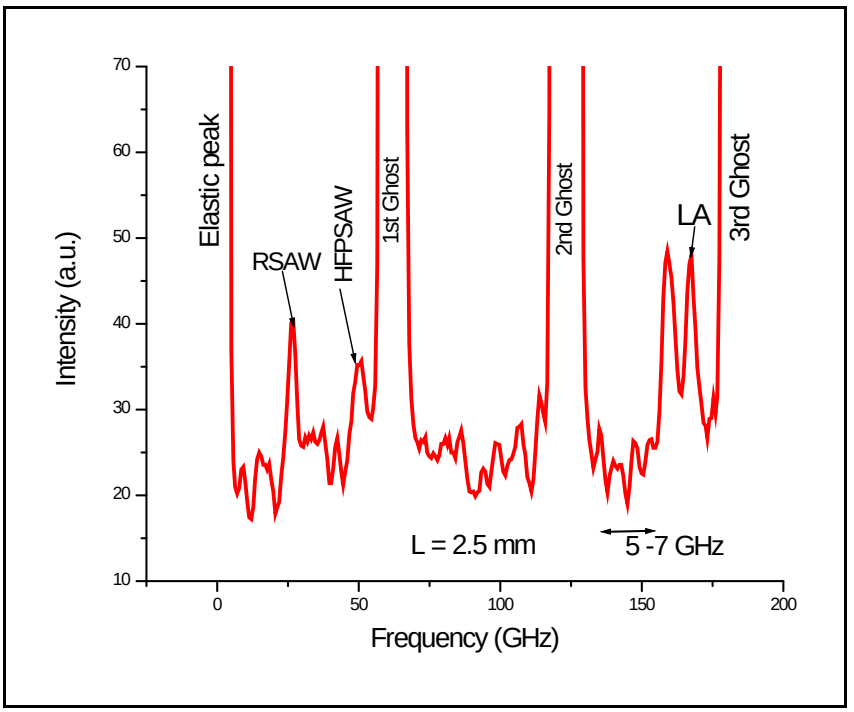

Figure 51: SBS spectrum for boron carbide film obtained using *L* = 2.5 mm showing the HFPSAW and bulk LA modes.

A further measurement was carried out using a smaller mirror spacing of L = 2.5 mm than that of figure 50 which resulted in a better resolved HFPSAW as shown in figure 51. The peaks at 26 GHz and 51 GHz, respectively, correspond to the Rayleigh mode (RSAW) and to the HFPSAW. The peaks at 26 GHz and 51 GHz, respectively, correspond to the Rayleigh mode (RSAW) and to the HFPSAW. The corresponding velocities of 7100 m/s for the RSAW and 13900m/s for the HFPSAW are in agreement with observations made in references [6.29] and [6.2].

In order to make use of the bulk modes in evaluating the corresponding bulk wave longitudinal velocity, independent refractive index measurements were conducted using reflectance measurements with the aid of a Varian Cary 500 UV-Vis-NIR spectrophotometer at 514.5 nm. From the value of the *square of absolute reflectance* obtained as 9.1, the value of the refractive index is calculated to be 3 using standard Fresnel relations used to describe reflectivity of light from a surface which depends on the angle of incidence and plane of polarisation of light [6.16]. For normal incidence, where reflection and transmission amplitude coefficients coincide for each of TE

(electric) and TM (magnetic) components of the electromagnetic wave, the reflectance is described by the expression:

$$R = \left(\frac{n_2 - n_1}{n_2 + n_1} \right)^2 \quad \text{.....(6-2)}$$

where n_1, n_2 are indices of refraction. This result does correlate with B_4C dielectric constant measurements in [6.28] from which a value of $2.4 < n < 3$ is obtained by extrapolation to a frequency of 11000 cm^{-1}.

Considering the RSAW and HFPSAW and using the Landau and Lifshitz analytical expression valid for an isotropic medium, relating the Rayleigh, longitudinal and transverse velocities as well as the density ρ [5.34], namely;

$$C_T^4 - (C_R + C_L)C_T^3 + 1.5C_R C_L C_T^2 - 0.5C_R^2 C_L C_T + \frac{1}{16} C_R^3 C_L = 0 \quad \text{.....(6-3)}$$

where $C_L = \rho V_L^2$, $C_R = \rho V_R^2$. One first solves for the actual transverse velocity V_T ~ 7260m/s, as V_L is already known. This result compares very well with the velocities obtained from Green's function approach (7300 m/s in figure 47). Further considering the bulk LA mode at 162 GHz, and relating this to the refractive index n, the velocity of the longitudinal bulk mode is obtained from the relation, $V_L = \frac{f\lambda}{2n}$ where using refractive index, n = 3.0 for the B_4C film, gives the longitudinal threshold velocity V_L (= 13700 m/s). This value again is close to the ultrasonically determined longitudinal velocity (13300 m/s) reported in [6.29] and the value (13900 m/s) obtained for the HFPSAW in figures 49 and 51.

The room temperature dispersion results for the frequency region up to 60 GHz in figure 47 are now considered. These results yielded the best-fit elastic constants as C_{11} = 396 GPa and C_{44} = 108 GPa corresponding to velocities V_L = 14100 m/s and V_T = 7300 m/s respectively, for the amorphous boron carbide film. Within the margins of experimental error (+/- 2%) there is good agreement between these results and those for the velocities obtained independently from HFPSAW and bulk LA modes as well as literature data

from ultrasonic meaurements [6.29]. One therefore can observe that the technique of using organ-pipe modes to extract elastic constants of thin films has great prospects when used in conjunction with SBS as is demonstrated by the results above. It is to be appreciated that the Green's function calculations did not incorporate the elasto-optic coefficients of boron carbide due to computational limitations and nonetheless there is reasonably good agreement in transverse and longitudinal velocity values obtained purely from SAWs, and from the ultrasonic technique [6.29].

Also worth noting is the fact that the peak spacing between neighbouring peaks/modes remains almost constant at 1.1 − 1.4 GHz up to 25 GHz (as determined by Green's function calculations in figure 52(a). But from about 32 GHz to about 50 GHz, the spacing increases gradually to 2 – 2.4 GHz which is experimentally observed in figures 44 and 52(b), providing further evidence of standing-wave excitations. The calculated anti-Stokes scattering cross section for θ_i = 40^o spectrum is illustrated in comparison to the experimental SBS spectrum in figure 52(a) and (b).

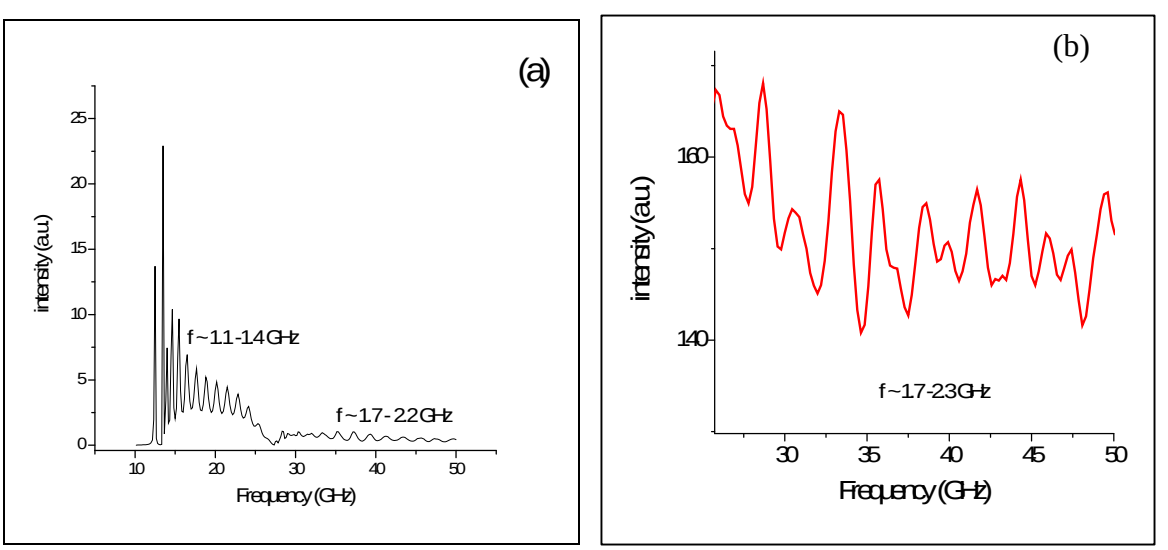

Figure 52(a): Green's function calculated spectrum for B_4C at 40^o incidence using best-fit elastic constants deduced from the dispersion data.
Figure 52(b): shows part of a SBS spectrum recorded at 40^o incidence showing well-resolved peaks within the range 30 - 50 GHz, having spacing of 1.7 - 2.3 GHz in agreement with fig 52(a).

The theoretically calculated nearest-neighbour frequency spacing δf ($\delta f = V/2d$) assuming the simple organ-pipe model (with one side closed), gives an ideal value of 1.7 GHz taking V to be the transverse velocity. For the spectral region up to 50 GHz which is dominated by transverse modes (the longitudinal component along the normal to the plane is evanescent in this region), this ideal value is reasonably close to the peak-spacing deduced from Green's function dispersion as well as the experimentally observed spacing of 1.7 - 2.4 GHz. For the spectral region extending beyond 100 GHz where the SBS spectrum is now dominated by longitudinal excitations, the ideal organ-pipe model predicts a mode-spacing of 3.5 GHz. Interestingly, for this region the spacing observed experimentally is approximately 5 - 8 GHz (figures 50 and 51) which would suggest mode suppression at first glance. However, the primary condition for mode suppression [6.24] is not met in this case, and additionally, for the lower frequency region no obvious mode suppression was observed for the same spectrum; there is no ready explanation at this moment for this anomaly in the peak-peak spacing in this region which lies close to the bulk LA mode, where the organ-pipe resonances will be stronger due to the effects of elasto-optic scattering.

6.1.2.2 Discussion of the high temperature measurements and results for the Young's modulus

These measurements were conducted by following the two modes, RSAW and HFPSAW as a function of temperature, which yielded the values of the elastic constants C_{11} and C_{44} as a function of temperature. The other alternative, technically demanding route was to track organ-pipe modes as a function of temperature and use Green's function calculations to extract the elastic constants at each temperature point, without resorting to a dispersion analysis, which at the present moment is impracticable at high temperatures due to the fixed θ_i. Therefore, the more practicable method was adopted and the results of high temperature measurements incorporating the thermal expansion coefficient of boron carbide (4.5×10^{-6} K^{-1}) [6.27] are plotted in figures 53 and 54. Equation 6-3 was used for these calculations.

The elastic constants, C_{11} and C_{44}, were observed to increase gradually and essentially linearly with annealing temperature (starting at 394 GPa and 93 GPa respectively) until at about 350 - 400^{o}C a sudden increase in C_{11} is observed (from 399 to 409 GPa) that is associated with a phase transition. Considering the expressions relating Young's modulus and elastic constant C_{11}, namely equations 1-37 and 1-38 in section 1.5.2, the calculated value of Young's modulus is observed to increase from 250 GPa to about 263 GPa at 400^{o}C (figure 54), a value which is almost half that reported for *crystalline* B_4C at room temperature (510 GPa) [6.26, 6.30] but well within range of values reported in literature. B_4C films have been synthesised by various techniques such as magnetron sputtering, cathodic - arc using a heated B_4C target, plasma-enhanced chemical vapor deposition, pulsed laser deposition [6.32] and reported film hardness ranged between 25 and 45 GPa [6.33, 6.34, 6.35], while Young's modulus varied between 200 and 400 GPa. Secondly, the phase change to a structure with a modulus of about 260 GPa over the temperature 400 - 800 ^{o}C, confirms the high-temperature stability of amorphous B_4C (*a*-B_4C) coatings. The high-temperature stability combined with the characteristic of having highest hot hardness makes *a*-B_4C coatings ideal candidates for cutting tools [6.36] and production of temperature-stable heterojunction boron carbide diodes or boron carbide/boron junction field effect transistors [6.3].

Coating deposition of B_4C performed using techniques mentioned above results in *a*-B_4C; however, it is also known that nano-crystalline films can be deposited under the same conditions as the amorphous films but at higher subtrate temperatures of about 350 - 400^{o}C [6.36]. Therefore, temperature of 400^{o}C can be regarded as the lower limit of a posssible phase transition [6.20] taking place in the amorphous film. This analysis is confirmed by results of figure 53 and similar observations have been reported by Somonov [6.37] for *a*-SiC where they also observed a phase transition from amorphous to nano-crystalline SiC at an annealing temperature of about 400^{o}C. Also, the research work of Chen [6.38] indicates that boron carbide films prepared by ion beam sputtering at room temperature are amorphous with a low hardness value (13 GPa), but when the annealing temperature reaches 350^{o}C the films crystallise and reach a hardness value of 43 GPa. Further, Han [6.39] and co-workers concluded with similar observations that

amorphous films deposited at room temperature show a high hardness (42.5 GPa) and high modulus (300 GPa) which increases to about 420 GPa with increasing substrate temperature. One can therefore infer that the change in phase is from amorphous to a probably nano-crystalline phase.

Table 6.1: Table of elastic constants of *a*-B_4C as a function of temperature (for mathematical definations* refer to section 1.5.2)

Temp (^oC) (nominal)	C_{11} (GPa)	C_{44} (GPa) (≡ G)	E (GPa)*	B (GPa)*	C_{12} (GPa)	υ*
20	394	93	250.3	270	208	0.345
100	396	93.4	251.4	271.5	209.2	0.346
150	396.8	93.5	251.7	272.1	209.8	0.346
200	397.4	95	255.2	270.7	207.4	0.343
250	398.6	96	257.5	270.6	206.6	0.341
300	398.9	96.1	257.8	270.8	206.7	0.341
350	409	98	263.1	278.3	213	0.342
400	410	98	263.2	279.3	214	0.343
450	410	98	263.2	279.3	214	0.343
500	412	99	265.7	280	214	0.342
600	415	97	261.4	285	221	0.347

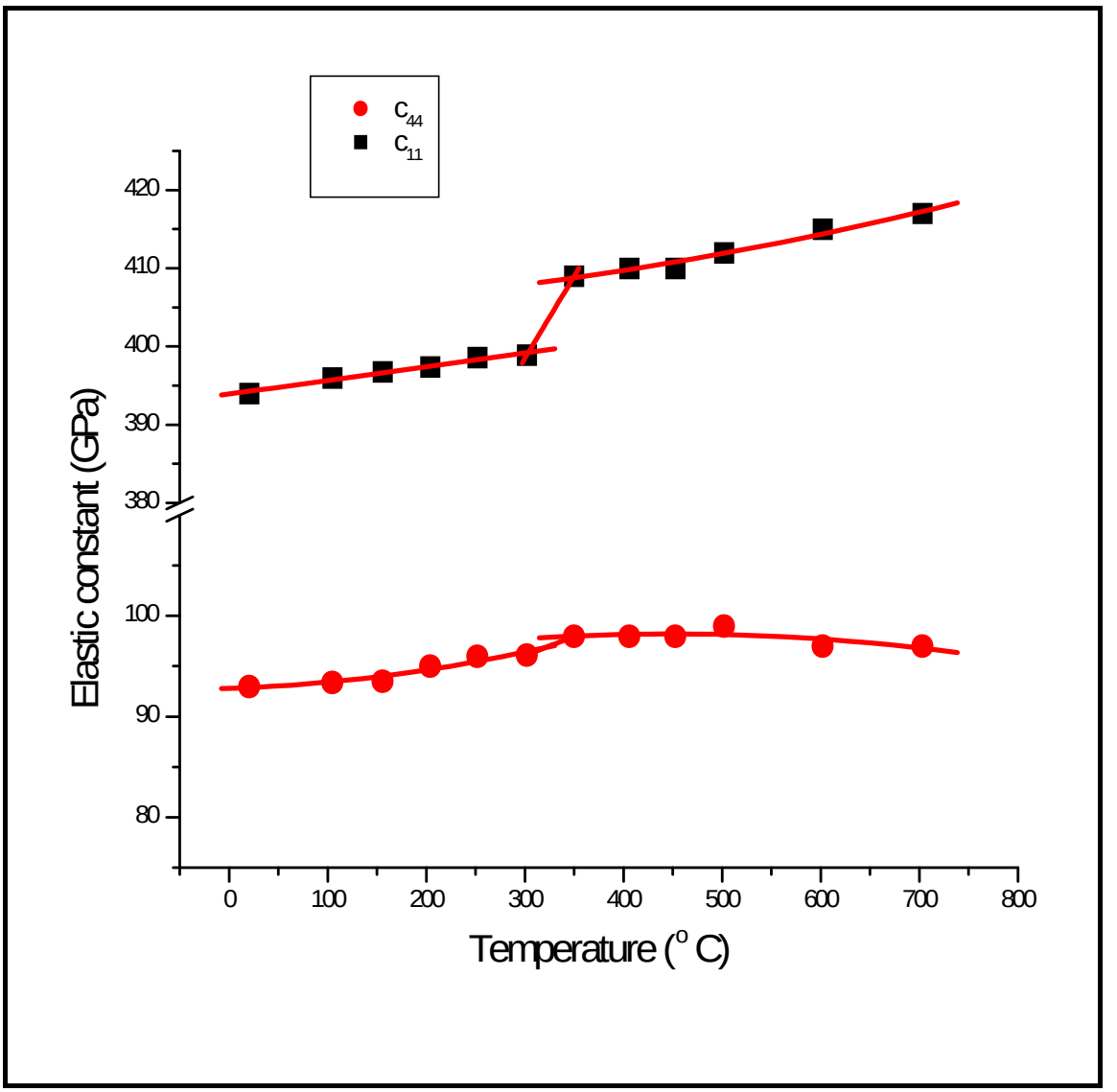

Figure 53: Phase transition from an amorphous to probably nano-crystalline phase is observed at 350 − 400°C.

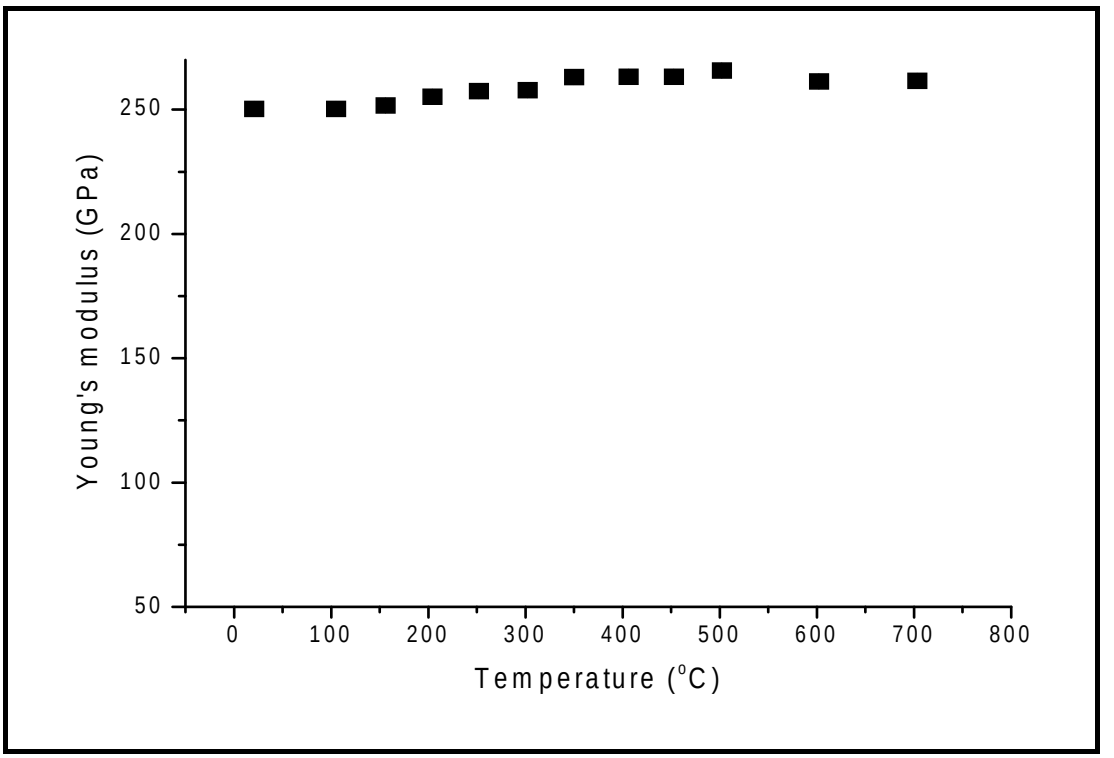

Figure 54: Young's modulus increases gradually from about 250 GPa to about 263 GPa between 200 and 400°C signalling a phase change to a structurally stronger phase thought to be a nanocrystalline phase of B_4C.

6.1.3 Conclusions

The elastic constants of an amorphous B_4C film have been successfully measured as a function of temperature, in the process, revealing a structural transition at about 350°C – 400°C similar to that reported for *a*-SiC. Surface acoustic modes (RSAW and HFPSAW were measured as a function of temperature and used to evaluate Young's modulus and bulk modulus as a function of temperature. The *E*- modulus stabilising at about 260 GPa, correlates with literature information about the high-temperature stability of boron carbide coatings which has drawn interest to their use in thermally-stable electronic components. Additionally, the bulk modulus (*B*) for *a*-B_4C was determined to be 250 GPa in agreeement with nanoindentation measurements by Chen et. al [6.19] on a 1.1 micron amorphous B_4C film grown on M2 steel gave a E-modulus value of 250 GPa and a hardness of ~ 30 GPa. The Poisson's ratio of *a*-Si (which is a related semiconductor) is known to lie between 0.28 and 0.45 [6.40] and Wittkowski et al. [6.40] estimated the

Poisson's ratio for *h*-BN to be about 0.35 which concurs with the value determined for *a*-B_4C film in Table 6.1. The shear modulus (93 GPa) is about *half* of the value reported for polycrystalline B_4C [6.31, 6.38] which ranges from 168 – 220 GPa.

The dispersion analysis using SBS revealed the interesting characteristics of organ-pipe modes measured at large $k_{//}h$ (or large incidence angles) where a complicated mixture of transverse and longitudinal waves contribute to the nearly regular profile of organ-pipe excitations. Results of a Green's function fit to the organ-pipe modes provides evidence of the potential for organ-pipe modes to be used for extracting elastic constants of thin films. Further analysis of the organ-pipe modes reveals the mode of the highest order ever observed experimentally using surface scattering techniques. The mode order is estimated using the expression;

$$\Delta f = f_{n+1} - f_n = 1.731 \left\{ \sqrt{\left(\frac{46}{\pi}\right)^2 + (n+\frac{3}{2})^2} - \sqrt{\left(\frac{46}{\pi}\right)^2 + (n+\frac{1}{2})^2} \right\}$$

and computed to be $n = 90$, for the $h = 2$ μm B_4C film.

Finally the elastic constants of this boron carbide film have been found using SBS to be C_{11} = 396 GPa and C_{44} = 108 GPa at room temperature. The elastic constants extracted using the Green's function method compare favourably with those obtained conventionally using SAWs and the bulk modes. An important technological statement that can be made arising from these results is that it is possible to embed nanocrystalline phases in an amorphous matrix by selecting appropriate conditions to control the phase change from an initial amorphous layer to a final mix with two phases. It is known that the segregation of nanocrystalline phases to grain boundaries of the first phase tends to strengthen the grain boundaries and stop grain growth, hence resulting in higher elastic modulus and increased hardness [6.13]. Part of this work dealing with the investigation and analysis of the organ-pipe modes has been presented at, and accepted for publication at the PHONONS 2007 Conference in Paris, and will be published in the Journal of Applied Physics: Conference proceedings journal.

In the following chapters, interesting observations made at high temperatures on boron – doped polysilicon will be correlated to parallel Raman measurements at the same high temperatures. Finally, explanations of this behaviour based on some fundamental physics and theory will be given.

Chapter 7

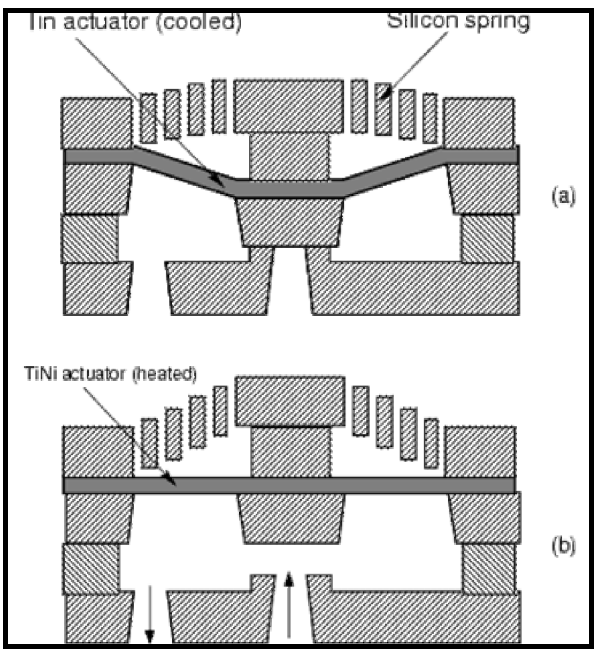

MEMS device

7 Boron doped Polysilicon

7.1 SBS investigation of boron doped polysilicon at high temperatures

Introduction

Micro Electro Mechanical Systems (MEMS), constitute a promising field expected not only to introduce new applications but also to develop the ones which already exist. Because of its interesting mechanical and electrical properties, both doped and undoped silicon films currently represent the first candidates as structural materials in MEMS applications [7.1,7.4]. However, doped silicon films are more advantageous when the structural layer must be an electrically conducting material. LPCVD polycrystalline silicon (commonly referred to as polysilicon) thin films are commonly used in micromechanical sensors and actuators[9]. Yet there are still some problems that limit the development of MEMS applications. One problem is the stiction (i.e. adhesion of Si membranes to bottom of cavities) of MEMS membranes during final step of rinsing and drying [7.2]. Another problem is the residual mechanical stress and its gradient. It is partly due to the mismatch of lattice constants and thermal expansion coefficients between the substrate and the thin film material, and partly due to the effect of the impurities on the grain growth during the deposition or the thermal annealing process [7.1]. Residual stress introduces some problems such as film cracking in the case of high tensile stress (positive) or film buckling in the case of compressive stress (negative) [7.3]. The stress gradient leads to out- of- plane deflection of the one-side fixed elements in a MEMS device. Generally, films that have a small tensile strain with a minimum stress gradient are more convenient for MEMS applications.

MEMS systems can be subjected to mechanical loads during fabrication [7.7], deployment [7.8] and operation [7.9] and are susceptible to failure due to fracture [7.9],

[9] Many films are not thermally stable at temperatures commonly used in conventional CVD. To reduce deposition temperatures so that existing films will not be adversely affected, Low pressure CVD (LPCVD) polysilicon films amorphously deposited using SiH_4 precursor gas are used in a conventional CVD setup.

buckling [7.10], and stiction [7.11]. Assessment of the reliability of micromachined structures requires accurate characterisation of mechanical stresses. Currently, direct measurement of local stresses must often accompany analytical or numerical models for deformation due to imprecise knowledge of material properties, inability to predict magnitudes of intrinsic residual stresses, and to generally assist in microsystems design [7.12]. Also for a reliable finite element simulation (FEM) of microstructures [7.14], the Young's modulus has to be known or the Poisson's ratio is assumed. Thus there is a clear need for experimental techniques capable of determining elastic moduli in addition to residual and applied stresses in micromachined structures so as to provide accurate data readily.

It is well known that Raman or micro-Raman spectroscopy can be used to characterise stresses with micron spatial resolution in macroscale structures and silicon microelectronic devices [7.15,7.16]. However the few existing spectroscopic studies of MEMS [7.17,7.18] do not comprehensively evaluate the utility and limitations of this technique in microsystems design. Both residual stress and Young's modulus (E) can however be measured simultaneously and independent of each other using the method of membrane deflection. Although this is an established method, the exact values of Poisson's ratio, σ and E depend on the theory used for the load- deflection behaviour of the test membrane [7.5,7.14]. The analytical theory, such as the extended analytical theory used by Maier-Schneider et al. [7.5], depends fundamentally on an assumed value for the Poisson ratio, yet the results for Young's modulus depend strongly on Poisson's ratio used for the calculations. For example, the assumption of $\nu = 0.23$ instead of 0.25 has been reported to lead to 5% higher values for Young's modulus [7.5]. This approach becomes problematic for the thinnest polysilicon films and the margin of error decreases with increasing film thickness.

Motivation for this study

Brillouin scattering has been used to study semiconductors for a long time to investigate processes or events such as velocity anisotropy, relaxation processes, phase transitions and a variety of acoustic interactions with other low-frequency excitations with much success (for a detailed compendium see the reviews by Comins [1.12], and Beghi et al., [1.13] and references therein). More importantly, SBS offers the possibility to determine the Young's modulus for the semiconductor films without need for making assumptions for the Poisson's ratio and high temperature SBS offers the added possibillity of studying the elastic response of these microstructures at temperatures identical to their operating environments .

In the present research, the primary objective was to determine the elasticity of the semiconductor film as a function of temperature, and in the process also determine independently, the value for the Poisson's ratio for the boron-doped polysilicon. SBS measurements at high temperature make it possible for the first time to accurately measure elastic constants and related engineering moduli and hence understand better the behaviour of these semiconductor films at high temperatures, at the same time obtain better information to refine existing models used to simulate stresses at elevated temperatures.

High deposition temperatures of thin films generally increase the production costs and thus there is a competition to develop techniques that enable lower deposition temperatures but retaining the same electrical and mechanical performance of the MEMS structures. In this regard, the intention was to measure the Young's modulus at typical operating temperatures of solid state MEMS devices with the hope to determine the extent of or non-deterioration in the material's elasticity [7.22]. The samples that were investigated were supplied courtesy of Prof L Hobbs of MIT (USA).

The second objective was to extend the temperature range beyond ordinary operating conditions and study the physical processes at play as well as measure the elasticity of the polysilicon in view of the well-known high-melting point of silicon. In this study Raman spectroscopy was also used to investigate the effect of different thermal annealing cycles on the average intrinsic stress of the boron-doped polysilicon film, study thermally induced boron activation effects on the strength of the material and correlate this behaviour with the SBS results of Young's modulus, *E* and bulk moduli, *B* measured at equivalent temperatures.

7.1.1 Doping of silicon with boron

In the semiconductor industry, dopants are usually introduced by ion implantation followed by subsequent activation anneal, diffusion, or gas-phase doping [7.23]. However, implantation and diffusion techniques require high temperatures that, depending on device structures, may not be compatible with all processing steps and materials [7.24] such as the substrate temperature. The material under investigation comprises boron-doped films of 50 micron thickness grown on each side of a Si(001) wafer and both doped with 3000 ppm of boron (~10^{19} atoms per cm^3). The samples provided consisted of pieces of about 4x4 mm^2 . Such film thickness (50 micron) is much larger than the magnitude of the wavevector parallel to the surface and thus qualifies such films as 'bulk' specimen in SBS, hence the first investigation was to then determine the surface anisotropy. For measurements purpose, it was decided to use the face that had a better surface finish or less surface damage than the other.

7.2 SBS investigations at room temperature

1) Dispersion

Epitaxy is defined as growth of a single crystal film upon a single crystal substrate, and if the composition of the film is the same as that of the substrate, the process is known as homoepitaxy, thus some surface anisotropy was expected from these specimens since epitaxial films retain crystallographic symmetry. The specimens were mounted and set-up to determine angular dependence of the Rayleigh surface mode of the epitaxial crystalline

film. However, results of this investigation showed very little or no anisotropy of the surfaces contrary to the expected [001] surface anisotropy and even repeat measurements on another sample produced a similar outcome as shown in figure 55. These somewhat unexpected results led to Raman investigation as the preferred choice to help assess the crystallinity of the samples.

2) Raman investigation

Raman measurements were made using a Jobin Yvon T64000 triple grating spectrograph in triple additive mode equipped with a liquid nitrogen cooled CCD detector. The spectrograph works in the backscattering geometry and the excitation light being the 514.5 nm line of Ar^+ laser. It was found that the material was *polycrystalline*, instead of crystalline (*c*-Si) as shown by the asymmetric line shape (see figure 56). Again several of the cut specimens were analysed at different surface positions and the same result found. This finding correlated with the earlier results of SBS dispersion which indicated a lack of anisotropy on the surfaces. Another important observation from the Raman spectra was the characteristic asymmetry of the line-shape associated with p-type doping of polycrystalline silicon, known as the Fano line-shape (see section 7.3.2.1).

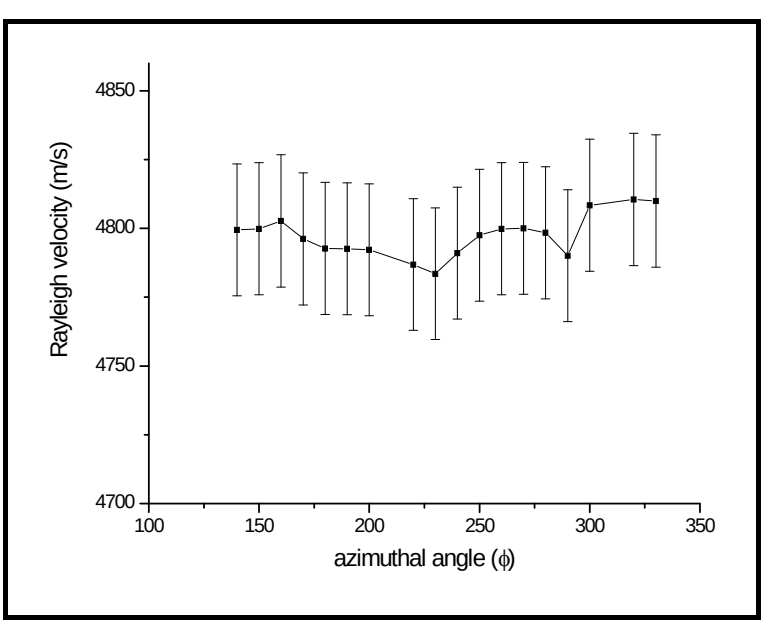

Figure 55: SBS dispersion profile for the boron - doped Si samples showing the very weak anisotropy. Error on the dispersion velocity is ±24m/s.

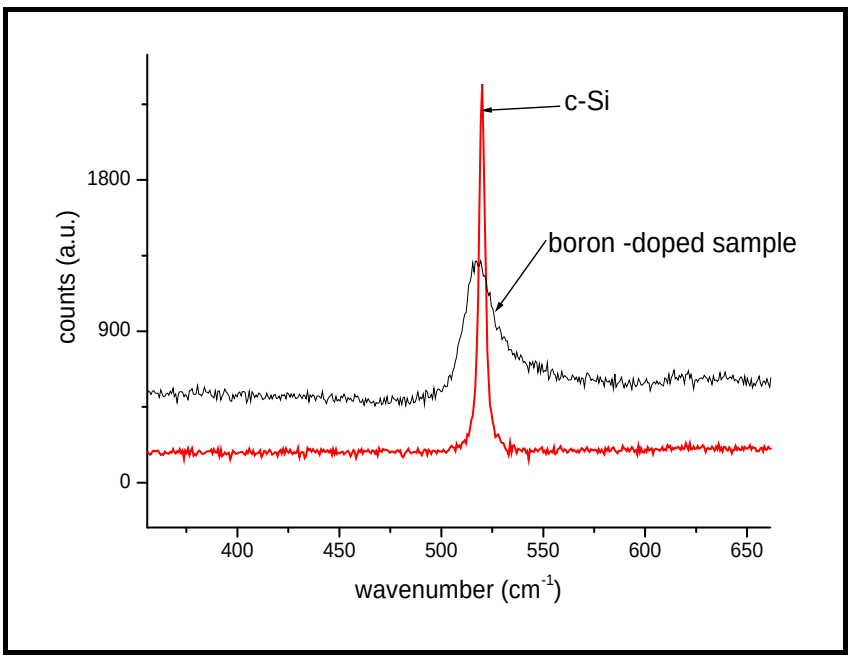

Figure 56: Room temperature Raman spectrum of the B-doped silicon sample showing the characteristic asymmetric line-shape towards higher wavenumbers associated with p-type polycrystalline silicon plotted on same vertical scale with spectrum for c-Si.

After establishing the polycrystalline nature of the film, high temperature SBS investigations were initiated starting at room temperature and treating the polycrystalline film as being isotropic, such that only two independent elastic constants are required to fully characterise the film's elasticity. As discussed in section, the relationship between the elastic constants is stated in section 1.5.2 as $C_{11} - C_{12} = 2C_{44}$ for isotropic materials.

The first part of the experiment investigated the variation of the modulus of elasticity of the B-doped Si epilayer within the temperature range 20^{o}C to 73^{o}C, and observed how the moduli responded at typical operating temperatures for electronic devices such as emitter layers. This work forms part of the MSc dissertation of L. Kotane [7.40]. The second part was to investigate the behaviour of the moduli over the extended temperature range and relate the results to Raman measurements of intrinsic stress at the same corresponding temperatures with a view to understand the mechanical strength, boron influence on the mechanical properties at ambient and higher temperatures and the overall material stability.

7.3 Brillouin scattering in Semiconductors

Some of the effects associated with Brillouin scattering in semiconductors will be the subject of the following sections. The spectral width of the scattered light, examined with high resolution, yields information about acoustic attenuation arising from anharmonicity, carrier damping, structural relaxations or other possible mechanisms [7.1,7.6, 7.8, 7.10]. The light scattering intensity and selection rules give insight into the fundamental nature of the coupling of phonons to the electronic states responsible for the optical properties [7.4].

7.3.1 Determination of refractive index at ambient conditions

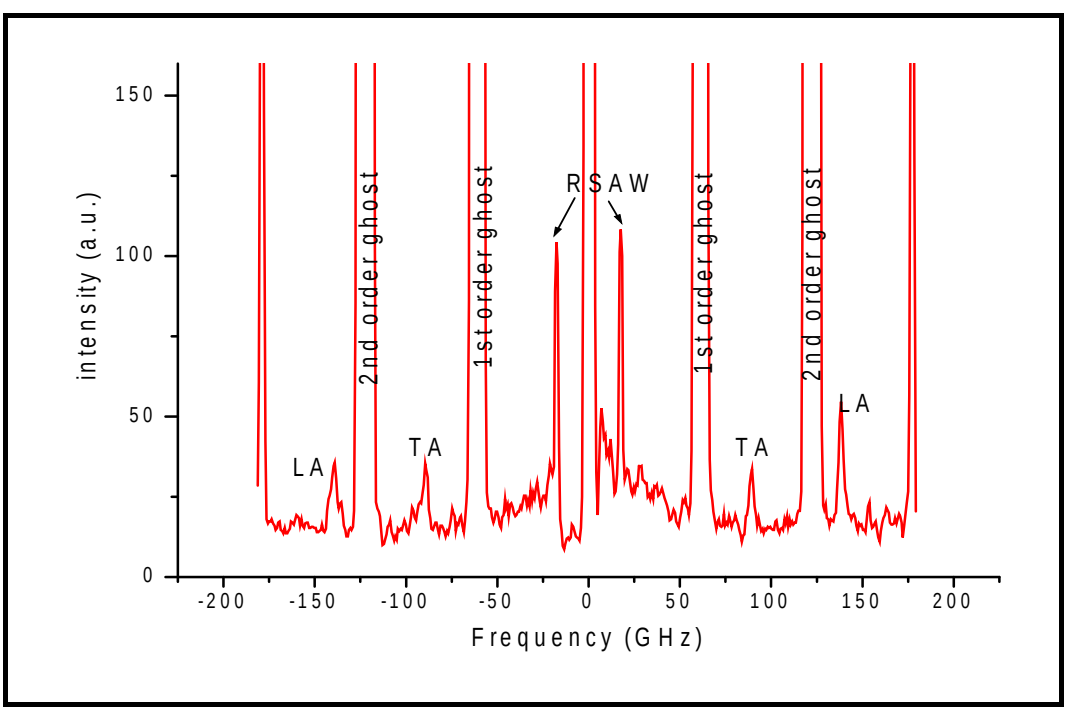

Figure 57: SBS spectrum for B-doped polysilicon showing surface and bulk modes at a scan amplitude of 5.7 (L = 2.5 mm) and at incidence angle 70.9°.

The spectrum in figure 57 was obtained using a wide scanning amplitude of 5.7 (which equates to almost 1800 nm) in order to observe the bulk acoustic modes, LA and TA, which occur at much higher frequencies. The significance of the bulk modes in this investigation is that they can be used to provide additional acoustic information for bulk specimen, in conjunction with data obtained from SAWs within the same investigation as

described below. Cubic symmetry guarantees the isotropy of quantities like the refractive index, represented by tensors of rank 2, and for the polycrystalline sample, the elastic behaviour is also isotropic.

Refractive index measurement

For some semi-opaque semiconductors, SBS can be used to determine refractive index (real and imaginary components) using information from the linewidths of bulk modes and their respective mode velocities. The absorptive part of the refractive index can be determined independently using the arguments in section 1.2.2 for opacity broadening when one measures the frequency spread for say, the TA mode using fitting procedures. Of necessity, one has to deconvolve the effects of instrumental and opacity broadening in order to find the linewidth resulting from the opacity (see section 3.2.2), and interferometer was set at *FSR* = 60 GHz, with a finesse of about 140. The instrumental line-width adjusted FWHM is 2.2 GHz for the bulk TA mode shown in figure 58, and the transverse velocity was estimated from the RSAW (17.64 GHz) in figure 57 using the isotropy approximation ($V_T = 1.14V_R$) [7.9] and found to be 5400 m/s. This value was checked against a more direct determination from the bulk transverse threshold (19 GHz) in figure 59 below which gives the velocity as 5200 m/s. Therefore with the transverse velocity known (taking the velocity to be 5400 m/s), the expression (see section 1.2.2) relating transverse velocity (v) to the imaginary refractive index resulting from the penetration of the incident light of wavevector (k_o) the effect of which is observed as the finite width of the bulk phonon ($\Delta\omega$ = 2.2 GHz), namely $\Delta\omega = 4v\,k_o \mathrm{I}m(n)$, was applied giving the (imaginary) refractive index n_e = 0.008.

Additionally, from the frequency shift f of the bulk TA mode (89 GHz), the *real* part of refractive index is obtained using the relation $V_{TA} = \frac{f\lambda}{2n}$, as n = 4.40 which represents a 4 % increase over that of *c*-Si (n = 4.22 for λ =514.5 nm [7.14,7.25]) and about 31% increase on undoped polysilicon [7.4]. The main conclusion from these results is that the boron-doped polysilicon (3000 ppm) almost retains the optical properties of *c*-Si with only a 4% increase in refractive index (real) and marginal difference for the imaginary

component [7.4, 7.21]. The plausible explanation for this effect is the increase in mass density arising from the smaller diffused-in boron atoms, and this observation will later be correlated with *E*-modulus increase [7.5] at room temperature compared to *c*-Si. Undoped polysilicon has a reported refractive index of 3.22 [7.5] which increases to about 3.42 at a temperature of 1100^{o}C and this increase was attributed to the presure dependence of the refractive index arising from the strained film by Maei-Schneider et al. [7.5].

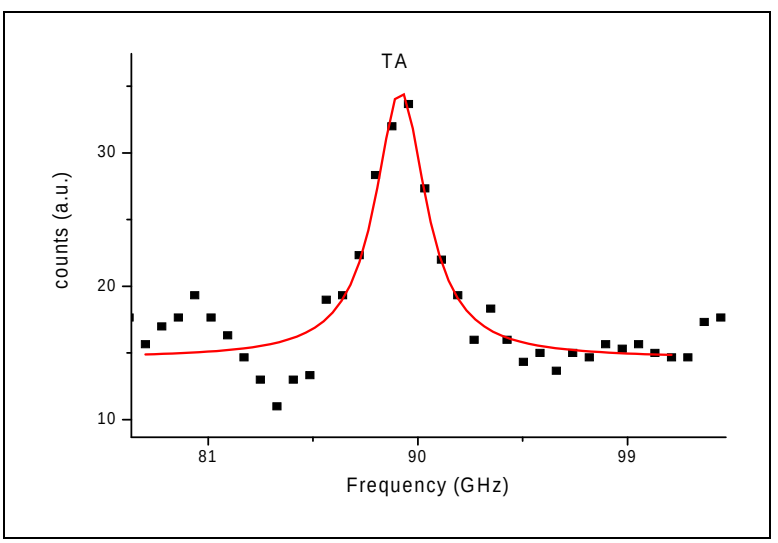

Figure 58: The bulk TA mode of boron-doped polysilicon recorded at θ_i = 71^{o}, scan amplitude 3.5 located at 90 GHz. FWHM was measured to be 2.2 GHz after deconvolution of the instrumental effects using instrumental response spectral width of 400 MHz. The continuous line is the Lorentzian fit applied to the bulk TA mode.

7.3.1.2 High temperature SBS: Part 1

For this part of the experiment which was performed using the high-temperature furnace discussed in section 3.3, a steady ramp rate of 2.4 ^{o}C per minute was maintained between the stages. The SBS accumulation times of the spectra ranged from 16 hours to 43 hours. The long accumulation times were necessary in order to record a well-developed broad Lamb shoulder and longitudinal dip as shown in figure 59 below. On this particularly good spectrum, it was possible to determine the transverse velocity from the transverse-wave threshold at 19 GHz; usually this mode is difficult to observe directly from a spectrum due to the overbearing effects of the very intense Rayleigh mode coupled with

the attendant background noise which swamp the region close to the RSAW peak. The spectra thus collected at different set-points comprised of a broad Lamb shoulder and a longitudinal dip as well as a Rayleigh peak, and these features permitted the full set of elastic constants to be determined. These elastic elastic constants were then plotted as a function of temperature.

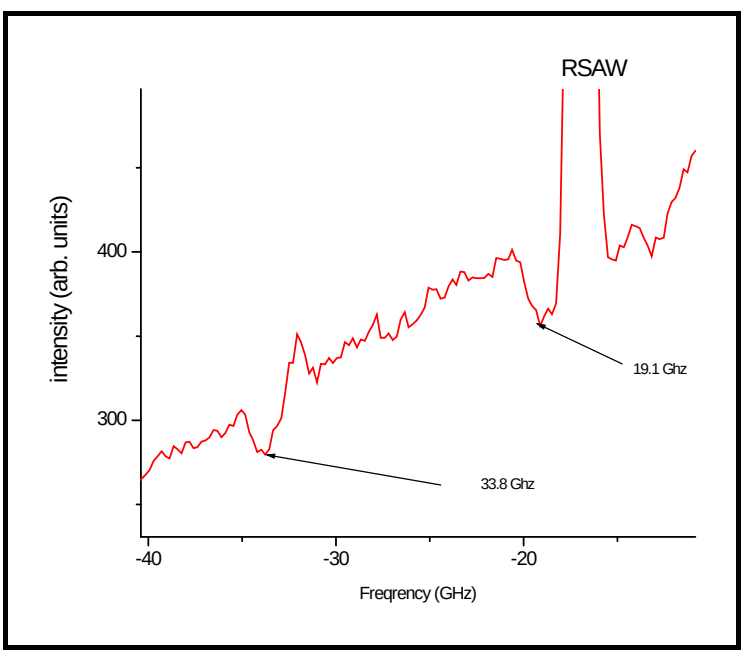

Figure 59: Typical SBS spectrum recorded for B-doped polysilicon at 55.7 °C (and similarly at every temperature set-point) showing the Lamp continuum and the longitudinal dip as well as the transverse wave threshold at 19 GHz. (using L=2.5 mm, scan amplitude 1.81)

To do this, a relation by Landau and Lifshitz given as equation (6-3) in section 6.1.2.1 was used, namely,

$$C_T^4 - (C_R + C_L)C_T^3 + 1.5C_R C_L C_T^2 - 0.5C_R^2 C_L C_T + \frac{1}{16}C_R^3 C_L = 0\,. \qquad (7.1)$$

Here, C_R, C_L and C_T, represent the product of Rayleigh, longitudinal and transverse squared-velocities with density, respectively [5.34]. The Landau-Lifshitz relation was used to determine the transverse velocity and hence the Lamé constant, λ. With the value of C_T known, standard relations for Young's modulus (E) and bulk modulus (B) in terms of the engineering moduli or Lamé constants (λ and μ) given in section 1.5.2 were then used plot the results in figure 60 .

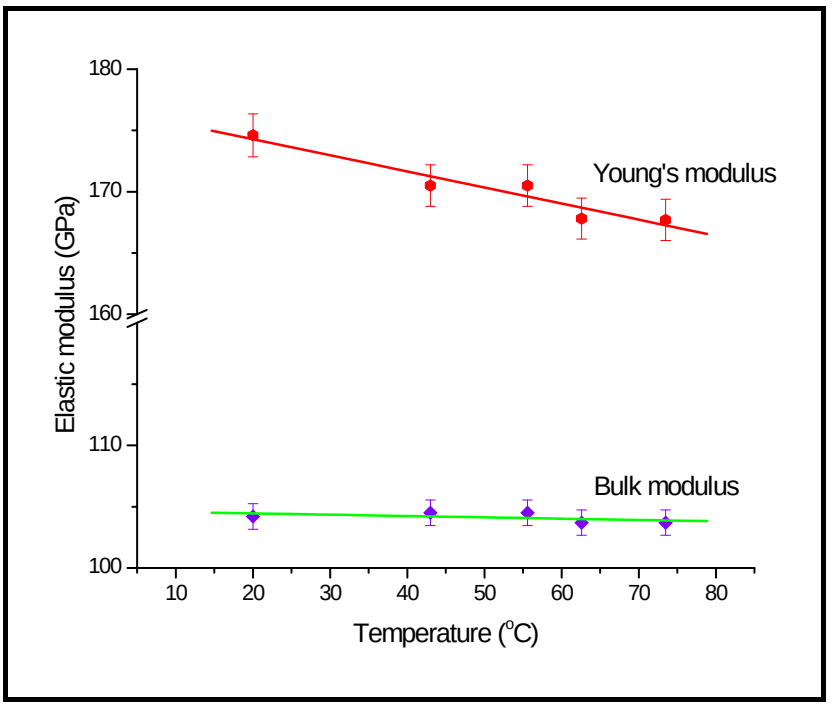

Figure 60: Linear variation of elastic moduli with temperature for B-doped poly-silicon as shown by L.M. Kotane (MSc dissertation [7.40] in preparation).

As shown in figure 60, the boron doping results in an approximately 7% increase in the bulk modulus and a 3.3 % increase in Young's modulus for the doped polysilicon compared to that of the undoped material [7.33]. More significant is the observation that at about 60^{o} C, the Young's modulus of the film is about 168 GPa, a value that is close to ambient *E*-value for *c*-Si (169 GPa) [7.21]. The thermal expansion co-efficient for polysilicon was not incorporated in the calculations performed in figure 60 for the following reasons: the linear thermal expansion coefficient of undoped polysilicon as measured by Pan [7.33] was found to average 2.7 x 10^{-6} $^{o}C^{-1}$ over the temperature range covering ambient to 400^{o}C. Pan also records that the coefficient varied very little with temperature (less than 8 % increase), but increased sharply between 400 and 800^{o}C, up to 4.4 x 10^{-6} $^{o}C^{-1}$.

The value of the density used for the calculations is 2.33 g/cm^{3}; a value that was determined by Horn [7.26] using an adaptation of the ' precision gradient method' for boron-doped polysilicon having a dopant concentration of 2.6 x 10^{19} cm^{-3}, having taken into consideration lattice contraction effects due to the introduction of the smaller boron atoms. These levels of boron concentration are of the same order as that of the sample

investigated in this report (2 $\times 10^{19}$ cm^{-3}). Finally, with the room temperature elastic constants measured as c_{11}= 197 GPa, c_{12} = 71 GPa and c_{44} = 63 GPa, the Poisson's ratio was calculated to be 0.26 (±0.01) and 0.28 at 60^{o}C using equation 1.40 (section 1.5.2). The former value being in agreement with literature [7.4, 7.14,7.16] for *p*-type polysilicon at room temperature.

7.3.2 High temperature SBS: Part 2 (Extended range)

Following the approach of the first part above, the temperature range was extended to 700^{o}C to determine how the moduli varied with temperature, as shown in figure 61. In addition, parallel Raman measurements were conducted using a high temperature Linkam TS1500 stage (see sections 3.4.1 and 7.3.2.1), at the same temperature points from which analysis of the asymmetry of the lineshape as well as stress was conducted as detailed in the following sections. In figure 61, an interesting observation is made, namely that of a marginal increase of the *E*-moduli between 200^{o}C to 300^{o}C (see Table 7-1). This increase is similar to that reported by Maier-Schneider [7.5] for an undoped polysilicon where the *E*- value increased from 158 GPa to 166 GPa over a large temperature range up to 1100^{o}C. Only beyond about 750^{o}C is silicon known to become increasingly ductile. In this report, the magnitude of the increase is clearly more pronounced for the bulk modulus, *B*, signifying a greater degree of stiffness [7.42] possibly arising from growth in grain size.

The Young's modulus, which in essence is a reflection of the atomic bond strength, does not appreciably change over the whole temperature range, signifying that there is no structural change to the material when it is annealed.

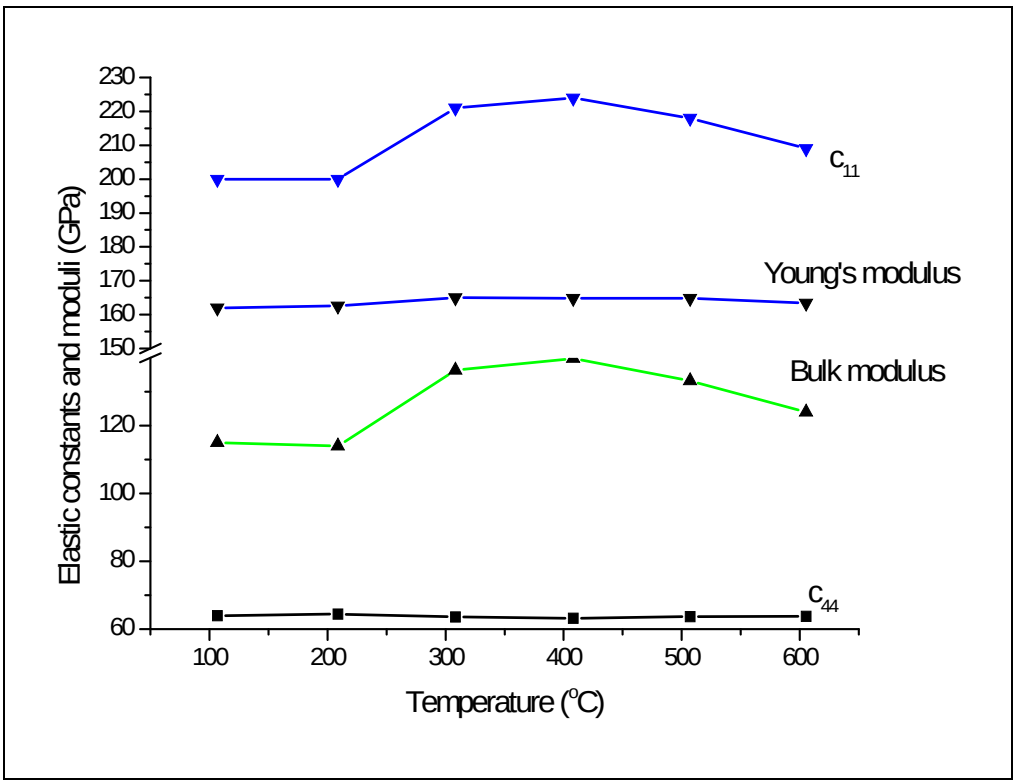

Figure 61: Young's modulus of the boron - doped polysilicon is observed to increase marginally by about 2 GPa and stabilising at 164 GPa as annealing temperature increases. The Bulk modulus shows a much larger change (30 GPa) thought to be associated with increase in grain size.

Table 7-1: Variation of elastic constants of boron-doped polysilicon for the high temperature investigation where E, B and υ represent Young's and Bulk moduli, and Poisson's ratio respectively.

Temp (°C) (nominal)	C_{11} (GPa)	C_{44} (GPa) (≡ G)	E (GPa)	B (GPa)	υ
100	200.0	64.0	162.0	115.0	0.26
200	200.0	64.4	162.6	114.0	0.26
300	221.1	63.6	165.1	136.3	0.30
400	224.0	63.2	164.8	139.8	0.30
500	218.1	63.7	164.8	133.2	0.30
600	209.0	63.8	163.4	124.0	0.28

While the increase in the bulk modulus arises from possibly grain growth, the earlier observation of an increase in the refractive index value as determined at room

temperature for the B-doped polysilicon (n = 4.40) when compared to the undoped polysilicon (n ranges from 3.22 - 3.4), can be attributed to the presence of dopants in sufficiently high concentration [7.5] which increases the mass density. Finally the slow linear decrease beyond 400^{o}C observed in figure 61 is more consistent with the anharmonic behaviour observed for solids [7.25] resulting from lattice expansion.

7.3.2.1 Raman Investigations

A brief note is given here concerning the experimental configuration: Raman measurements reported here were made using a T64000 (Jobin Yvon) spectrograph in triple addiditive mode equipped with a liquid nitrogen cooled CCD detector. The spectrometer works in backscattering geometry and excitation light was 514.5 nm laser and focused using a 20X objective. The incident laser power was chosen to be about 1 – 2 mW to minimise local heating effects due to the laser probe.

Acoustic phonons of q ≈ 0 can be detected by means of either ultrasound or Brillouin scattering. Raman scattering can thus be used to investigate the self-energies of optical phonons at q ≈ 0 in interactions with electronic excitations. It was known as early as in 1975 by Balkanski [7.29] that the one phonon Raman line shape of p-type Si depended sensitively on number of experimental variables i.e., the concentration of boron acceptors, the sample temperature and the energy of the exciting radiation. As the number of boron acceptors becomes larger [7.4] or the wavelength of incident photons increases, the one- phonon line broadens appreciably and becomes strongly asymmetric [7.7,7.31]. The same effect is observed as the temperature is lowered for boron concentrations exceeding about 5 x 10^{19} cm^{-3}[7.4]. The measured line-shape in figure 62(b) indicates, apart from the asymmetry, that there exists an anti-resonance on the low-energy side of the resonance, a characteristic of systems where there is a discrete state-continuum interaction [7.7].

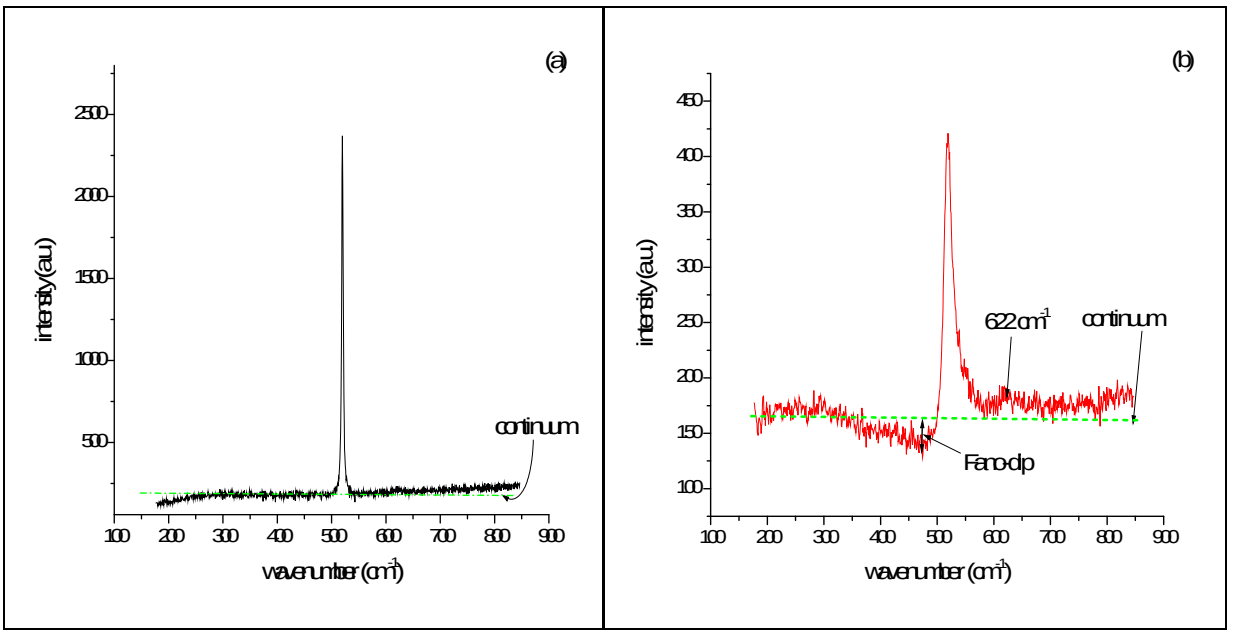

Figure 62: Raman spectra for B-doped polysilicon (62b) showing asymmetry towards high wavenumbers and the reduction below continuum level (or Fano-dip) around 494 cm^{-1} [7.36] in contrast to the spectrum for *c*-Si (62a).

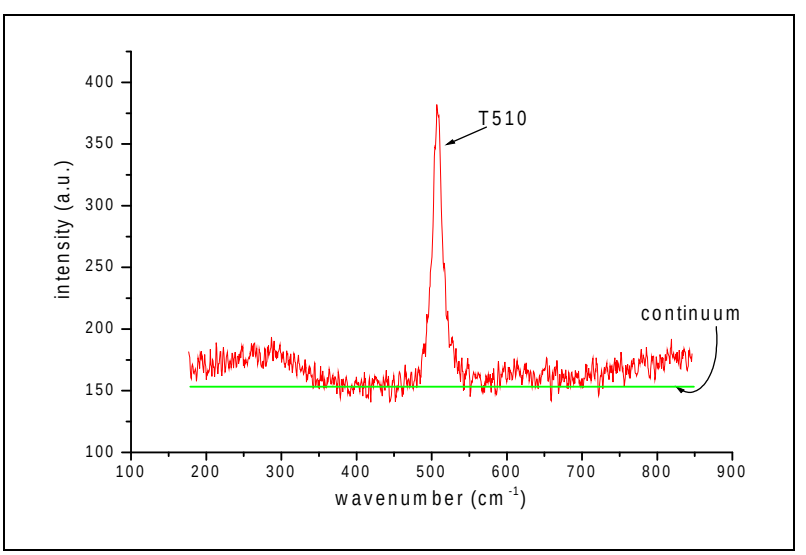

Figure 63 : The Raman spectrum at 510 ^{o}C shows a diminished Fano-dip and a more symmetric line-shape signifying the activation of dopants out of the substitutional sites at higher temperatures. The broad peak at ~ 280 cm^{-1} shows the contribution of amorphous silicon, which has insignificant effect on peak asymmetry in this case.

Boron, being a lighter atom than Si, produces a local vibrational mode that occurs at a higher frequency than the optic phonon of Si (520 cm^{-1}), being at 620 cm^{-1} for ^{11}B and 644 cm^{-1} for ^{10}B. These local modes are observable at room temperature for boron

concentrations of ~10^{19} cm^{-3} and higher as evidenced by the broad peak around 622 cm^{-1} in figure 62b. Since the boron acts as an acceptor in Si, an equal number of free holes is produced (assuming that all boron atoms are electrically activated), pushing the Fermi level out of the band gap into the valence bands at a concentration near 10^{19} cm^{-3}. Raman-active intervalence band transitions can then occur [7.29] producing a broad scattering continuum. The energies of both the optic phonon and the local modes of boron fall within this continuum and a Fano-type interference [7.4,7.31] occurs resulting in asymmetric line shapes observed in the Raman spectra for boron-doped polysilicon.

*Micro*crystalline and *poly*crystalline silicon have been investigated by Lengsfeld et al. [7.4] where they showed the existence of significant differences between the two materials, namely that, while doped poly-Si samples exhibited a Fano effect just like that in heavily doped *c*-Si samples, the same could not be said for the moderate to heavily doped microcrystalline (hydrogenated) samples, and thus they could distinguish between the two silicon structures. The sample investigated here definitely matches the Lengsfeld criterion for boron-doped polycrystalline silicon.

Line asymmetry recovery and high temperatures

For this part of the experiment, a Linkam TS1500 heating stage was attached to an Olympus BX40 microscope which allowed for in-situ Raman measurements to be made at high temperatures. The temperature was controlled by a TMS1500 programmable heater. In *p*-type Si, Fano resonances or interactions take place between the discrete state of the optical phonon and the hole continuum as observed in the Raman spectra [7.31]. The continuum can be identified as the hole continuum of the acceptor-to-band excitations, inter-valence transitions or free carrier absorption depending on experimental conditions [7.29]. The larger the continuum scattering relative to the discrete one, the more pronounced are the interference effects.

Studies have been conducted for similar dopant concentrations (10^{18} - 10^{19} cm^3) in thin 2 micron Si membranes doped with Sb and B respectively [7.32], where it was shown that

the Fano - dip due to an optical phonon disappears in the spectrum when the holes are missing in the acceptor sites either by an increase of the sample temperature or by doping compensation[10]. This observation was confirmed in this experiment at a temperature of 510^{o}C (figure 63) where the Fano-dip has completely disappeared and the line-shape is also symmetric . To gain better understanding of the physical processes occuring, let us start at room temperature. Boron atoms located at substitutional sites act as acceptors of electrons, and so valence electrons would move to the acceptor sites creating 'holes' which are then responsible for conduction which occurs by nearest neighbour and variable range hopping of holes between ionised B sites [7.42]. At room temperature only 0.2 % of the substitutional boron sites are ionised according to [7.42]. Therefore, if we surmise that at sufficiently high temperatures and large thermal soaking periods (also herein referred to as thermal budgets) e.g 510 ^{o}C for 20 hours, a substantial number of boron atoms are ionised (> 80 %) then the free electrons will result in charge-compensation of the holes in Si, depletion of the hole-continuum and the eventual diminishing of the Fano interaction that occurs with the discrete Raman phonons. The result would be a broadened, but symmetric peak such as the one observed at 510 ^{o}C. Conversely, when the sample is cooled to room temperature, a Fano-line shape would re-appear due to the recovery of the electronic effects. The thermal activation energy of ~ 10^{17} cm^{-3} B in Si has been determined to be 0.37 eV by [7.42] and this being a rather large value, considering the room temperature conditions (where $k_B T$ ~ 0.026 eV), this value suggests that the normal tendency is for the acceptor site to remain inactivated. Therefore, correlating the observation of the recovery of the Fano-line asymmetry at room temperature with the above information, it seems more likely that at room temperature there is not enough energy for the B to remain ionised, in other words, there is not enough energy to overcome the activation energy barrier (0.37 eV) so the acceptor sites retain their electrons once again.

[10] The reason for the interaction only with the *hole continuum* concerns the *shallow acceptor levels in Si which are separated by energies comparable to phonons.*

Temperature dependence study

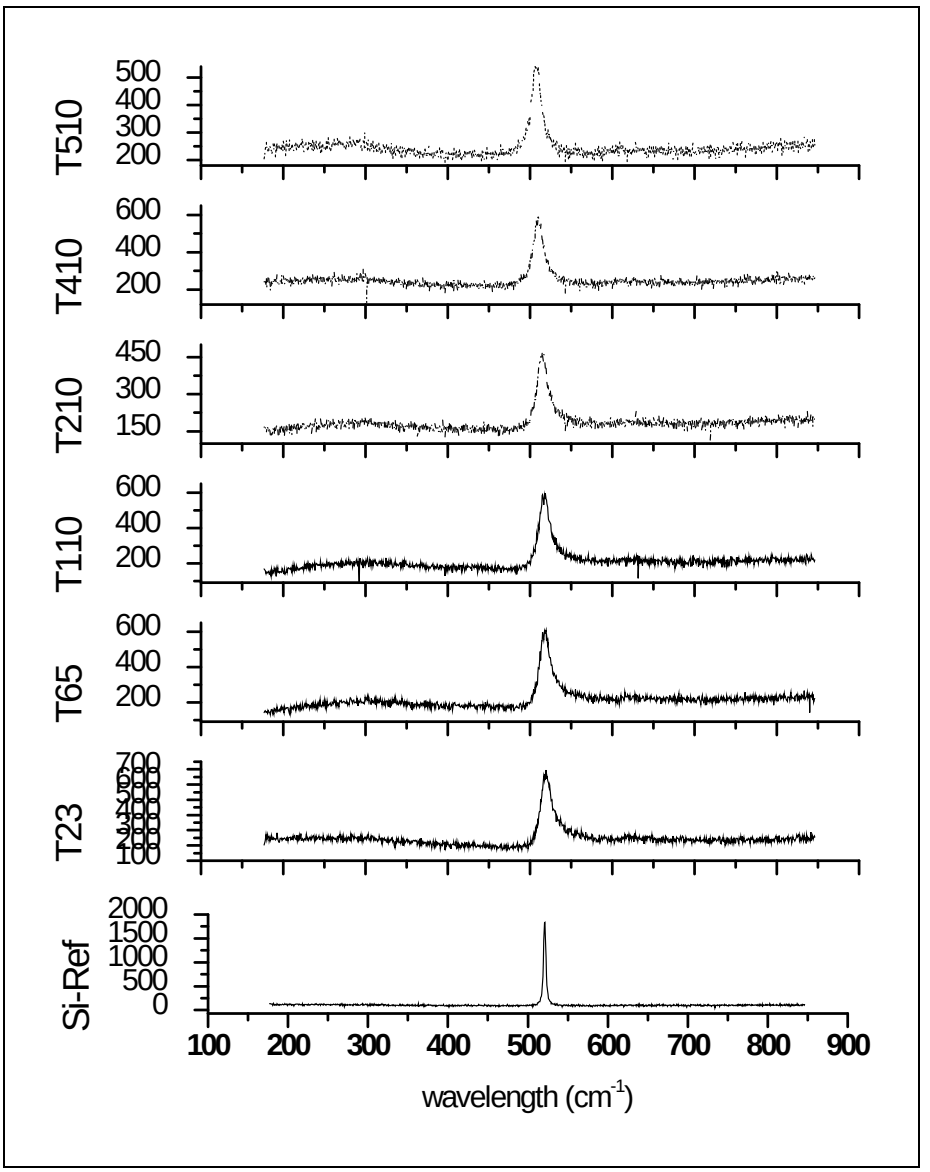

Figure 64: Phonon-softening of the Raman peaks as the annealing temperature is increased accompanied by a reduced peak asymmetry. On cooling to ambient, the asymmetric line-shape is recovered. T23 represents spectrum collected at temperature of 23°C, Si-Ref is the spectrum from a crystalline silicon sample.

The Raman spectra in figure 64 clearly show a *decrease* in phonon peak wavenumber and a corresponding general decrease in asymmetry of the line-shape with increase in sample temperature. With an increase in temperature from room temperature to 200°C, a decrease in peak wavenumber of about 5 cm^{-1} is observed. Strong phonon-softening is observed in the film (~ 14 cm^{-1}) over the whole temperature range. Considering the

difference in thermal expansion coefficients between silicon substrate (2.7 x 10^{-6} $^{o}C^{-1}$) and polysilicon (2.6 x 10^{-6} $^{o}C^{-1}$), the system is not expected to experience any significant tensile stresses that are normally associated with differential expansion between the substrate and the film that would normally result in *decrease* in Raman peak shifts. Thus the downshift of the phonon peak observed in figures 64 and 65 can be regarded as being due to general phonon softening. The contribution from tensile stress is negligible. The linear behaviour observed for the phonon downshift shown more clearly in figure 66 provides additional proof that anharmonicity resulting from lattice expansion as temperature is increased is the principal cause, as such behaviour is characteristic of basic anharmonic theorem.

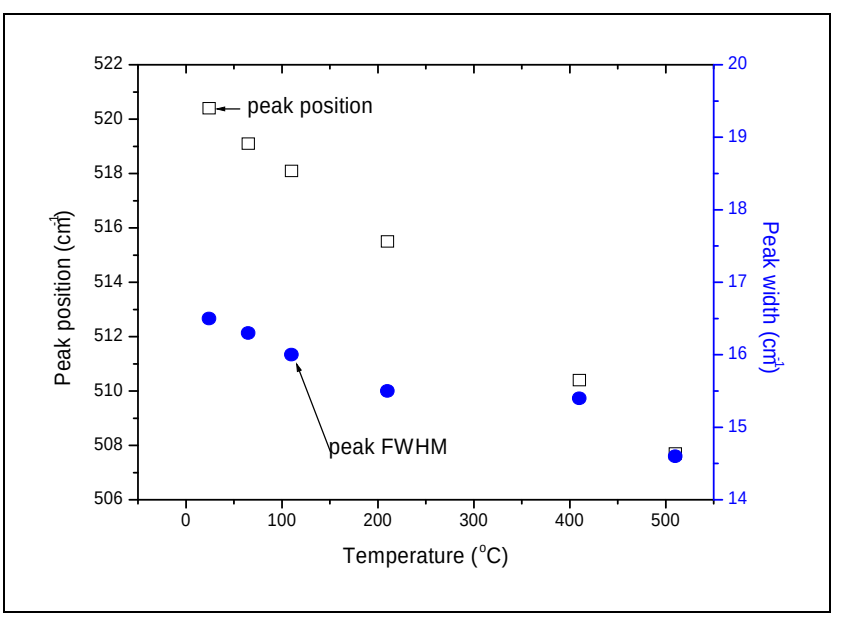

Figure 65: Variation of the peak shift and peak width of the first order Raman line of boron-doped polysilicon.

In the first order Raman spectrum, such effects always predict a frequency softening of the optical phonon and increase in its damping with increase in lattice temperature. In figures 65 one observes a linear decrease in phonon peak wavenumber and an almost linear and gradual *decrease* in peak-width with temperature. The phonon peak-width changes slowly, 1.1 cm^{-1} over the temperature range 23 to 400^{o}C followed by a steeper decrease of 1cm^{-1} at 500^{o}C. In most materials, the Raman phonon has a finite linewidth

indicative of the presence of decay channels, which shorten the phonon lifetimes. Two main mechanisms controlling phonon lifetimes in intrinsic materials are the phonon anharmonic interactions and phonon scattering from defects or impurity centres. Considering that the samples in question were prepared by thermally diffusing boron into Si, which results in a broadening arising from the Fano-effect, the phonon scattering from defects as well as anharmonic interactions play a minor role compared to the Fano-effect in contributing to phonon broadening and can be disregarded in this instance.

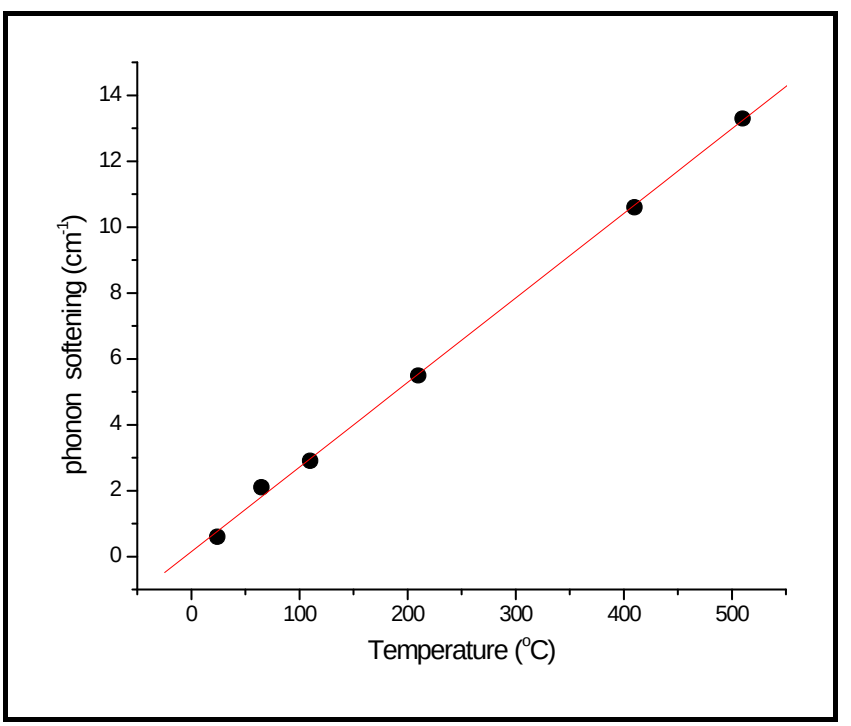

Figure 66: Raman phonon of B-doped polysilicon showing softening effects with increase in temperature attributable to anharmonic effects. The solid line is a fit to the experimental points.

Therefore, the most probable explanation for the observed narrowing of the peak width (~ 2 cm^{-1}) to that akin of a Lorentzian profile as temperature is increased to 510^{o}C, is the diminishing Fano-effect (as explained above in the section on line-asymmetry recovery), with possibly very small contributions from impurity scattering and anharmonic interactions. Again considering figure 66, the temperature variation of the Raman modes in solids is generally considered to be caused by the sum of two effects: first, the anharmonic effects that lead to the decay of a strongly interacting optical phonon into two or three weakly interacting acoustic phonons (through cubic or quartic phonon-phonon interactions) [7.38], and second, the electron-phonon interaction that causes changes to

the self-energy of an electron (phonon) in a phonon (electron) field. The anharmonic part corresponds to the expansion or dilatation of the crystal due to inclusion of a realistic anharmonic contribution to the harmonic crystal potential energy. In this instance, it is clear that the changes in the Fano-effect have a much smaller influence on the Raman peak frequency than those associated with lattice expansion as demonstrated by the differences in magnitude of changes in figure 65, where phonon peak position changes at a much steeper rate with temperature.

7.3.2.2 Conclusions

The Fano interaction is a very frequent phenomenon in physics and appears in various systems from rare gases to semiconductors and superconductors. In this project, the Fano interaction in semiconductors is observed for moderately doped polysilicon films and followed as a function of temperature. It is observed that the characteristic Fano-dip disappears at high temperatures while the line-shape also narrows considerably, indicative of the diminishing Fano-effect, whereby the hole-continuum is gradually destroyed by the free electrons from the ionised B acceptor sites, induced by the large thermal soaking periods (or thermal budgets) necessitated by SBS measurement conditions. An attempt was then made to relate these observations to SBS high temperature measurements of the same material under a similar heat treatment or annealing process. In the case of SBS results, a significant increase in bulk modulus (30 GPa) occurred between 200 and 400 ^{o}C thought to be signaling a growth in grain size of this polycrystalline film induced by the large thermal budgets. The insignificant increase in Young's modulus (E) with temperature is consistent with literature reflecting that silicon has a fairly stable E-value to temperatures as high as 1100^{o}C. In reference [7.5], the E- modulus of as-deposited polysilicon was ultrasonically determined to be having an effective value of 164 – 166 GPa and $\upsilon = 0.23$ after annealing at 1100^{o}C for 2 hours in nitrogen atmosphere.

The interesting observation of regeneration of the Fano-line asymmetry when the sample is cooled to room temperature was explained by considering the 'reverse-effect' to that of

thermal soaking for long periods which results in activation of the acceptor sites. When the sample is cooled down, there is not enough energy to maintain a breakdown of the activation energy barrier and so the favoured energy ground state would be such that ionised electrons return to the boron atoms and thus regenerate the hole-continuum with the Fermi energy level moving back into the valence band [7.32].

The Poisson's ratio measured at room temperature (0.26) shows good agreement with literature values for p-type silicon under the same conditions, whereas the Young's modulus value (168 GPa) measured at about 60^{o}C, indicates that this room-temperature deposited film performs just as well as crystalline silicon (p-type) operating at room temperature. In other words, this specimen shows no degradation effects as temperature is increased to 600^{o}C, which is the experimental limit for this investigation.

Finally, an attempt has been made to correlate phenomenon arising out of optical phonon interactions with results of acousto-optic investigations using SBS. The salient idea was to see if one could make a correlation between observations made in Raman spectroscopy, such as the cyclic behaviour of the line-shape, with similar cyclic properties observed using SBS under the same conditions. If such results were obtained, then one could draw a conclusion linking acoustic and optic phonon behaviour in semiconductors. The conclusion on this aspect is that there is no real direct correlation of physical processes responsible for the phenomena observed using Raman spectroscopy technique to those observed using SBS under the same conditions of temperature variation even though both techniques involve interactions with phonons. At 500^{o} C, the LO-TO phonon would have suffered ~ 2.8 % softening compared to *c*-Si values whilst the acoustic transverse mode suffers ~ 0.5 % reduction, which effects were explained by considering lattice expansion effects as well as phonon-phonon interactions which become significant at higher temperatures. Boron, being an acceptor of electrons presents a situation where if all B atoms are electrically activated, then the same number of free carriers as the B atoms are present. At such densities (~10^{19} cm^{-3}) and high temperatures, electronic contributions to the lowering of the elastic constants could become significant, according to the Keyes theory [7.41]. This means that of the total ~ 0.4 % softening

observed for C_{44} acoustic transverse mode at 500^{o}C, there would be small contribution from the electronic effects, though this contribution is difficult to quantify from such experiments as SBS. The significant overall result is that the boron-doped polysilicon semiconductor film is stable as temperature is raised to 600^{o}C in agreement with other available literature.

Chapter 8

8 Concluding remarks and outlook

The aim of the work presented in this thesis was to demonstrate the potential applications of surface acoustic waves (SAWs) measured using surface Brillouin spectroscopy on order to study elastic properties of different materials of technological value. In this work, the elastic constants were determined at room temperature and extended to higher temperatures where it was demonstrated that the elastic constants of some of the materials studied such as iron pyrite, show appreciable departure from general predictions of the quasi-harmonic theory as they exhibit influences of complex phonon-phonon interactions.

The use of SBS for measurement of elasticity and determination of the elastic tensor is a non-destructive technique, and this feature is certainly advantageous for studying semiconductors, rare materials such as new super or ultrahard materials being developed and more generally for materials science and technology at high temperatures in that one can work with very small samples. Elastic constants can be very important in cases where the material undergoes a structural transformation and an application was presented in the case of amorphous boron carbide film where a phase change to a possibly nanocrystalline state was observed when the film was heated at 350^{o}C. Another important result in this research on the B_4C film was the observation and subsequent simulation of excitations resembling organ-pipe modes, wherein it was demonstrated that these standing-wave excitations can be used in conjunction with Green's functions to successfully extract elastic constants of thin films that meet the necessary acoustic requirements.

In the work on B –doped polysilicon, in addition to measuring the elastic moduli as a function of temperature, the phenomenon of incident light penetrating substantially into the semiconductor was exploited by analysing the bulk TA phonons, their width being a measure of the attenuation of the incident light. From this analysis of bulk modes, useful information about the refractive index of B-doped polysilicon was obtained. The high-temperature study of the same material revealed that this MEMS material is structurally

stable up to high temperatures, in this case up to 500^{o}C, and the *E*-modulus is essentially stable at 164 GPa.

The elasticity tensor determined as a function of temperature provides very important reference information for modelling the behaviour of materials to be used under harsh conditions; and the elasticity data obtained for example, on boron-doped polysilicon has provided excellent feedback information. Additionally, the SBS technique allows one to obtain the elastic tensor as a function of temperature, for industrially important materials such as Ti alloys. In this study on TiC and TiCN, not only was the refractory nature of these alloys revealed but by closely monitoring the C_{11} and C_{44} elastic constants, it was noted that strong phonon-phonon interactions occuring at high temperatures produce deviations from the predictions of basic anharmonic theory.

In conclusion, several applications were presented in this thesis where Brillouin scattering was particularly successful in determining the elastic properties of materials. These involved determining elastic properties of small isotropic specimen, ranging from bulk samples to 'thin' films and single crystals and observing phase transformations. The most powerful aspect of SBS utilised in most of these applications is the possibility of probing the population of thermal acoustic phonons at the surface of the sample, more so since all of the population of surface excitations allowed by sample geometry can be observed via the ripple or elasto-optic contributions.

8.1 Future investigations on titanium compounds

The dependence of the elastic properties on temperature was determined in this investigation using one SAW, i.e. the Rayleigh mode only due to the nature and difficulty of working with these materials. However, it is also well-known that Ti forms a native oxide layer that provides the anti-corrosive characteristic, estimated to be 10 – 20 nm thick. When one considers the elastic constants of the rutile form of the oxide (*r*-TiO_2) which are: C_{11} = 267.4 GPa, C_{44} = 123.3 GPa and C_{12} = 180.8 GPa, and while TiC has C_{11} = 500.5 GPa and C_{44} = 188 GPa (and density of 4.28 gcm^{-3} for the oxide) one immediately notes the closeness of the density, C_{44} and C_{12} values. This observation

points to the idea that this oxide film can be used in a dispersion analysis with a possibility of observing Sezawa modes that can be used to extract elastic constants. So further work is envisaged whereby the titanium compounds are analysed together with the native oxide film as a film-on-substrate arrangement and Green's function methods applied to understand in detail the exact nature of such systems (whether, they are 'fast-on-slow' or converse), as well as extract the elastic constants of the subsrate, relying on the known information of the oxide film properties.

8.2 Future investigations on semiconductors

The interesting observations made at high temperatures, namely, the increase in bulk modulus of the semiconductor draws attention into the role of dopants, grain growth and lattice expansion at such conditions. In particular, SBS experimental conditions necessitate the use of large thermal budgets (product of set temperature and time) which inherently affects the growth characteristics of semiconductors in a different way to say SPEG (solid phase epitaxial growth or laser crystallisation techniques). With the emphasis in applying semiconductors in ever more extreme environments, it is pertinent to build a good understanding of the high temperature phonon acoustics of these materials. At high temperatures there is an interplay of many factors so that assuming lattice expansion only without understanding deeply the role of dopants under such conditions may prove inadequate. Free carriers have been known to influence elastic constants (Keyes theory [7.41]), particularly C_{44} in *p*-type silicon, and this can be correlated with thermal activation of boron at high temperatures. Thus it is envisaged that a joint SBS – electrical conductance experiment set-up for high temperature conditions would yield some clearer dependences and enable a better understanding of the response mechanism of semiconductors under extreme conditions of temperature.

8.3 Future investigations at high temperature and pressure

Experimental SBS at high temperature and pressure remains a daunting task yet to be accomplished. A close look at the high temperature results of iron pyrite work on Chapter 4 shows that higher order terms need to be incorporated in order to reproduce the

significant curvature of the elastic moduli at high temperatures, beyond about 500 ^{o}C. Some theoretical work has been reported on the high pressure elasticity of iron pyrite, and it will be useful to conduct high-pressure SBS measurements and even combine with high-temperature as this enables one to simulate the deep-earth geophysical conditions. Similar work on other materials would be very useful as it will help in the refining of the simulation models currently in use.

Finally, I thank the patient reader who accompanied me along this journey of SBS at high temperatures, exploring the very interesting phenomena along the way ……..

References and Bibliography

Chapter 1

1.1 L. Brillouin, Ann. Phys. (France) **17**, 88-96 (1922)

1.2 L.I. Mandel'shtam, Zn. Russ. Fiz. Khim. Obschchestra **58**:381 (1926)

1.3 E. Gross, Nature **126**: 201 (1930)

1.4 E.H.L Meyer and W. Ramm, Physik Z. **33**, 270 (1932)

1.5 Lord Rayleigh, London Math. Soc. Proc. **17**, 4 (1887)

1.6 G.I. Stegeman and F. Nizzoli in *Surface Excitations*, edited V.M. Agranovich and R. Loudon (Amsterdam), Ch. 4 page 195 (1984)

1.7 H. Lamb, Philos. Trans. R. Soc. London Ser **A203,** 1 (1904)

1.8 A.E. H. Love, *Some Problems in Geodynamics* (Cambridge University Press)

1.9 K. Sezawa et al., Earthquake Research Hist. (Tokyo) **17**, 1, (1939)

1.10 Stoneley, Proc. Roy. Soc. ,**106**, 416 – 428 (1924)

1.11 G.B. Benedek and K. Fritsch, Phys Rev **149**, 647 (1966)

1.12 J D Comins, Chapter 15, in *Handbook of Elastic Properties of Solids, Liquids, and Gases,* edited by Levy, Bass, and Stern. Vol 1: *Dynamic Methods for Measuring the Elastic Properties of Solids* (Academic Press 2001).

1.13 MG Beghi, AG Every and P Zinin, in *Brillouin Scattering Measurement of SAW Velocities for Determining Near-Surface Elastic Properties,*(CRC Press LLC, 2004).

1.14 Recent successful SBS results on new ultrahard diamond-like BC_x materials synthesized in laboratory conditions of HPHT in France

1.15 J.G. Dil, Rep. Prog. Phys., Vol. **45**, 286 – 297 (1982)

1.16 Mutti P, CE Bottani, G Ghislotti, M Beghi, GAD Briggs and JR Sandercock, *Advances in Acoustic Microscopy,* Vol **1**, Ch 7, Plenum Press NY, ed. A. Briggs (1995)

1.17 Bergman L, *Ultrasonics* (Bell, London) page 164 (1938)

1.18 A. Maradudin and D. L. Mills, Phys. Rev B**11**: 1392 (1975)

1.19 A. M. Marvin V. Bortolani, F. Nizzoli, J. Phys C**13**:299 (1980)

1.20 G.S. Agarwal, Phys. Rev. B**15**:2371 (1977)

1.21 V. Bortolani, A M Marvin, F. Nizzoli, G. Santoro, J. Phys. C:Solid State Phys. **16**:1757 – 1777 (1983)

1.22 Mishra and Bray, Phys. Rev. Lett. **39**:222 (1977)

1.23 A. S.Pine Phys. Rev B**5**, 2997 (1972)

1.24 J. R. Sandercock Phys. Rev. Letters 28, 237 (1972)

1.25 G. Dresselhaus and A.S. Pine Solid St. Commun. **16**:1001 (1975)

1.26 A. Dervisch and R. Loudon, J. Phys. C**9**, L669 (1976)

1.27 D.L. Mills, AA Maradudin, E Burstein, Ann. Phys **56**: 504 – 524 (1970)

1.28 B.I. Bennet, A A Maradudin, L R Swanson, Ann. Phys NY **71**: 357 (1972)

1.29 M.W. Elmiger, Doctoral Thesis, *Raman scattering under high pressure in samariumselenide and Brillouin spectroscopy from surface acoustic waves,* Swiss Federal Institute of Technology, Zurich (1988)

1.30 K.R. Subbaswamy and A.A. Maradudin Phys. Rev. B**18**:4181 -99 (1978)

1.31 A.G. Every, *Handbook of Elastic Properties of Solids, Liquids and Gases,*ed. Levy, Bass and Stem, vol.1 chapter 1, Academic Press (2001)

1.32 S. B. Tlali, B A Mathe, J D Comins AG Every, Phys. Stat. Sol C**11**:3073 – 3076 (2004)

1.33 A.M. Marvin, V. Bortolani, F. Nizzoli and G. Santoro, J. Phys C**13**, 1607 (1980)

1.34 B.A. Auld, *Acoustic Fields and Waves in Solids,* vol 11, J. Wiley (1973)

1.35 F. Nizzoli and J.R. Sandercock, *Dynamical Properties of Solids, ed. G.K. Horton and A. A. Maradudin, chapter 5.* Elsevier (1990)

1.36 G.W. Farnell and E.L Adler, *Physical Acoustics,* vol 9 (W.P. Mason and R.W. Thurston eds.) Academic Press (1972), p. 35

1.37 G. W. Farnell, in *Physical Acoustics* vol VII, ed. W. P. Mason, Academic Press page 109 (1970)

1.38 G.W. Farnell, in *Surface Acoustic Waves, Topics in Applied Physics*, vol 24 ed. A.A. Oliner, Springer (1978), page 13

1.39 G. W. Farnell and E.L. Adler, in *Physical Acoustics* vol IX, ed. P. Mason and R.W. Thurston, Academic Press (1972), page 35

1.40 F.E. Stanke and G.S. Kino, J. Acoust. Soc. Am. **75**, 665 (1984)

1.41 M.F. Markam, Materials Research **1**, 107 (1962)

1.42 L.L. Bonilla and J.B. Keller, J. Mech. Phys. Solids **33**, 241 (1985)

1.43 I.M. Kaganova and A.A. Maradudin, Physica Scripta vol. T**44**, 104-112 (1992)

1.44 L.M. Lifshitz and L.N. Rosenzweig, Zh. Eksp. Teor. Fiz. **16**, 967 (1946). Ibid **21**, 1184 (1951)

1.45 J.F. Nye, *Physical Properties of Crystals* (Oxford: Clarendon) (1985)

1.46 T.C.T. Ting, *Anisotropic Elasticity: Theory and Applications* (Oxford: Oxford University Press) (1996)

1.47 R. Hill, *The elastic behaviour of a crystalline aggregate,* Proceedings of the Physical A**65**, 349-354 (1952)

1.48 R.F.S. Hearmon, *The elastic constants of polycrystalline aggregates*, Physics of the Solid State, New York Academic p. 401 (1969)

1.49 Watt J P, *The elastic properties of composite materials,* Reviews of Geophysics and Space Physics **14**: 541-563 (1976)

1.50 E. Anastassakis and M. Siakavellas, J. Appl. Phys. **90** (1) 144 – 152 (2001)

1.51 M.G. Beghi, A.G. Every, P.V. Zinin, *Ultrasonic Nondestructive Evaluation, chapter10.* CRC Press LLC (2004).

Chapter 2

2.1 L.D. Landau and E.M. Lifshitz, in *Theory of Elasticity* (Pergammon Press) (1959)

2.2 I. Fredholm, Acta Math. (Stockholm) **23**: 1 (1900)

2.3 A G Every, KY Kim, A A Mazenev, J. Acoust. Soc. Am. **102**:1346 (1997)

2.4 J. H. M. T. van der Hijden in *Propagation of transient elastic Waves in Stratified Anisotropic Media* (North Holland), (1957)

2.5 R. Loudon, Phys. Rev. Lett. **40**, 581 (1978)

2.6 A.G. Every, Meas. Sci. Technol. **13**, R1- R19 (2002)

2.7 P.R. Stoddart, *Surface Brillouin Scattering Studies of High Temperature Elasticity.* PhD thesis, University of the Witwatersrand, Department of Physics, Johannesburg, South Africa, 1999.

2.8 K. Brugger, Phys. Rev **133**:A1611(1964)

2.9 Thurston and Brugger, Phys. Rev **133**:A1604 (1964)

2.10 Y. Hiki, J F Thomas, A V Granato, Phys. Rev **153**:764 (1967)

2.11 K.D. Swartz, J. Acoust. Soc. Am. **41**:1083 (1967)

2.12 Garber and Granato Phys Rev B**11**:3990 (1975a)

2.13 Garber and Granato Phys Rev B**11**:3998 (1975b)

2.14 N.W. Ashcroft and N.A. Mermin in *Solid State Physics* (Saunders College, Phil), (1987)

2.15 A.R. Oganev, P. Dorogokupets, J. Phys: Condens. Matter **16,** 1351 – 1360 (2004)

Chapter 3

3.1 E. Gross, Nature **126**, 201 (1930)

3.2 P. Fleury, in *Physical Acoustics* p.1, vol 6, Mason W., and Thurston R., eds,. New York Academic (1970)

3.3 J.R. Sandercock, Proc. 2nd Int. Conf. On Light Scattering in solids ed. M. Balkanski, Paris: Flammarion p. 9 – 12

3.4 J. R. Sandercock, Solid State Commun. **26**, 545-551 (1978)

3.5 J.R. Sandercock, *Operator Manual for tandem interferometer,* version 3 (1993)

3.6 R. Mock, B. Hillebrands and J. R. Sandercock, J. Phys. E: Sci. Instrum. **20**, 656 (1987)

3.7 P. Mutti, E Bottolani, G Ghislotti, M Beghi, J R Sandercock, GAD Briggs, *Advances in Acoustic Microscopy*, vol.1, ed. A. Briggs, Plenum Press (1995)

3.8 R. Loudon and J.R. Sandercock, J. Phys. C**13**, 2609-22 (1980)

3.9 M.W. Elmiger, *Raman Scattering under High Pressure in Samarium Selenide and Brillouin Spectroscopy from Surface Acoustic Waves,* PhD thesis, Eidgnenössiche Technische Hochschule, Zurich, Switzerland, (1988)

3.10 J.C. Crowhurst, *Surface Brillouin Scattering Studies of high Pressure Elasticity.* PhD thesis, University of the Witwatersrand, Department of Physics, Johannesburg, South Africa, 2001.

3.11 P. Mutti, *Surface Acoustic Waves for Semiconductor Characterisation.* D Phil thesis Oxford University (1993).

3.12 F. Adar, *Handbook of Raman Spectroscopy,* Marcel Dekker, NY (2001) eds. Lewis IR, Edwards HGM.

Chapter 4:

4.1 G. A. Saunders, W Qingxian, E F Lambson, N Lodge, D Paine, W Honle, J. Phys : Condens. Matter **2** 3713 (1990)

4.2 W. Voight, Lehrbuch der Kristallphysik (Leipzig: B.G. Teubner), p.741 (1928).

4.3 N. Benbattouche, G. A. Saunders, E. F. Lambson and W. Honle, J. Phys. D: Appl. Phys. **22** 670 (1989).

4.4 A.E. H. Love, in *A treatise on the mathematical theory of elasticity* (Dover, 1944) 4th edtn

4.5 G. Simmons and F. Birch, J. Appl. Phys., **34** 2736, (1963).

4.6 L. Pauling in The Nature of the chemical bond (Ithaca NY: Cornell University Press) page 181(1945)

4.7 W. Bindloss, J. Appl. Phys. **42** 1474 (1974).

4.8 http:www.fis.unipr.it/bersami.

4.9 M. Krs, M Novak, M Krsova, P Pruner, J Jansa, Phys. Earth planet. Inter. **70**:273-287 (1992)

4.10 M. Sithole, *Elastic and Atomistic Simulation Studies of iron disulphide* PhD. Thesis, University of the North (2000)

4.11 C de las Heras, I J Ferrer, C Sanchez, J. Phys. Condens. Matter **6**:10177 -10183 (1994)

4.12 M.J. Dekker et al., Geophys. J. Int. **141**, 809- 819 (2000)

4.13 G. T. Lindroth, in *Rock-forming minerals vol.5, non-silicates: sulphides* by W.A. Deer, R.A. Howie and J. Zussman

4.14 G. Leibfried and W. Ludwig, in Solid State Physics, ed. F. Seitz and D. Turnbull (New York, Academic) page 276

4.15 H. M. Sithole, P E Ngoepe, K Wright, Phys. Chem. Minerals **30**, 615 (2003)

4.16 S. Merkel, A. P. Jephcoat, J. Shu, H. K. Mao, P. Gillet and R. J. Hemley, Phys. Chem. Minerals, **29** 1-9, (2002).

4.17 P.E. Ngoepe and S.C. Parker, Mol Sim **8**, 345 (1992)

4.18 P.J. Chaba, P.E. Ngoepe, P.E. Mol. Sim. **21**, 161, (1998)

4.19 P.J Botha, J.C.H. Chiang, J.D. Comins, P.M. Mjwara, P.E. Ngoepe, J. Appl. Phys. **73**, 7268, (1993)

4.20 P.E. Ngoepe, W.M. Jordan, C.R.A. Catlow and J.D. Comins, Phys Rev. B**41**, 3815, (1990),

4.21 T.T. Netshisaulu, P.E. Ngoepe, J.D. Comins and C.R.A. Catlow, Rad Effects and Defects in Solids), **134,** 111 (1995)

4.22 J.A. Garber and A.V. Granato, Phys. Rev. B**11**, 3990, (1975)

4.23 P.M. Mjwara, J.D. Comins, P.E. Ngoepe, W. Buhrer and H. Bill, J. Phys. Condensed Matter **3**, 4289, (1991)

4.24 J.D. Gale, J. Chem. Soc. Faraday Transactions, **93**, 629. (1997)

4.25 B.G. Dick and A.W. Overhauser, Phys. Rev., **112**, 90, (1958)

Chapter 5:

5.1 L.I. Johansson Surf. Sci. Rep. **21**: 177 (1995)

5.2 M. Ohring in The Materials Science of Thin films (San Diego, CA: Acad) 1992

5.3 Introduction to Transition Metal Carbides, Chapter 8: www.ropine.com

5.4 E.K**.** Storms, The Refractory carbides, Academic Press, New York (1967)

5.5 W. Lengauer, Handbook of Ceramic Hard Materials ed. R. Riedel (Wiley–VCH)

5.6 I.J. Jung et al., Acta Mater. Vol 47 (11), 3219 -45 (1999)

5.7 G. E. Hollox, Review Paper(1968): *Microstructure and Mechanical Behaviour of Carbides* published in Mater. Sci. Eng.,**3**, 121-137, (1968/69)

5.8 C. Kral, W. Lengauer, D Rajafa, P Ettmeyer, Critical Review on the elastic properties of transition metal carbides, nitrides and carbonitrides; J. Alloys and Compounds **265** , 215-233 (1998)

5.9 P.T. Jochym, Euro. Phys. Journal **B10**, 9-13 (1999)

5.10 D. J. Rowcliffe, G E Hollox, J. Mat. Sci. **6**, 1270 -1276 (1971)

5.11 V. Bortolani, F. Nizzoli, G Santoro, Surface density of acoustic Phonons in GaAs; Phys Rev **41** (1) 39 – 42 (1978)

5.12 E. Török, A J Perry, Thin Solid Films, **153**, 37 (1987)

5.13 C. Kral, W Lengauer, D Rajafa, P Ettmeyer, J. Alloys Comp., **265**, 215 (1998)

5.14 H.S. Kim, G Bugli, Djega-Mariadassou G, J. Solid St. Chem. **142**, 100 (1999)

5.15 S. Jhi, SG Lovie, M L Cohen, JW Morris, Phys Rev Letters **87** (7), 075503-1

5.16 M. Guemmaz, G Moraitis, A Mosser, MA Khan, JC Parkbas, J. Phys: Condens. Matter **9**:8453 – 63 (1997)

5.17 SAIP 2003 Poster by J.A.A. Engelbrecht, UPE (R.S.A.), S. Kang (Seoul National University); XRD Determination of $TiC_{1-x}N_x$ Alloy concentrations.

5.18 S.T. Oyama, Solid State Chem. **96** : 442 (1992)

5.19 G.G. Fuentes, E Elizalle, J M Sanz, J. Appl. Phys. **90** (6) 2737 – 43 (2001)

5.20 W. Pang, AG Every, JD Comins, PR Stoddart, X Zhang, J. Applied Physics **86**, Vol1, 311-317, (1999)

5.21 TiC JPDS Card Number 32-1383 (Cu K_α radiation)

5.22 SAIP 2003 by JAP Engelbtracht (UPE) and S. Kang (Seoul National University); 'XRD Determination of $TiC_{1-x}N_x$ alloy concentrations.'

5.23 L. Pintschovius, W Reichardt, B Scheeres, J. Phys C : Solid State Phys. **11**, 1557 (1978)

5.24 M. Amer, MW Bassoum, EL Raghy, I Weiss, S Lechair, D Liptak, Journal of Applied Physics **84** (10), 5817-5819 (1998)

5.25 R. Kieffer and F. Kölbl, Powder Met. Bull. 4, 4 (1949)

5.26 Toth L. E. *Transition Metal Carbides and Nitrides;* Academic Press NY 1971

5.27 Tracy H.J. PhD Thesis, Massachusetts Institute of Technology, Cambridge, MA, 1990

5.28 www.timet.com/cod-p11.htm

5.29 P. Lindahl, A E Rosen, P Gustafson, U Rolander and HO Andren, in International Journal of Refractory Metals and Hard Materials vol 18 (6), 273 – 279 (2000)

5.30 W. Minnear and R C Bradt, Elastic properties of polycrystalline TiO_{2-x}, J. American Ceramic Society **60**, 458 (1977)

5.31 www.ropine.com/chapter8.html

5.32 R. Jorna, D Visser, V Bortolani, F Nizzoli, J. Appl. Phys. **65** (2) :718 -25 (1989)

5.33 Albuquerque, R Loudon and D R Tilley, J. Phys. C: Solid St. Phys. **13** :1775 -89 (1980)

5.34 R Mock and G Güntherodt, J. Phys. C: Solid State Phys., **17**, 5635 – 5644 (1984)

5.35 R. Chang, L.J. Graham, Journal of Applied Physics **37**, 3778 (1966)

5.36 D.A. Speck et al, Carborundum Company Report, 1968, cited in.

5.37 R.A. Young, in the Rietveld Method: Oxford University Press, NY 1993

5.38 A.K. Cheetham and P. Day in Solid State Chemistry: Technique, Oxford Press University , 1974

5.39 G.S. Upadhyaya, Nature and Properties of Refractory Carbides, page 429

5.40 S-H Jhi, J. Ihm, Phys Rev B**56**, 13826 (1997)

5.41 N.A. Ivanov, SI Alyamovskii, BV Mifanov, Elastic properties of nonstoichiometric titanium carbonitrides; Izvestiya Akademii Nauk, USSR, Neorganicheskie Materialy, Vol **12** no. 7, pp1209 -1211 (1976)

5.42 G. Levi, WD Kaplan, M Bamberger, Structure Refinement of (TiCN); Materials Letters **35**, 344 -350 (1998).

5.43 C.R. Krann, J. W. Morris Jr, S-H Jhi and J. Ihm; paper entitled :"Relationships between Atomistic Bonding and Intrinsic Macroscopic Hardness".

5.44 W.B. Holzapfel, Phys. Rev. B**67**, 026102 (2003)

5.45 M.H. Grimsditch, A. K. Ramdas, Elastic, Elasto-optic constants of rutile from Brillouin study, Phys Rev **B14**, 1670 (1976)

5.46 Lynch, C G Olson, DJ Peterman, Phys Rev **B22** (8) 3991 (1980)

5.47 Z. Sklar, in *Quantiative Acoustic Microscopy of Coated Materials*, University of Oxford, 1993

5.48 K. Aimer et.al, J. Alloys and Compounds, **215**,121 – 126 (1994)

5.49 CRC Handbook of Materials Science, vol II (Metals, Composites and Refractory Materilas) by Charles T. Lynch, CRC Press , 1974 – 1980

5.50 X Zhang and R. Sooryakumar, Appl. Phys. Lett. **80** (24), 4501 – 4503 (2002)

5.51 P Jedrzejowski, JE Klemberg-Sapiela and L. Martinu, Thin Solid Films 466, 189-196 (2004)

Chapter 6

6.1 C. Wood, D Emin, Phys. Rev **B**29, 4582 (1985); D. Emin, ibid. **38**, 6041 (1988); in Boron-rich Solids, edited by D. Emin, T.L. Aselage, A.C. Switedick, B. Morosin and C.L. Beckel (AIP, New York, 1991) pp 65 -76.

6.2 N. K. Bourne, Proc Royal Society London **A**, **458**, 1999-2006 (2002)

6.3 G. A. Samara, HL Tardy, EL Venturini, EL Aselage, D Emin, Phys Rev **B48**, 1468 (1993)

6.4 R. Telle in M.V. Swain (Ed.), Structure and Properties of Ceramics, Materials Science and Technology, vol. 11 VCH Publishers, Weinheim (1994), pp 173-266.

6.5 R.R. Ridgeway, Trans. Am. Electrochem. Soc. **66**,117 (1934)

6.6 W.D. Nix, Mater. Sci. Eng., **A37**, 234 -236 (1997)

6.7 W.C. Oliver and G. Pharr: J. Mater. Res., **7**, 1564-1580 (1992)

6.8 J-H Ahn and D. Kwan, Mater. Sci. Eng., **A253**, 151 -172 (1998)

6.9 B. Rother and D. A. Dietrich: Surf. Coat. Technol.,**614**, 74 – 75 (1995)

6.10 R.A. Adrienski, Mater. Trans. 42, 1471 (2001)

6.11 S. Veprek and S. Reiprich: Thin Solid Films **64**, 264 (1995)

6.12 V. Provenzano and R.L. Holtz: Mater. Sci. Eng., **A204**, 125 (1995)

6.13 A.A. Voevodin J. P. O'Neill, J. S. Zabinski., Surf. Coat. Technol. **36**, 116-119 (1999)

6.14 S. Zhang, Y. Q. Fu, and H.J. Du, Surf. Coat. Technol, in press.

6.15 S. Veprek and M Haussmann, Surf. Coat. Technol. **394**, 86-86 (1996)

6.16 http://scienceworld.wolfram.com/physics/FresnelEquations.html

6.17 S. Ulrich, H. Holleck, H. Lieste, L. Niederberger, E. Nold, K. Sell, M. Stubber, J. Ye, C. Ziebert, P. Pesch, S. Sattel; Surf. Coat. Technol. **200**, 7 -13 (2005)

6.18 J.P. Mollart and M. Baker, Surf. Coat. Technol. **491**, 74 -75 (1995)

6.19 Y Chen, Y-W Chung, S.Y Li, Surf. Coat. Techn. **200**, 4072 – 4077 (2006)

6.20 Private Communication with Thomas Wittkowski (University of Kaiserslautern)

6.21 B. J. Hinch, C Koziol, JP Toennies, G Zhang, Europhys. Lett. **10**, 341 (1989)

6.22 N.S. Luo, P Ruggerrone, JP Toennies, Phys. Rev. **B54**, 5051, (1996)

6.23 X Zhang R Sooryakumar, A G Every and M Manghnani, Phys Rev **B64**, 081402(R), 2001

6.24 X. Zhang R S Badhu and R Sooryakumar , Phys. Rev. **B67**, 075407 (2003)

6.25 X. Zhang, JD Comins, AG Every, PR Stoddart, W Pang, Phys. Rev. **B58**, 13677 (1998)

6.26 V. Domnich, Y Gogotsi, Y Dub, Applied Physics Letters **81**, 3783, (2002)

6.27 I A Bairameshvili, J Less Common Metals **67**, 455 (1979)

6.28 A Link, R Soorykumar and RS Bandhu, J. Appl. Phys. **100**, 013507 (2006)

6.29 Landolt Bornstein Group III Vol. 41 Subvolume C, page 15

6.30 PhD Thesis of Thomas Wittkowski (University of Kaiserslautern), page 97-100

6.31 G.A. Gogotsi, V Domnich, J. Less Common Metals **117** ,225 -230, (1986)

6.32 Y Chen, Y-W Chung and S-Y Li, Surface Coatings Technology **200**, 4072 - 4077 (2006)

6.33 MU Guruz, VP Dravid and YW Chung, Thin Solid Films **414**, 129 (2002)

6.34 LG Jacobsohn, RD Averitt and M Nastasi, J. Vac. Sci. Technol., A, Vac. Surf. Films **21** (5), 1639 (2003)

6.35 S Aoqui, H Miyata, T Ohshima, T Ikegami and K Ebihara, Thin Solid Films **407**, 126 (2002)

6.36 S Ulrich, H Holleck, H Leiste, L Niederberrger, E Nold, K Sell, M Stuber, J Ye, C Ziebert, P Pesch and S Sattel, Surface and Coatings Technology **200**, 7-13 (2005)

6.37 A V Somonov, OG Tovmachenko and VM Puzikov, Journal of Wide Bandgap Materials, **9**, (3), 139 – 147 (2002)

6.38 H-Y Chen, J Wang, H Yang Surface Coating Technology **128/129**, 329-333 (2000)

6.39 Z Han, G Li, J Tian and M Gu, Materials Letters **57**, 899 – 903 (2002)

6.40 T. Wittkowski, J. Jorzick, K. Jung, B Hillebrands, Thin Solid Films **333**, 137 – 143 (1999)

Chapter 7:

7.1 X Zhang, J D Comins, A G Every, P R Stoddart and W Pang, Phys. Rev **B58**, 13677 – 13685, 1998+

7.2 H. Mahfoz-Kotb, A C Salaun, T Mohammed-Brahim, F Le Bihan and M El-Marssi, Thin Solid Films **427**, 422 – 426 (2003)

7.3 I. De Wolf, Spectrscopy Europe 15/2 (2003)+

7.4 P. Lengsfeld, S Brehme, K Brendel, Ch Genzel and N H Nickel , phys stat sol (b) **235**, 170 -178 (2003)

7.5 D. Maier-Schneider, A Koprululu, S Ballhauen Holm and E Obermeier, J. Micromech. Microeng. **6**, 436-446, (1996)

7.6 M. Beghi, A.G. Every and P. Zinin in *Ultrasonic Nondestructive Evaluation*, CRC Press, 2004

7.7 F Cerdeira and M Cardona, Phys. Rev **B5**, 1440 (1972) +

7.8 A M Marvin, V Bortolani, F Nizzoli and G Santoro, J. Phys. C: Solid St. Phys., **13,** 1607 – 16, (1980)

7.9 K.S. Chen, AA Ayon, SM Spearing, J. Amer. Ceram. Soc. Vol **83** p1476-84 (2000)

7.10 J R Sandercock, Solid State Comm. **26**, 547, (1978)

7.11 C.H. Mastrangelo, Tribo. Lett. Vol **3**, p223 – 238, (1997)

7.12 V.T. Srikar and S.M. Spearing, J. Microelectromech. Syst., vol **12**, p3-10 (2003)

7.13 V.T. Srikar, AK Swan, MS Ünlü, BB Goldberg and SM Spearing, J. Microelectromech. Syst., vol **12** p779 – 787 (2003)

7.14 HJ Pan, HKH Choy, proc. IEEE Solid State Sensors and Actuators Workshop (Hilton Head Island, SC , p70-73 (1990)

7.15 M. J. Pelletier, Analytical Applications of Raman Spectroscopy, Oxford, U.K.: Blackwell Science (1999)

7.16 E. Anastassakis, A Pinchuk, E Burstein, F Pollak, M Cardona, Solid State Commun., vol **8** p133 – 138 (1970)

7.17 D. Goustouridis et al, Sens. Actuators, vol **A76** p 403-408, (1999)

7.18 V.T. Srikar et al, proc. Materials Research Society Symposium vol.741, J9.5 (2003)

7.19 Oei D-G and S.L. McCarthy, Mater. Res. Soc. Symp. Proc. **276**, 85 – 90 (1992)

7.20 R. Mock and G Guntherodt, J. Phys. C: Solid State Phys. **17** 5635 - 5644(1984)

7.21 E. Anastassakis and E. Liarokapis, J. Applied Phys. **62** (8), 3346-52 (1987)

7.22 S. Polymenakos, V C Stergiou, A G Kontos, C Tsamis, Y S Raptis and D Tsoukalas, J. Micromech Microeng. **12**, 450 – 457 (2002)

7.23 A.T. Fiory, K K Bourdelle, Y Chen, Y Ma, J M McKinley, P K Roy and H W Koh, in *Implant and annealed Methods for PSMOS gates* in Electrochemical Society, 199th meeting, Washington DC, 2001.

7.24 R. Kalyanaraman, V C Venezia, L Pelaz, T E Haynes H-J L Gossmann and C S Rafferty, Appl. Phy Lett **82**, 215 (2003)

7.25 J. D. Comins, the *Handbook of Elastic Properties of Solids, Liquids and Gases*, vol 1: " Surface Brillouin Scattering", eds M. Levy, H.E. Bass and R. Stern, Academic Press, New York, (2001)

7.26 F. H. Horn, Physical Review vol. **97,** 1521 (1955)

7.27 A.K. Sood and M. Cardona, Solid State Communications, vol. **60**, (8), p629 -631 (1986)

7.28 F. Cardeira and M. Cardona, Phys. Rev B **5**, 1440 (1972)

7.29 M. Balkanski, K P Jain, R Beserman and M Jouanne, Phys. Rev B**12**, 4328 (1975)

7.30 M. Chandrasekhar, J B Renucci and M Cardona, Phys Rev **B22**, 4825 – 4833 (1980)

7.31 U. Fano, Phys Rev **124**, 1866 (1961)

7.32 R Gajić, D Braun, F Kuchar, A Golubovic, R Korntner, H Loschner, J Butchke, R Springer and F Letzkus, J. Phys. Condens. Matter **15** (2003), 2923 -2931

7.33 Chi Hsiang Pan, J. Micromech. Microeng. **12**, 548 – 555 (2002)

7.34 V. Paillard, M. A. Laguna, P. Puech, P. Temple-Boyer, B. Caussat, J. P. Couderc, B. de Mauduit, Appl. Phys. Lett. **73** (12), 1718 – 1720 (1998)

7.35 Jie Yang, H Kahn, An-Qiang He, S M Phillips, A Heuer, IEEE J. Micromech. Sys. vol **9** (4), 485 – 487 (2000)

7.36 N.H. Nickel, P Lengsfeld and I Sieber, Phys Rev **B 61**, 15 558 – 15 561, (2000)

7.37 A.T Collins, Mater. Sci. Eng. **B11**, 257 (1992)

7.38 SK Donthu, S Tripothy, DZ Chi, JS Chua, J. Raman Spectrosc. **35**, 536-540, (2004)

7.39 Tor A Fjedly, F Cerdeira and M Cardona, Phys Rev **B8**, 4734 (1973)

7.40 L. M. Kotane, MSc thesis, University of the Witwatersrand, South Africa (in preparation)

7.41 R. W. Keyes, *Solid State Physics* ed. F. Seitz, D. Turnbull and H. Ehrenreich, vol 20, p37-90 (1967)

7.42 C Kittel, *Introduction to Solid State Physics*, 5th edition, John Wiley & Sons, New York, 1976

7.43 J W Ager, W Walukiewicz, M McCluskey, M Plano and M I Landstrass, Appl. Phys. Lett. **66**, 616, 1995

7.44 C Li, Y-Li Chin and P Wu, Intermetallics **12**, 103 -109, (2004)

PUBLICATIONS

Publications of Conference Proceedings

1. 'High frequency organ-pipe modes in amorphous boron carbide observed using surface Brillouin scattering' by B.A. Mathe, J.D. Comins and A.G. Every ; PHONONS 2007 Conference publication in Journal of Physics : Conference Series **92** (012096) (2007) .
2. 'The study of guided waves in surfaces and thin supported films using surface Brillouin scattering and acoustic microscopy' by A.G. Every, B. A. Mathe and J.D. Comins ; Ultrasonics **44**, e929-e934 (2006).
3. 'Brillouin scattering studies and computational simulations of the elastic properties of pyrite (FeS2) at high temperatures' by S. B. Tlali , B. A. Mathe, L. M. Kotane, F.R.L. Schöning , J.D. Comins , A.G. Every , H.M. Sithole , P.E. Ngoepe, K.V. Wright; physica status solidi c**1** , No.11, 3073-3076 (2004)

Presentations /Conference Reports

1. 2nd International Conference of the African Materials Research Society, University of Witwatersrand, Johaneesburg, South Africa (2003); Oral Paper entitled 'Brillouin scattering studies of iron pyrite (FeS_2) at high temperatures' by S Tlali, B A Mathe, LM Kotane, JD Comins and AG Every.
2. 49th Annual Conference of the South African Institute of Physics (University of Free State, 2004) Oral paper entitled 'The High temperature elastic properties of iron pyrite determined by Brillouin scattering and computational simulations' by; S Tlali, B A Mathe, LM Kotane, FRL Schoning, JD Comins,AG Every, HM Sithole, PE Ngoepe and K Wright.
3. 50th Annual Conference of the South African Institute of Physics (University of Pretoria, 2005) Poster presentation entitled 'High temperature surface Brillouin scattering studies of an amorphous boron carbide film' by; B A Mathe, JD Comins, AG Every, and T Wittkowski.

4. 3rd International Conference of the African Materials Research Society, Marrakech, Morroco (2005); Oral Paper entitled ‘High temperature surface Brillouin scattering studies of an amorphous boron carbide film’ by; B A Mathe, JD Comins, AG Every, and T Wittkowski.
5. 52nd Annual Conference of the South African Institute of Physics (University of Witwatersrand, 2007) Oral presentation entitled ‘High temperature elasticity of polycrystalline $TiC_{0.97}$ and $TiC_{0.4}N_{0.6}$ alloys studied by surface Brillouin scattering ’ by; B A Mathe, JD Comins, AG Every, and W Lenguer.
6. PHONONS 2007 Conference, Paris, France; Poster presentation entitled ‘High temperature elasticity of titanium alloys determined using SBS’ by B.A. Mathe, J.D. Comins and A.G. Every ’ .